SYSTEM-LEVEL PERFORMANCE AND RELIABILITY OF SOLAR PHOTOVOLTAIC FARMS: LOOKING AHEAD AND BACK

by

Muhammed Tahir Patel

A Dissertation

Submitted to the Faculty of Purdue University

In Partial Fulfillment of the Requirements for the degree of

Doctor of Philosophy

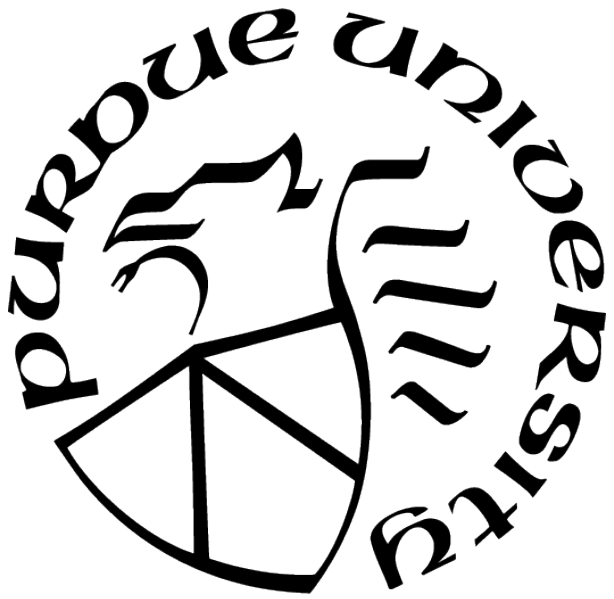

School of Electrical and Computer Engineering

West Lafayette, Indiana

December 2021

THE PURDUE UNIVERSITY GRADUATE SCHOOL
STATEMENT OF COMMITTEE APPROVAL

Dr. Muhammad Ashraful Alam, Chair

Department of Electrical and Computer Engineering

Dr. Mark Lundstrom

Department of Electrical and Computer Engineering

Dr. Peter Bermel

Department of Electrical and Computer Engineering

Dr. Rakesh Agrawal

Department of Chemical Engineering

Approved by:

Dr. Dimitrios Peroulis

Department of Electrical and Computer Engineering

I dedicate this thesis to my parents, my wife, and my sister who have been a great source of support and inspiration in my life.

ACKNOWLEDGMENTS

I would like to express my deepest and sincere gratitude to my advisor, Professor Muhammad A. Alam. I really appreciate his expert guidance, meaningful mentorship, constant care, and support throughout my Ph.D. I learnt several professional and personal qualities from him during this time. He is in his interactions with people. His approach to solving any problem is systematic and simple. I appreciate him working very closely with his students and colleagues. In his own words, “I like to work with you in the trenches." I have observed that this creates long-lasting personal and professional bonds. Moreover, his dedication and style of teaching is contagious. It is abundantly clear to me that he has had a life-lasting impact on me.

I sincerely thank Prof. Mark Lundstrom, Prof. Peter Bermel, and Prof. Rakesh Agrawal for not only being part of my Ph.D. committee but also providing insightful suggestions and constructive feedback during my research studies through in-person meetings and during NPT presentations. I would especially like to thank Prof. Bermel for providing me access to his computational resources for the high-speed and bulky worldwide simulations required for my research. Prof. Lundstrom always kept me aware of the “big picture" problem that we were trying to solve. On the other hand, Prof. Agrawal brought a very different perspective to my research through agro-photovoltaics and photovoltaic materials chemistry.

I acknowledge and appreciate my research collaborations with Dr. Ann Christine Catlin, Steven Clark, and W. Guneshi from Purdue University, Dr. Chris Deline, Dr. Michael Woodhouse, and Dr. Silvana Ayala Pelaez from National Renewable Energy Laboratory, Dr. Joshua Stein from Sandia National Laboratory, Dr. M. Ryyan Khan and M. Sojib Ahmad from East-West University, Dhaka, Dr. Ramachandran A. Vijayan from Sastra University, Thanjavur, and Dr. Hassan Imran and Dr. Nauman Butt from Lahore University of Management Science. I would like to thank Dr. Jim J. John and Dr. Aaesha Alnuaimi from Dubai Energy and Water Authority for sharing their experimental data with us.

I would like to thank Vicki Johnson, Christine M. Ramsey, Matt Golden, and Elisheba VanWinkle for assisitng me with all the administrative queries and process during my graduate school. The smooth handling of these processes helped me remain focused on my research.

Being part of the Alam CEED group has been a great learning and fulfilling experience. It would not have been possible without the past and previous members of the group. I have fond memories of the time spent in and out of the lab space while evolving as a graduate student with them. Thus, I would like to extend my heartiest thanks to the past group members - Mohammad Ryyan Khan and Xingshu Sun who were like co-mentors to me. Xin Jin, Woojin Ahn, Aida Ebrahimi, SangHoon Shin, Piyush Dak, Raghu V. K. Chavali, Ramachandran Vijayan, Hassan Imran, Nicolo Zagni, Amir Hanna, Ratul Baruah, and Hai Jiang who helped me with valuable discussions during the Ph.D. process. A warm thanks to the present lab mates - Reza Asadpour, Bikram Mahajan, Yen-Pu Chen, Marco Fratus, Ajanta Saha, Jabir Bin Jahangir, Md. AsaduzZaman Mamun, and Juan David - for all the insightful arguments, feedback, and banter during the day-to-day grind. I will truly cherish them. To my colleagues from other groups- Evan Witkoske, Mohit Singh, Allison Perna, Abhishek Shankar, Suchitra Ramesh, Yubo Sun, Zhiguang Zhou, Shuvro Chowdhury, and Jan Kaiser - I really enjoyed the sporadic conversations regarding all things under the sky. It helped me remain aware of the outside world and increased the breadth of my knowledge and I am grateful for that.

Finally, I have my deepest appreciation for my family - my parents, wife, sister, grandparents, my uncles and aunts. I am grateful to my wife, Safiya, for always comforting me, being patient with me, and helping me navigate through adulthood. She is a gem of a person. I am also thankful to have my sister, Sameera, who has been an inspiration for hard work and a silent guardian for me. Last but not least, I would like to show my utmost gratitude, respect, and love for my parents, Firoza Patel and Mehboob Patel without whom I would not be who I am today. They have truly been the ever-lasting supporters, advisors, and selfless carers of me. All of my achievements, including the completion of Ph.D., are dedicated to them.

TABLE OF CONTENTS

LIST OF TABLES

LIST OF FIGURES

ABSTRACT

In a world of ever-increasing demand for energy while preventing adverse effects of climate change, renewable energy has been sought after as a sustainable solution. To this end, the last couple of decades have seen an advancement in research and development of solar photovoltaic (PV) technology by leaps and bounds. This has led to a steady improvement in the cost-effectiveness of solar PV as compared to the traditional sources of energy, e.g., fossil fuels as well as contemporary renewable energy sources such as wind and hydropower. To further decrease the levelized cost of energy (LCOE) of solar PV, new materials and technologies are being investigated and subsequently deployed as residential, commercial, and utility-scale systems. One such innovation is called bifacial PV, which allows collection of light from the front as well as rear surfaces of a flat PV panel.

In this thesis, we present a detailed investigation of bifacial solar PV farms analyzed across the globe. We define the problem, explore the challenges, and collaborate with researchers from academia and the PV industry to find a novel solution.

First, we begin by developing a multi-module computational framework to numerically model a utility-scale bifacial solar PV farm. This requires integrating optical, electrical, thermal, and economic models in order to estimate the energy yield and LCOE of a bifacial PV system. The first hurdle is to re-formulate the LCOE so that the economist and the technologist can collaborate seamlessly. Thus, we re-parameterize the LCOE expression and validate our economic model with economists at the National Renewable Energy Lab (NREL).

Second, we extend the existing optical and electrical models created for *stand-alone* bifacial PV panels to models that can simulate a large-scale bifacial solar PV farm. This brings the challenge of mathematically modeling solar farms and light collection on the rows of PV panels elevated from the ground by taking into account the mutual shading between the rows, reflections from the ground, and elevation-dependent light absorption on the rear surface of the PV panels from several neighboring rows. Next, we integrate temperature-dependent efficiency models to take into account the effects of location-dependent ambient

temperature, wind speed, and technology-varying temperature coefficients of the solar PV system in consideration.

Third, we complete the comprehensive modeling of bifacial solar PV farms by including two types of single-axis tracking algorithms viz. sun-tracking and power tracking. Using these algorithms, we explore the best tracking orientation of solar farms i.e., East-West tracking vs. North-South tracking for locations around the world. We further find the best land type suitable for installation of these E/W or N/S tracking bifacial solar PV farms.

Fourth, we reduce the computation time of numerical modeling by utilizing the advantages of machine learning algorithms. We train neural networks using data from the already-built models to emulate the numerical modeling of a solar farm. Amazingly, we find the computation time reduces by orders of magnitude while accurately estimating the energy yield and LCOE of PV farms.

Fifth, we derive, compare, and experimentally validate the thermodynamic efficiency limits of photovoltaic-to-electrochemical energy conversion for the purpose of storing solar energy for future needs.

Finally, we present some new ideas and guidelines for future extensions of this thesis as well as new challenges and problems that need further exploration.

1. INTRODUCTION

In the wake of dramatic climate change across the globe, renewable energy has received widespread attention from academia and industry. Amongst the various types of energy sources, solar energy is one of the front-runners for the renewable energy growth around the world [1]–[4]. To compare the economic viability of various sources of energy, e.g., wind, hydropower, coal, natural gas, solar energy etc. [5], [6], the energy research community uses levelized cost of energy (LCOE) as a techno-economic metric. As shown in Fig. 1.1, solar energy is cost-competitive with with other sources of energy [7], [8]. The costs for utility-scale solar (about 11% per year) as well as onshore wind (about 5% per year) have been declining over the past five years [7], [8], as shown in Fig. 1.2. The rate of decline, however, has reduced over the years.

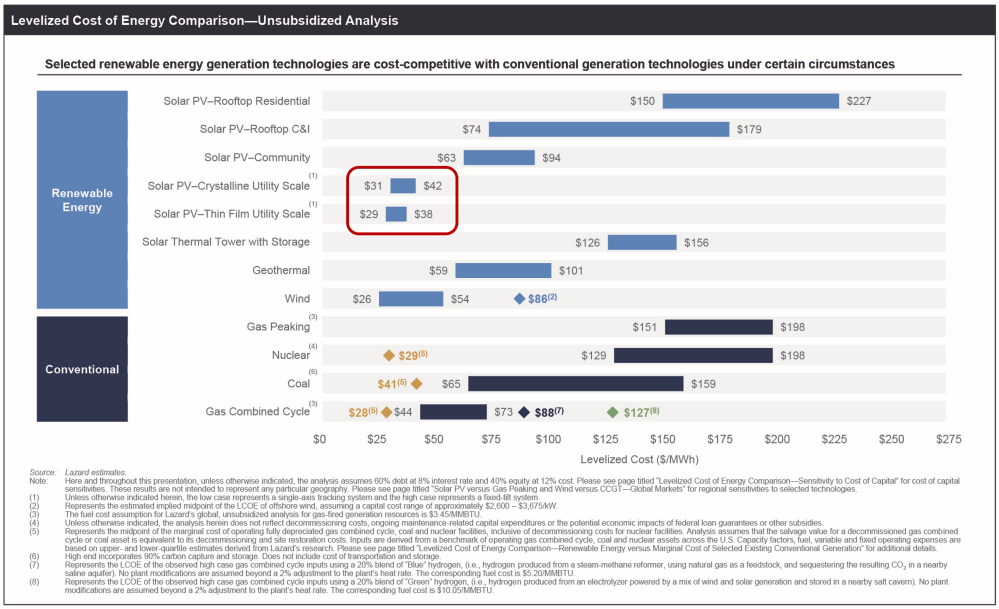

Figure 1.1. LCOE comparison for various sources of energy. Utility-scale solar PV is now cost-competitive with traditional sources of energy as well as wind energy. [7]

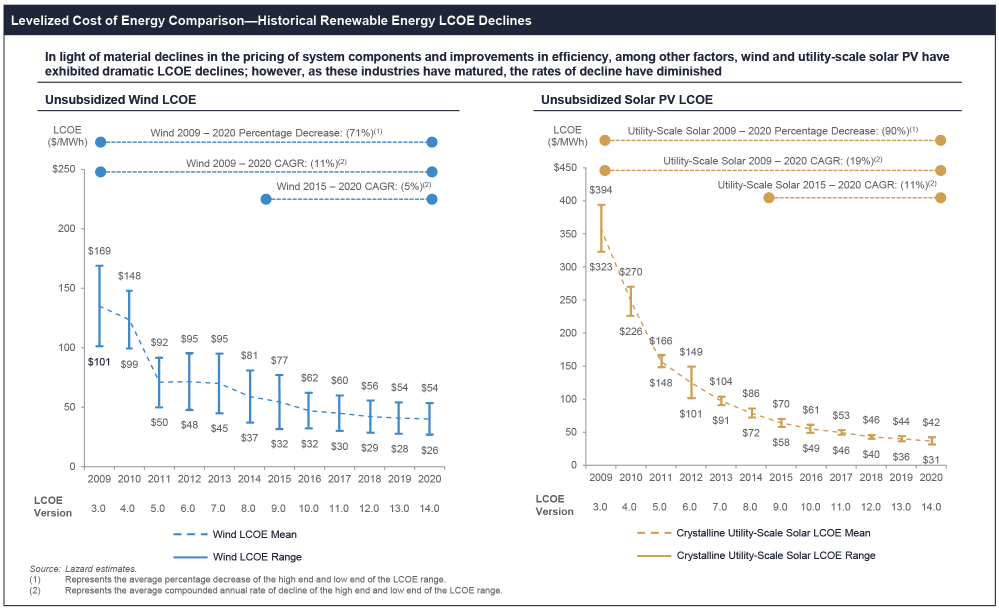

Figure 1.2. LCOE reduction for on-shore wind energy and utility-scale solar energy over the years. [7]

There has been persistent and integrated efforts of research institutes, PV industry, and government initiatives [4], [5] to reduce LCOE of solar PV. Researchers are exploring new materials [9], [10], the PV companies are optimizing manufacturing and module design [11], and farm-installers are developing new farm topologies, e.g., floating solar, and streamlining installation [12], [13].

The majority of groundbreaking research progress aimed to lower the LCOE of PV has been focused on: 1) increasing the efficiency of solar cells ($\sim$ 1% efficient c-Si solar cells in 1951 [14] to $\sim$ 28.8% for GaAs solar cells in 2011 [10]); 2) reducing CAPEX (the fixed cost of new factories and equipment) [15]; 3) adopting low-cost fabrication processes [16]; 4) exploring earth-abundant materials [17]; 5) using new cell architectures, from back-surface field (BSF) to point contacts; 6) Increase PV module size; and/or 7) changing module design from monofacial to bifacial.

However, understanding and estimating LCOE poses several challenges – from performing a detailed analysis of several costs involved to estimation of energy output of a solar PV system. Moreover, optimization of solar farm designs based on cost or energy independently does not guarantee a minimum in LCOE. Furthermore, reliability of solar modules, another key to

reduce LCOE of PV, still remains an intractable challenge [18]. For example, manufacturers guarantee 25 years of warranty (i.e., guaranteed to retain 80% of the initial power output), whereas field reports show PV lifetimes of less than 15 years, significantly increasing the LCOE of solar panels. Hence, it is very critical to develop degradation-resilient solar panels. Degradation of PV systems, however, is a very complex phenomenon that evolves over years due to various slow and/or rare events that ultimately cause failure. The existing empirical approach fails to capture the essential physics of PV reliability [19]. A lack of fundamental understanding prevents the advancement of predictive LCOE modeling and reliability-aware designs for PV systems.

As portrayed in Fig. 1.3, our proposed work will establish a comprehensive framework that will facilitate an opto-electro-thermo-economical model that is equipped with PV reliability models. Our reformulation of LCOE into LCOE* will not only allow an ease of communication between PV economists and technologists, it will more importantly empower the technologist to find an optimum design of a generalized solar PV farm at any given geographical location around the world, as seen in Fig. 1.4.

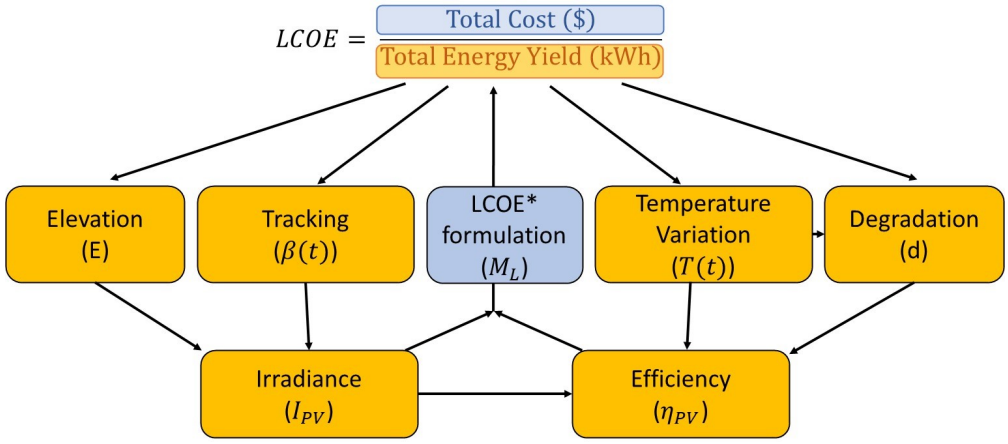

Figure 1.3. General overview of the thesis framework.

Furthermore, a physics-guided machine learning model for performance and degradation analysis of PV systems will enable the use of empirical/phenomenological/incomplete physical models for energy yield estimation and degradation mechanisms to forecast the LCOE and lifetime of PV modules and systems (forward modeling). What is more interesting is that

this physics-guided machine learning algorithm will empower us to perform a deconvolution of efficiency degradation into various underlying degradation mechanisms (inverse modeling) using large-scale PV field data from sites around the globe. Once developed, this tool can allow PV industry to manufacture PV modules and systems that are more resilient to varying weather conditions specific to different geographical locations, thereby increasing the lifetime of solar PV systems and eventually reducing the LCOE.

Finally, to maximize the outreach of this tool, we published our tool as part of a dataset in the Digital Environment for Enabling Data Science (DEEDS) platform that allows storage, preservation, analysis, and collaboration of scientific research.

1.1 LCOE*: Re-thinking Levelized Cost of Energy (LCOE) for Photovoltaic systems

Levelized cost of energy (LCOE) is the widely accepted metric to compare and assess the economics of various sources of energy. For solar energy, LCOE refers to the ratio of the total cost of a PV system and the total energy yield over its lifetime. Alternatively, it can be defined as the selling price of electricity per unit energy to break-even the cost of installing and operating a PV system over its lifetime.

$$\text{LCOE} = \frac{\text{Total cost over system lifetime}}{\text{Total electrical energy produced over system lifetime}} \tag{1.1}$$

Estimating LCOE requires an integrated effort of PV economists and PV technologists. While economists deal with the cost analysis (i.e., the numerator in Eq. 1.1), the technologists work on the physical design of a solar PV system for energy evaluation (i.e., the denominator in Eq. 1.1). In order to calculate and minimize LCOE, both economists and scientists require data from each other. For example, economists need the electrical and mechanical specifications – power capacity of the farm, module technology, inverter, racks, lifetime etc. – from the scientists, whereas scientists need available land area (/cost), subsidies and taxes, bank discount rate etc. – from economists to perform the same LCOE calculation and optimize the solar farm design. In simple terms, the LCOE formula is an implicit function of various cost and physical design parameters of a PV system. Due to this implicit nature of

the formula, the economists and the technologists require a constant exchange of information to calculate LCOE for a farm or for a region, see Fig. 1.4(left). Hence, there is a need to decouple the costs and energy yield aspects of the LCOE formula to provide a simpler, more transparent, and physically-intuitive perspective of LCOE such that it is easier for economists and scientists to work in parallel towards the goal of minimizing LCOE.

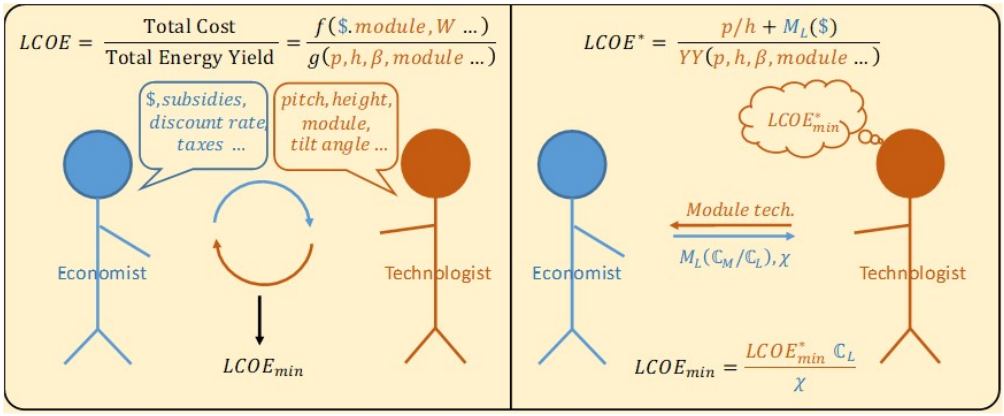

Figure 1.4. A depiction of how to deconvolve physical and economic parameters of the LCOE formulation for ease of communication between economists and technologists.

In chapter 2, we achieve this objective of decoupling the economic and physical design parameters to facilitate simultaneous assessment of costs by economists and energy yield by technologists. Using a fundamentally different perspective, we reformulate LCOE in terms of what we call LCOE* (essential levelized cost of energy). We first analyze the LCOE formulation and collected the costs into three categories: (1) The costs that vary with the size of land, (2) the costs that are directly affected by the number of modules, and (3) fixed costs that neither vary with the size of land nor the number of modules. Once all the costs are bagged into these three categories and the geographical location-based constants are brought together the LCOE formula reduces to the so-called "essential levelized cost of energy (LCOE*)". The new LCOE* formula has a cost parameter, named cost ratio (M_L), and physical design parameters, such as, pitch, height, tilt angle, albedo etc. Fig. 1.4(right) schematically portrays how the LCOE* helps decouple the functions of an economist and a technologist and how it differs from traditional LCOE calculation involving an iterative

communication, see Fig. 1.4(left). This way, after receiving the cost parameter (M_L) from the economist, the technologist can work independently on the design optimization of a solar PV system towards reducing the LCOE. Our results validate the LCOE* formulation by comparing the LCOE calculated by our approach to the traditional LCOE published in the literature.

The first step towards estimating LCOE is to re-formulate it into LCOE* that presents an uncluttered view on LCOE with physical parameters and costs deconvolved. Next, we need calculate the energy yield of a PV system. Thus, building upon previous modeling works, we develop an analytical model that estimates the energy output of a bifacial solar PV farm that includes the effect of mutual shading between rows of PV panels. Then, the cost and energy models are collated to estimate LCOE* and LCOE. Finally, we optimize the physical design of the farm in order to minimize the LCOE.

In the next sections, we describe several models and technological innovations to maximize the energy yield of a bifacial solar farm in order to reduce the LCOE.

1.2 Developing an opto-electro-thermal model for energy estimation of bifacial solar farms

Towards designing energy-efficient modules and farms [20]–[24], a module design based on bifacial solar panels have shown $\sim 50\%$ increase in power output compared to monofacial panels [20]. The International Technology Roadmap for Photovoltaic (ITRPV) predicts that the worldwide market share for bifacial technology will increase to 40% by 2028 [21]. A recent literature review by Guerrero-Lemus et al. [22] explains the optimism surrounding the initiation, growth, and scalability of this technology. To this end, various standalone module designs have been recently investigated numerically [23]–[27] and experimentally [28]–[31]. These demonstrate the dependence of irradiance intensity, spectral distribution, the fraction of direct, diffuse, and albedo light, etc. on the design of stand-alone bifacial modules. Guo et al. [32] have done a global analysis of east-west-facing vertical bifacial modules, Ito et al. [33] have presented a comparison of vertical bifacial modules and tilted modules, and Sun et al. [26] have provided a global perspective of bifacial modules with optimized tilt angle, azimuth angle, and elevation. The bifacial gain of stand-alone modules is significant

enough to support the optimistic view of the technology. However, there has been a gap in understanding and modeling of energy for bifacial solar farms. More importantly, the reports to date focus on bifacial energy gain, but it is unclear if the gain is sufficient to offset the additional cost of a bifacial solar farm to make the technology commercially viable.

With the foundation of an already developed opto-electrical model for *stand-alone* PV modules [26], we have now developed sophisticated numerical models to include optimized fixed-tilt, elevation, several temperature-dependent efficiency models and integrated them together to propose and opto-electro-thermo-economic model for a generalized tilted bifacial farm. We further improved this model by incorporating sun-tracking and power-tracking algorithms and finalized the comprehensive numerical software for tracking bifacial solar PV farms.

In our thesis, we explain in great detail all the aspects of this opto-electro-thermo-economic model for estimating the energy yield and levelized cost of energy of tracking bifacial solar farms around the world.

1.2.1 Optimized fixed-tilt solar PV farms

We explore the design optimization of tilted bifacial solar farms for all the locations across the globe. The results are easily generalized to the remaining locations of the world if we allow a location-specific turn-on of the solar farm. The objectives are: (i) To find the key design parameters, (ii) appropriately model the insolation and light collection at the farm-level, and (iii) subsequently incorporate a parameterized cost analysis (through LCOE*) to eventually find an optimized design that minimizes the cost of electricity produced.

To estimate the energy yield of a solar farm, the simulation proceeds in three steps. First, we calculate the amount of sunlight incident at a particular location defined by its latitude and longitude. We then segregate the the incident light into direct, diffuse, and albedo light components. Next, we quantify the amount of each light component collected by the solar panels installed at that location. This is the step where the fixed-tilt and spacing between the rows of solar panels become essential to the modeling framework. A different design -

combination of tilt (and N/S or E/W orientation) and row-spacing delivers a unique energy estimate. Finally, we find the daily and yearly power/energy-output of the bifacial solar farm.

All the solar farm designs are then evaluated to find the best design with an optimum fixed-tilt angle and row-spacing for that particular location (lat/long). We perform this analysis worldwide, in order to generate a global map of optimized bifacial solar PV farm designs and the estimated energy associated to them.

1.2.2 Integrating temperature-dependent efficiency of solar farms

Research studies have explored the effects of temperature-dependent efficiency on standalone modules with a focus on finding an accurate temperature coefficient. Both bifacial and monofacial modules have been studied with temperature dependence in previous works. In our earlier study, we estimated the energy output and LCOE of ground-mounted (unelevated) bifacial farms at standard testing conditions (STC). Nonetheless, a study of elevated bifacial farms based on temperature-dependent efficiency, as a prototypical and practical farm, remains unexamined.

With the foundation of an opto-electrical model developed earlier, we explored several temperature-dependent efficiency models and integrated them together to propose and opto-electro-thermal model for a generalized tilted bifacial farm. We validate our proposed model with the experimental data from Sandia National Labs. Moreover, we improved the analytical model for energy generation of PV farms to incorporate elevation (or ground clearance) of PV panels. This required remodeling the albedo light collection by a panel that can now "see" the ground under several adjacent rows of PV panels. We used this comprehensive model to compare energy output, LCOE, and design optimization of: (1) standalone module vs. farm output, (2) monofacial vs. bifacial farm output, and (3) elevated vs. unelevated farms.

1.2.3 Incorporating tracking algorithms

One way to reduce the levelized cost of energy (LCOE) is to design a photovoltaic (PV) system to produce the maximum energy for a specified area of the solar farm. Among the cost-effective options, one can either increase the total irradiance of fixed-tilt farms using bifacial

modules or increase the normal irradiance on monofacial modules by solar-tracking. Both technologies are becoming popular as bifacial modules are expected to have $\sim 40\%$ market share by 2028 [34], whereas solar-tracking has been implemented by $\sim 70\%$ of newly installed utility-scale PV systems since 2015 [35], [36]. Indeed, market analysis from multiple groups worldwide suggest that single-axis tracking may account for 25-40% of all new utility-scale PV installation, motivated in part by the adoption of bifacial modules [37]. The location-specific viability of bifacial tracking solar farms has not been quantified, however.

To investigate the worldwide performance of bifacial single-axis tracking PV farms with fixed-tilt bifacial PV farms, we compare the performance of two different tracking algorithms termed as tracking the sun (TS) and tracking the best orientation (TBO) or power-tracking [38]. By using a self-consistent optical- electrical-thermal model, we address the following key questions: (i) How do the energy yields compare between east/west (E/W) facing and north/south (N/S) facing bifacial single-axis tracking solar farms? (ii) How does the site-specific climate affect the performance of these farms? (iii) How do the location-dependent land costs affect the optimum design and LCOE of these farms? and (iv) What is the optimum row-spacing (pitch) for minimum LCOE?

1.3 Physics-based Machine Learning for PV performance and reliability

The advent of machine learning and its widespread application allows us to go beyond the physics-based numerical modeling of PV systems. The machine learning models are analogous to the compact models of various electrical components that are part of a circuit. Similarly, machine learnt models are compact and fast modules/packages that are capable of emulating the previously developed sophisticated numerical models. Therefore, we explored application of machine learning to PV system performance and reliability.

1.3.1 Why ML-based analysis of PV systems?

Fast-paced growth in the demand and supply of solar PV systems – residential, commercial, and utility-scale – has accelerated the deployment of PV systems around the world. Parallel to this field deployment, there has been a concerted effort to model emerging PV systems

to estimate their energy yield and levelized cost of energy (LCOE). The modeling effort is particularly important because there has been a proliferation of farm topologies (e.g., monofacial, vertical and tilted bifacial, E/W and N/S tracking systems, etc.) available for deployment. To make this comparison feasible, several models and software have been developed to predict the energy yield over the lifetime of the PV farm [39]. SunPower Corp. has developed EnergyLink that constantly monitors various types of PV systems [40]. Sandia National Labs have created a library of codes and software called PVLib that can be used for PV system analysis [41]. National Renewable Energy Laboratory (NREL) provides Bifacial Radiance for energy estimation of bifacial PV systems and RdTools for PV degradation analysis [42], [43]. Driesse et al. [44] have performed a comparative analysis on several module efficiency models for energy prediction and rating. Similarly, the Purdue Group has designed physics-based numerical models for energy yield and LCOE calculation [45], [46].

These sophisticated models can not only accurately predict the energy yield and LCOE, but they can also find the optimum design of standalone PV modules and utility-scale solar PV farms. However, due to their computational and algorithmic complexities, the existing models require significant computational resources to calculate the worldwide energy yield of a specific farm configuration, even for a relatively coarse grid of latitudes and longitudes [45]. Moreover, it is often difficult to validate the model prediction because the location of the actual farm may not coincide with the simulation grid. Unfortunately, traditional nearest-neighbor or spline-based interpolation techniques cannot be used because the weather and terrain can vary dramatically over few miles, let alone several degrees of latitude/longitude (coarse grid).

1.3.2 ML-based energy prediction

An emerging field of physics-based machine learning allows us to tackle the complexity and computation time issues of the PV simulation model. Physics-based machine learning utilizes the already existing physical/empirical models in conjunction with machine learning tools to perform symbolic regression [47], for efficient compact modeling [48], for forecasting complex dynamical phenomena [49], to improve the accuracy of ML models in data-deprived

applications [50], [51], and for reduction in computation time, as we will see in this chapter. A survey of physics-guided and hybrid physics-ML models is presented in Ref. [52]. Moreover, the following reasons led us to explore a hybrid physics-ML model for estimation of worldwide energy yield of solar PV farms.

(1) Recent IEA-PVPS report [53] informs us that there are 15-16 models with various degrees of accuracy. ML will make this duplication of effort unnecessary, saving enormous time in code development.

(2) Even with a debugged code, it may take years to generate highly refined results that can be used to develop policies. ML will do it in minutes.

(3) The model will show that if one uses monthly energy yields of just 4-6 locations, we can create a worldwide map of yearly energy yield. Richness of the data depends on latitudinal-diversity of the information, not the number of datapoints themselves. It has implications of creating databases and validation protocols (Not all locations are the same).

(4) An earth-based modeling can be functionally extrapolated to other planets, giving an approximate prediction of the energy yield. This transfer learning will become a validation tool for solar simulators used for planetary missions.

In our thesis, we develop a novel functional interpolation tool based on machine learning, which can accurately estimate the yearly energy yield (YY) and effective levelized cost of energy (LCOE*) [45] in minimal computation time. As a new and potentially transformative approach to computational modeling, this tool addresses many challenges of traditional PV modeling, namely, the need for supercomputing resources, expertise in scientific computing, long run-time, etc.

1.3.3 ML-based PV reliability analysis

Physics-guided machine learning (PGML) has come to surface in last couple of years. These studies have been performed for specific applications. Moreover, with respect to PV reliability, the currently available acceleration tests are empirical, with little to no physics known, and hence cannot accurately predict lifetime for solar PV modules in the field. The

challenge is to find a physics-guided machine learning approach to solve PV reliability issues and further generalize the theory for broader applications.

The idea is to take an example problem, for example, deconvolution of degradation mechanisms in PV systems, and find an algorithm to extract essential features (physical parameters) from tentative physical equations or empirical observations and feed these essential features as inputs to the machine learning tool. This will enable faster and more accurate segregation of an intricate amalgamation of several PV degradation mechanisms. Such an approach will serve two important goals. (i) Generic – A theory/algorithm that can perform physics-based machine learning to achieve faster and accurate results. (ii) More specifically, and yet a pressing issue – a holistic methodology for quick diagnosis of PV reliability by looking at previous data (inverse modeling) and predicting the future degradation or lifetime of PV modules (forward modeling). To this end, we have (i) developed a toy PGML model with the help of synthesized data using available empirical/physical PV degradation forward models; and (ii) used weather data from early-deployment phase to further improve the toy PGML model.

1.4 Exploring thermodynamic efficiencies of Photovoltaic-Electrochemical systems

Earth's rotation around the sun leads to spatial (latitude), seasonal, and diurnal variation in sunlight intensity. Storing solar energy in various other forms of energy (e.g. chemical, mechanical, gravitational) provides a solution to this challenge.

Having developed physics-based numerical and and machine learning models, we began exploring creating compact models for PV-EC combined energy storage systems.For electrochemical (EC) energy storage, a variety of approaches have been proposed, including batteries, organic and/or inorganic reactions, artificial photosynthesis [54], etc. In this thesis, we report the thermodynamic performance limit of PV-to-EC energy conversion through an illustrative example of splitting of water into hydrogen and oxygen.

A generalized configuration for such PV-to-EC conversion is relevant for research efforts worldwide.We model a system that is characterized by five PV and four EC variables. The PV variables are: the intensity of sunlight (S), the fraction of incident light reflected from

the ground (albedo, R), number of series-connected cells in the PV module (M), number of subcells in a multi-junction (Tandem) solar cell (N) and the set of bandgaps of the solar cell ($[E_g]$)). The EC parameters are: the number of series-connected electrochemical cells (K), the thermodynamic potential of the reaction (μ_{th}), effective exchange current density ($J_{0,ec}$) and effective Tafel slope (β).

This set of 9 variables is sufficient to calculate the thermodynamic upper limit of an 'idealized' PV-EC system, with the same level of rigor and relevance as the Shockley-Queisser (SQ) analysis for a stand-alone PV system [55]. Similar to the SQ limit, we realize that practical considerations, such as series and shunt resistances [56]–[58], diode non-ideality factor, self-heating in both PV and EC, spectral difference, and non-ideal Tafel slope, may in practice make it impossible to reach the PV-EC limit derived here. Nonetheless, the PV-EC thermodynamic limit provides physical insights and scope of improvement for modeling experts and experimentalists alike.

1.5 Thesis Outline

The objective of our research is to create, simulate, and analyze a comprehensive numerical model for energy and LCOE estimation of bifacial solar PV systems. To achieve this goal, we integrated a set of sub-modules comprising of optical, electrical, thermal, tracking, and economic model, as shown in Fig. 1.3. The details of the above-mentioned numerical models and the analysis of the results of worldwide simulations are described in the upcoming chapters as enumerated below.

In ***chapter 2***, we delineate a method to re-formulate levelized cost of energy (LCOE) to deconvolve the cost and physical parameters and call it essential levelized cost of energy (LCOE*). We further develop and integrate the irradiance, light collection, and electrical models to estimate the yearly energy yield of a generalized fixed-tilt bifacial solar PV farm. The estimated energy is fed into the LCOE* formula and the physical parameters are optimized to minimize LCOE and thus find the best design of the farm. We finally, analyze the global trends of energy yield, LCOE, and optimum tilt angles.

In ***chapter 3***, we extend the opto-electro-economic model to include the temperature-dependent efficiency models. Next, we validate these models with experimental data for daily energy from Sandia National Labs. We compare the energy yields and LCOE of bifacial and monofacial solar farms for various PV materials and technologies viz. Silicon, CdTe, Aluminum Back Surface Field (Al-BSF), Silicon Heterojunction (SHJ), and Passivated Emitter and Rear Contact (PERC). A worldwide comparison of these technologies with and without temperature-dependent efficiency models shows us the stark difference between the two methods for energy and LCOE estimation.

In ***chapter 4***, we complete the comprehensive modeling of bifacial solar farms by incorporating tracking algorithms in the package. We analyze two tracking algorithms, namely, sun-tracking and power-tracking algorithms and compare their performance in calculating the daily output of farms at four locations around the world. Next, we analyze North-South facing and East-West facing orientations of bifacial solar farms around the world. We find that E/W facing farms are favorable for locations lying between $50°N$ and $50°S$ whereas N/S facing farms are more promising for locations lying outside of the 50° latitude band. We also explore the types of land suitable for tracking bifacial solar farm installation and conclude that "Savannas" and "Barren lands/deserts" are apt for E/W PV farm deployment.

Once the comprehensive tool was completed, we sought ways to reduce the computation time for worldwide solar farm simulations. We found physics-based machine learning to be an aptly suitable solution for the same.

Thus, in ***chapter 5***, we present a methodology to use machine learning as a tool to learn the previously-created complex opto-electro-thermo-economic models and then use the trained machine to accurately predict the energy yield, LCOE, and optimum design of a generalized solar PV farm. This method drastically reduces the computation time to simulate a million locations worldwide by orders of magnitude, i.e., from years to seconds.

In ***chapter 6***, we investigated the problem of daily and seasonal variation in PV energy output. This led us to explore a photovoltaic-elctrochemical storage system. We developed an electrical compact model for a generalized PV-EC system and used water-splitting as an example to calculate the thermodynamic limits of the efficiency of PV-to-EC energy conversion. We find that that thermodynamic limit of conversion is 52% and subsequently describe the

optimum design of this PV-EC system in terms of various physical and electrochemical parameters.

Finally, in ***chapter 7***, we summarize and conclude the thesis while proposing ideas or projects that can be explored in the future.

2. A WORLDWIDE COST-BASED DESIGN AND OPTIMIZATION OF TILTED BIFACIAL SOLAR FARMS

The steady decrease in the levelized cost of solar energy (LCOE) has made it increasing cost-competitive against fossil fuels. The cost reduction is supported by a combination of material, device, and system innovations. To this end, bifacial solar farms are expected to decrease LCOE further by increasing the energy yield; but given the rapid pace of design/manufacturing innovations, a cost-inclusive optimization of bifacial PV systems at the farm-level (including land costs) has not been reported. In our worldwide study, we use a fundamentally new approach to decouple energy yield from cost considerations by parameterizing the LCOE formula in terms of "land-related cost" and "module-related cost" to show that an interplay of these parameters defines the optimum design of bifacial farms. For ground-mounted solar panels, we observe that the panels must be oriented horizontally and packed densely for locations with high "land-related cost", whereas the panels should be optimally tilted for places with high "module-related cost". For systems with relatively high module-related costs and for locations with $|\text{latitude}| > 30°$, the bifacial modules must be tilted $\sim 10 - 15°$ higher and will reduce LCOE by 2-6% compared to their monofacial counterparts. The results in this chapter will guide the deployment LCOE-minimized ground-mounted tilted bifacial farms around the world.

2.1 Introduction

Solar energy is spearheading the renewable energy growth around the world [1]–[4]. Levelized cost of energy (LCOE) is used as a metric to compare the economic viability of various sources of energy, e.g., wind, hydro-power, coal, natural gas, solar energy etc. [5], [6]. So far, solar energy still falls behind its competitors in this comparison [2], [59]. There has been persistent and integrated efforts of research institutes, PV industry, and government initiatives [4], [5] to reduce LCOE of solar PV. Researchers are exploring new materials [9], [10], the PV companies are optimizing manufacturing and module design [11],

↑**Note:** The material in this chapter has been adapted from Ref. [45].

and farm-installers are developing new farm topologies, e.g., floating solar, and streamlining installation [12], [13].

Towards designing energy-efficient modules and farms [20]–[24], a module design based on bifacial solar panels have shown $\sim 50\%$ increase in power output compared to monofacial panels [20]. The International Technology Roadmap for Photovoltaic (ITRPV) predicts that the worldwide market share for bifacial technology will increase to 40% by 2028 [21]. A recent literature review by Guerrero-Lemus et al. [22] explains the optimism surrounding the initiation, growth, and scalability of this technology. To this end, various standalone module designs have been recently investigated numerically [23]–[27] and experimentally [28]–[31]. These demonstrate the dependence of irradiance intensity, spectral distribution, the fraction of direct, diffuse, and albedo light, etc. on the design of stand-alone bifacial modules. Guo et al. [32] have done a global analysis of east-west-facing vertical bifacial modules, Ito et al. [33] have presented a comparison of vertical bifacial modules and tilted modules, and Sun et al. [26] have provided a global perspective of bifacial modules with optimized tilt angle, azimuth angle, and elevation. The bifacial gain of stand-alone modules is significant enough to support the optimistic view of the technology.

Unfortunately, a combined effect of panel-to-panel (mutual) and panel-to-ground (self) shading in a solar farm may erode the perceived advantage of stand-alone bifacial farms. Recently, Appelbaum [60] has investigated the effect of shading when bifacial modules in a farm are installed in multiple rows for east-west and south-north orientations. Khan et al. [61] have done a global analysis of vertical bifacial solar farms and observed a 10-20% energy gain for practical row-spacing. In a more recent study [62], they have proposed a ground-sculpting of farms to enhance the power output and achieve $\sim 50\%$ bifacial gain. Moreover, the vertical farm design reduces soiling and cleaning cost. In fact, limited experimental study in Tucson (Arizona, USA) and Forst (Lausitz, Germany) do show the vertical bifacial farms outperforming the optimally tilted bifacial farms for certain months/weather conditions [63]. It is not clear if these conclusions can be generalized to all locations in the world.

Most importantly, the reports to date focus on bifacial energy gain, but it is unclear if the gain is sufficient to offset the additional cost of a bifacial solar farm to make the technology commercially viable. A recent study [64] has offered a careful and systematic cost-based

analysis of bifacial PV systems. Although the analysis took various module-related costs into consideration, it did not include the land-related costs. Moreover, the self-shading for modules was considered while mutual shading was omitted. In other words, the cost may have been underestimated, while energy yield overestimated. A generalization of the previous study that predicts the LCOE-optimized bifacial farm design (including land cost and mutual shading) would be of great interest.

The calculation of farm-level levelized cost of energy (LCOE) is difficult because some of the factors (e.g. land cost, module and installation cost, degradation rates, and bankability) may not be known for years to come. Therefore, in this chapter we reformulate/re-parameterize the LCOE calculation in a way that allows design optimization and decision making for any PV technology even when all the cost details are not known. Specifically, the new approach has the benefit of providing a clear understanding of the impact of various parameters on bifacial LCOE and a worldwide mapping/analysis will show us a trend in the economic viability of bifacial PV technology.

Our main contribution in this chapter is that we explore the design optimization of tilted bifacial solar farms for all the locations across the globe with latitude below 60°. The results are easily generalized to the remaining locations of the world if we allow a location-specific turn-on of the solar farm. The objectives are: (i) To find the key design parameters, (ii) appropriately model the insolation and light collection at the farm-level, and (iii) subsequently incorporate a parameterized cost analysis to eventually find an optimized design that minimizes the cost of electricity produced. Our generalized model shown in Fig. 2.1 will reproduce, as special cases, various types of farms designed to date. For example, specialized designs are achieved by fixing one of the seven bifacial farm parameters defined in table 2.1, namely, $\beta = 90°$ defines a vertical bifacial farm; $p = \infty$ yields a stand-alone (unit length in z-direction) or a single row (infinite length in z-direction) of bifacial PV module(s); and turning off the back-surface light-collection creates a monofacial solar farm. Other designs can be obtained by varying several parameters simultaneously.

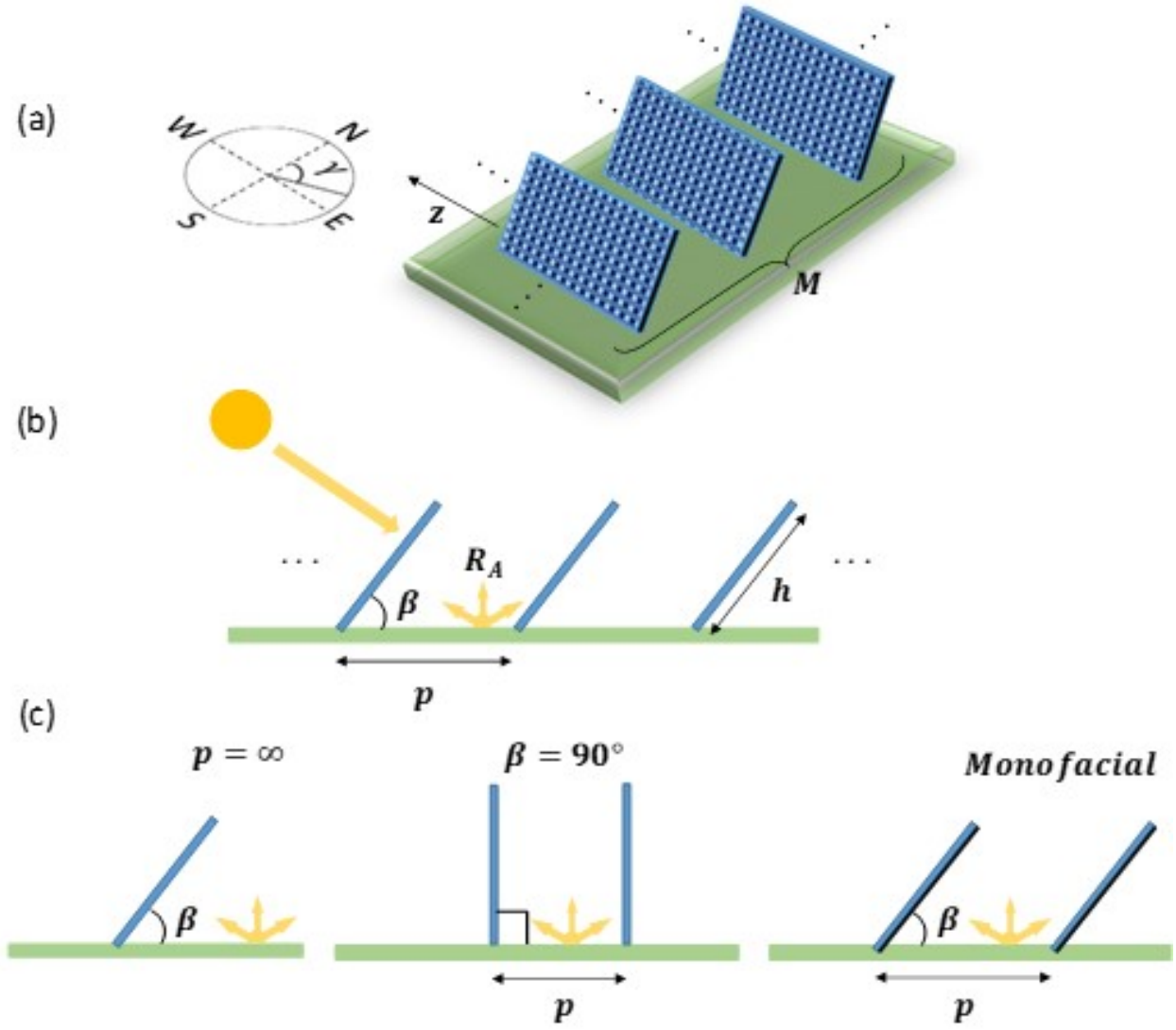

Figure 2.1. (a) A 3-D Schematic of a generalized tilted bifacial solar farm. (b) A 2-D view of arrays of ground-mounted panels, assuming infinite (or unit) length for a single row (or a single module) in the third dimension. (c) Derived designs, namely, standalone module, vertical farm, and monofacial farm, as derivatives of the general design.

In Sec. 2.2 we explain the models used in our study – In Sec. 2.2.1, we start with re-parameterization of LCOE in terms of land cost (C_L), module cost (C_M), and yearly energy yield (YY). Next, in Sec. 2.2.2, we describe the methodology to calculate the local irradiance by using the available meteorological data. The outcome of this analysis will provide the illumination/energy incident on the solar farm area. We then discuss, in Sec.

Table 2.1. Physical and economic parameters of a ground-mounted tilted bifacial farm.

No.	Parameters	Definition
1.	Pitch (p)	Row-to-row distance between the bottom edges of consecutive arrays
2.	Height (h)	Height of the panels
3.	Array tilt angle (β)	Angle between the array (panels) and the ground (horizontal)
4.	Array azimuth angle (γ)	Angle between the projection of normal to the front face of the arrays on the ground and the North Pole
5.	Albedo (R_A)	Fraction of incident light reflected from the ground
6.	Land cost (c_L)	The cost of a single solar module per unit height (includes fabrication and installation costs)
7.	Module cost (c_M)	The cost of a single solar module per unit height (includes fabrication and installation costs)

2.2.3, the light collection model for estimating the fraction of incident light absorbed by front/rear faces of the solar modules to calculate the power output from the farm in terms of annual energy yield.

Thenceforth, in Sec. 2.3, we optimize the bifacial farm to minimize the levelized cost of energy. Finally, in Sec. 2.4, we present the results of the simulations and a global perspective of minimized levelized cost of energy for optimum system parameters. Our conclusions are summarized in Sec. 2.5 of this chapter.

2.2 MODELING

An LCOE-aware modeling and optimization of bifacial solar farm involves a series of calculations. In this section, we will focus on three aspects of the modeling framework: (A) Re-parameterizing LCOE, (B) Irradiance modeling, and (C) Collection of light. These topics are discussed below.

2.2.1 Levelized Cost of Energy (LCOE)

LCOE is defined as the ratio of the total cost of a PV system and the total energy yield of the system over its lifetime [65], i.e.,

$$LCOE = \frac{Total\,Cost\,(\$)}{Total\,Energy\,Yield\,(kWh)} = \frac{C_{sys}(Y=0) + (\sum_{k=1}^{Y} C_{om}(k)) - C_{rv}(Y)}{E(Y)} \tag{2.1}$$

where $C_{sys}(Y=0)$ is the fixed cost paid once during installation (i.e., Y=0) of the system. This includes the cost of modules ($c_{m,0}$), the cost of land ($c_{l,0}$), and the balance of system cost ($c_{bos,0}$) such as labor, permit, racks, inverters, etc. The recurring operations and maintenance cost (C_{om}) scales with the cost of maintaining individual modules ($c_{om,m}$) and the cost of maintaining the land ($c_{om,l}$). Finally, C_{rv} is the residual value of the modules ($c_{rv,m}$), the land ($c_{rv,l}$), and the equipment to be regained when the farm is decommissioned. C_{om} and C_{rv} are a function of the lifetime (number of years, Y) for which the solar farm is operated. The total cost (numerator) in the LCOE expression in Eq. 2.1 can be equivalently written as the sum of effective module-related cost (C_M), effective land-related cost (C_L), and fixed balance of systems cost ($C_{bos,f}$), as shown in the following equation:

$$LCOE \equiv \frac{C_M + C_L + C_{bos,f}}{E(Y)} \tag{2.2}$$

where

$$\begin{aligned} C_M &= c_{m,0} + \left(\sum_{k=1}^{Y}(c_{om,m}(k)(1+r)^{-k})\right) - C_{rv,m}(Y)(1+r)^{-Y} \\ C_L &= c_{l,0} + \left(\sum_{k=1}^{Y}(c_{om,l}(k)(1+r)^{-k})\right) - C_{rv,l}(Y)(1+r)^{-Y} \end{aligned} \tag{2.3}$$

Subscripts m, l, and bos stand for module, land, and balance of systems. Moreover, r is the discount rate that normalizes future costs in terms of current cost in order to have a fair comparison using a single metric.

The key insight of Eq. 2.2 is that the costs associated with a solar farm reflects two essential costs, namely, effective module-related cost (C_M) and effective land-related cost C_L).

The costs that scale with the number of modules (e.g., module size, material cost, racking, wiring in panels, inverters etc.) are included in C_M. Those costs that vary with the area of land (e.g., cost of land, fencing, cost for land curing/sculpting, etc.) are collected in C_L. Since the (typically small) fixed cost associated with balance of systems (e.g. permit cost) does not scale with the number of modules or the land, hence, we collect them into the residual cost,$C_{bos,f}$. The denominator of Eq. 2.2 describes the total energy yield $E(Y)$ of the solar farm:

$$E(Y) = \sum_{k=1}^{Y} E_0(1-d)^k(1+r)^{-k} \tag{2.4}$$

Here, $E_0 = P_0 \times T_Y$ is the energy output for the first year expressed as the product of first year power output (P_0) and total number of active hours in a year (T_Y). The yearly energy degradation rate (d) defines the lifetime (Y, in years) of the solar farm. The discount rate (r) accounts for the following fact: If we continue to sell a unit of energy for c \$/watt-hour, the present value of the lifetime revenue must account for the fact that future earnings are less valuable than present earning.

Given the dimensions of a solar farm and the modules installed, LCOE expression in Eq. 2.2 can be simplified even further, i.e.,:

$$LCOE = \frac{\mathbb{C}_M(r) \times h \times M \times Z + \mathbb{C}_L(r) \times p \times M \times Z + C_{bos,f}}{YY(p,h,E,\beta,\gamma_A,R_A) \times M \times Z \times h \times \chi(d,r)} \tag{2.5}$$

where C_M is the cost per unit meter of module (height), C_L is the cost per unit meter of land (pitch), M is the number of rows/arrays of modules and Z is the number of modules in an array (in the z-direction, into the page). $YY(= E_0)$ is the yearly energy yield per meter of a pristine module for one period/pitch (p) such that the yearly energy of the farm is $E(Y) = YY \times M \times Z \times h \times \chi(d,r)$, where $\chi = \sum_1^Y (1-d)^k(1+r)^{-k} \times YY$ is a function of the physical design parameters $(p, h, \beta, \gamma, R_A)$. Further, the residual cost associated with the balance of system ($c_{bos,f}$) is typically negligible as compared to the essential costs, C_M and

C_L [13], and does not affect the design optimization of the farm. With these considerations, we arrive at the "essential levelized cost of energy" ($LCOE^*$), as follows:

$$LCOE^* \equiv \frac{LCOE.\chi}{C_L} = \frac{C_M/C_L + p/h}{YY(p, h, \beta, \gamma, R_A)} = \frac{p/h + M_L}{YY} \tag{2.6}$$

Eq. 2.6 defines an important design parameter $M_L(\equiv C_M/C_L)$ as the ratio of cost of module per unit length (height) over cost of land per unit length (pitch). This is one of the most important conceptual novelty of this work. Although in this chapter we illustrate the concept with reference to a bifacial PV technology, the approach applies to and will greatly simplify the design of any PV technology (monofacial, concentrator, etc.). Note that Eq. 2.6 expresses LCOE explicitly in terms of the seven fundamental farm design variables shown in Table 2.1.

The parametric reformulation of LCOE in terms of LCOE* decouples the cost analysis (embedded in M_L) from design considerations (reflected in p/h and YY). In other words, we can optimize a farm with M_L as a parameter, realizing that M_L will evolve as the process technology evolves. Eq. 2.6 shows that LCOE is proportional to LCOE*, since C_L and χ are location-specific constants. Therefore, minimizing LCOE is equivalent to minimizing LCOE* for a given location. In the following sections, we will estimate the yearly energy yield at a particular location and then account for the costs to finally arrive at the location-based LCOE*.

2.2.2 Irradiance model for calculating I_{DNI} and I_{DHI}

To estimate the energy yield of a solar farm, the simulation proceeds in three steps. First, we calculate the amount of sunlight incident at a particular location defined by its latitude and longitude. Next, we quantify the amount of light collected by the solar panels installed at that location. Finally, we find the daily and yearly power/energy-output of the farm.

Location-based light intensity

To calculate the temporal solar irradiance data at a particular location, we need to know the solar trajectory (or Solar path) and the intensity of light [26], [61]. The solar path can be acquired/simulated by using the NREL's solar position algorithm [66] which has been implemented in Sandia PV modeling library (PVLib) [41]. This gives us the zenith angle (θ_z) and azimuth angle (A) of the sun at any time of the day on a given date for the desired location. Here, θ_z is the refraction-corrected zenith angle, which depends on altitude and ambient temperature. We use the Haurwitz clear sky model to generate the Global Horizontal Irradiance (GHI or I_{GHI}) [67], [68] with a time resolution of one minute. The clear sky model, however, often overestimates insolation, especially when the atmosphere is cloudy or overcast. Hence, to account for local variation of GHI caused by cloudiness and altitude, we scale the integrated GHI over time to match the satellite-derived 22-year monthly average GHI data from the NASA Surface meteorology and Solar Energy database [69]. Therefore, our modeling framework takes into consideration the impacts of geographic and climatic factors to model the location-specific solar irradiance.

Direct and Diffused light from GHI

Since GHI is measured on a flat ground while the solar panels are tilted, we need to decompose the amount of direct light, called Direct Normal Irradiance (DNI or I_{DNI}), and the amount of diffused (scattered) light, called the Diffuse Horizontal Irradiance (DHI or I_{DHI}), which are related to the GHI as follows:

$$I_{GHI} = I_{DNI} \times cos(\theta_Z) + I_{DHI} \tag{2.7}$$

Since we have one equation and two unknown variables, I_{DNI} and I_{DHI}, thus, we estimate one of the variables, I_{DHI}, using the Orgill and Hollands model, which empirically calculates

the diffuse fraction using the clearness index of the sky, defined as the ratio between I_{GHI} and extraterrestrial irradiance (I_0) on a horizontal surface, as shown below.

$$k_t = \frac{I_{GHI}}{I_0 cos(\theta_Z)} \tag{2.8}$$

Here, I_0 comes from an analytical expression in Ref. [70].

Once we calculate I_{DHI} using I_{GHI} and k_t, Eq. 2.7 gives us I_{DNI}. Further, instead of the isotropic sky model [71], we deploy the Perez model [70], [72], [73] to account for the anisotropic (angle-dependent) decomposition of I_{DHI}. This fixes the overestimation of energy yield due to isotropic model [30]. A similar calculation for estimation and decomposition of solar insolation has been previously done by others [26], [61].

Angle of incidence (AOI)

We need to calculate the AOI to find the component of direct light (I_{DNI}) falling on the tilted panel's front and/or the back face (depending on the tilt angle). The AOI for N-S facing tilted panels can be analytically expressed as [74]:

$$AOI_{Front} = \theta_F = cos^{-1}(cos\theta_Z\, cos\beta + (sin\theta_Z\, sin\beta\, cos((\gamma - 180) - (A - 180)))) \tag{2.9}$$

and

$$AOI_{Back} = \theta_B = cos^{-1}(cos\theta_Z\, cos(180 - \beta) + (sin\theta_Z\, sin(180 - \beta)\, cos((\gamma - 180) - (A)))) \tag{2.10}$$

where θ_F and θ_B are angles of incidence on front and back surfaces of the panel, respectively, and A is the azimuth angle of the sun.

We now have the irradiance and angle of incidence information to proceed with estimation of light collection and energy generation by the solar panels.

2.2.3 Collection of light for calculating YY$(p, h, \beta, \gamma, R_A)$

The panels have height h, tilted at an angle β, separated by pitch (or period) p, and are oriented at array azimuth angle $\gamma = 180°$ (i.e., south-facing panels) for farms in the northern hemisphere and $\gamma = 0°$ (i.e., north-facing panels) for farms in the southern hemisphere (see Fig. 2.1). For simplicity, we assume that the arrays run sufficiently long in East-West direction that the edge effects can be neglected. Moreover, the bottom edge of the panel is assumed to be touching the ground. The collection of light on panels requires different approaches for the three components of irradiance, i.e., direct, diffuse and albedo light, and hence, we will analyze them individually. We will first calculate the light collection and energy output for each panel/array and then account for the energies from all the arrays to estimate the total energy yield from the farm. Our model for light collection is similar to and based on the one developed by Khan et al. [61]. We assume the PV module efficiency under direct and diffuse irradiance to be $\eta_{dir} = 18.9\%$ and $\eta_{diff} = 15.67\%$ [61], [75]–[77], respectively. Reflection losses at the module surface cause the difference in η_{dir} and η_{diff} efficiencies. Moreover, the cell efficiency for front and the back faces are experimentally found to differ by 1–2% [22], whereas, the typical bifaciality factor for high quality commercial bifacial PV modules is $\sim$ 90% [78]. For simplicity, we neglect this difference with the understanding that it will slightly overestimate the energy yield. It is important to note that there can be partial shading of panels or non-uniform illumination during the day. This can cause some of the solar cells in a panel to reach reverse breakdown. This is mitigated by placing bypass diodes (3 in our case) connected across different sub-sections of series-string. The effect of shading and bypass diodes on the power output of the panel is discussed by Deline et al. [79]. Our model accounts for partial shading effects [61]. Now, let us look at the three individual components of incident light.

(a) Direct light collection

Starting from I_{DNI} estimated earlier, we find that the component of direct illumination normal to the front surface of the panel is given by $I_{DNI}\, cos\theta_F$. Next, we use an empirical

model [80] to incorporate the angle-dependent reflectivity ($R(\theta_F)$) of the panel. Finally, including the efficiency η_{dir}, we arrive at the power output per unit panel area.

$$\begin{aligned} I_{PV:DNI}^{F,Panel} &= I_{DNI}\, cos\theta_F\, (1 - R(\theta_F))\, \eta_{dir}; l > shadow \\ &= 0; l \leqslant shadow \end{aligned} \tag{2.11}$$

The contribution of power from the shaded area of the panel is assumed to be zero. Thus, the power output per unit height of a panel is equal to $I_{PV:DNI}^{F,Panel}$. Now, the power output per pitch of the farm ($I_{PV:DNI}^{F,Farm}$) is given by:

$$\begin{aligned} I_{PV:DNI}^{F,Farm} &= \frac{1}{h} \int_0^h I_{DNI}\, cos\theta_F (1 - R(\theta_F))\, \eta_{dir}\, dl \\ &= \frac{(h - shadow)}{h}\, I_{DNI}\, cos\theta_F\, (1 - R(\theta_F))\, \eta_{dir} \end{aligned} \tag{2.12}$$

Note that the integral is implemented as a summation from the bottom edge of the panel to the top edge with a step-size of 0.01 m. Similarly, we can find the direct light collection for back surface ($I_{PV:DNI}^{B,Farm}$) with the tilt angle equal to $180° - \beta$ and $AOI_Back = \theta_B$. Therefore, the total power output per unit farm area due to direct light ($I_{PV:DNI}^{Farm}$) is the sum of $I_{PV:DNI}^{F,Farm}$ and $I_{PV:DNI}^{B,Farm}$.

(b) Diffuse light collection

The estimation of the diffuse light collection is more involved as compared to direct light. Using the widely-accepted technique of the average diffuse masking angle [81] overestimates the magnitude of collected diffuse light, especially for panels with large tilt angles. A view factor approach has been previously applied to find the average diffuse light collection [82]. Here we find diffuse light incident on each point on the panel to appropriately find the incident diffuse light distribution over the panel faces. This model ensures a more accurate representation of the effect of non-uniform illumination (from direct, diffuse, and albedo light).

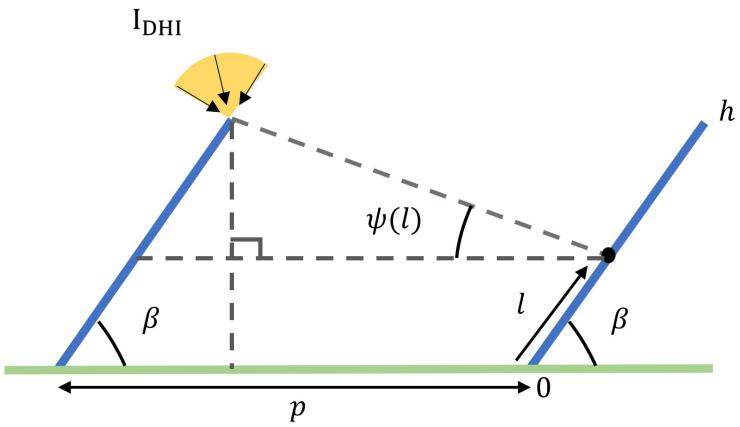

Figure 2.2. Schematic diagram for diffuse light collection on the panel

The spacing between the arrays is such that there is no mutual shading for direct light for most part of the day, however, the isotropic diffuse light does result in mutual shading. The diffuse light falling on the front face of a panel is partially shaded by the panels of the adjacent arrays. The point at length l from the bottom of the panel views an angle $\psi(l)$ shaded or masked by the adjacent panel (see Fig. 2.2). The angle $\psi(l)$ is geometrically calculated as:

$$\psi(l) = tan^{-1}\left[\frac{(1 - l/h)\, sin\beta}{p/h - (1 - l/h)\, cos\beta}\right] \tag{2.13}$$

The diffuse light intensity on the front face, at position l along the panel is given by $I_{DHI} \times F_{dl-sky}(l)$. The view factor from dl to the unobstructed sky, $F_{dl-sky}(l) = 1/2\,(1 + \cos(\psi(l) + \beta))$ [83]. Thus, we arrive at the power generated per unit panel area.

$$\begin{aligned} I^{F,Panel}_{PV:DHI}(l) &= I_{DHI} \times F_{dl-sky}(l) \times \eta_{diff} \\ &= I_{DHI} \times \frac{1}{2}\,(1 + cos(\psi(l) + \beta))\,\eta_{diff} \end{aligned} \tag{2.14}$$

Hence, the total integrated power output per pitch is given by

$$I^{F,Farm}_{PV:DHI} = I_{DHI}\eta_{diff}/h \int_0^h \frac{1}{2}\,(1 + cos(\psi(l) + \beta))\, dl \tag{2.15}$$

Similarly, for the back surface, with array tilt angle equal to $180° - \beta$, the total power output per unit farm area due to diffuse light ($I^{Farm}_{PV:DHI}$) is the sum of $I^{F,Farm}_{PV:DHI}$ and $I^{B,Farm}_{PV:DHI}$.

(c) Albedo light collection

The estimation of the collection of albedo light is the most complex and lengthy amongst the three components and the complete formulation can be found in appendix Sec. 2.6.1. The final expression is as follows:

$$I^{Farm}_{PV:Alb} = I^{Farm}_{PV:Alb,dir} + I^{Farm}_{PV:Alb,diff} \tag{2.16}$$

where total albedo light collected on the panel ($I^{Farm}_{PV:Alb}$) is the sum of albedo due to direct light ($I^{Farm}_{PV:Alb,dir}$) and diffuse light ($I^{Farm}_{PV:Alb,diff}$).

(d) Energy Output

Finally, the total power generated due to light collected from all the components of irradiance is as follows

$$I^{Total}_{PV} = I^{Farm}_{PV:DNI} + I^{Farm}_{PV:DHI} + I^{Farm}_{PV:Alb} \tag{2.17}$$

For energy output, we integrate the power generated over the desired period of time. We define the energy yield per pitch of a farm over a period of one year as yearly yield (YY).

$$YY(p, h, \beta, \gamma, R_A) = \int_0^1 I^{Total}_{PV}(p, h, \beta, \gamma, R_A)\, dY \tag{2.18}$$

Next, we will consider the overall optimization of LCOE*.

2.3 Optimization Methodology

Once we have the energy output (YY) from a farm in terms of the fundamental variables ($p, h.\beta, \gamma$,and R_A), we incorporate this information into Eq. 2.6. For example, let us assume that albedo ($R_A = 0.2$), array azimuth ($\gamma = 180°$ or $0°$), module height ($h = 1m$), and M_L

is fixed. Therefore, the optimization of the bifacial farm reduces to the optimization for 2 physical parameters (p, β) to minimize LCOE*. Fortunately, p and β are correlated, as explained in the next section.

2.3.1 Mutual shading constraint correlating p and β

Mutual shading refers to the shading (or obstruction of direct sunlight) of one array of panels by the neighboring array. The effect of partial shading has been incorporated using bypass diodes as shown in previous studies [61]. Partial shading reduces light collection and energy output, and the non-uniform illumination increases self-heating and module degradation [60], [61], [84]. To avoid mutual shading, the arrays are separated by a distance (pitch) equal to the length of the shadow (at 9am in winter) of an array on the ground. The length of the shadow is longest when Sun's elevation is the smallest. This happens on the shortest day of the year, which is 21st December for the northern hemisphere and 21st June for the southern hemisphere. Assuming the farm is regularly active from 9 am, the pitch of the farm is fixed as the length of the longest shadow observed at 9 am on the shortest day. In principle, the turn-on time may be latitude-dependent; however, our presumption of 9 am turn-on standardizes the analysis. The zenith angle of the sun together with the array tilt angle (β) gives us the pitch equal to the longest shadow at 9 am for a specific location. We calculate the zenith angle (90° – elevation angle) of the sun at 9 am using the Ephemeris model in the Sandia PV library [41]. The analytical formula for pitch is derived using geometry (see Fig. 2.3) and expressed below.

$$\begin{aligned} S_L &= h\, cos(\gamma - A)\, sin\beta \,/\, cot(\theta_{zw}) \\ p_{ns}/h &= S_L \,/\, h + cos\beta \end{aligned} \tag{2.19}$$

where S_L is the extended shadow length.

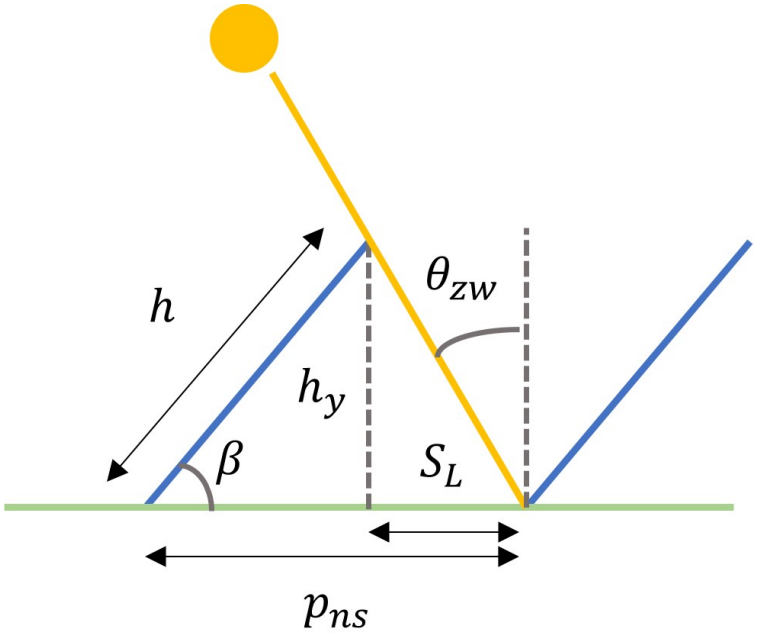

Figure 2.3. Schematic diagram for diffuse light collection on the panel

Consequently, the mutual shading constraint allows us to calculate the pitch as a function of the array tilt angle, i.e., $p_{ns} = f(\beta)$. The corresponding plot is shown in Fig. 2.13 in the appendix. Since $p_{ns} = f(\beta)$, and assuming albedo $R_A = 0.2$, the yearly yield YY is now a function of β alone, i.e., $YY(p, \beta; h = 1\ m, \gamma = 0°, R_A = 0.2) \longrightarrow YY(\beta; h = 1\ m, \gamma = 0°, R_A = 0.2)$. Therefore, for a specific value of M_L, LCOE* (Eq. 2.6) is optimized by the optimization of the array tilt angle, namely $\beta_{opt}(M_L)$. Consequently, we vary β from 0° to 90° (in steps of 1°) and calculate the yearly energy output of the farm (YY) via simulation of the above-mentioned irradiance and light collection models. Further, we calculate the LCOE* for a particular value of M_L and then find the minimum of LCOE*, and the corresponding optimum array tilt angle, β_{opt}. With $p_{ns}^{opt} = f(\beta_{opt})$, the minimum essential levelized cost of energy ($LCOE^*_{min}$) is

$$LCOE^*_{min} = \frac{p_{ns}^{opt}/h + M_L}{YY(\beta_{opt})} \tag{2.20}$$

The simulations yield interesting and noteworthy results that are discussed in the following section.

2.4 Results and Discussions

As noted previously, the LCOE* is dependent on several physical and economic parameters. Assuming $h = 1m, \gamma = 0°$ or $180°$, and $R_A = 0.2$, and finding a relationship between pitch and array tilt angle, $p = f(\beta)$, we finally derived Eq. 2.20 that depends only on two variables, namely Cost ratio (M_L) and array tilt angle (β). In the following discussions, we will calculate M_L-dependent optimum tilt-angle for a specific location (Sec. 2.4.1) and globally (Sec. 2.4.2(a)), optimum-tilt angle dependent yearly yield (Sec. 2.4.2(b)), M_L-dependent minimum levelized cost of energy (Sec. 2.4.2(c)), and LCOE*-reduction of bifacial design over monofacial (Sec. 2.4.2(d)). We also analyze results for three special cases of M_L over various β to understand the location-specific design optimization of farms.

2.4.1 Tilt-optimized Bifacial Solar Farm in Washington, D.C.

Before we proceed with the global analysis, it is instructive to examine the optimization of β to minimize the $LCOE^*$ for a specific location, e.g., Washington DC ($38.91°N, 77.04°W$). The variation of LCOE* with the array tilt angle is analyzed and plotted for two extreme cases shown below.

(a) $M_L \to 0$ (i.e., $c_M \ll c_L$, the land is much more expensive than the modules)

In this case, we observe from Fig. 2.4(a) that the minimum LCOE* occurs at an optimum tilt angle, $\beta_{opt} = 0°$. This implies that wherever the land is much more expensive than the module, the installed panels should be installed flat on the ground, stacked end-to-end next to each other, to ensure maximum packing of the arrays (i.e., period (p) = height (h)). Moreover, this case is applicable to most land-constrained designs i.e., mega-city installations where land is limited.

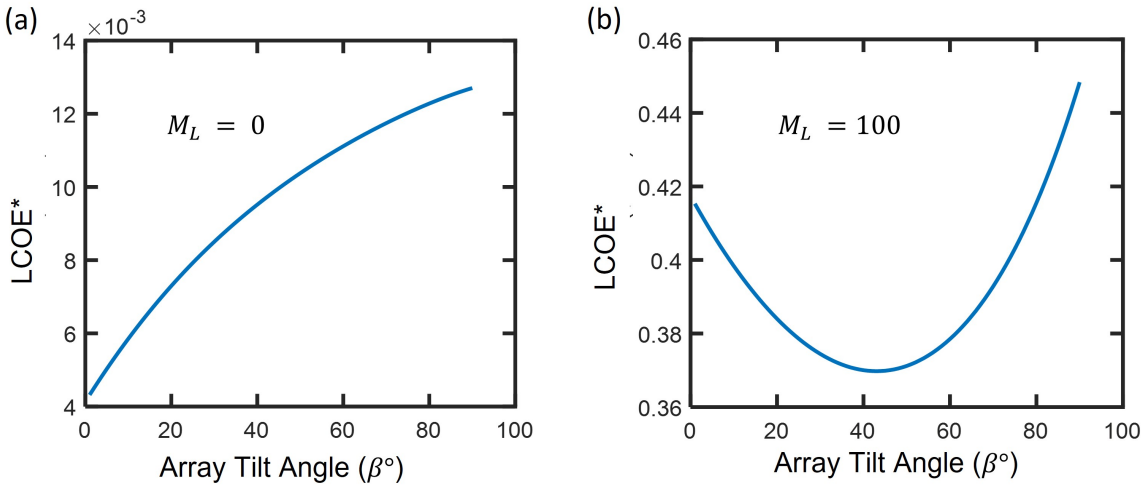

Figure 2.4. LCOE* vs. β (a) $M_L = 0$, (b)$M_L = 100$.

(b) $M_L = 100$ **(i.e.,** $c_M \gg c_L$**, the land is much more expensive than the modules)**

For the other extreme case, where the modules are much more expensive than the land, Fig. 2.4(b) shows the variation of LCOE* with array tilt angle for the same location $(38.91°N, 77.04°W)$. Intriguingly, we find that there exists an optimum $\beta(\sim 42°)$ to achieve minima in LCOE*. The optimum angle for bifacial farm is higher ($\sim 10°$) compared to angle-optimized monofacial cells (i.e., $\beta \sim 32°$).

(c) $0 < M_L < 100$ **(i.e.,** $c_M \sim c_L$**)**

Several locations in the world might fall in this category, where the land and module costs are comparable. Historically, M_L has ranged from ~ 0.1 to 15 [85]. Thus, we specifically explore the variation of LCOE* and β_{opt} over this typical range of M_L (see inset of Fig. 2.5(a),(b)). For Washington, DC $(38.91°N, 77.04°W)$, we find that the minimum LCOE* increases linearly until $M_L \sim 8$ and then deviates from linearity (increases sub-linearly) for higher M_L (see Fig. 2.5(a)). This slope-change is understood by using Fig. 2.5(b) where the optimum tilt angle (β_{opt}) increases abruptly at $M_L^* \sim 8$. A similar trend is seen in YY vs. M_L. For $M_L < 8$, the higher yearly yield associated with the tilted modules is negated by the high land cost (low M_L).

Interestingly, the optimum tilt angle (Fig. 2.5(b)) can be approximated in terms of M_L using the following empirical formula.

$$\beta_{opt}^{ana} = c_1 M_L + \exp\left[c_2\left(1 - \frac{1}{(M_L - M_L^*)^{c_3}}\right)\right] \tag{2.21}$$

where $c_1 = 0.07, c_2 = 3.6$ and $c_3 = 1.6$ are location-based empirical constants. Here, $M_L^* \sim 8$ is the threshold cost ratio, below which $\beta_{opt} = 0°$. Note that since YY depends on latitude/longitude of a location, so does the M_L^* for that location. The location-specific M_L^* (typically 0-10) is calculated numerically (see Fig. 2.15 in appendix).

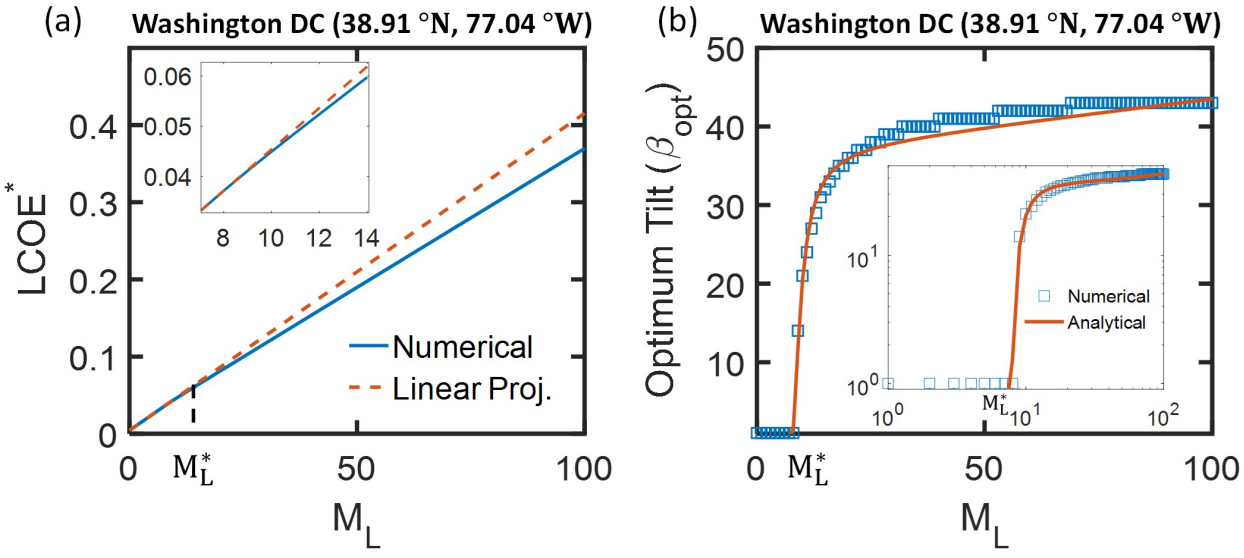

Figure 2.5. (a) LCOE* vs. M_L. (b) Comparison between numerical analytical values of β_{opt} vs. M_L. Inset of (a) and (b) show exactly where the transition occurs ($M_L^* \sim 8$).

Discussion of result from Washington, D.C

To rationalize the trends in LCOE*, we examine the (relative) contributions of essential costs vs. energy yield. In this regard, we reconsider Eq. 2.6, where total cost $C = p/h + M_L$

and yearly energy yield is YY. Hence, the relative error in LCOE* is given by the following expression.

$$\frac{\Delta LCOE^*}{LCOE^*} \equiv \frac{\Delta C(p/h, M_L)}{C(p/h, M_L)} - \frac{\Delta YY(p/h, \beta)}{YY(p/h, \beta)} \tag{2.22}$$

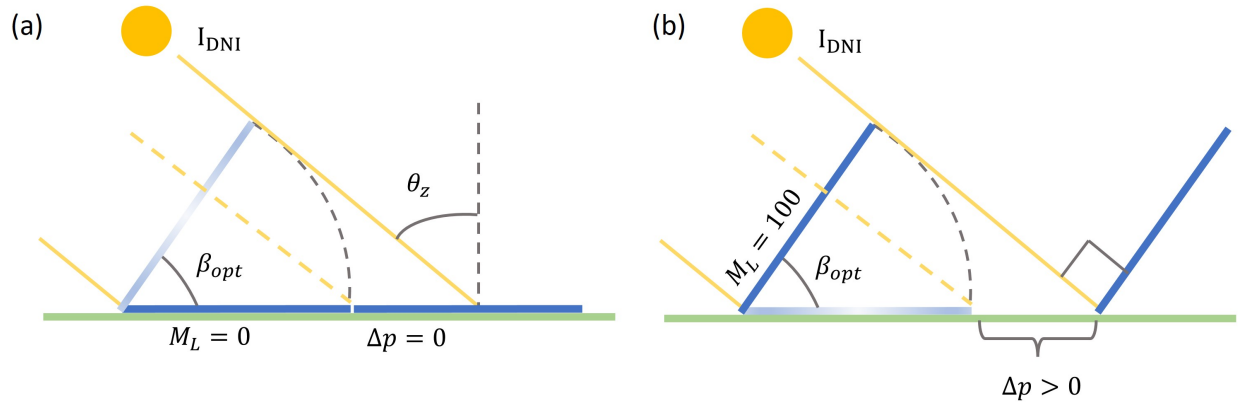

Figure 2.6. (a) For $M_L = 0$, stacking panels next to each-other (i.e., $\Delta p = 0$) maximizes light collection per unit area of the module. The cosine incidence of direct light on the panels is shown. (b) For $M_L = 100$, the light collection is increased with titled and optimally-separated modules.

Here, the cost is a function of p/h and M_L whereas yearly energy yield is a function of p/h and β. With the objective of achieving negative (or less positive) $\Delta LCOE^*$, let us now examine the results through the above equation, and Fig. 2.6.

For $M_L = 0$, the land cost is much higher than the module cost, which necessitates maximum collection of light for the lowest land area (pitch). This is achieved when $\Delta p \to 0$ (as shown in Fig. 2.6(a)), such that the panels collect all the light falling on the ground (I_{GHI}) with least amount of land used. Although I_{GHI} is collected completely by the farm, each of the panels collect cosine of direct light ($I_{DNI} \cos\theta_Z$), see Fig. 2.6(a)) throughout the day. Fig. 2.6 shows that $\Delta p \to 0$ reduces the total light collection as compared to $\Delta p > 0$ (i.e., $\Delta YY < 0$), but this is counterbalanced by the reduction in the cost of land ($\Delta C < 0$). Overall, LCOE* is reduced (i.e., ΔLCOE$* < 0$). Therefore, in this case, the optimum design involves stacking the panels next to each other flat on the ground to minimize LCOE*.

For $M_L = 100$, the land cost is much lower than the module cost, and it is vital to maximally collect light per unit area of the module. This is attained by collecting direct light incident perpendicular onto the front face of the panel and collecting the albedo light on both faces to increase the energy yield i.e., $\Delta YY > 0$. This comes at the expense of increased cost ($M_L = 100$) i.e., $\Delta C > 0$, but overall the magnitude of ΔYY is greater than that of ΔC, therefore, LCOE* decreases (i.e., $\Delta LCOE^* < 0$). Fig. 2.6(b) shows the schematic of the economically viable design where I_{DNI} falls perpendicular to the front face and Δp depends on the mutual shading constraint at that location. We now understand the variations in LCOE* and optimum tilt angle for various cases at a particular location (Washington, D.C.). This enables us to scrutinize the global trends in optimum tilt angle (β_{opt}), yearly energy yield (YY), and LCOE*.

2.4.2 Global Analysis for Tilt-optimized Bifacial Farms

In this section, we will examine the results of worldwide simulations and draw inferences from these results. Note that beyond |latitude| > 60°, the days are extremely short during winters and there is no sunlight at 9am on the shortest day. Based on the mutual shading constraint assumed in this chapter (e.g. 9 am turn-on time), we do not include the results for |latitude| > 60°. The constraint is can be easily relaxed with a later turn-on time for higher latitudes and the LOCE can be calculated at any latitude across the world.

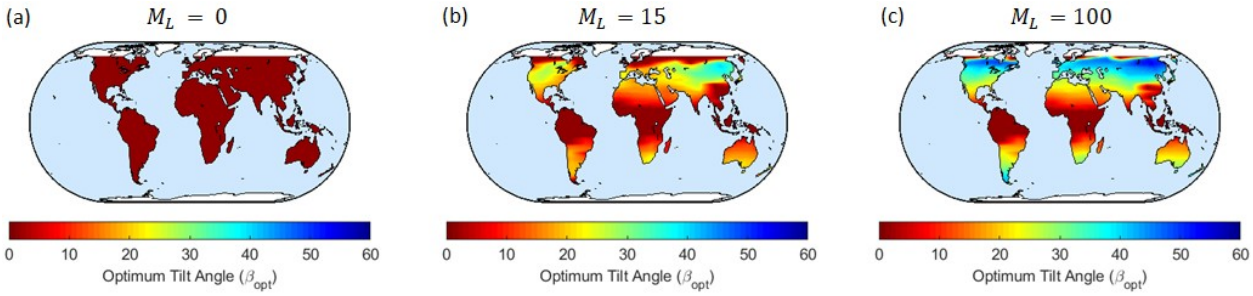

Figure 2.7. Global map of optimum array tilt angle associated with the minimum LCOE* for that location with $R_A = 0.2$: (a) $M_L = 0$ (b) $M_L = 15$ (c) $M_L = 100$

(a) Optimum tilt angle (β_{opt})

For Case 1, where module cost is much smaller than the land cost ($M_L \to 0$), Fig. 2.7(a) clearly shows that the panels should be deployed horizontally on the ground. Similar to Washington, D.C., this conclusion unequivocally holds for all the locations around the world. The explanation also remains the same as described earlier in Sec. 2.4.1.

For Case 2, where modules are much more expensive than land ($M_L = 100$), Fig. 2.7(c) illustrates the latitude-dependent optimum tilt angle for a cost-optimized solar farm, the physical explanation of which was explained in detail in Sec. 2.4.1. The latitude-wise increasing trend in optimum angles is broken for places such as Central and East China (Chongqing and Xi'an) due to the contributions from diffused light.

For Case 3, with comparable module vs. land-cost, typical values of $M_L(\sim 15)$, Fig. 2.7(b) displays the optimum tilt angle between Case 1 and 2, in accordance with the plot in Fig. 2.4(b). Note that, at higher latitudes, as the optimum tilt angle increases (for Cases 2 and 3), the East-West facing vertical bifacial farms become cost competitive with tilted bifacial farms (although with an increased land area) [32], [61], [64], [86].

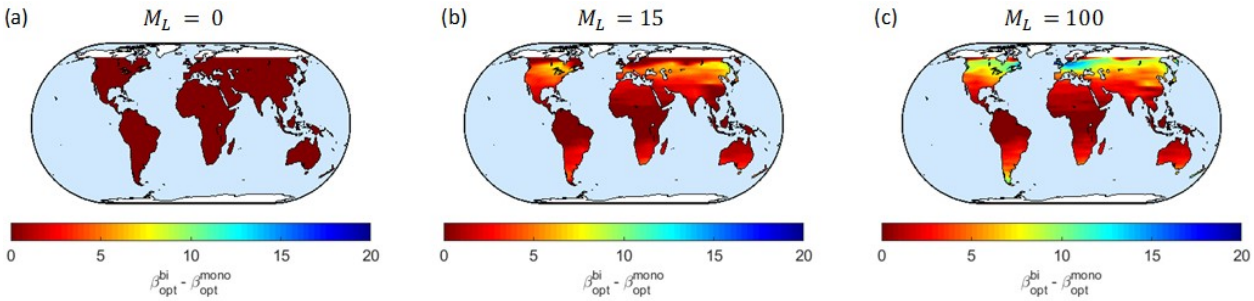

Figure 2.8. Global map of difference in optimum array tilt angle between bifacial and monofacial designs with $R_A = 0.2$: (a) $M_L = 0$ (b) $M_L = 15$ (c) $M_L = 100$

Fig. 2.8 demonstrates the difference in the optimum tilt angle for bifacial vs. monofacial design. For $M_L > 0$, we see β_{opt} for bifacial is greater than that of monofacial farms in order take advantage of the bifaciality and collect more light at the back surface of the panel. $\Delta\beta_{opt} \sim 10° - 15°$ for $|\text{latitude}| > 30°$ and areas with high diffuse light fraction, e.g. Canada,

Western Europe, Central China etc. An added benefit to higher tilt angle is a reduction in cleaning cost due to a decrease in soiling [87].

(b) Local and Global Yearly Energy Yield (YY)

Next, we analyze the yearly energy output from a tilt-optimized solar farm for two limiting cases: (i) $M_L = 0$, i.e., the module costs negligible as compared to land. These locations can be cosmopolitans, megacities, and cities, and, in general, densely populated areas; (ii) $M_L = 100$ where modules are much more expensive compared to land. These can be remote locations and sparsely populated areas. Fig. 2.14 in appendix shows the global map for these two cases. We notice a slight improvement in the yearly yield for $M_L = 100$ as compared to $M_L = 0$. This is also evident from the simulation for a single location (e.g., Washington DC) where YY for $M_L = 0$ case is 231 kWh/m^2 while YY for $M_L = 100$ is 278 kWh/m^2. This is because the collection of direct light and albedo light are enhanced for $M_L = 100$ as compared to $M_L = 0$ (both for the same city). We also find that the energy yield steadily reduces with increasing latitude, except for some specific places like Central and East China, and West Brazil where the trend is broken. These regions are characterized by lower clearness index with higher fraction of diffuse light compared to places near the equator.

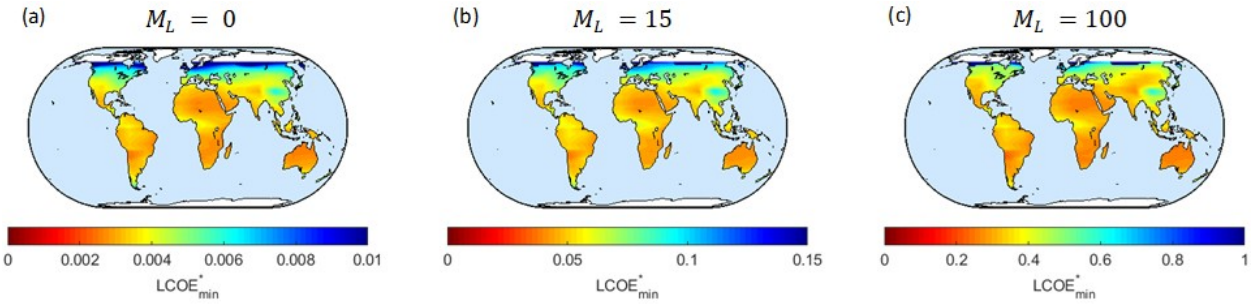

Figure 2.9. $LCOE^*_{min}$ global maps, with $R_A = 0.2$: (a) $M_L = 0$ (b) $M_L = 15$ (c) $M_L = 100$.

(c) Minimum Levelized Cost of Energy ($LCOE^*_{min}$)

Given the information about optimum tilt-angle (Sec. 2.4.1,2.4.2) and energy yield (Sec. 2.4.2), we can now calculate minimum LCOE* for locations around the world. Fig. 2.9 shows

that, unlike the yearly energy yield world maps, the $LCOE^*_{min}$ for $M_L = 0$ follows a similar (but inverse) trend as YY for $M_L = 0$, i.e., the maximum in YY are exactly the minima in $LCOE^*_{min}$. On the other hand, these two parameters for $M_L = 100$ do not show an exact inverse trend. This difference elucidates the role of essential costs in LCOE* calculations. world maps depend sensitively on module vs. land costs. When the land cost is very high as compared to module cost ($M_L = 0$), then the LCOE* is dominated by the yearly energy yield, and hence we observe the similar (but inverse) trend since LCOE* is inversely proportional to YY. Whereas in the reverse case ($M_L = 100$), LCOE* is dominated by M_L. Therefore, we see in Fig. 2.9(c) that LCOE* remains almost uniform throughout the globe pertaining to the much larger value of M_L as compared to p/h.

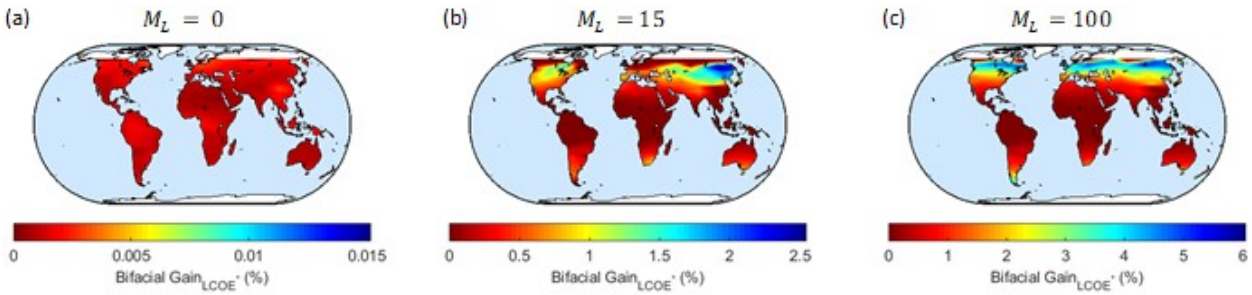

Figure 2.10. Bifacial gain in terms of LCOE* reduction, with $R_A = 0.2$: (a) $M_L = 0$ (b) $M_L = 15$ (c) $M_L = 100$.

(d) LCOE* improvement of bifacial over monofacial

To scrutinize the viability of bifacial solar farms, it is important to juxtapose the performance of bifacial solar farms with their monofacial counterparts. The cost of bifacial modules has been falling consistently over the years [21], [31]. Even though our approach can easily compare technologies with different M_L, the following discussion assumes an optimistic case where the costs of bifacial and monofacial modules (i.e., M_L) are equal. Fig. 2.10 shows the absolute percentage decrease in $LCOE^*_{min}$ when we decide to install a bifacial farm vs. a monofacial farm. Clearly, for $M_L = 0$, bifacial LCOE* is equal to monofacial LCOE* since the panels are flat on the ground and the back surface does not collect any light. This result would be different and in favor of bifacial solar farms if the panels are elevated above the

ground (and spaced apart) so that the albedo light can be collected. Note that the slight apparent improvement in LCOE* for $M_L = 0$ (and at tilt-angle $\beta \to 0°$) is a numerical artifact associated with minimum angle spacing of 1 degree.

For $M_L = 100$, on the other hand, there is a negligible reduction in LCOE* for latitudes less than $+/-30°$ from the equator. We find that $LCOE^*_{min}$ reduces by $\sim 2-6\%$ for $|\text{latitude}| > 30°$. Since the panels are tilted facing the direct light for $M_L = 100$, hence this observation indicates that a bifacial farm is more economical than a monofacial farm in terms of LCOE*, for places where diffuse light is a dominant component of light over direct light. The analysis in Sec. **??**(a) justifies this conclusion.

Finally, due to the improvement in energy yield for bifacial solar farms for these locations, there is a decrease in LCOE* ($\sim 2-6\%$) for a bifacial farm compared to a monofacial farm, which is displayed clearly in Fig. 2.10(c) (e.g., Northern USA, Germany, UK, and Central Asia). We have assumed that the monofacial and bifacial costs are similar to produce a Bifacial $\text{Gain}_{\text{LCOE}^*}$ of $2-6\%$. In other words, bifacial modules should be no more than 2-6% expensive for the solar farm to be economically viable [88]. Additional margin in LCOE may be obtained when the modules are elevated, and the reduced cleaning cost associated with higher tilt angle is accounted for. These would be important topics of future research.

Note that all of the above global maps with albedo $R_A = 0.5$ are presented in the Appendix (see Figs. 2.16-2.20).

2.5 Summary and Conclusions

We have parametrically explored the economic viability of ground-mounted tilted bifacial solar farms and explained how the farm topology must be optimized for a given location, and module and land cost considerations. We have redefined the levelized cost of energy (LCOE) in terms of 'essential levelized cost of energy' ($LCOE^*$) that is ultimately a function of module to land cost ratio (M_L) and array tilt angle (β). The redefined LCOE* decouples cost analysis from energy yield modeling, thereby dramatically simplifying the optimization of solar farms based on new technologies. Our model provides an optimistic lower bound for LCOE (for ground-mounted cells with a fixed albedo). In practice, various non-idealities

(e.g. efficiency degradation with temperature, power mismatch among the strings due to spatially and spectrally varying albedo, etc.) will increase the LCOE. Therefore, our idealized lower-bound LCOE is a necessary (but not sufficient) precondition for the economic viability of the bifacial technology.

Using a previously developed global irradiance model [61]. we calculated the spatial distribution of light on the ground and panel faces while considering all variations of shadows for all the locations in the world. The collection of direct, diffuse, and albedo light on the panels were then integrated over time to obtain the yearly yield for the specific solar farm configuration (defined by panel tilt and array period). Once we correlate the configuration of a farm to the cost of its installation and the yearly yield, we can determine LCOE*.

The array tilt β defines the array period through the mutual shading constraint, which in turn sets the number of panels required in a solar farm. Therefore β is implicitly related to the farm cost (and of course the energy). Note that the mutual shading constraint at 9 am on the shortest day of the year limits the global optimization using array tilt (β) and period (p) as independent variables. In the end, cost ratio (M_L) and array tilt angle (β) are the handles to control the LCOE*. For a fixed M_L, we numerically and analytically found an optimum tilt angle (β_{opt}) for each location.

Our analysis leads to the following **conclusions**:

- For places where land is scarce and expensive ($M_L \to 0$), panels should be laid flat on the ground ($\beta_{opt} = 0°$) to ensure maximum energy collection over a given land area. On the contrary, for practical values of $M_L (\sim 1 - 15)$ when the land is relatively inexpensive, panels have location specific optimum tilt ($\beta_{opt} \sim 0° - 60°$) to achieve least LCOE*.

- PV installers can use an analytical expression of the form of Eq. 2.21 to find the location-specific optimum array tilt angle (β_{opt}) as a function of M_L. Moreover, β_{opt} is constantly zero until a threshold value (M_L^*) of cost ratio that varies with the location (latitude/longitude).

- The difference in optimum tilt angle ($\Delta\beta_{opt}$) between bifacial and monofacial designs can reach up to $10° - 15°$ for $|\text{latitude}| > 30°$ and places with high diffuse light

fraction, e.g., Canada, Western Europe, Central China, etc. Moreover, higher tilt angle makes the design soiling-resistant, in turn reducing cleaning cost.

- For the same module-to-land cost ratio and similar lifetimes (reliability), ground-mounted bifacial solar farm design is more economically viable over monofacial design for locations where the diffuse fraction is high. The relative reduction in LCOE* (Bifacial Gain_{LCOE^*}) is $\sim 2-6\%$, for bifacial solar farm design over monofacial for locations with higher fractions of diffuse light (low clearness index, k_t) e.g., locations with $|\text{latitude}| > 30^\circ$ (Central Europe, Northern parts of North America, and Central China). Alternatively, bifacial modules can be at most $\sim 2-6\%$ more expensive compared to monofacial modules for a bifacial solar farm to be cost-competitive compared to a monofacial farm.

Although this is the first report of LCOE-optimized farm design inclusive of land costs, the present work can be generalized in a number of ways. One can use the current approach to easily account for location-specific albedo and tilt-angle. Furthermore, currently the bifacial panels are slightly more expensive (but also known to be more reliable [13], [26]) than monofacial modules. This cost and reliability differences can be accounted for easily in our formulation. Instead of ground-mounted panels, the farm design can deploy elevated panels. The elevation of panels could increase the albedo light collection depending on the farm design, but this gain must be balanced against the increase in the installation (module) cost. It is also possible to sculpt the ground to increase albedo and re-optimize the configuration. Moreover, the effect of temperature on estimation of energy output and maintenance costs can be included to make the analysis more comprehensive.

To conclude, the reduction in LCOE through optimized farm design and continually reducing bifacial module prices makes bifacial PV technology an economically preferable alternative over monofacial solar farm.

2.6 Appendix

2.6.1 Albedo Light Collection

For the albedo light collection, we will start with the same approach used by Khan et al. [61] for vertical bifacial panels and generalize it for the tilted bifacial design.

We first account for albedo from direct light. The direct light collected on the ground is given by:

$$I_{Gnd:DNI}\ (x) = I_{DNI}\ \cos\theta_Z(t) \tag{2.23}$$

where $s_1(t) < x < p - s_2(t)$. Here s_1 is the time-varying shadow length in the morning and s_2 is the time-varying shadow length in the afternoon (see Fig. 2.11). s_1 and s_2 can be calculated using Eq. 2.19 on $S_L(t)$. The unshaded part $p - s_1$ on the ground subtends angle $(\psi_0,\ \pi/2)$ at the point l on the front panel face (see Fig. 2.11) in the morning while the unshaded part $p - s_2$ subtends (ψ_1, ψ_2) in the afternoon. These angles are geometrically calculated as:

$$\left.\begin{aligned} \psi_0\,(l) &= \tan^{-1}\left[\tfrac{-(p-s_1(t)+l\cos\beta)}{l\sin\beta}\right] - \beta \\ \psi_1\,(l) &= \tan^{-1}\left[\tfrac{-(p+l\cos\beta)}{l\sin\beta}\right] - \beta \\ \psi_2\,(l) &= \tan^{-1}\left[\tfrac{-(s_2(t)+l\cos\beta)}{l\sin\beta}\right] - \beta \end{aligned}\right\} \tag{2.24}$$

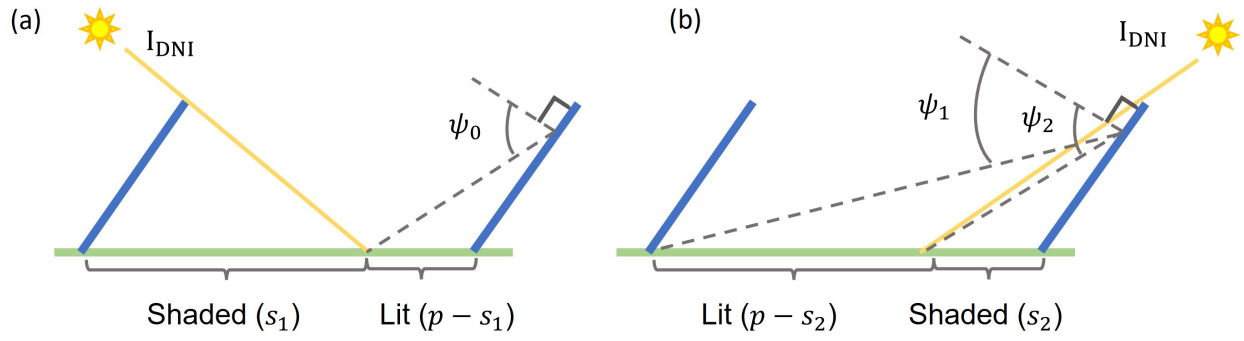

Figure 2.11. Schematic for albedo from direct light: (a) before noon and (b) afternoon

Using these angles, we find the view factor from the point l from the ground to the unshaded part of the ground.

$$\begin{aligned} F_{dl-gnd} &= \frac{1}{2}\left(1-\sin\psi_0\left(l\right)\right), in\ morning; \\ &= \frac{1}{2}\left(1\sin\psi_2\ \left(l\right)-\sin\psi_1\left(l\right)\right), in\ afternoon. \end{aligned} \tag{2.25}$$

Therefore, the power generated per area of the panel for the front face is given by

$$I^{F,Panel}_{PV:Alb.dir}\left(l\right) = I_{Gnd:DNI} \times R_A\ \times F_{dl-gnd}(l) \times\ \eta_{diff} \tag{2.26}$$

where R_A is the fraction of incident light reflected from the ground. Thus, the power generated per pitch of the farm is given by

$$I^{F,Farm}_{PV:Alb.dir}\left(l\right) =\ 1/h \int_0^h I^{F,Panel}_{PV:Alb.dir}(l)dl \tag{2.27}$$

Note that the integral is implemented as a summation from the bottom edge of the panel to the top edge with a step-size of 0.01 m. By incorporating the collection from the back surface, we will have the total albedo due to direct light ($I^{Farm}_{PV:Alb.dir}$).

For albedo from the diffuse light we combine the method used by Khan et al. and the view factors for our tilted panels. Similar to the collection of direct light on the ground, we find the collection of diffuse light on the ground taking into account the masking due to adjacent panels/arrays. Fig. 2.12(a) illustrates the masking and collection of diffuse light at a point x positioned between two adjacent panels. The angles $[\theta_1, \theta_2]$ subtended at point x by the topmost points of the panels are given by

$$\begin{aligned} \theta_1(x) &= \pi - tan^{-1}\left[\frac{h-\sin\beta}{h\cos\beta - x}\right] \\ \theta_2(x) &= tan^{-1}\left[\frac{h-\sin\beta}{p-x+h\cos\beta}\right] \end{aligned} \tag{2.28}$$

The view factor from the ground to the sky is $F_{dx-sky}\ (x) = 1/2\,[\sin(\pi/2 - \theta_2\ ) - \sin(\theta_1 - \pi/2)]$, which can be used to find $I_{Gnd:DHI}$ as

$$I_{Gnd:DHI} = 1/p \int_0^p I_{DHI} \times F_{dl-gnd}(x)dx \tag{2.29}$$

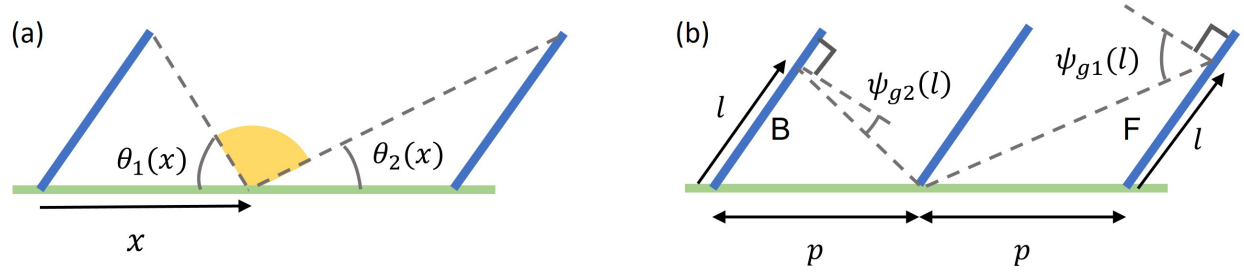

Figure 2.12. Schematic for (a) diffuse light collection on the ground (b) view factor calculation for albedo light collection.

Now, the albedo light collected on the panels from the ground requires us to calculate the view factor from the ground to the panels (see Fig. 2.11(b)). This view factor is given by $F_{dx-dl-F}\ (x) = 1/2[1 - \sin(\psi_{g1}/2)]$ for front face, and $F_{dx-dl-B}\ (x) = 1/2[1 - \sin(\psi_{g2}/2)]$, where

$$\begin{aligned} \psi_{g1} &= \pi/2 - \beta - \tan^{-1}\left[\frac{l\ \sin\beta}{p + l\ \cos\beta}\right] \\ \psi_{g2} &= \pi/2 - \beta - \tan^{-1}\left[\frac{l\ \sin\beta}{p - l\ \cos\beta}\right] \end{aligned} \tag{2.30}$$

Finally, we arrive at the power per unit panel area as follows

$$I^{F,Panel}_{PV:Alb.diff}(l) = I_{Gnd:DHI} \times R_A \times F_{dl-gnd}(l) \times \eta_{diff} \tag{2.31}$$

and the power per pitch of farm is

$$I^{F,Farm}_{PV:Alb.diff} = 1/h \int_0^h I^{F,Panel}_{PV:Alb.diff}(l)\ dl \tag{2.32}$$

Adding the light collected at the back surface, we get the total albedo due to diffuse light ($I^{Farm}_{PV:Alb.diff}$). Hence, total albedo light collection is given by

$$I^{Farm}_{PV:Alb} = I^{Farm}_{PV:Alb.dir} + I^{Farm}_{PV:Alb.diff} \tag{2.33}$$

2.6.2 Mutual Shading Constraint

The mutual shading constraint at a particular locations on the shortest of day of the year (21st December for Northern Hemisphere and 21st June for the Southern Hemisphere) gives us a relation between the pitch (period) of the farm and tilt angle of the panels (arrays). Fig. 2.13 shows this relationship.

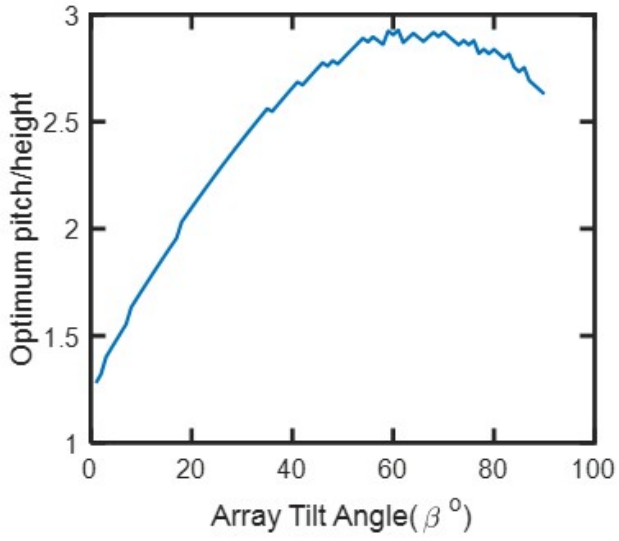

Figure 2.13. The plot shows the pitch as a function of array tilt angle achieved using the mutual shading constraint on the shortest day of the year for Washington, D.C.

2.6.3 Yearly Yield

The yearly energy yield for the two extreme cases is shown in Fig. 2.14. Notice the high energy yield at Sahara Desert and relatively low yields at places with high fraction of diffuse light e.g., Central China and places with |latitude| $> 30°$. The trends of LCOE* and YY are

perfectly inverse of each other for $M_L = 0$ while $M_L = 100$ shows the effect of high cost ratio leading to weaker dependence of LCOE* on YY.

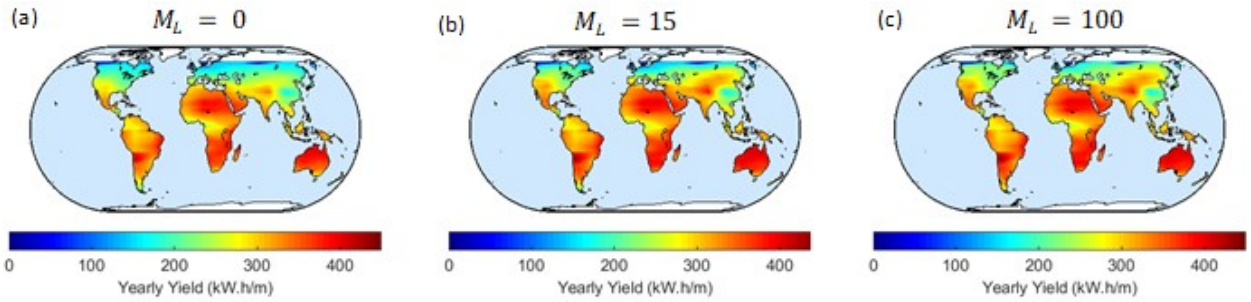

Figure 2.14. Global maps showing yearly energy yield of bifacial solar farms, with $R_A = 0.2$, for (a) $M_L = 0$ (b) $M_L = 15$ (c) $M_L = 100$.

2.6.4 Typical values of M_L^*

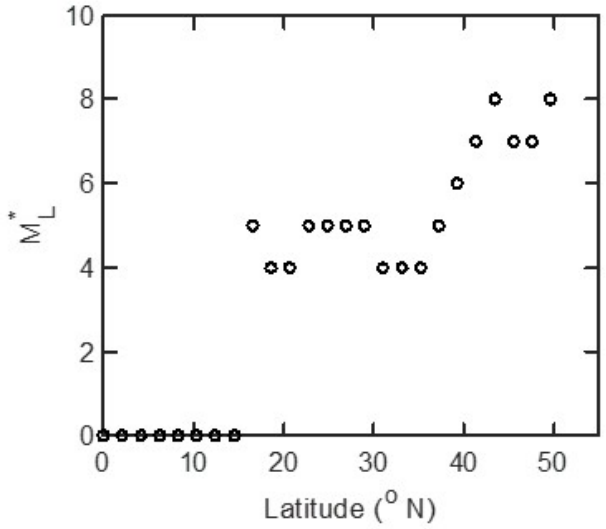

Figure 2.15. Typical values of M_L^* with increasing latitude at longitude = 0°.

2.6.5 Results for $R_A = 0.5$

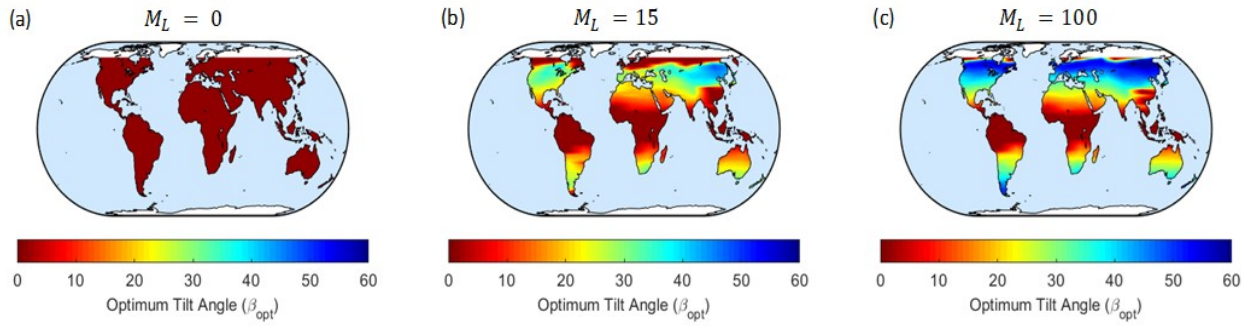

Figure 2.16. Global map of optimum array tilt angle associated with the minimum LCOE* for that location with $R_A = 0.5$, for (a) $M_L = 0$ (b) $M_L = 15$ (c) $M_L = 100$.

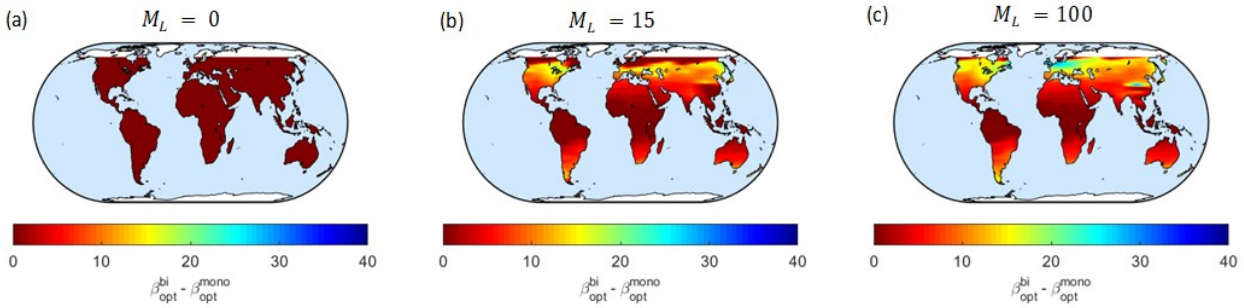

Figure 2.17. Global map of difference in optimum array tilt angle between bifacial and monofacial designs with $R_A = 0.5$, for (a) $M_L = 0$ (b) $M_L = 15$ (c) $M_L = 100$.

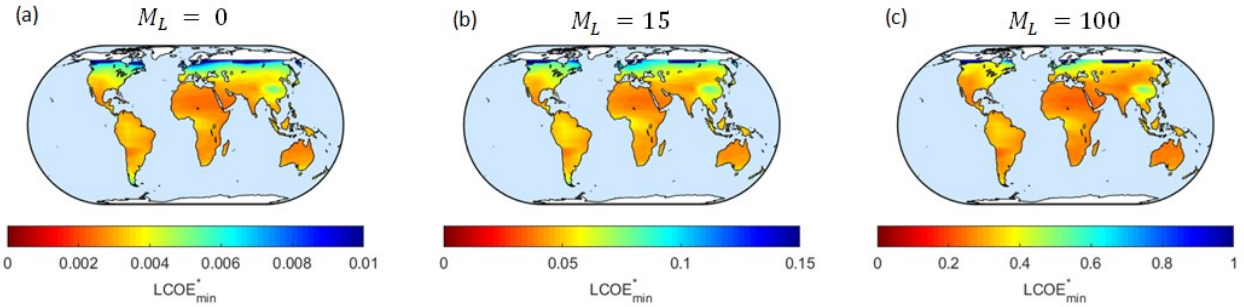

Figure 2.18. $LCOE_min^*$ global maps, with $R_A = 0.5$, for (a) $M_L = 0$ (b) $M_L = 15$ (c) $M_L = 100$.

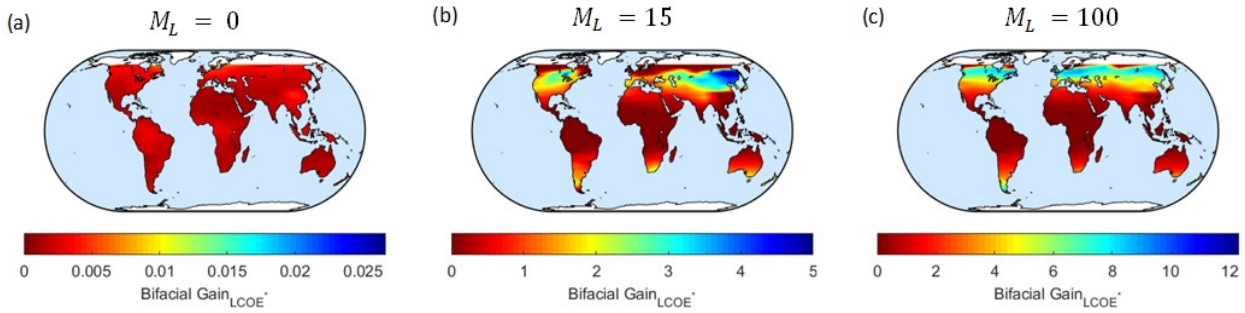

Figure 2.19. Bifacial gain in terms of LCOE* reduction, with $R_A = 0.5$, for (a) $M_L = 0$ (b) $M_L = 15$ (c) $M_L = 100$.

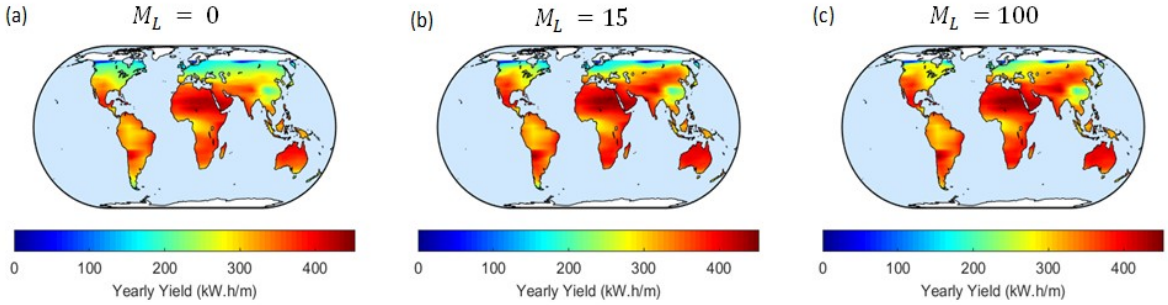

Figure 2.20. Global maps showing yearly energy yield of bifacial solar farms, with $R_A = 0.5$, for (a) $M_L = 0$ (b) $M_L = 15$ (c) $M_L = 100$.

2.6.6 Estimating $\mathbb{C}_M, \mathbb{C}_L$, and χ.

In the main article, we have explained how to convert LCOE to LCOE* so that the technology and economic considerations can be treated independently. We have also explained how the farm topology optimized to minimize LCOE*. To translate LCOE* back to LCOE by Eq. 2.6, we need to first determine $(M_L \equiv (C_M W_h)/(C_L W_p))$, calculate $LCOE^*(M_L)$, and then find $LCOE = (C_L/\chi)\, LCOE^*$. In other words, the back-conversion requires practical and location-specific values of C_M, C_L, and χ.

As an illustrative example, we can consider the cost benchmark report by NREL [85], which provides a detailed cost dissection for residential, commercial, and utility-scale PV systems. Fig. 2.21 shows the historical cost benchmark summary for fixed-tilt 100 MW utility-scale PV.

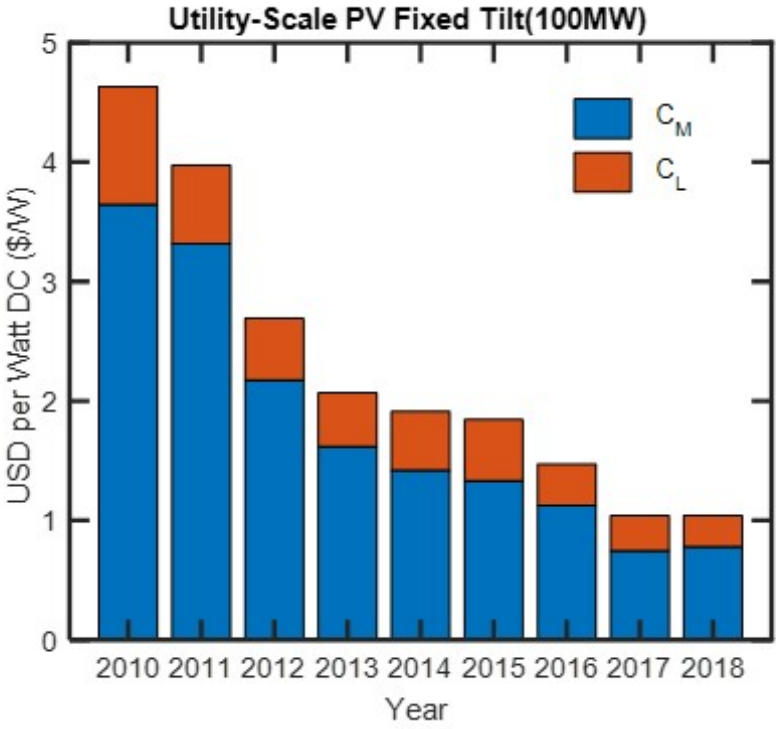

Figure 2.21. Historical trend in LCOE with cost dissection [85]. These costs are regrouped into effective module cost (C_M) and effective land cost (C_L).

According to the definitions of C_M and C_L, we regroup the cost categories into the effective module cost (module cost, inverter, hardware BOS, and soft costs – install labor) and effective land cost (soft costs - others). Since Fig. 2.21 costs are expressed in Dollars per watt ($/W) while C_M and C_L involve Dollars per meter ($/m), therefore

$$\mathbb{C}_M = C_M\ W_h \quad \$/m;\ \mathbb{C}_L = C_L\ W_p \quad \$/m;\ M_L = \mathbb{C}_M\ W_h/\mathbb{C}_L\ W_p \tag{2.34}$$

Here W_h and W_p are W/m of module height and W/m of land, respectively, of a solar farm. W_h is the product of cell efficiency (fraction) and the input power (1000 W/m^2), which is equal to 191 W/m assuming 1 m width of the module. For W_p, we follow the rule that 1 MW of plant requires 4 $acres$ (4046.86 m^2) of land [89]. For 100 MW fixed-tilt plant (Fig. 2.21), $W_p = 100\ MW/(400 \times 4046.86\ m) = 61.77\ W/m$, assuming unit width of the land. Assuming a degradation rate $d = 0.7\%$, bank discount rate $r = 6.5\%$ and farm lifetime $Y = 25\ years$, we calculate $\chi = 12.4$. The yearly energy yield is calculated using the farm

models as described in Section 2.4.2(b) of the main text of this chapter . We can now estimate LCOE using the values of $\mathbb{C}_M, \mathbb{C}_L, \chi$,and YY to compare it with real LCOE values.

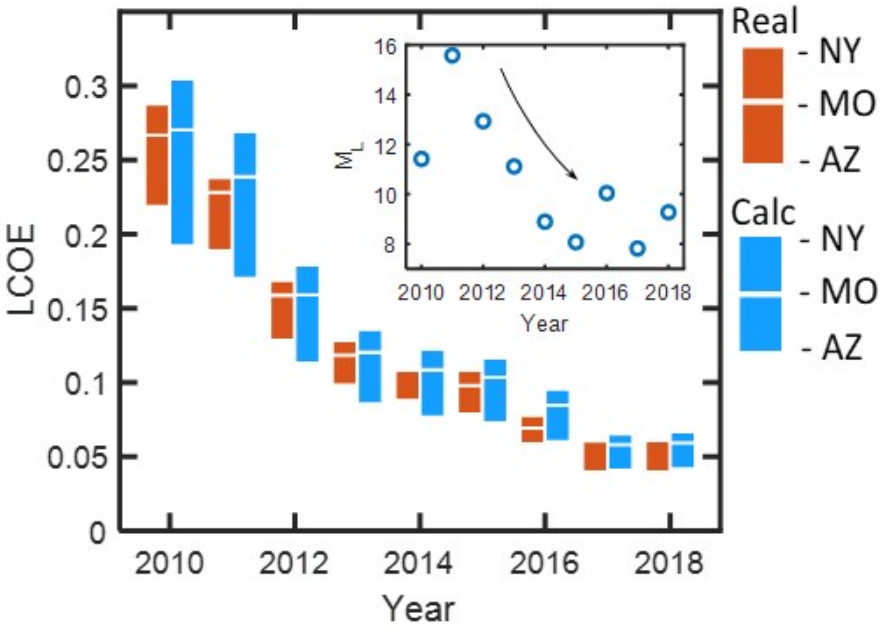

Figure 2.22. Calculated LCOE vs. standard (real) LCOE for three locations. (Inset) Yearly trend shows that M_L ranges from 7-16 based on [85].

To validate the conversion of LCOE* to LCOE, let us compare the LCOE predicted by our approach to the published (or "real") LCOE for three locations – Phoenix, AZ, Kansas City, MO and New York City, NY [85]. Since the costs in Fig. 2.22 represent the average values across USA, thus the M_L, $\mathbb{C}_L$ and χ values are presumed to be the same for all the locations. However, the yearly energy yields differ substantially and is reflected in their respective LCOE. The overall agreement is excellent, the slight difference is attributed to the local variations in M_L, d, and Y.

3. TEMPERATURE-DEPENDENT ENERGY GAIN OF BIFACIAL PV FARMS: A GLOBAL PERSPECTIVE

In the previous chapter, we developed an opto-ectro-economic model for bifacial solar PV farms. However, as the bifacial farms proliferate around the world, it is important to investigate the role of temperature on the energy yield and the levelized cost of energy (LCOE) of bifacial solar farms relative to monofacial farms, stand-alone bifacial modules, and various competing bifacial technologies. In this chapter, we integrate irradiance and light collection models with experimentally validated, physics-based temperature-dependent efficiency models to compare the energy yield and LCOE reduction of various bifacial technologies across the world. We find that temperature-dependent efficiency changes the energy yield and LCOE by approximately $\mathbf{-10}$ to $\mathbf{15}\%$. Indeed, the results differ significantly depending on the location of the farm (which defines the illumination and ambient temperature), the elevation of the module (increases incident energy), as well as the temperature-coefficients of various bifacial technologies. The analysis presented in this chapter will allow us to realistically assess location-specific relative advantage and economic viability of the next generation bifacial solar farms.

3.1 Introduction

The PV industry is actively developing bifacial module technology to reduce the levelized cost of energy (LCOE) of the utility-scale solar PV farms [1]–[6], [9], [11]–[13], [59], [90]. This is because a bifacial solar panel collects light at both the front and rear surfaces as compared to the monofacial panels that collect only at the front. A recent literature review by Guerrero-Lemus et al. [22] explains how bifacial technology has developed from its infancy in the 1960s to practical applications and scalability. Despite the possibility of higher output from the same footprint, bifacial PV technology had to wait until recent innovations for accelerated deployment. The International Technology Roadmap for Photovoltaic (ITRPV) predicts that the worldwide market share for bifacial technology will increase from 15% in

↑**Note:** The material in this chapter has been adapted from Ref. [46].

2020 to 40% by 2028 [21]. Since bifacial solar PV farm deployments are now increasing, it is important to understand how module-level bifacial gain translates to location and technology-specific energy yield and LCOE of bifacial farms. Specifically, a realistic assessment of the relative merits of emerging bifacial PV technologies must account for efficiency losses from the thermal effects of the bifacial solar panels installed in utility-scale solar farms. Other spectral and angle-of-incidence effects also affect efficiency during the early morning and late evening hours of the day. However, these effects are diminished during the operating hours of the PV farms, which contribute to energy production.

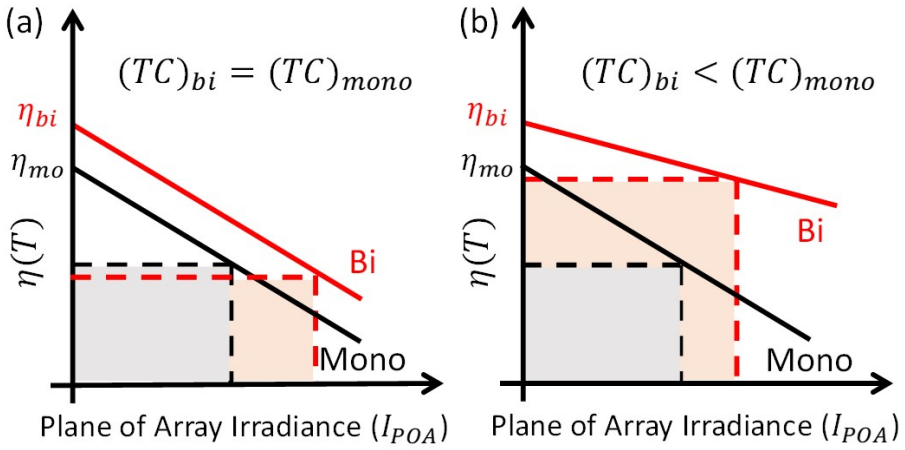

Figure 3.1. Effect of temperature coefficient (TC) and irradiance on efficiency of monofacial (black) and bifacial (red) solar panels. Note that energy yield is a product of Plane of Array irradiance (P_{POA}) and efficiency. Hence, higher energy yield requires higher efficiency and higher P_{POA}. (a) Same PV technology; (b) different PV technologies.

Fig. 3.1 shows a linear relation between efficiency and irradiance (for typical operating conditions) and summarizes the importance of temperature-aware performance modeling of solar cells. The output power density (P_{out}) is determined by the temperature-dependent efficiency ($\eta(T)$) and the input irradiance (I_{POA}), i.e., $P_{out} = \eta\,(T)\, I_{POA}$. Therefore, various technologies can be compared simply by comparing the rectangular boxes in Fig. 3.1. Since the cell temperature is a function of the ambient temperature T_{amb}, input power I_{POA}, environmental conditions (such as wind speed, relative humidity, and sky temperature), mounting configuration and module construction, and technology-specific thermal coefficient

of maximum power, TC, i.e., $T_{cell} = f(T_{amb}, I_{POA}, TC, \ldots)$, the conclusions reached regarding bifacial gain based on temperature-independent efficiency, η_{STC}, [45] may not translate into practice. Indeed, the bifacial gain may be negative or positive depending on the geographical location that determines T_{amb} and I_{POA} as well as PV technology that affects the TC and the efficiency gain ($\eta_g = (\eta_{bi}/\eta_{mo})_{STC}$), where η_{mo} is the efficiency of the monofacial cells while η_{bi} is the normalized output of bifacial cells [91], [92]. If the bifacial and monofacial panels have the same temperature coefficients, i.e., $(TC)_{bi} = (TC)_{mono}$, as in Fig. 3.1(a)), higher irradiance would lead to additional heating of bifacial panels, leading to higher degradation of efficiency. Thus, for the limiting (and hypothetical) extreme case of albedo, $R_A = 1$, bifacial panels would outperform monofacial panels only when $I_{POA} < (2\eta_g - 1)/(k(TC)(4\eta_g - 1))$ where k is a location-specific constant and η_g is the bifacial-to-monofacial efficiency gain. The general condition for arbitrary R_A is derived in Eq. 3.25 (see appendix Sec. 3.5.1). On the other hand, when bifacial panels have a lower TC as compared to the monofacial panels (Fig. 3.1(b)), even higher irradiance would not degrade the efficiency below that of monofacial panels. Thus, bifacial PV panels have an optical advantage over monofacial panels but thermal loss at higher temperatures of operation may potentially negate some of the optical gains. In short, temperature-dependence fundamentally alters the conclusions regarding location-specific bifacial energy gain across the world.

Recent studies have therefore focused on the temperature-dependent performance of stand-alone monofacial and bifacial PV modules [93]–[98]. For example, Ref. [93]–[95] contains a systematic and detailed analysis of temperature coefficients for different PV materials and technologies. The open rear surfaces of a bifacial cell increase power-input due to albedo and power-loss due to IR radiation. In principle, therefore, the bifacial cells can operate cooler than a monofacial cell [97]. Several theoretical studies have explored the temperature-dependence of several performance parameters of solar cells as well as solar PV systems [96], [98]. Lopez-Garcia et al. [99] have experimentally (indoor and outdoor) analyzed the temperature coefficients (TC) of bifacial c-Si PV modules. They concluded that bifacial TC was observed to be lower than monofacial TC. Recent studies [64], [100]–[102] based on a coupled optical-electrical-thermal model of the bifacial photovoltaic module were performed that observed a 22% bifacial gain in yearly energy yield and suggested tilt and

elevation optimizations for stand-alone bifacial module performance. In short, many groups have carefully studied the temperature-dependent performance of stand-alone modules.

Compared to the extensive literature for stand-alone modules, there are only a few reports of temperature-independent yield loss of various monofacial and bifacial technologies at the farm level [45], [61], [62]. The standalone module and a farm differ significantly in terms of albedo collection related to the row-to-row mutual shading, leading to substantial changes in self-heating. In comparison to Ref. [45], this study includes two important generalizations: (1) Increase of the energy-yield with elevation and (2) the decrease in energy yield with temperature. Compared to the previous analysis in Ref. [45], our key conclusion regarding the general location-dependent advantage of bifacial solar modules over monofacial modules remain the same. However, our new work shows that optimum elevation and lower temperature coefficient make bifacial cells attractive for places that we previously thought would only offer marginal improvement.

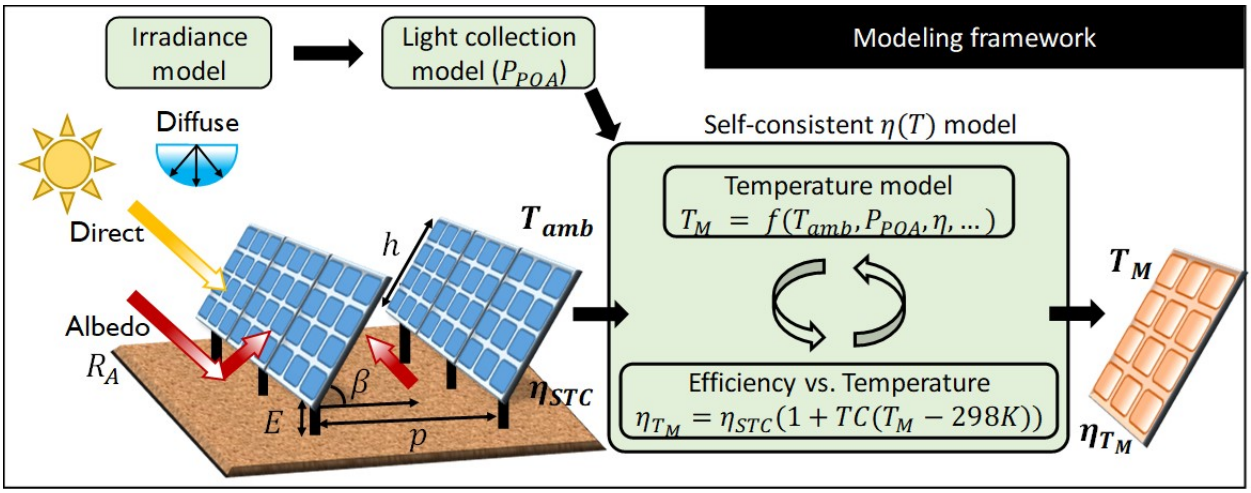

Figure 3.2. Flow diagram of the modeling framework with physical parameters for temperature-dependent energy yield estimation.

In this chapter, we model a generalized bifacial solar PV farm that includes the effects of temperature-dependent efficiency, as portrayed in Fig. 3.2. The integrated model will combine optical, thermal, and electrical models with economic analysis to estimate the energy yield and LCOE of a solar PV farm with a focus on bifacial modules, see Fig. 3.2. The effects of temperature on a module and farm at different locations over the globe are

compared, and it is found that the stand-alone modules are affected by temperature more than the farms. Moreover, the roles of temperature coefficients of different materials (e.g., Aluminum Back Surface Field (Al-BSF) and Silicon Heterojunction (SHJ)) are explored from the perspectives of efficiency degradation and bifacial gain (bifacial vs. monofacial). Lower temperature coefficient ($0.26\%/°C$) for SHJ (bifacial) shows reduced efficiency degradation and yields higher bifacial gain (20-40% globally) compared to Al-BSF (monofacial) that has a higher temperature coefficient ($0.41\%/°C$). Next, combined dependencies of temperature and elevation on the energy yield are considered and it is observed that the energy yield saturates after a threshold value of elevation (typically, $E_0 = 2m$). About $\mathbf{1-15}\%$ increase in energy yield between elevated ($E = 2\ m$) and unelevated ($E = 0\ m$) bifacial farms is observed around the world.

In Sec. 3.2 we describe the optical, thermal, and electrical models used in our study, and the associated equations are organized in Tables 3.1 and 3.2. In Sec. 3.3 we show the results and discuss important trends and features. We vary several design parameters of a solar PV farm e.g., elevation, PV technology, bifacial/monofacial, and TC, to quantify the effects of temperature-dependent efficiency on energy yield, LCOE, and optimum design (tilt angle) of the farm. Finally, in Sec. 3.4, we summarize the study and conclude the chapter.

3.2 Modeling and Validation

An LCOE-aware modeling of bifacial solar farm involves the calculation of irradiance, collection of sunlight, and an electrical output coupled to economic analysis. The optimized design (panel orientation, tilt, elevation, and spacing) of the farm then can be evaluated in terms of energy or LCOE.

Consider a solar farm oriented at an azimuth angle γ_A from the North, with panels of height h, tilted at an angle β, elevated from the ground to E, and with pitch p over a ground of albedo R_A as shown in Fig. 3.2. In the following discussions, we will focus on three aspects of the modeling framework for the specified solar farm: (A) Re-parameterizing LCOE, (B) Irradiance modeling, and (C) Collection of light. These topics are discussed below.

Table 3.1. Equations associated with optical model: Irradiance and light collection models.

$$I_{GHI} = I_{DNI} \times \cos\theta_Z + I_{DHI} \tag{3.1}$$

$$I_{PV:DNI}^{F,\ Farm} = I_{DNI} \cos\theta_F (1 - R(\theta_F))\eta_{dir} \tag{3.2}$$

$$I_{PV:DHI}^{F,Farm} = I_{DHI}\ \eta_{diff}/h \int_0^h \frac{1}{2}\left(1 + \cos\left(\psi\left(E, l\right) + \beta\right)\right)dl \tag{3.3}$$

$$I_{PV:Alb.dir}^{F,Panel}\left(l\right) = I_{Gnd:DNI} \times R_A\ \times F_{dl-gnd}(E, l) \times\ \eta_{diff} \tag{3.4}$$

$$I_{PV:Alb.dir}^{F,Farm}\left(l\right) =\ 1/h \int_0^h I_{PV:Alb.dir}^{F,Panel}(E, l)dl \tag{3.5}$$

$$I_{PV:Alb.diff}^{F,Panel}(l) = I_{Gnd:DHI} \times R_A \times F_{dl-gnd}(E, l) \times \eta_{diff} \tag{3.6}$$

$$I_{PV:Alb.diff}^{F,Farm} = 1/h \int_0^h I_{PV:Alb.diff}^{F,Panel}(E, l)dl \tag{3.7}$$

$$I_{PV:Alb}^{Farm} = I_{PV:Alb.dir}^{Farm} + I_{PV:Alb.diff}^{Farm} \tag{3.8}$$

$$I_{PV:Alb}^{Farm} = I_{PV:Alb.dir}^{Farm} + I_{PV:Alb.diff}^{Farm} \tag{3.9}$$

$$YY_T(p, \beta, h, E, \gamma_A, R_A) = \int_0^1 I_{PV(T)}^{Total}(p, \beta, h, E, \gamma_A, R_A)\ \ dY \tag{3.10}$$

Table 3.2. Equations associated with thermal models.

$$\eta\left(T_{cell}\right) = \eta_{STC}(1 - TC(T_{cell} - T_{STC})) \tag{3.11}$$

$$T_{cell} = T_{amb} + I_{POA} \times e^{a+(b\times WS)} + \Delta\mathrm{T} \times \frac{I_{POA}}{1000} \tag{3.12}$$

$$T_{cell} = T_{amb} + c_T \frac{\tau\alpha}{u_L} I_{POA}\left(1 - \frac{\eta(T_{Cell})}{\tau\alpha}\right) \tag{3.13}$$

$$T_{cell} = T_{amb} + (I_{POA} - \eta I_{POA} - \gamma I_{POA}(subband)) * \frac{F}{1000} \tag{3.14}$$

$$\begin{aligned} T_{cell} = T_{amb} + (I_{POA_{top}} - \eta_{top} \times I_{POA_{top}} + I_{POAbot} - \eta_{bot} \times I_{POA_{bot}} \\ - I_{POA}(subband)) * \frac{F}{1000} \end{aligned} \tag{3.15}$$

$$I_{POA} = I^{Farm}_{PV:DNI}/\eta_{dir} + (I^{Farm}_{PV:DHI} + I^{Farm}_{PV:Alb})/\eta_{diff} \tag{3.16}$$

3.2.1 Levelized Cost of Energy (LCOE)

LCOE is defined as the ratio of the total cost of a PV system and the total energy yield of the system over its lifetime [65], i.e.,

$$LCOE = \frac{\text{Total Cost (\$)}}{\text{Total Energy Yield (kWh)}} = \frac{C_{sys}(Y=0) + (\sum_{k=1}^{Y} C_{om}(k)) - C_{rv}(Y)}{E(Y)} \tag{3.17}$$

where $C_{sys}(Y=0)$ is the initial fixed installation cost of the system (i.e., at $Y=0$). $C_{sys}(Y=0)$ includes the cost of modules ($c_{m,0}$), the cost of land ($c_{l,0}$), and the balance of system cost ($c_{bos,0}$) such as labor, permit, racks, inverters, etc. The recurring operations and maintenance cost (C_{om}) scales with the cost of maintaining individual modules ($c_{om,m}$) and the cost of maintaining the land ($c_{om,l}$). Finally, C_{rv} is the residual value of the modules ($c_{rv,m}$), the land ($c_{rv,l}$), and the equipment to be regained when the farm is decommissioned. C_{om} and C_{rv} are a function of the lifetime (number of years, Y) for which the solar farm is operated.

Since the costs vary with the number and size of PV modules and the solar-farm land, the LCOE expression can be described using the dimensions of a solar farm and the modules installed, as shown in Eq. 3.18 below.

$$LCOE = \frac{\mathbb{C}_M(r) \times h \times M \times Z + \mathbb{C}_L(r) \times p \times M \times Z + C_{bos,f}}{YY_T(p, h, E, \beta, \gamma_A, R_A) \times M \times Z \times h \times \chi(d, r)} \tag{3.18}$$

Here $\mathbb{C}_M$ is the cost per unit meter of the module (height), $\mathbb{C}_L$ is the cost per unit meter of land (pitch), M is the number of rows/arrays of modules, and Z is the number of modules in an array (in the z-direction, into the page). $YY(=E_0)$ is the yearly energy yield per meter of a pristine module for one period/pitch (p) such that the yearly energy of the farm is $E(Y) = YY_T \times M \times Z \times h \times \chi(d, r)$, where $\chi = \sum_{k=1}^{Y} (1-d)^k (1+r)^{-k} \times YY_T$ is a function of the physical design parameters $(p, h, E, \beta, \gamma_A, R_A, T)$. The lifetime ($Y$, typically 25 years) of a solar farm is defined as the time duration before the performance (efficiency) of a solar farm degrades by 20%. Thus, the degradation rate (d, typically 0.7%/year) defines the lifetime of a solar farm. The discount rate (r) accounts for the devaluation of predicted future earnings.

Further, the cost associated with the balance of system ($c_{bos,f}$) is typically negligible as compared to the essential costs, C_M and C_L [13], [103], and does not affect the design optimization of the farm. With these considerations, we arrive at the 'essential levelized cost of energy' ($LCOE^*$), as follows:

$$LCOE^* \equiv \frac{LCOE.\chi}{\mathbb{C}_L} = \frac{\mathbb{C}_M/\mathbb{C}_L + p/h}{YY_T} = \frac{p/h + M_L}{YY_T} \tag{3.19}$$

Here, $M_L(\equiv \frac{\mathbb{C}_M}{\mathbb{C}_L})$ is the ratio of the cost of module per unit length (height) to the cost of land per unit length (pitch). M_L essentially captures the costs of a solar farm whereas p/h and $YY_T(p, h, E, \beta, \gamma, R_A)$ contains information about the physical parameters of the farm. M_L varies with the technology and location in the world. In this work, we assume a typical value of $M_L = 15$ [45]. Given M_L, we can perform the physical design optimization of a solar farm to find a minimum $LCOE^*$. Eq. 3.19 shows that LCOE is proportional to LCOE*, since $\mathbb{C}_L$ and χ are location-specific constants. Therefore, minimizing LCOE is equivalent to minimizing LCOE* for a given location. Chapter 2, Sec. 2.2.1 provides a more detailed derivation and discussion on LCOE and LCOE*.

Next, we will estimate the amount of sunlight falling on a farm at any location in the world.

3.2.2 Irradiance Modeling and Light Collection

The energy yield of a bifacial solar farm for a given albedo is numerically modeled in three steps.

Irradiance model

We calculate the amount of sunlight incident at a location defined by its latitude and longitude. This requires the Sun's trajectory (zenith (θ_Z) and azimuth angle (A)) and the irradiance [61]. The Global Horizontal Irradiance (GHI or I_{GHI}) is ideally given by Haurwitz clear sky model [67], [68]. We renormalize this irradiance based on the NASA Surface meteorology and Solar Energy database [69] to find the local variation in GHI. The GHI is

split into direct light (DNI or I_{DNI}) and diffuse light (DHI or I_{DHI}) using Orgill and Hollands model [70].

Light collection on panels

We quantify the amount of light collected by the solar panels installed at that location. The panels have height h, tilted at an angle β, separated by pitch (or period) p, and are oriented at an array azimuth angle $\gamma_A = 180°$ (i.e., south-facing panels) for farms in the northern hemisphere and $\gamma_A = 0°$ (i.e., north-facing panels) for farms in the southern hemisphere or $\gamma_A = 90°$ for panels facing E-W direction. The collection of light on panels from the three components of irradiance, i.e., direct, diffuse, and albedo light are formulated separately and analyzed accordingly. Our approach to model the collection of light follows Ref. [45] and the equations are summarized in Table 3.1. We calculate the angle of incidence (AOI) of light to find the component of direct light (I_{DNI}) falling on the tilted panel's front and/or the back face (depending on the tilt angle). θ_F is AOI for front face, R is the angle-dependent reflectivity ($R(\theta_F)$) of the panel, $\psi(l)$ is the viewing angle at length l, and F_{dl-gnd} is the view factor. We extend the ground mounted panel-array model in [45] to include calculations for elevated panels. The pattern of light falling on the ground, estimated by the view factor ($F_{gnd-sky}$), and subsequently the albedo light collected by the panels, estimated by the view factor (F_{dl-gnd}), both vary with the elevation (E) of the panels. A detailed explanation of the albedo light model varying with elevation is presented in the appendix.

Energy yield

We finally find the daily and yearly energy-output of the farm. Using the Eqs. 3.2, 3.3, and 3.8 in Table 3.1, we arrive at Eq. 3.9 to find the time-varying spatially distributed light collection on the panels. This information is used in the circuit model to find the equivalent power generation. To estimate energy output, we integrate the power generated over the desired duration of time. We define the energy yield per pitch of a farm over one year as yearly yield (YY) given by Eq. 3.10. Now, we can vary the albedo to determine the variation in YY.

3.2.3 Temperature-dependent efficiency models

The temperature-dependent efficiency loss involves a complex interplay of increased absorption due to bandgap reduction vs. increased dark-current and reduced mobility. At practical illumination intensity, it is well-known that the efficiency $\eta(T)$ scales linearly with the module/cell temperature, see Eq. 3.11 in Table 3.2 where the rate/slope of degradation is given by the absolute temperature coefficient (TC) [96], [104].

The module/cell temperature further depends on the ambient temperature (T_{amb}), wind speed (W_S), module mounting type, the efficiency of the module, and other factors. In this work, we have considered King (Eq. 3.12, 3.2), Skoplaki (Eq. 3.13, Table 3.2) and Alam-Sun (Eq. 3.14, Table 3.2) models to estimate the module/cell temperature based on location-specific the ambient temperature.

Briefly, **King's model** (Eq. 3.12) [94], [105] accounts for the wind speed (WS) and cell to module temperature differences (ΔT) where the parameters 'a' and 'b' are negative and are used as fitting parameters for the module type and deployment. Notice that this simple model does not explicitly account for output power (efficiency is absent in the analytical expression) hence, it doesn't need to be solved self-consistently with Eq. 3.11, Table 3.2.

Unlike King's model, **Skoplaki's model** (Eq. 3.13) model [106], [107] accounts for the module efficiency. It also includes: (i) u_L, which is the heat loss coefficient used as a fitting parameter to the experimental energy yield and found to be 21.5 for our experimental data (ii) c_T is the correction term, which accounts for averaging the ambient temperature and irradiance. We found that instantaneous data (every 1-min) does not require any correction term to predict the energy yield. In addition, we found that c_T increases with the duration of the average i.e., daily average requires a smaller correction term than the monthly average.

Finally, the **Alam-Sun model** (Eq. 3.14) generalizes the Skoplaki's model, which allows us to account for the temperature rise due to the sub-bandgap absorption. The model uses a parameter ($0 < \gamma < 1$) to account for the fraction of sub-bandgap irradiance/power that is not absorbed by the solar module. When $\gamma = 0$, the Alam-Sun model reduces to the Skoplaki model. Sub-bandgap absorption is an important consideration because the bifacial glass-glass modules may have reduced sub-bandgap absorption compared to monofacial glass-backsheet

modules. The relatively cool bifacial modules (for the same I_{POA}) would improve the bifacial gain. A slightly generalized version of the Alam-Sun model is necessary to account for the asymmetric absorption from the rear side of the module.

These cell temperature estimation models are coupled to the temperature dependence of efficiency and solved self-consistently. Once the temperature-dependent efficiency is obtained, we multiply it with the incident light intensity to deliver the energy output (i.e., the rectangular box in Fig. 3.1). Fig. 3.3 demonstrates the validity of the T-dependent simulation model with the experimental data from Sandia National Labs, Albuquerque, NM, USA. We use the experimentally available I_{POA} along with the Skoplaki model to find that the experimentally observed energy yield (Black circles) accurately matches the simulated T-dependent energy yield (Red-solid line). Note that the T-independent efficiency model overestimates the energy yield (Blue-dashed line). Fig. 3.3(inset) is a zoomed-in version of Fig. 3.3, which shows the accuracy of simulated T-dependent energy yield. Further, Fig. 3.4 summarizes the importance of the sub-bandgap absorption (Alam-Sun model, Eq. 3.14) and the effect of $0 < \gamma < 1$ on efficiency.

3.2.4 Energy Output with temperature dependence

Finally, the power generated by the panels under STC (described in section 3.2.2) is corrected using the temperature-dependent efficiency model i.e., Eqs. 3.11, 3.13, and 3.16 from Table 3.2. For energy output, we integrate the power generated over the desired period of time. We define the energy yield per pitch of a farm over one year as yearly yield (YY).

$$YY_T(p, \beta, h, E, \gamma, R_A) = \int_0^1 I_{PV(T)}^{Total}(p, \beta, h, E, \gamma_A, R_A)\ dY \tag{3.20}$$

Fig. 3.3 validates our temperature-dependent energy yield prediction with experimental data from Sandia National Laboratory. The deployed panels were manufactured by Canadian Solar (CS6K-275M 275W mono-Si) with a module efficiency $\eta_{STC} = 16.8\%$, temperature coefficient $TC = 0.41\%/°C$, and outer dimensions of 1650 $\times$ 992 mm. The modules are installed S-facing, 35° fixed-tilt at Sandia National Laboratories in Albuquerque, New Mexico USA $(35.05°N, 106.54°W)$ at an elevation of 1663 m above sea level and are mounted in a

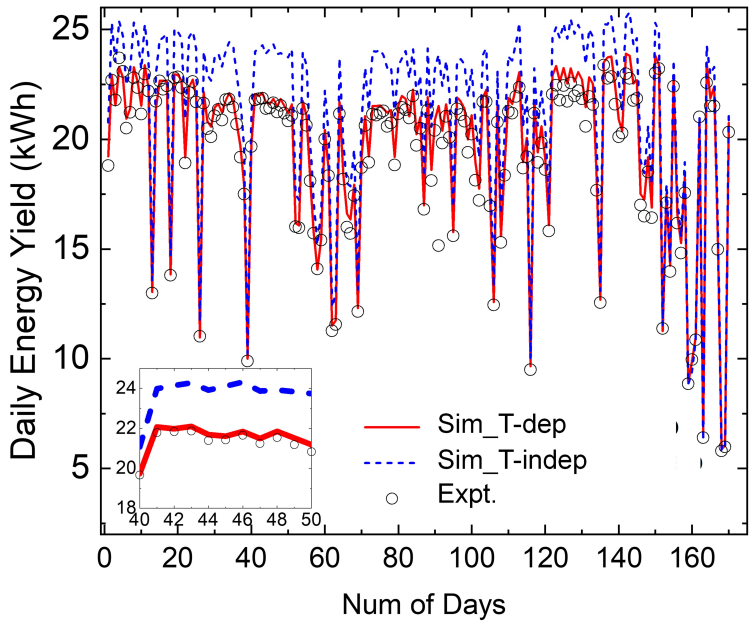

Figure 3.3. Daily and Monthly energy yield for Albuquerque, NM, USA. Simulation is done based on the nameplate efficiency along with and without its temperature dependence. (Inset) A zoomed-in version of the plot from day 40 to 50. Note that we have not considered other sophisticated models like spectral irradiance here.

2-up landscape fashion. Row spacing is 4.88 m. They are grid-connected in four strings of 12 modules. Performance data presented in this chapter is derived from string-level I-V curves that were measured at 30-minute intervals over a period of $\sim$ 170 days. The T-dependent energy estimation (dashed blue line) follows the experimental data (black circles) almost exactly while the T-independent energy (solid red line) is overestimated.

3.3 Results and Discussions

As the first step of calculating the temperature-dependent energy yield and LCOE, we first examine the temperature dependence of monofacial and bifacial module configurations. The cell temperature is calculated self-consistently with efficiency and irradiance. Fig. 3.4 shows the trend in $\eta(T)$ between monofacial and bifacial modules. Although the bifacial modules collect more light (irradiance), the apparent temperature coefficient (slope of the red line in Fig. 3.4(b)) is relatively lower. This can be explained using the effect of spectral

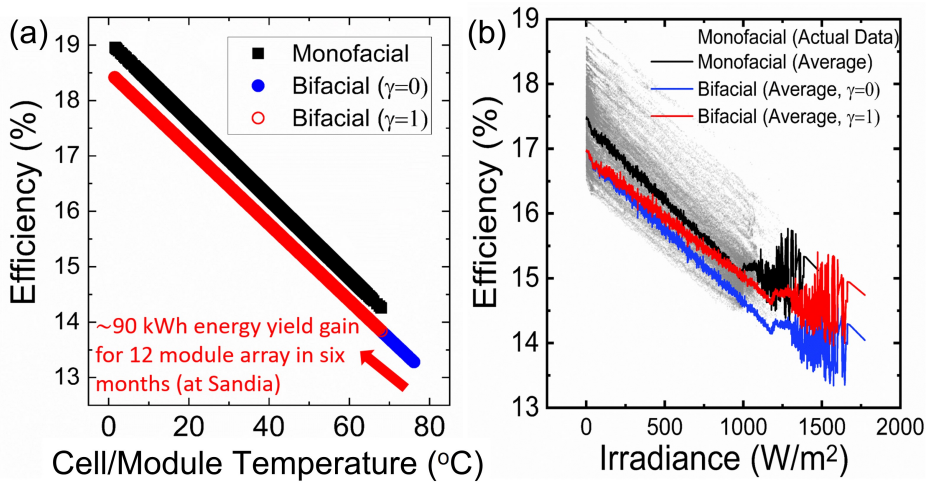

Figure 3.4. (a) Efficiency vs. T for both monofacial and bifacial solar panel. The TC is same for both the panels, which is reflected in the slopes – however, bifacial is cooler (shown as blue arrow) and lead to $\sim$ 90 kWh gain when the sub-band spectra is assumed transparent ($\gamma = 1$). (b) Averaged efficiency vs. Irradiance for both monofacial and bifacial solar panel where the background symbols (small open circles) represent the actual data for monofacial string. The change in the slope indicates the change in the temperature of the panel due to the sub-band transparency.

irradiance on the modules, as shown in Fig. 3.4(b). Referring to the Sun-Alam model, γ is the fraction of sub-bandgap irradiance/power that is not absorbed by the solar module. Looking at the two extreme cases of $\gamma = 0$ (monofacial with an opaque back sheet) and $\gamma = 1$ (bifacial with a transparent back sheet), we see that the efficiency vs. irradiance plot has a steeper slope for monofacial case. The rapid decrease in efficiency is a consequence of increased temperature (Fig. 3.4(a)) due to additional sub-bandgap (or IR) absorption.

Since TC is a significant parameter in temperature-dependent efficiency estimation, it requires an effort from the solar PV community to reduce TC through material and process engineering. Note that all the temperature-dependent parameters are denoted by subscript T while temperature-independent parameters are denoted by subscript 0.

3.3.1 Self-heating affects a stand-alone module more than modules in a farm

A bifacial module in a solar PV farm collects less irradiance (I_{POA}) as compared to a standalone bifacial module due to mutual shading (periodic shading on the ground). Thus, our self-consistent model predicts the temperature of a standalone module to be somewhat higher than that of a module in a farm. Note that the temperature difference would change somewhat ($< 3 - 4°$) once the "heat-island effect" is accounted for [108]. The relatively small correction reflects two counter-balancing effects of ground illumination vs. heat-trapping in a farm vs. in a stand-alone module. In general, the temperature-dependent efficiency (η_T) and energy yield (YY_T) degradation, with respect to temperature-independent η_{STC}(or η_0) and YY_0, are more prominent for a standalone module as compared to a farm, see Fig. 3.5. We observe that the degradation in YY is enhanced for standalone bifacial modules as compared to bifacial farms.

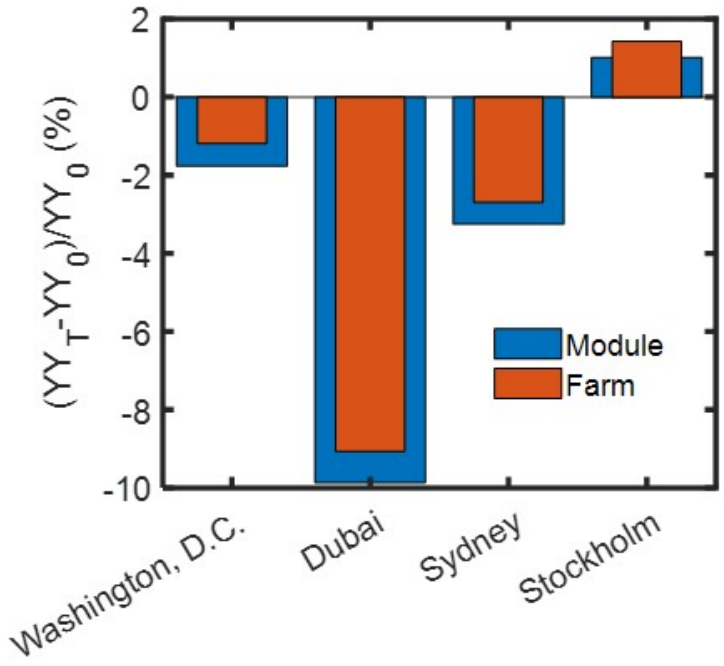

Figure 3.5. Comparing module and farm-level η_T vs. η_0 based percentage change in energy yield for different locations around the world. We observe that degradation is higher for an elevated ($E = 2\ m$) standalone module as compared to an elevated farm, except for locations at very high latitude, e.g., Stockholm.

In Fig. 3.5, we consider four specific locations with increasing latitudes, namely, Dubai ($24.5°N, 55.5°E$), Sydney ($33.85°S, 150.65°E$), Washinton D.C. ($38.91°N, 77.04°W$), and Stockholm ($59.32°N, 17.84°E$) with decreasing average annual temperatures 34, 22, 20, 11 °C (high) and 23, 14, 8, , 5 °C (low), respectively. For locations with hotter climates the percentage change in YY_T and YY_0 is negative, due to efficiency degradation at higher temperatures. On the other hand, for places with very cold climates, like Stockholm, the associated percentage change is positive and higher for a farm in comparison to a standalone module. The apparent exception at Stockholm arises due to colder weather i.e., $T_{amb} < T_{STC}$, during most of the year. Negative ambient temperature and low irradiance (I_{POA}) for a farm, leads to lower T_{cell}(farm) as compared to T_{cell}(module), see Eq. 3.13. Thus, from Eq. 3.11, η_T (farm) $> \eta_T$ (module) and $\Delta YY = I_{POA} \times \Delta\eta_T$ is higher for a farm as compared to a *stand-alone* module.

3.3.2 Technology and geography dictate the temperature-dependent yield loss of monofacial vs. bifacial farms

The worldwide maps in Fig. 3.6 depict the dependence of gain/loss in energy yield between temperature-dependent efficiency (η_T) vs. constant efficiency (η_0 or η_{STC}). Clearly, hotter places like the Sahara Desert, Mexico, and southern India, show a loss in energy yield due to degradation in efficiency with higher temperature as compared to efficiency at STC (η_{STC}). On the other hand, for colder locations like Siberia, Gobi Desert, and northern Canada and Europe, with lower average temperatures, show an improvement in efficiency, with respect to η_{STC}, leading to higher energy yield.

This general trend is quantitatively shown in Fig. 3.6 (row 1) for monofacial farms: globally, we observe -7% to $+12\%$ of change in temperature-dependent energy yield (YY_T) with respect to energy yield (YY_0) estimated using constant efficiency. Fig. 3.6 (row 2) shows a lower magnitude of change (-7% to $+10\%$) for bifacial farms. Here we assume the same temperature coefficient (TC=0.41%/°C) for monofacial and bifacial modules (rows 1 and 2 in Fig. 3.6) with the same Al-BSF technologies. Since the amount of light collected by the bifacial panels (I_{POA}) is higher than the monofacial panels, the change in cell/module temperature, from Eq. 3.13 in Table 3.2, is higher for bifacial modules leading to a higher change in efficiency. However, the normalized output (efficiency) for bifacial modules is higher than the

monofacial modules (as shown by the y-intercepts in Fig. 3.1(a)). Overall, the combination of higher normalized output and higher degradation of efficiency for bifacial modules leads to an approximately similar percentage change in energy yield between temperature-dependent vs. constant efficiencies. Moreover, Fig. 3.6 (row 3) displays the same quantities for bifacial silicon heterojunction technology, which has a lower TC (=0.26%/°C). Lower TC leads to lesser degradation of efficiency with temperature and eventually the range of change in YY (-5% to $+5\%$) is lower as compared to Al-BSF (TC=0.41%/°C).

Fig. 3.6 also displays the trend in relative percentage change between minimum LCOE* estimated using temperature-dependent efficiency ($LCOE^*_{min,T}$) with respect to LCOE* calculated using constant efficiency ($LCOE^*_{min,0}$). Since LCOE* is inversely proportional to the yearly energy yield (YY), hence, the trends are reversed as compared to energy yield. Colder places show a decrease in LCOE* by $\sim 8\%$, whereas places with hotter climates show a $\sim 8\%$ increase for bifacial farms. The change (-8% to $+8\%$) in LCOE* after temperature correction is significant and cannot be ignored while estimating the levelized cost of energy of a solar PV farm.

The design of solar modules in a farm (represented by the optimum tilt angle and the associated pitch for no mutual shading) does not change significantly. Fig. 3.6 (maps on the right) shows the difference in the optimum tilt angle when we consider η_T vs. η_0. This difference varies from $-3°$ to $+3°$ around the globe. Hence, for all practical purposes, the design optimization presented in [45] does not require adjustments even after temperature-dependent efficiencies are included. However, an accurate estimation of YY and LCOE* is achieved using a more accurate temperature-dependent efficiency model.

3.3.3 Technology-choice and geographical location determine the temperature-dependent bifacial gain

Since it has been established that the temperature-dependent model is essential for the correct estimation of YY and LCOE*, we will now explain the bifacial gain. We will compare the Silicon Heterojunction (SHJ) ($TC = 0.26\%/°C$) and Aluminum Back Surface Field (Al-BSF) ($TC = 0.41\%/°$C) bifacial panel performance to that of Al-BSF monofacial panels ($TC = 0.41\%/°C$). The global trends in bifacial gains for YY and LCOE* for constant

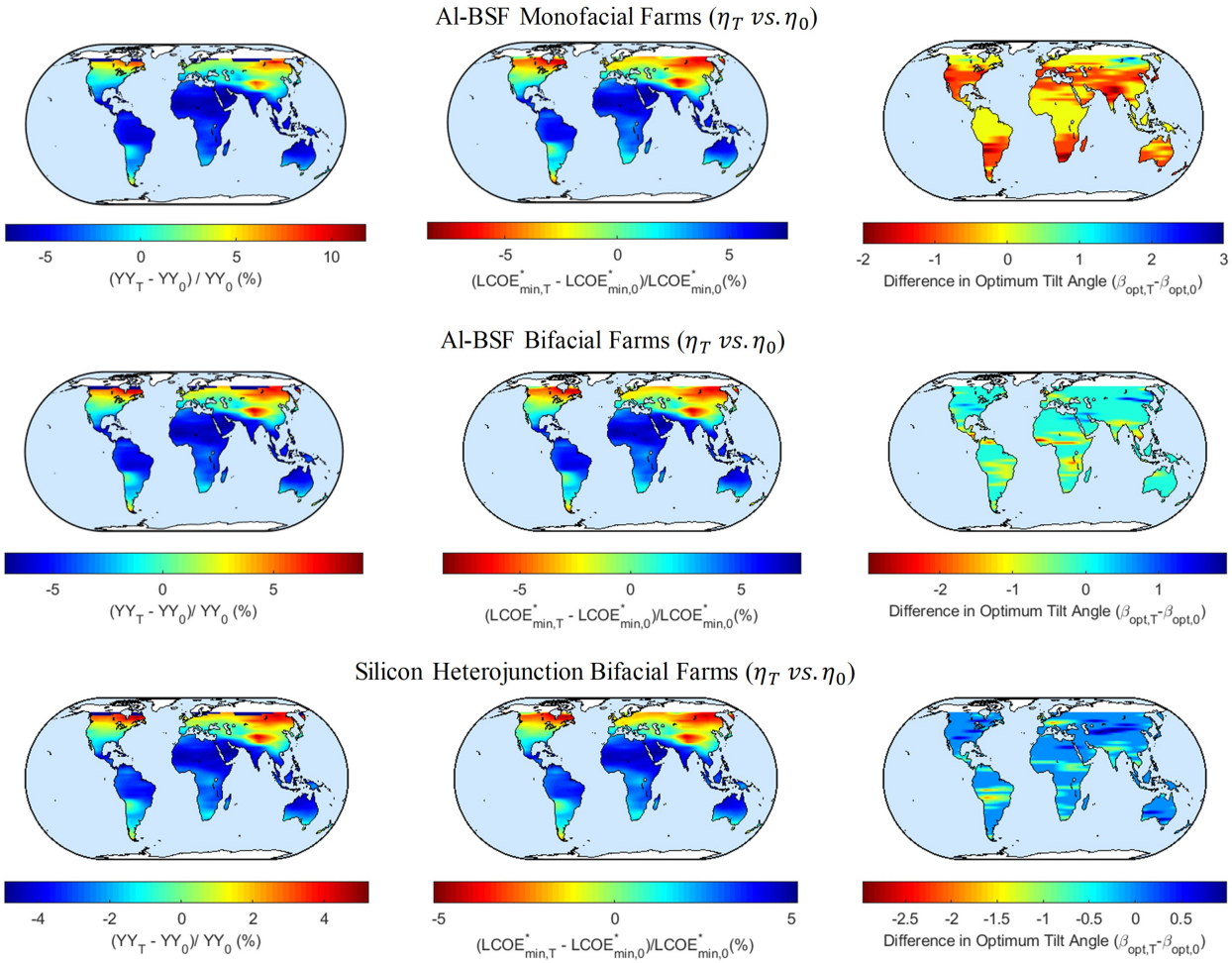

Figure 3.6. Global maps comparing yearly energy yield (YY), LCOE*, and difference in optimum array tilt angle ($\Delta\beta_{\text{opt}}$) for temperature-dependent efficiency (subscript T) and temperature-independent efficiency (subscript 0). Note that $R_A = 0.5$ and $M_L = 15$. (Row 1) Monofacial Farms, e.g., Al-BSF, (Row 2) Bifacial farms with a high temperature coefficient (TC=0.41%/°C) , and (Row 3) Bifacial farms with a lower temperature coefficient (TC=0.26%/°C)), e.g., Silicon Heterojunction (SHJ) solar cells.

efficiency calculations can be found in [45]. Fig. 3.7 displays the same parameters for temperature-dependent Al-BSF (bifacial) (row 1) and SHJ (bifacial) (row 2) versus Al-BSF monofacial farm calculations. We observe that the bifacial gain for the yearly yield of Al-BSF is 0-20% for latitudes $< 50°$ and reaches up to 30% for even higher latitudes. The reduction in LCOE* for bifacial over monofacial is 0-10% around the world. These percentages are higher than that estimated (2-12%) for temperature-independent (constant) efficiency in

Ref. [45]. Whereas, calculations comparing SHJ (bifacial) and Al-BSF (monofacial) show a much higher bifacial gain for yearly yield (12-45%) and reduction in LCOE* for bifacial over monofacial parameters (15-25%) around the world. This is due to the higher temperature coefficient for Al-BSF as compared to SHJ panels leading to larger performance degradation of Al-BSF panels and lower bifacial gain. The relative gain simply reflects the fact that the efficiency of bifacial PV degrades less than monofacial PV at a given ambient temperature.

Recall that in Fig. 3.1, we conceptually compared monofacial and bifacial farms with different efficiencies and temperature coefficients. The observations shown here clearly align with our hypothesis of enhanced temperature-dependent performance for bifacial panels with higher $\eta_{STC}(SHJ) = 19.7\%$ and lower temperature coefficient ($TC(SHJ) = 0.26\%/°C$) as compared to monofacial panels with lower η_{STC} $(Al-BSF) = 16.8\%$ and higher temperature coefficient (($TC(Al-BSF) = 0.41\%/°C$).

Clearly, temperature coefficient (TC) is an important parameter for accurate efficiency and energy estimation and it varies for different PV technologies. Although bifacial modules collect more light, most bifacial technologies have a lower TC than monofacial ones leading to further enhanced bifacial gain. Furthermore, bifacial technologies do not absorb sub-bandgap (IR) radiation leading to lower heating. Fig. 3.8 portrays this trend for panels deployed at Sandia National Labs, Albuquerque, and validates our hypothesis. Since the temperature coefficient of Al-BSF ($TC = 0.41\%/°C$) is higher than CdTe ($TC = 0.32\%/°C$), the energy yield for the former is lower. Further, for both PERC and SHJ, T-dependent estimation shows higher energy yield for bifacial as compared to monofacial due to lower IR absorption. We saw similar results for the global maps in Fig. 3.7. Thus, we explored the change in energy yield for bifacial farms and monofacial farms with different TC.

3.3.4 Temperature-Dependent Energy Yield of Elevated Farms: Self-Heating vs. Improved Light Collection

The energy yield increases with elevation due to improved collection of albedo light at the back face of the panel. Increased light collection increases the temperature, suggesting the need for a temperature-aware model to find optimum elevation and a corresponding bifacial gain. Next, we explore the effect of elevation on temperature-dependent energy yield.

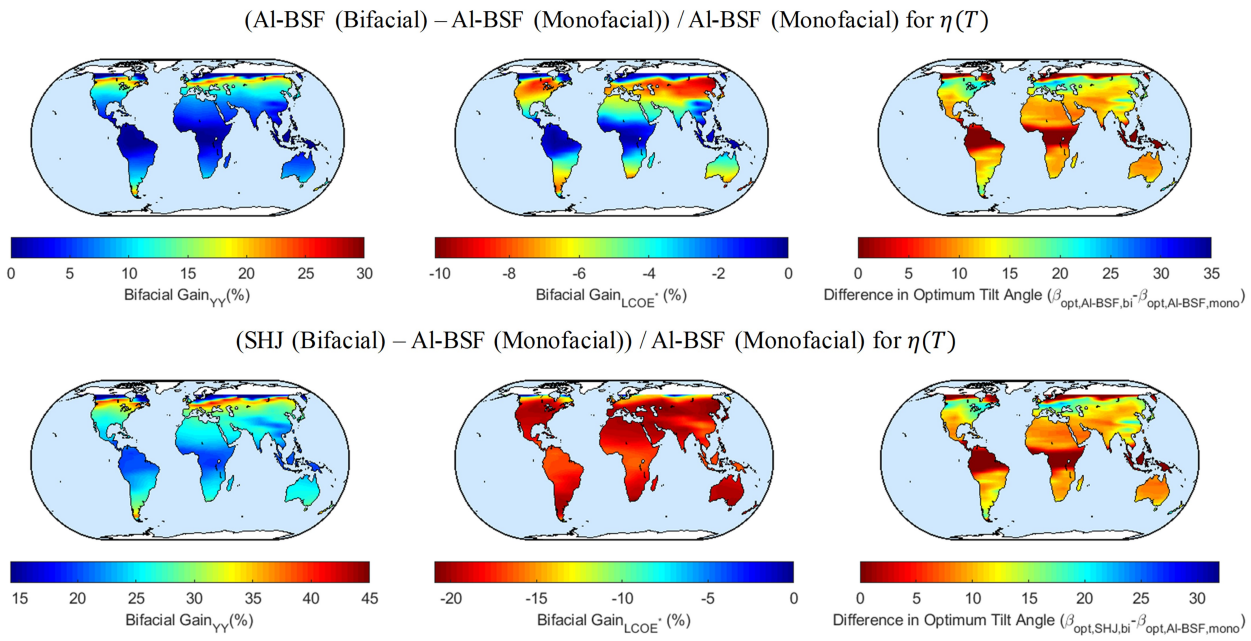

Figure 3.7. Global maps comparing bifacial gain in yearly energy yield, LCOE*, and difference in optimum array tilt angle for Al-BSF monofacial farms (TC=0.41%/°C) vs. (Row 1) Al-BSF and (Row 2) Silicon Heterojunction bifacial farms (TC=0.26%/°C). Note that $R_A = 0.5$ and $M_L = 15$.

Ref. [26] shows that the energy yield of the module starts to saturate after a certain elevation. We observe a similar trend in the farm-level, i.e., yearly energy yield saturates after a certain elevation, as shown in Fig. 3.9. For Washington D.C., USA, YY increases from 345 kWh/m for ground-mounted panel-array ($E = 0\ m$) and saturates to 365 kWh/m at a high elevation of panels ($E = 5\ m$). At elevations $E_0 \sim 1.5\ m$, 95% of this saturated yield can be achieved (for $h = 1\ m$). Such elevation threshold, where 95% of the maximum/saturated yield would be attained is location-specific. For example, in Jeddah, KSA, this elevation threshold is $E_0 = 2\ m$. We observed that this saturating trend is observed globally. Moreover, the light collection (I_{POA}) on the panels increases with elevation, leading to a rise in the temperature-dependent degradation of efficiency (see Eqs. 3.12, 3.13, and 3.14 temperature models). Thus, on one hand, elevation increases light collection which enhances energy yield. On the other hand, increasing light collection simultaneously increases the temperature and decreases efficiency, eventually decreasing the energy yield. Overall, it is observed that the

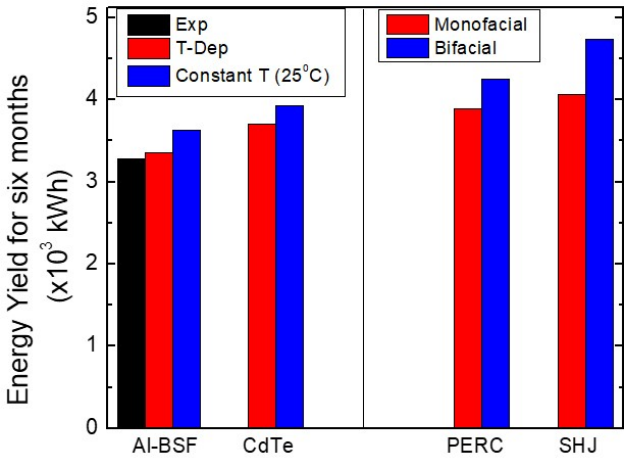

Figure 3.8. Energy yield estimated for different technologies illustrating the temperature effect (left) and monofacial and bifacial effect (right).

energy yield increases until a threshold elevation (E_0) and then saturates to a maximum value.

Fig. 3.10 shows the percentage change in yearly energy yield and LCOE* between an elevated bifacial farm (with $E = 2\ m$) and previously estimated unelevated bifacial farm ($E = 0\ m$). We chose $E = 2\ m$ since it is beyond the elevation threshold E_0 for energy yield saturation around the world. Evidently, the energy yield improves by 1-20% around the globe with a monotonically increasing trend with latitude. Consequently, LCOE* decreases by the same amount with a similar trend worldwide. Interestingly, the optimum tilt angle varies from -10% to $+10\%$ depending on the latitude and the fraction of diffuse light illuminating the bifacial panels. Thus, elevating the farms by $1 - 2\ m$ enhances the energy yield and reduces LCOE* (assuming a negligible increase in costs). In practice, elevating the modules to $E = 2\ m$ incurs higher costs due to at least two factors: (1) higher wind loads will require more steel and deeper foundation; (2) installing at that height increases labor costs due to the need for ladders and other work aids. To incorporate this increased cost, a higher value of the cost ratio (M_L) in Eq. 3.19 should be used. Consequently, the optimum value of elevation would be lower, $1\ m < E_0 < 2\ m$. Thus, Fig. 3.13 shows the gain in energy yield for a practical and affordable elevation of $E = 1\ m$ with respect to $E = 0\ m$. A detailed

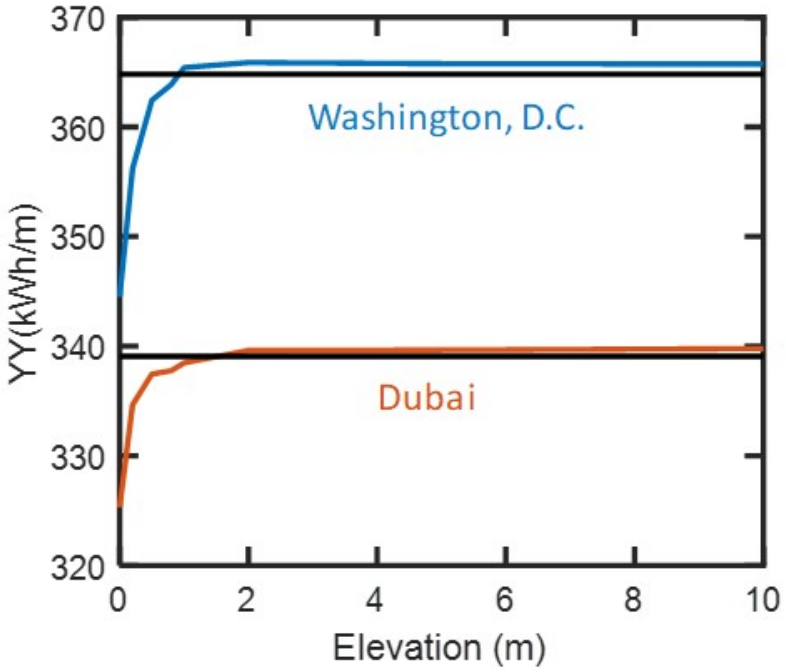

Figure 3.9. Temperature – dependent yearly energy yield of the farm (with $p = 2\ m$ and $h = 1\ m$) saturates with elevation of panels above the ground. Here we show the simulation for Washington D.C. as an example.

LCOE-dependent analysis of the elevated bifacial farm design will be a part of a future analysis.

3.4 Summary and Conclusions

In this chapter, we have analyzed the effects of temperature-dependent efficiency degradation on the energy yield and LCOE of monofacial and bifacial solar PV farms. Our approach involved combining an irradiance model, an updated light collection model for elevated farms, and temperature-dependent efficiency models to arrive at the final energy output of a solar farm. The light collection and temperature estimation models had to be solved self-consistently in order to arrive at the practical and more accurate efficiency for a particular location. We applied these models for locations around the world to deliver the global maps that quantify the percentage change in energy yield and LCOE* between

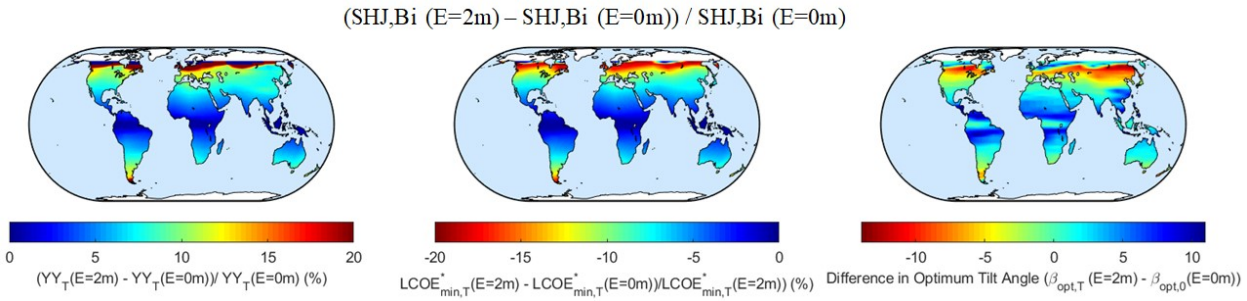

Figure 3.10. Global trends in change in yearly energy yield, LCOE*, and difference in optimum tilt angle of an elevated bifacial farm ($E = 2\ m$) and an unelevated bifacial farm ($E = 0\ m$).

temperature-dependent and constant temperature calculations while presenting general global trends.

Our analysis leads to the following key **conclusions**:

- The generalized Alam-Sun thermal model allows us to account for sub-bandgap absorption. The effect is significant: Almost, 90 kWh more energy can be generated from 12 bifacial-module string for a period of 6 months due to the reduced self-heating associated with the transmittance of sub-band irradiance.

- A comparison between energy yield and LCOE for temperature-dependent efficiency ($\eta(T)$) and temperature-independent efficiency (η_{STC}) conveys a percentage change of $-\mathbf{7}\%(Al-BSF)$, $-\mathbf{5}\%(SHJ)$ for locations close to the equator ($|\text{latitude}| < 30°$) and $+\mathbf{12}\%(Al-BSF)$, $+\mathbf{5}\%(SHJ)$ for locations close to the poles ($|latitude| > 30°$).

- The bifacial gain for SHJ (bifacial) vs. traditionally used Al-BSF (monofacial) with temperature-dependent efficiency conveys a percentage change of $+\mathbf{12}\%$ for hotter locations close to the equator ($|\text{latitude}| < 30°$) and can reach up to $\mathbf{25-45}\%$ for colder places close to the poles ($|\text{latitude}| > 30°$). Whereas, bifacial gain for Al-BSF shows a percentage change of $\sim \mathbf{0-30}\%$. This presents an incredible opportunity for SHJ bifacial farm deployment.

- The trend in the difference in optimum tilt angle ($\Delta\beta_{opt}$) for bifacial designs is $0° - 30°$ when comparing the same technology (Al-BSF(Bifacial) vs. Al-BSF(Monofacial)) or two different technologies (SHJ(Bifacial) vs. Al-BSF(Monofacial)).

- Elevated farms show two counter-balancing trends, where light collection on the panels (I_{POA}) increases leading to an increase in temperature and a decrease in efficiency. Overall, temperature-dependent elevated farms ($E = 1 - 2$ m) outperform unelevated farms in terms of yearly energy yield by up to 20% depending on the latitude.

- Bifacial PV technologies (SHJ) with lower TC and low sub-bandgap (IR) absorption can outperform their monofacial counterparts. The extent of enhancement in performance depends on the bifacial technology used and the geographical location of the farm.

In conclusion, it is important to accurately calculate the energy yield (YY) and LCOE*. The bifacial solar farm energy yield using temperature-dependent efficiency fulfills this purpose. Although the design of the farms in terms of the optimum tilt angle is not affected significantly, the absolute values of energy yield and LCOE for field-deployed temperature-dependent solar farms differ considerably for several locations around the world. This affects the overall economic evaluation of location-specific solar farms. Since bifacial panels have a lower temperature coefficient compared to monofacial panels, therefore, they are advantageous for relatively steady energy output due to daily and monthly temperature variations, especially for locations with lower total irradiance. Moreover, using PV materials with lower temperature coefficients, e.g., Silicon Heterojunction (SHJ) and PERC, would lead to stable outputs and enhanced performance of bifacial solar farms throughout the world.

Finally, the scope of this study was limited to the initial temperature-dependent efficiency degradation associated with a newly installed solar farm. The long-term analysis of temperature-dependent degradation mechanisms and PV lifetime are not considered in our study. Moreover, the spectral dependence of PV efficiency is beyond the scope of this work and needs further investigation [107], [109]–[111]. Moreover, given the importance of TC, it

will be important to focus on methods to lower the temperature coefficient of bifacial solar materials/technologies and reduce cell temperature variation through improved packaging. These would become a central issue for concentrated solar photovoltaics as well. Further, one could improve the power output at the back surface by using a different kind of solar cell, e.g., DSSC, that performs better under low-light illumination [112]–[114]. Thus, the temperature-dependent energy-gain of a tandem [92], [104], [115] or 'mixed' bifacial solar cell will be an interesting and important generalization of the results presented in this chapter.

3.5 Appendix

3.5.1 Threshold I_{POA} for YY_T(Bifacial) > YY_T(Monofacial)

The objective is to find the threshold plane of array irradiance I_{POA} for the power output of temperature-dependent bifacial panels to be more than that of monofacial panels. We first define efficiency gain ($\eta_g = (\eta_{bi}/\eta_{mo})_{STC}$) as the ratio of the normalized output of the bifacial module over the efficiency of the monofacial module at STC. Next, we use $\eta(T_M) = \eta_{STC}(1 - TC(T_M - T_{STC}))$(Eq. 3.11 in Table 3.2) and $P_{out} = \eta(T)\, I_{POA}$ to arrive at the following equation.

$$P_{out} = I_{POA}\ \eta_{STC}\ (1 - TC(T_M - T_{STC})) \tag{3.21}$$

Assuming $T_M = T_{cell}$ and neglecting the negligible effect of η in Eq. 3.13 of Table 3.2, we get

$$T_{cell} = T_{amb} + k\ I_{POA} \tag{3.22}$$

Here k is a location-specific constant. Now, we take bifacial POA irradiance $(I_{POA})_{bi} = I_{POA}(1 + R_A)$, where I_{POA} is monofacial POA irradiance and R_A is the albedo value. Thus, combining Eqs. 3.21 and 3.22, we get a generalized form of output power as shown below.

$$P_{out} = I_{POA}\,(1 + R_A) \times \eta_{STC}(1 - TC(\Delta T_0 + kI_{POA}(1 + R_A))) \tag{3.23}$$

where $\Delta T_0 = T_{amb} - T_{STC}$. For temperature-dependent bifacial output power to be greater than the monofacial counterpart,

$$\frac{(P_{out})_{bi}}{(P_{out})_{mono}} > 1 \implies \frac{I_{POA}\,(1+R_A)\,\eta_{bi,STC}\,(1-(TC)_{bi}\,(\Delta T_0 + kI_{POA}(1+R_A)))}{I_{POA}\eta_{mo,STC}\,(1-(TC)_{mono}\,(\Delta T_0 + kI_{POA}))} > 1 \tag{3.24}$$

Simplifying the above equation gives us,

$$\frac{(1-(TC)_{bi}\,(\Delta T_0 + kI_{POA}(1+R_A)))}{(1-(TC)_{mono}\,(\Delta T_0 + kI_{POA}))} > \frac{1}{\eta_g\,(1+R_A)} \tag{3.25}$$

Eq. 3.25 is the generalized condition on I_{POA} for bifacial panels to generate higher power output compared to monofacial panels. In special cases, where $(TC)_{bi} = (TC)_{mono} = TC$, $\Delta T_0 = 0$, i.e., $T_{amb} = T_{STC}$, and the extreme value of $R_A = 1$, we can derive the following specialized condition (Eq. 3.26) mentioned in the introduction of the main text.

$$I_{POA} < \frac{(2\eta_g - 1)}{k \times\ TC \times (4\eta_g - 1)} \tag{3.26}$$

The above equation is physically-intuitive in a sense that bifacial PV would outperform monofacial PV when the collected plane of array irradiance is lower than a certain threshold value. Moreover, this threshold value should depend only on the above-mentioned parameters that vary with the PV technology (η_g, TC) and the geographical location (k, R_A).

3.5.2 Albedo Light Collection for Elevated Panels

Albedo light collection for elevated panels requires a rigorous estimation of view factors from the sky to ground (including masking) i.e., ground pattern as well as the collection of albedo light reflected from the ground on the panels. Fig. 3.11 and 3.12 display these aspects schematically. Fig. 3.11 displays the algorithm to calculate the amount of light falling on a point on the ground from all parts of the sky that are visible. Note that, there would be only one opening towards the sky for unelevated panels. However, elevated panels allow views of the sky from neighboring periods as well. For each opening (view) of the sky from a point

on the ground, we use the view factor formula, VF $= 0.5\ (\cos(\theta_1) + \cos(\theta_2))$. A product of the total view factor and the intensity of diffuse light gives the total diffuse light falling on a point on the ground. Similarly, for direct light estimation, whenever the direct beam from the Sun falls inside any of the openings (views), we include that into total direct light falling on the point on the ground. A summation of direct and diffuse light falling on that particular point gives us the total illumination on the point on the ground.

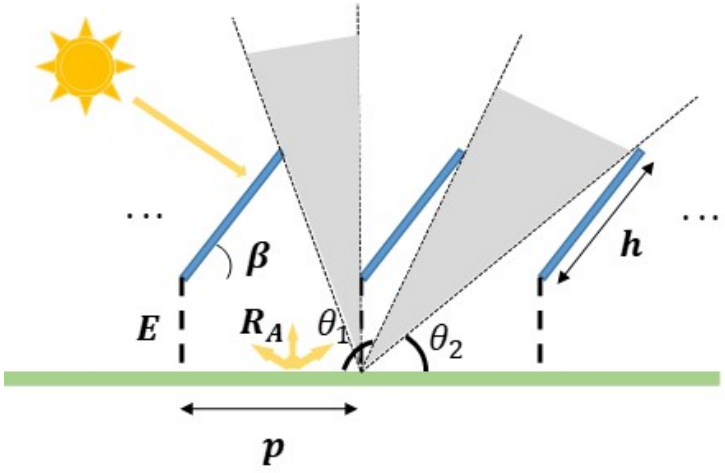

Figure 3.11. Ground pattern: illumination at a point on the ground from the visible sky.

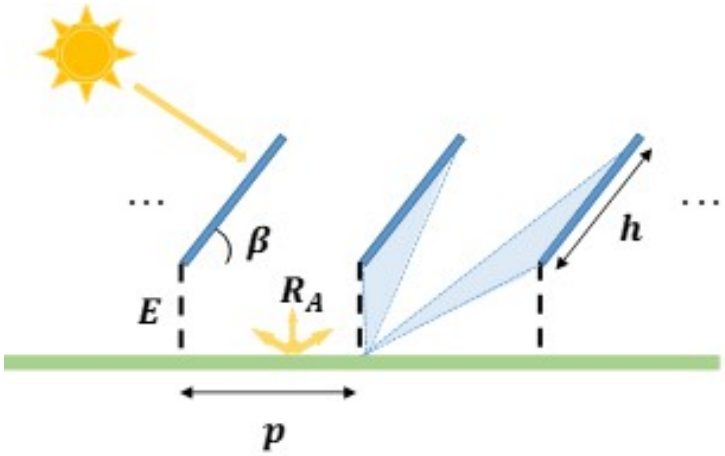

Figure 3.12. Light collection: illumination collected by the panel that is reflected from the ground.

Next, we estimate the amount of ground-reflected light collected on the front and rear sides of the panel. For unelevated panels, only one period on the ground is visible to the panels, whereas the panels can see multiple periods for elevated panels, see Fig. 3.12. The above-mentioned view factor (VF) formula is now used to find the amount of light falling from a point on the ground on the panel. An integration over all the points on the ground seen by the panel gives the total light collected on the panel. A product of the total intensity of albedo light collected on the panel with the efficiency of the module equals the total power output of the panel. An overall integration of total power over time finally leads us to the total energy generated by the panel due to albedo light. A detailed explanation for the estimation of albedo light collection for elevated farms can be found in Ref. **Younas2019**, [42].

3.5.3 Energy gain for bifacial farms elevated at E = 1 m

An increase in elevation increases the yearly energy yield of a bifacial farm as compared to an unelevated bifacial farm. However, elevating the farm also increases the racking, labor, and maintenance costs. Thus, instead of maximizing energy at $E = 2\ m$, an economically viable option is to elevate the farms at $E = 1\ m$. Fig. 3.13 shows the percentage increase in energy yield between elevated ($E = 1\ m$) and unelevated ($E = 0\ m$) bifacial farms.

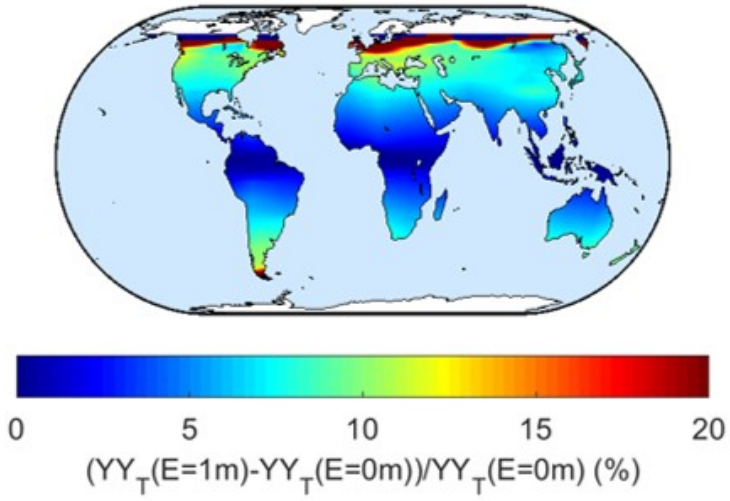

Figure 3.13. Global trends in the change in yearly energy yield of an elevated bifacial farm ($E = 1\ m$) and an unelevated bifacial farm ($E = 0\ m$).

4. GLOBAL ANALYSIS OF NEXT-GENERATION UTILITY-SCALE PV: TRACKING BIFACIAL SOLAR FARMS

In chapters 2 and 3 we integrated optical, electrical, thermal, and economic models to estimate the energy yield and LCOE of fixed-tilt bifacial solar farms. Through these models the bifacial gain of East-West vertical and South-facing optimally-tilted bifacial farms are well established. One wonders if bifacial gain (and the associated LCOE) may be further improved by tracking the sun. Tracking bifacial PV has advantages of improved temperature sensitivity, enhanced diffuse and albedo light collection, flattened energy-output, and reduced soiling. Monofacial tracking already provides many of these advantages, therefore the relative merits of bifacial tracking are not obvious. In this chapter, we use a detailed illumination and temperature-dependent bifacial solar farm model to show that bifacial tracking PV delivers up to 45% energy gain when compared to fixed-tilt bifacial PV near the equator, and $\sim 10\%$ bifacial energy gain over tracking monofacial farm with an albedo of 0.5. An optimum pitch further improves the gain of a tracking bifacial farm. Our results will broaden the scope and understanding of bifacial technology by demonstrating global trends in energy gain for worldwide deployment.

4.1 Introduction

The global energy demand is approaching unprecedented levels with the projected population of ~ 10 billion people by 2050 [117]. Protecting the environment while meeting the energy demands will involve a delicate balancing act in the coming decades. It has been suggested that renewable energy resources can satisfy the energy demand with the smallest environmental footprint. Among all renewable energy resources, the direct conversion of solar energy to electricity by photovoltaic technology (PV) is one of the most promising sources of green and sustainable energy with the advantage of limited environmental impact and low maintenance cost.

↑**Note:** The material in this chapter has been adapted from Ref. [116]

One way to reduce the levelized cost of energy (LCOE) is to design a photovoltaic (PV) system to produce the maximum energy for a specified area of the solar farm. Among the cost-effective options, one can either increase the total irradiance of fixed-tilt farms using bifacial modules or increase the normal irradiance on monofacial modules by solar-tracking. Both technologies are becoming popular as bifacial modules are expected to have $\sim$ 40% market share by 2028 [34], whereas solar-tracking has been implemented by $\sim$ 70% of newly installed utility-scale PV systems since 2015 [35], [36]. Indeed, market analysis from multiple groups worldwide suggest that single-axis tracking may account for 25-40% of all new utility-scale PV installation, motivated in part by the adoption of bifacial modules [37]. However, the location-specific viability of bifacial tracking has not been quantified. The solar-tracking of bifacial PV modules sounds appealing, but the only concern is that whether bifaciality would be beneficial in solar-tracking configuration, as maximizing direct beam will cast a deep shadow on the ground and reduce the contribution from the ground albedo. Fortunately, the recent location-specific case-studies predict the promising potential of bifacial PV farms in solar-tracking configuration [118], [119]. For example, the detailed calculation by Egido et al. [120] predicts that a *standalone dual-axis tracking* bifacial PV module (with the ground painted white) has almost 80% higher annual energy yield as compared to its fixed monofacial counterpart. For the same white-paint albedo, a 20% to 90% increase in energy yield was demonstrated across different months for single-axis tracking of standalone bifacial PV modules as compared to fixed-tilt bifacial and monofacial modules, respectively. Similarly, Oria and Sala reported a 70% increase in annual energy yield using single-axis tracking of standalone bifacial modules with highly reflective albedo collectors as compared to their fixed monofacial counterparts [121]. Shoukry et al. [122] demonstrated that both bifaciality and tracking have their own unique contributions depending upon the geographical locations with bifaciality providing up to 44% advantage as compared to single-axis tracking that provided 18% energy gain as compared to fixed monofacial counterpart. There are other studies in the literature that demonstrate the promising potential of standalone bifacial and/or tracking PV panels both experimentally [123], [124] and computationally [118], [125]. There is an emerging consensus that the irradiance incident on a module can be enhanced through bifaciality/tracking.

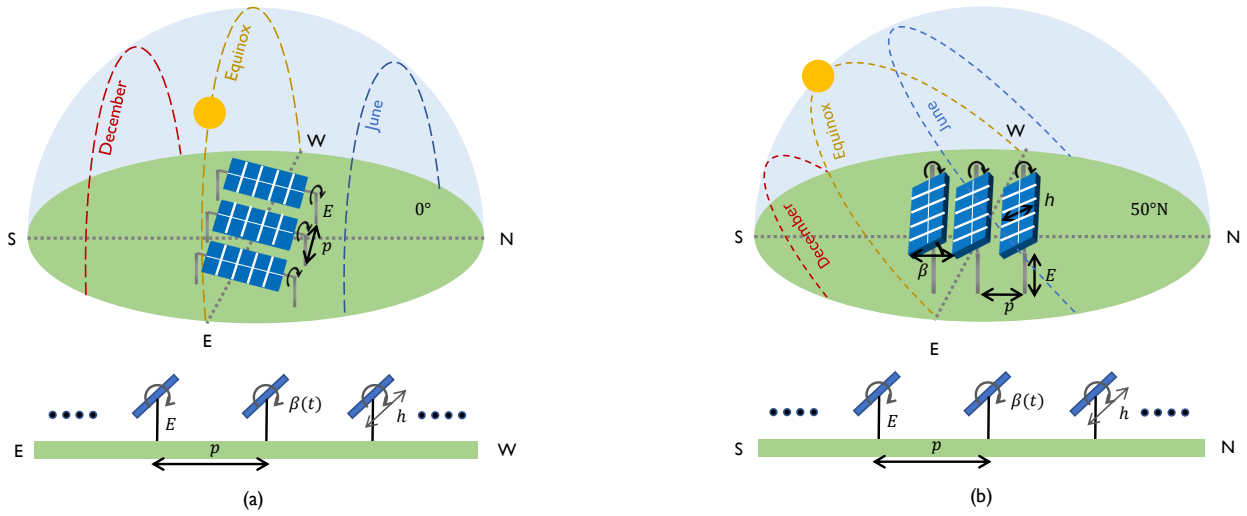

Figure 4.1. Schematic of a single-axis tracking bifacial solar PV farm (a) E-W facing (b) N-S facing. The solar path varies with latitude as well as time making one of the designs geographically more suitable.

Despite these promising initial results, one still wonders if temperature-dependent efficiency degradation due to additional solar irradiance would erase any performance gain. Indeed, several research groups have explored the temperature-dependent performance of stand-alone PV modules [26], [100], [102], [126]. By combining the irradiance, light collection, and electro-thermal models, several research groups have demonstrated that the bifacial gain and corresponding reduction in LCOE depend on the geographical location and one must optimize the module tilt and row-separation to maximize the bifacial gain [26], [64].

Along with standalone PV modules, several research groups investigated monofacial/bifacial PV farms both in fixed and/or mobile configurations. Stefano et al. [127] demonstrated that the bifaciality of single-axis mobile PV arrays could enhance their performance by 12%. Stein et al. [128] reported $\sim 10\%$ bifacial gain for single-axis mobile PV systems. By using their mathematical model, Janssen et al. [119] demonstrated that single-axis tracking of monofacial and bifacial PV arrays could increase energy yield up to 15% and 26% respectively as compared to standard monofacial fixed-tilt system. A number of studies also reported the temperature-dependent performance of tracking PV systems based on theoretical analysis or simulated results [129]–[131]. Recently, based on their optical-electrical-thermal model, Patel et al. [46] showed that temperature-dependent efficiency could change LCOE of fixed-tilt

bifacial solar farms by $\sim$ 10% to 15% worldwide for different module technologies. Using a collection of solar farms in Brazil, Verissimo et al. suggest that country-specific tracking results show solar-farm topology can have a significant impact on the energy yield and LCOE of the system [132]. Rodriguez-Gallegos et al. [133] have also shown that the single-axis tracking bifacial PV system exhibit minimum LCOE worldwide, even though dual-axis tracking bifacial PV systems produce higher energy. A dual-axis system, however, has higher LCOE because its higher energy yield is partially counterbalanced by its higher initial, operational, and maintenance costs as compared to that for the single-axis system. After all, the single-axis system is simpler to design and operate both in E/W facing orientation to track the sun daily and in N/S facing orientation to track the sun over the seasons. Without taking into account location-specific land cost, the research [133] showed that single-axis bifacial PV farms exhibit a 16% decrease in LCOE for locations at latitudes within a range of $\pm 60°$. These results further demand a careful evaluation of global-scale LCOE for single-axis tracking bifacial PV farms by considering the site-specific land costs. Indeed, as discussed in Ref. [45], the land-cost dramatically changes the optimum spacing, and the energy yield of a solar farm.

This work is the culmination of our series of studies on *standalone* and farm-level bifacial PV design considerations. We performed worldwide analyses investigating the optimum design parameters for energy maximization of a single bifacial PV module [26], a vertical bifacial PV farm [61], a ground-sculpted bifacial PV farm [62], and cost minimization of a fixed-tilt bifacial PV farm [45], [46]. The purpose of this study is to investigate the worldwide performance of bifacial single-axis tracking PV farms with fixed-tilt bifacial PV farms. We compare the performance of two different tracking algorithms termed as *tracking the sun* (TS) and *tracking the best orientation* (TBO) [38]. By using a self-consistent optical-electrical-thermal model, we address the following key questions: (i) How do the energy yields compare between east/west (E/W) facing and north/south (N/S) facing bifacial single-axis tracking solar farms? (ii) How does the site-specific climate affect the performance of these farms? (iii) How do the location-dependent land costs affect the optimum design and LCOE of these farms? and (iv) What is the optimum row-spacing (pitch) for minimum LCOE?

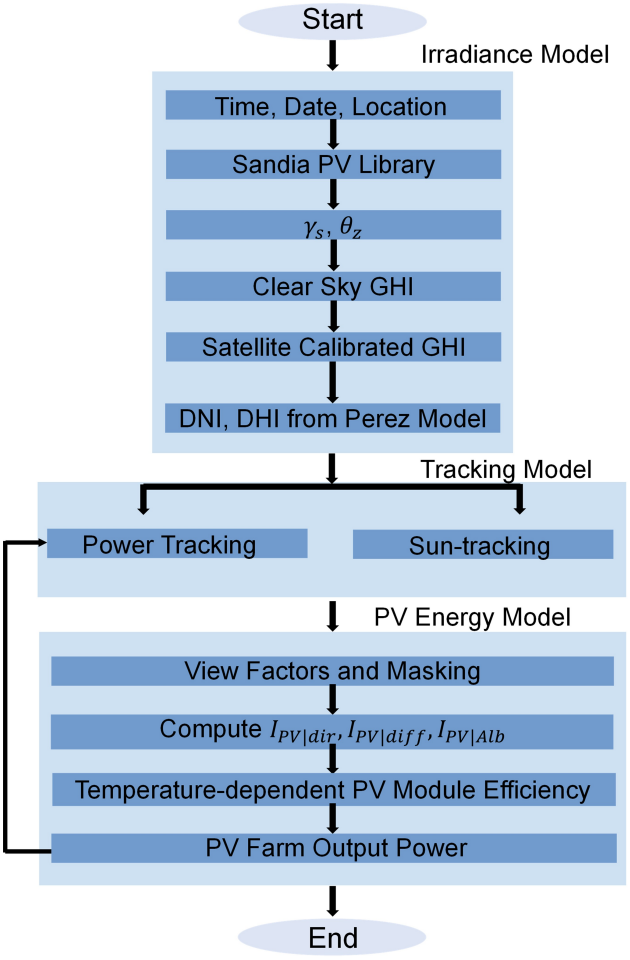

Figure 4.2. The simulation workflow integrates irradiance, light collection, and tracking models to calculate the energy yield of a bifacial tracking solar farm.

This chapter is divided into four sections. Section 4.2 describes the modeling approach. Section 4.3 discusses the results and the conclusions are provided in Section 4.4.

Table 4.1. Equations associated with optical model: Irradiance and light collection models.

$$I_{GHI} = I_{DNI} \times \cos\theta_Z + I_{DHI} \tag{4.1}$$

$$I_{PV:DNI}^{F,\ Farm} = I_{DNI} \cos\theta_F (1 - R(\theta_F)) \eta_{dir} \tag{4.2}$$

$$I_{PV:DHI}^{F,Farm} = I_{DHI}\ \eta_{diff}/h \int_0^h \frac{1}{2} \left(1 + \cos\left(\psi\left(E, l\right) + \beta\right)\right) dl \tag{4.3}$$

$$I_{PV:Alb.dir}^{F,Panel}\left(l\right) = I_{Gnd:DNI} \times R_A\ \times F_{dl-gnd}(E, l) \times\ \eta_{diff} \tag{4.4}$$

$$I_{PV:Alb.dir}^{F,Farm}\left(l\right) =\ 1/h \int_0^h I_{PV:Alb.dir}^{F,Panel}(E, l) dl \tag{4.5}$$

$$I_{PV:Alb.diff}^{F,Panel}(l) = I_{Gnd:DHI} \times R_A \times F_{dl-gnd}(E, l) \times \eta_{diff} \tag{4.6}$$

$$I_{PV:Alb.diff}^{F,Farm} = 1/h \int_0^h I_{PV:Alb.diff}^{F,Panel}(E, l) dl \tag{4.7}$$

$$I_{PV:Alb}^{Farm} = I_{PV:Alb.dir}^{Farm} + I_{PV:Alb.diff}^{Farm} \tag{4.8}$$

$$I_{PV:Alb}^{Farm} = I_{PV:Alb.dir}^{Farm} + I_{PV:Alb.diff}^{Farm} \tag{4.9}$$

$$YY_T(p, \beta, h, E, \gamma_A, R_A) = \int_0^1 I_{PV(T)}^{Total}(p, \beta, h, E, \gamma_A, R_A)\ \ dY \tag{4.10}$$

Table 4.2. Equations associated with thermal models.

$$\eta\left(T_{cell}\right) = \eta_{STC}(1 - TC(T_{cell} - T_{STC})) \tag{4.11}$$

$$T_{cell} = T_{amb} + c_T \frac{\tau\alpha}{u_L} I_{POA} \left(1 - \frac{\eta(T_{Cell})}{\tau\alpha}\right) \tag{4.12}$$

$$I_{POA} = I^{Farm}_{PV:DNI}/\eta_{dir} + (I^{Farm}_{PV:DHI} + I^{Farm}_{PV:Alb})/\eta_{diff} \tag{4.13}$$

4.2 Modeling Framework

To model a tracking solar PV farm, one must generalize and integrate several sub-models developed in previous studies [26], [45], [46], [61], [62]. We begin by integrating the irradiance model and a tracking algorithm to find the intensity of direct light falling on the solar modules. Next, we used a light collection model with view factors and masking formulae to estimate the diffuse and albedo light collection. Finally, the thermal model combined with the PV energy (electrical) model produces the total energy generated by the solar PV farm. A flow diagram in Fig. 4.2 demonstrates the complexity of a self-consistent model necessary to predict the performance of a tacking solar farm.

4.2.1 PV farm power and energy model

As shown in Fig. 4.1, we model a solar farm with the following design parameters: azimuth angle (γ_A) from the North; panel height (h); panel angle (β); elevation from the ground (E); pitch (p); and ground albedo (R_A). First, we use the **irradiance model** and estimate the ground illumination for a particular time of the day with a time step of 1 minute at a location specified by its latitude and longitude. We follow the modeling described in [45], [46], [61]. We use the PV library from Sandia National Laboratory to calculate the Sun's trajectory

(zenith (θ_Z) and azimuth angle (A)) and the irradiance [61]. The Global Horizontal Irradiance (GHI or I_{GHI}) is ideally given by Haurwitz clear sky model [67], [68]. Renormalizing this irradiance based on the NASA Surface meteorology and Solar Energy database [69] yields the local variation in GHI. The 22-year monthly average GHI data from NASA SSE has a spatial resolution of $1° \times 1°$ (latitude x longitude). The GHI is then split into direct light (DNI or I_{DNI}) and diffuse light (DHI or I_{DHI}) using Orgill and Hollands model [70]. Perez model [134] further improves the accuracy by estimating both the circumsolar and isotropic components of diffuse light. The bifacial module output based on this insolation models has been shown to closely match experiments [26].

Second, we quantify the amount of **light collected by the solar panels** installed at that location. The panels have height h, tilted at an angle β, separated by pitch (or period) p, and are oriented at an array azimuth angle $\gamma_A = 180°$ (i.e., south-facing panels) for farms in the northern hemisphere and $\gamma_A = 0°$ (i.e., north-facing panels) for farms in the southern hemisphere or $\gamma_A = 90°$ for panels facing E-W direction. The collection of light on panels from the three components of irradiance (i.e., direct, diffuse, and albedo) are formulated separately and analyzed accordingly. Our approach to model the collection of light involves the view-factor calculation described in [45], [46]. The corresponding equations are summarized in Table 4.1 with a glossary of the terms defined in Table 4.5. A correctly implemented view-factor model gives identical results compared to the ray-tracing approach [135].

Third, we incorporate the **temperature-dependent efficiency model**, which require the collected light intensity, efficiency at STC, and ambient temperature as inputs and yield the effective efficiency as output [46]. The temperature-dependent efficiency loss involves a complex interplay of increased absorption due to bandgap reduction vs. increased dark-current and reduced mobility. At practical illumination intensity, it is well-known that the efficiency $\eta(T)$ scales linearly with the module/cell temperature, see Eq. 4.11 in Table 4.2 where the rate/slope of degradation is given by the absolute temperature coefficient (TC) [96], [104].

Finally, we find **the daily, monthly, and yearly energy-output** of the farm. Using the equations 4.2, 4.3, and 4.8 in Table 4.1, we arrive at Eq. 4.9 to find the time-varying spatially distributed light collection on the panels. This information combined with the

thermal model (summarized in Table 4.2) is used in the circuit model to find the equivalent power generation. The circuit model includes the bypass diode model to take into account the partial shading of the PV panels and their effect on the PV performance [61], [79]. To estimate energy output, we integrate the power generated over the desired period of time. We define the energy yield per pitch of a farm over one year as yearly yield (YY) given by Eq. 4.10. The associated levelized cost of energy (LCOE) is modeled and estimated using the concept of essential levelized cost of energy (LCOE*) as detailed in Refs. [45], [136]. Following equation describes the relation between LCOE and LCOE* where M_L is the ratio of module-related costs $\mathbb{C}_M$ and land-related costs $\mathbb{C}_L$. χ is a constant that includes the degradation rate and bank discount rate.

$$LCOE^* \equiv \frac{LCOE.\chi}{\mathbb{C}_L} = \frac{\mathbb{C}_M/\mathbb{C}_L + p/h}{YY(p, h, \beta, \gamma, R_A)} = \frac{p/h + M_L}{YY} \tag{4.14}$$

4.2.2 Tracking model

In a PV tracking system, instead of a fixed panel tilt, the tilt angle $\beta(t)$ varies with time. There are two types of tracking algorithms: (a) **sun-tracking** orients the modules to maximize the direct light, and (b) **power-tracking** orients the modules to maximize power or energy.

As the name suggests, a **sun-tracking** system minimizes the angle between the sun and the panel. To compute the time-dependent tilt angle of E/W facing modules by the **sun-tracking algorithm**, first, we compute the angle of incidence (θ_{AOI}) between the direct light (DNI) and the normal of the module face. Solar tracking (TS) minimizes the angle of incidence towards 0° so that the face of the solar panel follows the sun (direct light). Fig. 4.3 shows the hourly variation of the tilt angle β for TS for June and December at Washington D.C. ($38.9°N, 77.0°W$) and Dubai ($24.5°N, 55.5°E$) in the northern hemisphere.

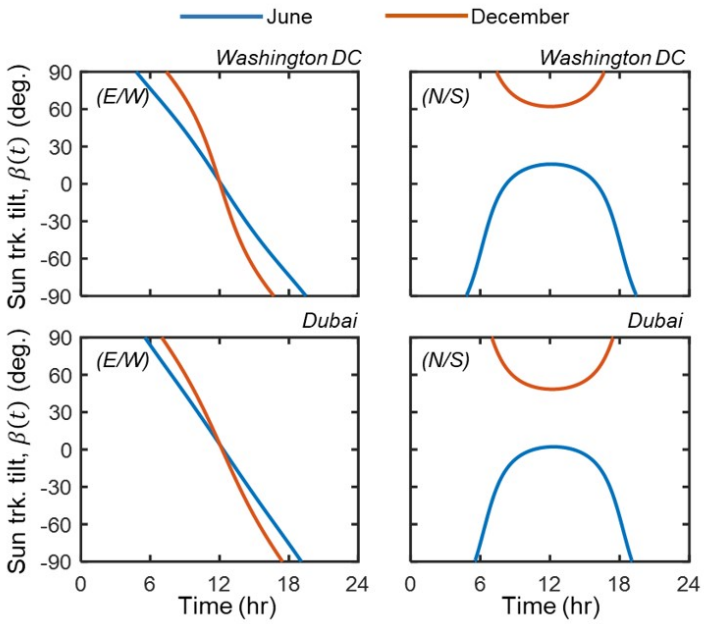

Figure 4.3. Using sun-tracking algorithm, we plot the tilt angle as a function of time for EW facing tracking PV modules (left column) and NS facing tracking PV modules (right column) for June (Blue) and December (Red) at Washington, D.C., $38.9°N, 77.0°W$ (top row) and Dubai, $24.5°N, 55.5°E$ (bottom row).

For E/W tracking, the panels follow the sun throughout the day, and thus the tilt angle $\beta(t)$ goes from $+90°$ (East-facing) to $-90°$ (West-facing) from sunrise to sunset. For N/S tracking, during summer (June) around sunrise, $\beta(t)$ is negative i.e., North-facing panels with $\gamma_A = 0°$ becomes close to $0°$ at solar noon and goes back to negative during sunset. This is because the sun's path, from sunrise to sunset, lies almost entirely in the North except near solar noon where the sun could be in the south of the panels. Whereas, during winter (December), $\beta(t)$ remains always positive i.e., South-facing panels with $\gamma_A = 180°$ will remain facing South because the sun's path is entirely in the South. Further, the panels face the south-inclined sun normally at solar noon where the $\beta(t)$ is equal to the zenith angle of the sun. Thus, the sign of tilt angle (and the array azimuth angle) varies with the sun's path according to the latitude of a geographical location throughout the year. The days in December are shorter than days in June, which is evident from the sunrise and sunset points. Moreover, $\theta_{AOI} = 0°$ is not achievable for both months, thus, the algorithm minimizes θ_{AOI} for the closest normal incidence. Finally, the initial angle being $\pm 90°$ is impractical for a

solar farm because in this scenario the first row of panels will cast a row-to-row shadow on all the other panels.

The second approach involving power-tracking optimizes the time-dependent tilt angles to achieve maximum power at each time-step—this will also maximize daily energy. The optimization is governed by the combined effects of (a) relative contributions of instantaneous DHI and DNI, (b) position of the sun, and (c) panel-to-panel shading. This power-tracking or the best orientation (TBO) algorithm is targeted towards maximizing output, not the light collection. Thus, during the early and late part of the day, the system will compromise light collection to avoid shading loss and maximize power output.

Fig. 4.4 shows the time-dependent optimized tracking angles $\beta\,(t)$ in June and December for Washington D.C. and Dubai. During the early and late parts of the day, the irradiation is mostly sky-diffuse light. At these times, in contrast to the TS algorithm, the panel optimally faces the sky (i.e., $\beta\,(t) \approx 0$) for both E/W and N/S tracking configurations. As the day progresses, the fractional contribution of DNI increases, and the $\beta\,(t)$ will compete between facing the sky and the sun. This is prominently observed for optimal tilt for E/W tracking panels in Fig. 4.4. After a certain time, e.g., 7 am in June, the panels closely follow the sun. In general, even when the DNI fraction is higher, the $\beta(t)$ is shallower than sun-tracking angles to improve the collection of DHI. The N-shape profile of $\beta\,(t)$ in E/W tracking is narrower in winter seasons due to shorter days. For N/S tracking, $\beta(t)$ is larger in December compared to June due to the more tilted sun-path.

To compare the tracking algorithms in terms of insolation collection, Rodriguez-Gallegos et al. [38] performed a PV tracker performance analysis using these two algorithms – tracking the sun (TS) and the best orientation (TBO) – for 3 different configurations, namely, horizontal single-axis tracker (HSAT), tilted single-axis tracker (TSAT), and dual-axis tracker (2T). They found that TBO shows a higher insolation collection compared to TS but the difference is below 1.8% for |latitude| $< 60°$ and 3.3%, 7.1%, and 2.9% for HSAT, TSAT, and 2T, respectively.

A few points regarding practical tracking algorithms are noteworthy. First, the power-tracking or TBO algorithm requires the panels to back-track at least twice during the day (observe the peaks and troughs in Fig. 4.4). This may cause additional mechanical wear

and tear of moving parts and electrical issues with the motor. In contrast, the sun-tracking algorithm continuously follows the sun during the day, which avoids backtracking and related reliability issues, if any. Second, the maximum value of the tilt angle for tracking the panels is 60° to avoid rotational load on the axis and avoid mutual shading between the rows of panels at higher tilt angles. Third, in practice, the panels are kept at an initial tilt of 60° (not horizontal at 0°) to reduce dew-enhanced soiling that would reduce the output of the solar panels.

Now that we have described the sun-tracking algorithm, in the following section, we will discuss the energy yield of solar farms based on the power-tracking algorithm.

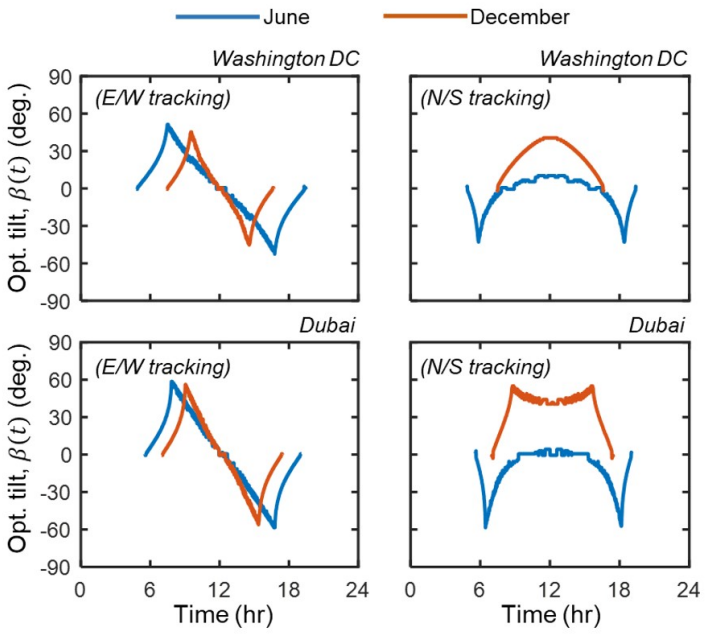

Figure 4.4. Using power-tracking algorithm, we plot the tilt angle as a function of time for E/W facing tracking PV modules (left column) and N/S facing tracking PV modules (right column) for June (Blue) and December (Red) at Washington, D.C. (top row) and Dubai (bottom row).

4.3 Power and energy yields at specific locations

In this section, we will summarize the modeling and simulation results through energy yield and then discuss LCOE-optimized solar farms. For an intuitive understanding of the results, we first compare the monthly energy output for various farm designs at four locations

– Dubai ($24.5°N, 55.5°E$), Washington, D.C.($38.9°N, -77.0°W$), Stockholm ($59.3°N, 17.8°E$), and Sydney ($33.8°S, 150.6°E$). Next, we present the global energy yield maps for fixed-tilt, East-West (E/W), and North-South (N/S) tracking farm designs. By default, we assume an east-west (E/W) tracking bifacial farm with a pitch over height, $p/h = 2$ and elevation above the ground, $E = 1\ m$ (we will discuss pitch and height-optimized design later in section 4.4). We then compare this default design with various other PV farm configurations, namely, fixed-tilt bifacial farm, E/W tracking monofacial farm, and N/S tracking bifacial farm. Finally, we will present the effect of varying pitch on the yearly energy yield and LCOE* for the default EW tracking PV farm design.

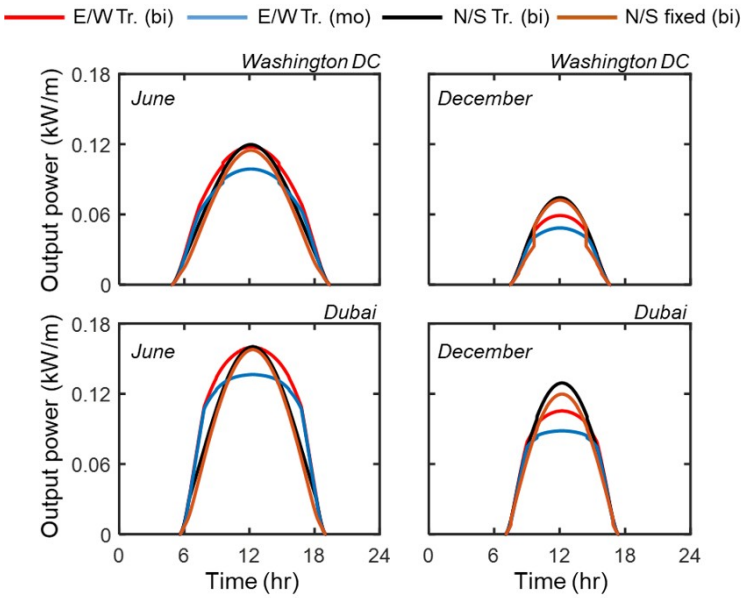

Figure 4.5. Daily output power for Washington D.C. and Dubai during summer months (June) and winter months (December). E/W tracking performs better in summer months and lower latitudes while N/S tracking has a higher output during winter months and higher latitudes.

4.3.1 Power output

E/W tracking vs. N/S Fixed-tilt Systems

The power outputs of the PV farm using the power-tracking (or TBO) algorithm along with N/S fixed-tilt systems are shown in Fig. 4.5. We find that the energy yields of E/W tracking bifacial farms are always higher than that of E/W tracking monofacial farms for

Dubai and Washington, D.C. In June (for both Washington DC and Dubai), E/W tracking yields higher energy compared to N/S systems slightly before and afternoon, resulting in overall higher output from E/W tracking PV. In December, as the sun-path is more tilted, the E/W systems cannot adequately follow the sun (θ_{AOI} is high even at noon). Thus, the N/S tracking and fixed-tilt systems give more output than E/W tracking systems in December. Although the net gain depends on the location, the counterbalancing energy yield for summer and winter holds for any location, as discussed in the next section.

N/S tracking vs. N/S Fixed-tilt Systems

The N/S tracking panels have a higher output than N/S fixed-tilt panels as it can avoid shading in mornings and evenings and correct for panel tilt for seasonal sun-path variations. For example, in Fig. 4.5 there is a clear effect of partial shading in Washington D.C. in December for N/S fixed panels as we can observe the lowered output before 9 am or after 3 pm.

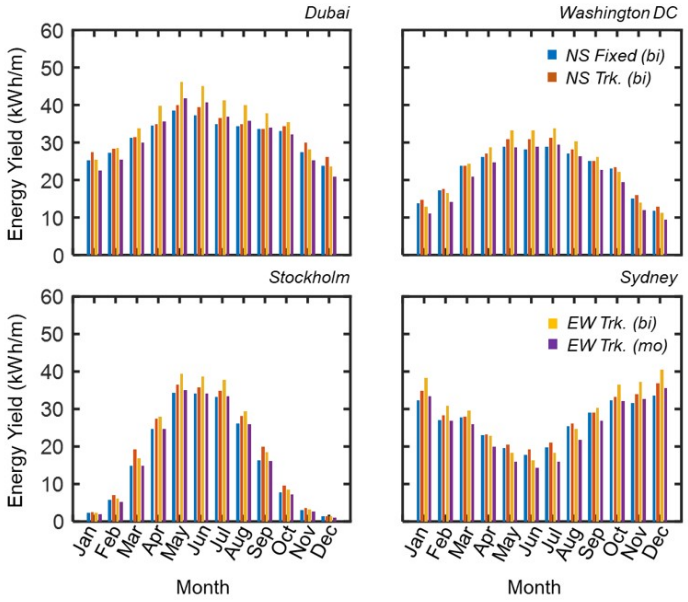

Figure 4.6. Monthly energy yield for various farm designs, namely, N/S Fixed tilt (Blue), N/S Tracking (Red), E/W Bifacial Tracking (Yellow), and E/W Monofacial Tracking (Purple).

4.3.2 Monthly/Seasonal energy yield variation

The monthly energy yield for various PV module configurations is shown in Fig. 4.6. Various locations in both the northern and the southern hemispheres are explored here. During summer months in the respective hemispheres, E/W bifacial solar tracking scheme performs best, whereas, in the other months, N/S bifacial solar tracking scheme performs better. One of the important points to note is that N/S bifacial fixed-tilt performs best during Nov. to Jan. in Stockholm. Here, although higher irradiance is collected at bifacial modules for N/S solar tracking configuration, higher module temperature lowers its efficiency as compared to its fixed-tilt counterpart. Moreover, the average monthly energy gains for Dubai, Washington, D.C., Stockholm, and Sydney, respectively are as follows:

1. E/W tracking vs. N/S tracking: 5.75%, 0.16%,- 3.00%, and 1.08%.
2. E/W tracking bifacial vs E/W tracking monofacial: $\sim$ 11%, $\sim$ 15%, $\sim$ 18%, and $\sim$ 13%.
3. N/S tracking vs. N/S fixed tilt: $\sim$ 6%, $\sim$ 5%, $\sim$ 14%, and $\sim$ 6%.

The yearly minimum and maximum energy gains are shown in Fig. 4.16. The minimum is observed in the winter months and maximum in the summer months of the respective hemisphere. In terms of energy yield, it is apparent from these results that E/W tracking would be better near the equator and N/S tracking would be beneficial for higher latitudes.

We have so far used a fixed $p/h = 2$ for the daily and monthly energy calculations, however, the same p/h would not generate the maximum energy for all the farm designs due to the difference in row-to-row shading throughout the day. Thus, for energy maximization and cost minimization, we need to find the optimum pitch over height ratio (p/h) for specific farm design, as discussed in the next section.

4.3.3 Optimum p/h, YY, And $\mathrm{LCOE}_{\mathrm{min}}$

The Pitch of a solar farm – defined as the spacing between the rows of the PV panels – is an important design parameter. A farm is optimized by first quantifying how yearly energy yield and LCOE depend on the pitch of a solar farm.

For the daily power output and monthly energy calculations in the previous sections, we assumed the pitch over height ratio $p/h = 2$, for all the locations. In practice, higher p/h improves the energy yield (per panel) due to an increase in albedo light collections and reduction in mutual shading between the rows of solar panels, see Fig. 4.7(a).

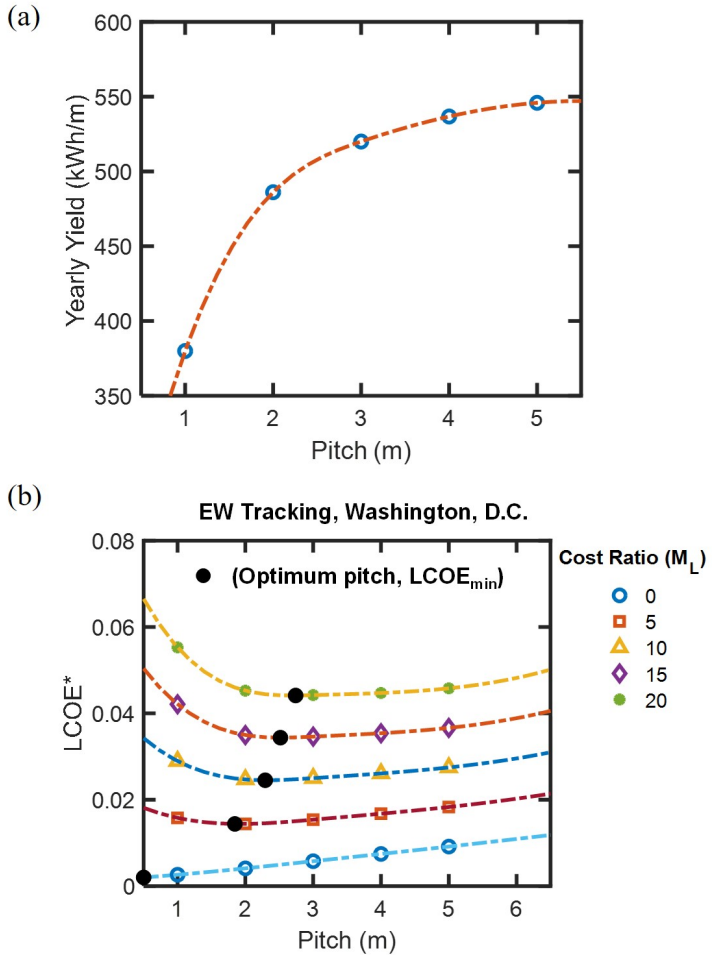

Figure 4.7. (a) An increasing trend in yearly energy yield with increasing pitch. The yearly energy yield saturates at higher values of pitch. (b) For a given value of cost ratio (M_L), an optimum pitch provides a minimum LCOE*. The optimum pitch increases with increase in module to land cost ratio (M_L).

However, once land-cost is brought into consideration (in other words, when the land is limited), then an optimum value of p/h yields the minimum LCOE. This optimum p/h is depicted in Fig. 4.7(b) for an E/W-tracking system at Washington, D.C. We find that the optimum p/h increases with increasing module-to-land cost-ratio (M_L). For a given module-related cost, a decrease in cost-ratio implies an increase in the land-related costs, leading to a reduction in the optimum pitch. Moreover, the optimum pitch and the associated minimum value of LCOE varies with the geographical location.

4.4 Global-scale merits of various farm designs

Given the understanding of power and energy-yield at the four cities across the world, now we are ready to compare the technologies across the globe. As discussed in Ref. [45], however, we must optimize the row-spacing depending on the LCOE-considerations.

In recent years, the M_L has ranged from 9 to 15 [45], [136]. Therefore, the optimum p/h for minimum LCOE lies between 2 and 3 for most locations around the world, see Fig. 4.8(c). For $M_L = 12$, the global yearly energy yield and minimum LCOE* at optimum p/h are shown in Fig. 4.8. (This result led to the default choice of $p/h = 2$ in Sec. 4.3.) Nonetheless, it is preferred that prior to the PV farm deployment, we optimize the farm design through an analysis of LCOE (proportional to LCOE*) variation with the pitch for each farm site around the world.

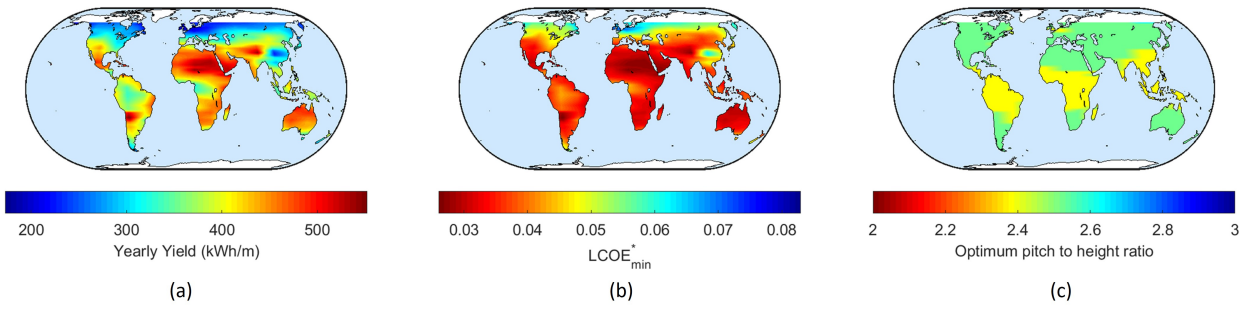

Figure 4.8. Global trends in yearly energy yield (YY), LCOE*, and optimum pitch/height of an elevated bifacial farm ($E = 1\ m$) for albedo $R_A = 0.5$ and $M_L = 12$.

4.4.1 Energy Yield of E-W Tracking Bifacial Solar Farms

Fig. 4.8(a) shows the yearly energy yield of an E/W tracking bifacial PV farm with an optimum pitch over height for $M_L = 12$. The yearly energy output per unit panel height reaches approximately 550 kWh/m for geographical locations close to the equator and deserts across the globe. These locations receive the highest fractions of direct light and thus, a tracking system benefits the most at these places. However, for locations with high diffuse light fraction, i.e., Beijing, Northern Europe, and North America, the yearly yield is significantly lower, $\sim 200 - 300$ kWh/m. The E/W tracking PV farms are not advantageous in these regions. The yearly energy yield in Fig. 4.8 will be taken as a reference for the comparisons performed in the following sections.

4.4.2 Tracking PV farm vs. fixed-tilt bifacial farm

Let us now determine if a single-axis tracking PV farm should be a preferable choice of deployment as compared to a fixed-tilt farm at any specific location around the world. The energy surplus/deficit of a tracking PV farm over a fixed-tilt PV farm depends on the geographical location, see Fig. 4.9. The E/W tracking bifacial PV farm outperforms the N/S fixed-tilt bifacial PV farm by $\sim 45\%$ near the equator and at lower latitudes. The highest energy gain is observed in desert regions, e.g., Sahara, Atacama, Australian, and Kalahari. These regions receive a high fraction of direct light irradiance and E/W tracking PV relies on tracing the direct light, thus leading to increased energy gain. However, for sites with low direct light fraction and in turn high diffuse fractions, e.g., $|\text{latitude}| > 45°$ and Northeast China, the fixed-tilt bifacial farm is comparable or slightly better in energy gain. Given the additional land-area needed, higher initial and O&M cost, tracking may not be suitable for these locations.

Moreover, a comparison between E/W tracking monofacial farm and N/S fixed-tilt bifacial farm shows that tracking monofacial farm is advantageous only for locations with high fractions of direct light i.e., $|\text{latitude}| < 30°$, whereas N/S fixed-tilt bifacial farm performs better for higher latitudes and for regions where the diffuse light fraction is relatively higher. Fig. 4.13 clearly displays this trend.

Overall, it will come as no surprise that tracking PV farms are advantageous for locations with a high direct light fraction while fixed-tilt bifacial farms perform better at sites with the high diffuse light fraction. Our contribution is to quantify the energy gain associated with various configurations of optimized solar farms.

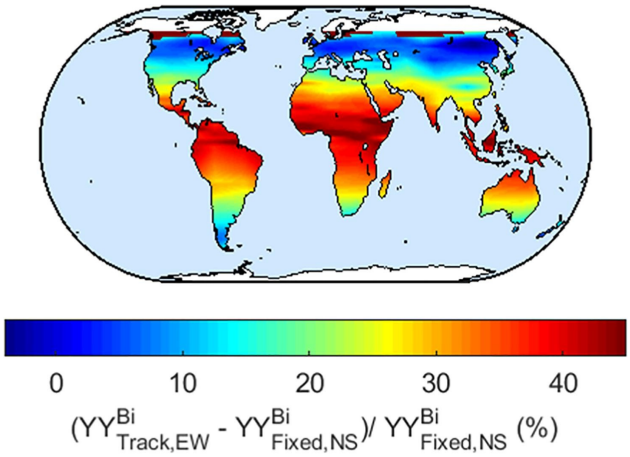

Figure 4.9. Percentage gain in yearly energy yield in East-West tracking bifacial PV farm compared to North-South facing fixed-tilt bifacial farm. The energy gain for E/W tracking is highest near the equator and in the deserts around the world whereas fixed-tilt performs slightly better at very high latitudes. For this calculation, the albedo $R_A = 0.5$.

4.4.3 E/W vs. N/S Tracking bifacial farm design

Next, we explore a conventional E/W single-axis tracking PV farm design with an N/S single-axis tracking one. In contrast to the hourly tracking of direct sunlight in an E/W tracking PV, an N/S tracking farm tracks the seasonal change in sun path (solar elevation/zenith angle) and varies comparatively less during the day. Since N/S fixed-tilt bifacial farm generates more energy output as compared to an E/W tracking farm at higher latitudes, we expect an N/S tracking farm to perform even better than a fixed-tilt bifacial farm.

Fig. 4.10 displays a worldwide comparison between an E/W tracking farm and an N/S tracking farm. As expected, we observe that N/S tracking farm to achieve higher energy output than E/W tracking farm for locations with high diffuse light fraction, e.g., Northern Canada and Siberia. Moreover, in comparison to E/W tracking farm, the (negative)

percentage yearly energy gain is higher for an N/S tracking farm (Fig. 4.10) than an N/S fixed-tilt bifacial PV farm (Fig. 4.9) for higher latitudes. Thus, with $\sim 15\%$ energy gain, E/W single-axis tracking PV farm is a better design for locations with $|\text{latitude}| < 50°$ and regions with a high direct light fraction. An N/S single-axis tracking farm on the other hand shows $\sim 5\%$ higher energy yield than the E/W tracking design for sites with $|\text{latitude}| > 50°$ and those with a high diffuse light fraction.

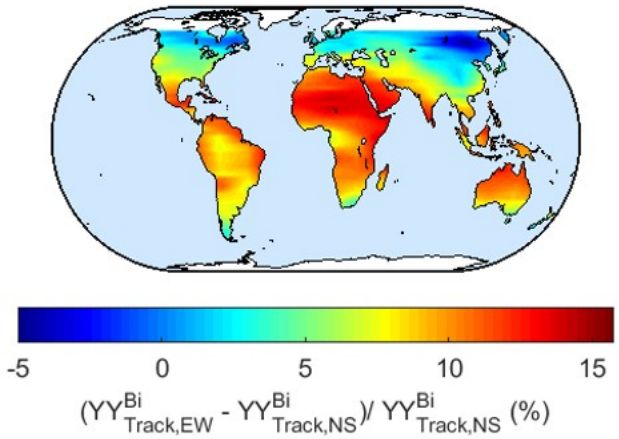

Figure 4.10. Percentage gain in yearly energy yield in East-West tracking bifacial PV farm compared to North-South tracking bifacial PV farm. The energy gain for E/W tracking is highest near the equator and in the deserts around the world whereas N/S tracking performs better at very high latitudes. For this calculation, the albedo $R_A = 0.5$.

4.4.4 Does Land-type Matter for Energy Yield?

In the previous sections, we analyzed the global energy yields for various tracking and fixed-tilt PV configurations. However, it is interesting to examine these solar farm designs in the context of the type of land of the installation site. This investigation may be especially useful for the new range of agro-photovoltaic (agrivoltaics) applications around the world. For example, it has been recently claimed that croplands in moderate climatic conditions are preferred locations for solar farms as well [101].

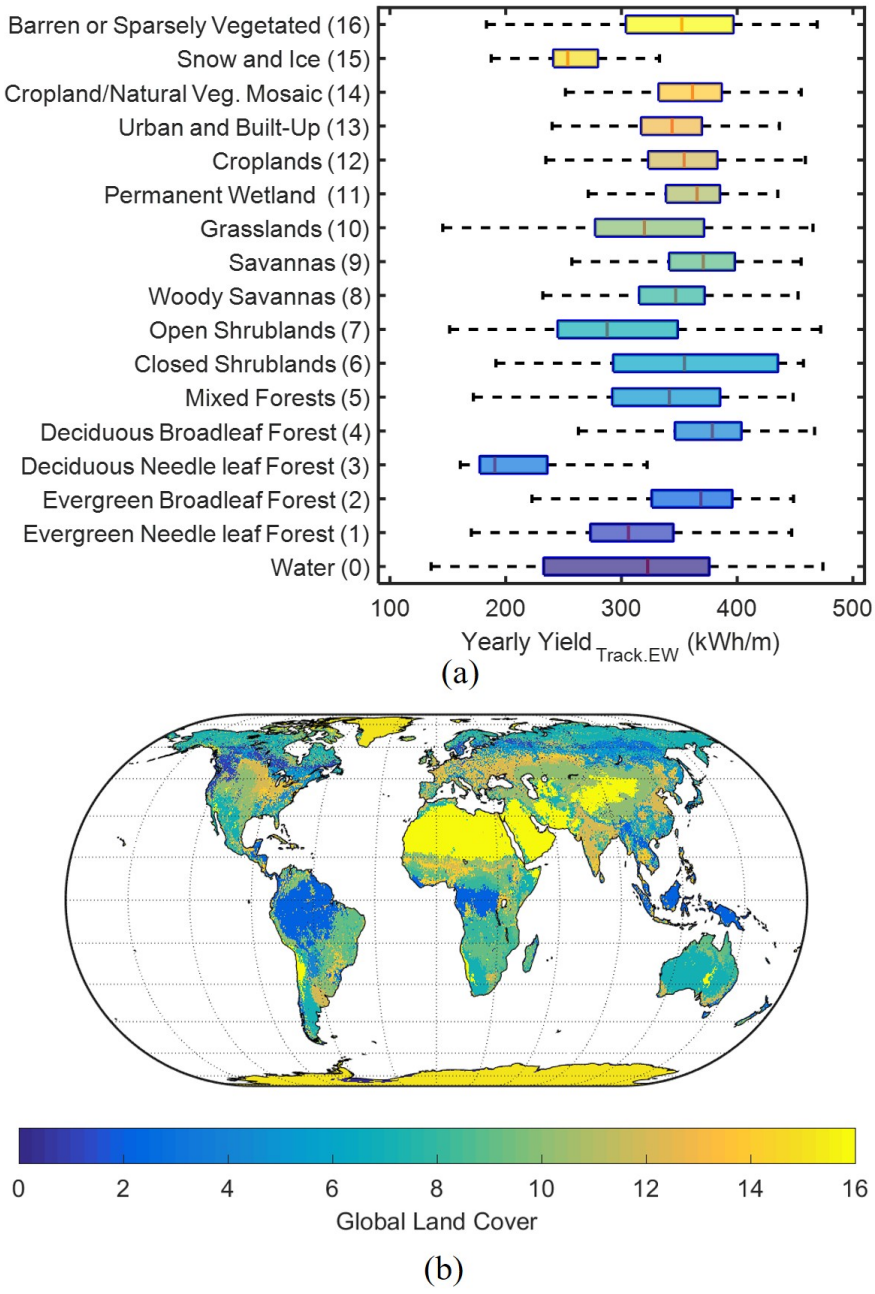

Figure 4.11. (a) Yearly energy yield of E/W tracking bifacial PV farm over various types of land. (b) A map of the 17 land types corresponding to the y-axis in (a). "0" corresponds to "Water" while "16" refers to "Barren or sparsely vegetated" land type. Albedo data is acquired from NASA MODIS [137]–[139].

In addition to the model described in Section 4.2, we further embed a monthly-average value of albedo for all the land types around the world. The global monthly albedo data is

acquired from NASA MODIS [137]–[139] and yearly-average value of albedo for the 17 land types is tabulated in the appendix Table 4.3. Fig. 4.11 summarizes our result of the analysis succinctly. We consider 17 types of land as shown on the y-axis of Fig. 4.11 (a) – the data was collected from Ref. [140]. These land types are also marked on the world map in Fig. 4.11 (b), where "16" corresponds to "Barren or Sparsely Vegetated" land, and "0" refers to "Water". We observe that, on average, maximum energy yield is expected for the land types "2" (Evergreen Broadleaf Forest), "4" (Deciduous Broadleaf Forest), and "9" (Savannas). However, the land types (2 and 4) are rich in biodiversity and we should avoid installing PV farms there to preserve ecological balance. "Savannas" (9) and "Barren lands/Deserts" (16) show good potential for E/W tracking farm deployment in terms of yearly energy yield. Land type "3" (Deciduous Needle leaf Forest) and "15" (Snow and Ice) are the least favorite for tracking E/W bifacial PV.

In summary, we can infer from Fig. 4.11 that installing E/W tracking bifacial PV farms in parts of Deserts, and Savannas are highly viable. The regions of croplands and grasslands have medium potential for energy yield (E/W tracking) and thus can be combined with agricultural usage and animal husbandry.

4.5 Summary and Conclusion

In this chapter, we have investigated the energy yield and comparative performance of various solar farm design configurations such as single-axis tracking vs. fixed-tilt and bifacial vs. monofacial. Our modeling framework combines the irradiance model, light collection model, temperature-dependent efficiency model, and a single-axis tracking model to estimate the energy yield of a solar farm. The tracking algorithm constraints the panel tilt angle to vary such that the angle of incidence is 0° i.e., the direct light falls normally on the panel. These models are simulated for locations worldwide that finally output global maps that quantify the percentage change in energy yield while comparing various farm designs.

Our analysis in this study leads to the following key **conclusions**:

- An E/W single-axis tracking bifacial PV farm generates up to $\sim 45\%$ higher yearly energy yield than an N/S facing fixed-tilt bifacial PV farm for locations

at |latitude| $< 30°$ Fig. 4.9. A higher fraction of direct light leads to higher energy gain. An E/W tracking monofacial farm vs. fixed-tilt bifacial farm shows similar global trends with maximum energy gain reaching $\sim 10\%$ near the equator (Fig. 4.13). However, fixed-tilt bifacial farm outperforms tracking monofacial farm by $\sim 5 - 15\%$ for |latitude| $> 30°$ (Fig. 4.14).

- As shown in Fig. 4.10, an E/W single-axis tracking bifacial PV farm tracks the hourly movement of the Sun whereas an N/S single-axis tracking bifacial farm mostly tracks the seasonal/monthly movement of the Sun. The former provides up to $\sim 15\%$ more energy for locations close to the equator (|latitude| $< 50°$) and the latter generates up to 5% for locations close to the poles (|latitude| $> 50°$).

- Monthly/Seasonal variation in energy yield shows that the E/W tracking produces higher energy output in summer months whereas N/S tracking is favorable in winter months due to a southward inclination of the solar path in the Northern hemisphere and vice versa for the Southern hemisphere, as seen in Fig. 4.6.

- On an average, maximum PV energy yield is achieved at "Evergreen and Deciduous Broadleaf Forests" land types. However, to preserve the biodiversity at these forests, it would be ideal to install E/W bifacial tracking PV on the next best land type for high energy yield, namely, "Deserts" and "Savannas", as illustrated in Fig. 4.11.

- An optimum pitch over height ratio yields minimum LCOE of an E/W tracking farm. The value of optimum p/h increases with the module-to-land cost-ratio (M_L) and varies with the geographical location of the farm. Whereas the yearly energy of the farm increases monotonically with p/h and saturates for very high values of pitch, as shown in Fig. 4.7. For a typical value of $M_L = 12$, the optimum p/h lies between 2 and 3, as seen globally in Fig 4.8.

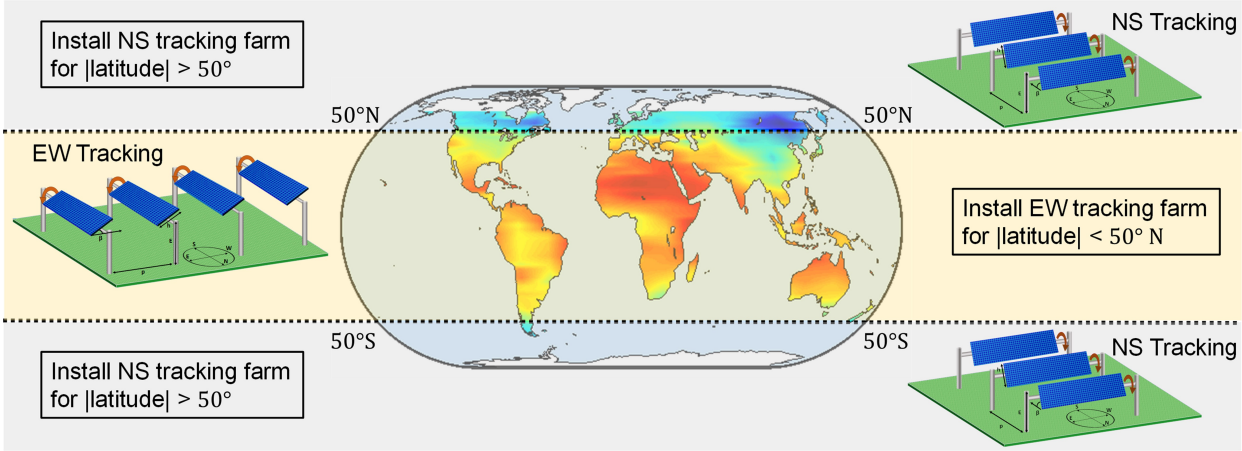

Figure 4.12. In conclusion, EW tracking bifacial farms outperform NS tracking bifacial farms for |latitude| $<$ 50° and vice-versa for |latitude| $>$ 50°.

Fig. 4.12 summarizes our key conclusion that an E/W single-axis tracking bifacial PV farm is the best PV farm design for most regions (|latitude| $<$ 50°) around the world. The energy gain with respect to a fixed-tilt bifacial or an N/S tracking farm varies according to the incident direct light fraction and the solar path at the geographical location of the solar PV farm. Moreover, for minimizing LCOE of a farm an optimum pitch can be used according to the estimated essential module to land cost ratio (M_L) for the deployment site. Thus, in terms of energy maximization, a bifacial tracking PV would be a worthwhile farm technology in most locations of the world.

In principle, the results can be easily generalized to any bifacial module technology with appropriate modification of front and backside efficiency. Thus, this study can be extended to a quantitative investigation of location-specific advantages of different solar cells. Our conclusions about the latitude-dependent choice of various farms are very general and should apply to various solar cell technologies.

As future applications of our model beyond the scope of this study, one can consider the possibility of using bifacial PV for AgroPV applications, for potential reduction in cost due to reduced height associated with vertical and tracking bifacial modules [141]–[143]. Our model can be extended to include various types of crop-specific tracking algorithm to control shading and perform co-optimization of the farm design. The role of bifacial PV in floating solar is unclear. Also, next generation PVK-HIT tandem solar cells could improve the efficiency

further [104], [144], [145]. Moreover, the reliability and lifetime are important concerns, especially regarding the mechanical failure of the trackers [18], [146]–[148]. The practical viability of solar tracking vs. power-tracking are not fully understood. Storage-integrated solar farming is another important aspect to consider in worldwide optimization of farm design. Finally, spectral dependence of albedo can slightly modify our numerical results, however that will not change the conclusions. The static global maps displayed in this study can be explored interactively to find data point values for each location using DEEDS – a web-based platform for scientific research [149]–[151].

4.6 Appendix

4.6.1 Monofacial E/W tracking vs. N/S fixed bifacial

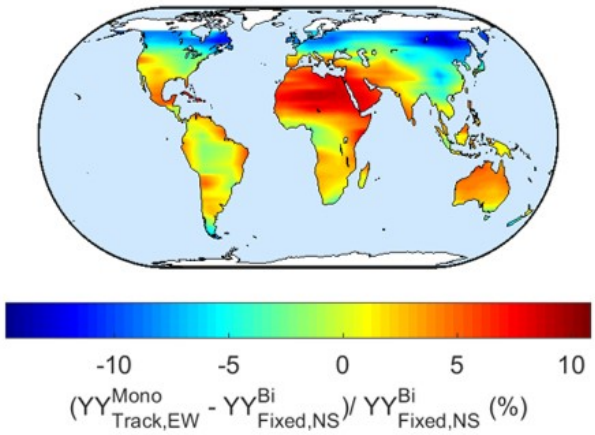

Figure 4.13. Percentage change in yearly energy yield between an EW tracking monofacial PV farm and a NS facing fixed-tilt bifacial farm.

4.6.2 Bifacial gain for EW tracking PV farm

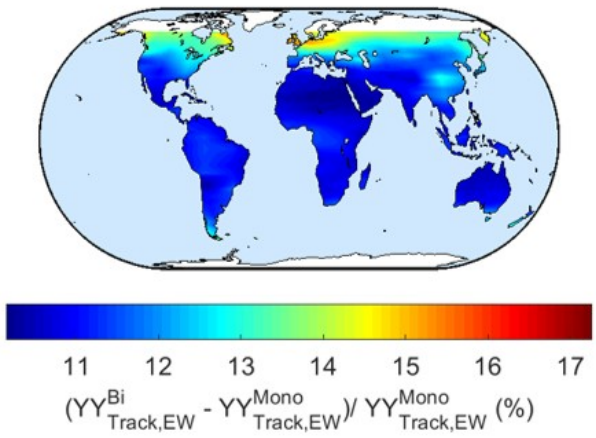

Figure 4.14. Percentage change in yearly energy yield between an EW tracking bifacial PV farm and an EW tracking monofacial farm.

$$Bifacial\ Gain = \frac{YY_{bifacial} - YY_{monofacial}}{YY_{monofacial}} \times 100 \tag{4.15}$$

4.6.3 E/W Tracking PV temperature dependence

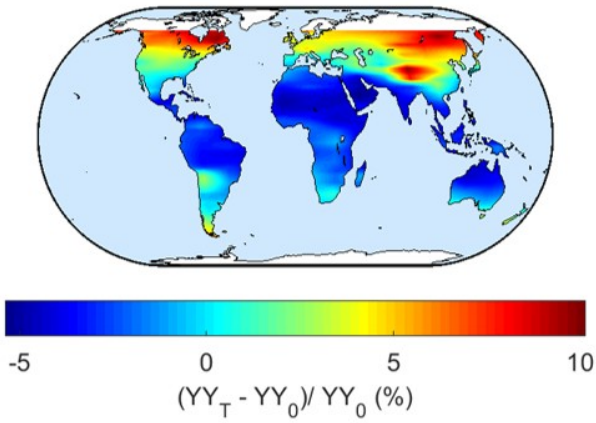

Figure 4.15. Difference in yearly yield estimation for E/W tracking bifacial PV farm with and without temperature-dependent efficiency model.

4.6.4 Monthly energy gain between various PV farms

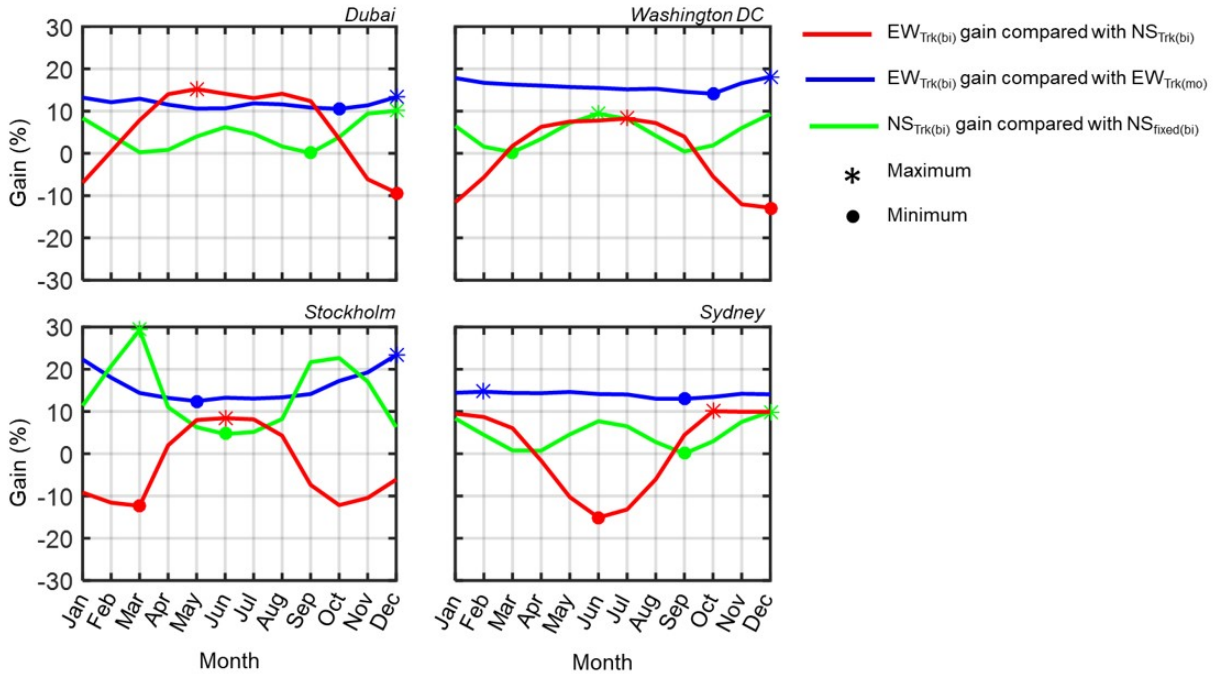

Figure 4.16. Difference in monthly energy yield estimation between combinations of E/W tracking, N/S tracking, and N/S fixed tilt bifacial PV farms. The maximum values are denoted by an Asterix (*) and minimum by a dot (.).

4.6.5 Yearly average albedo for various land types

Table 4.3. Yearly average albedo for various land types

Land Cover Type [140]	**Yearly Average Albedo** [137]
Water (0)	0.1
Evergreen Needle leaf Forest (1)	0.174
Evergreen Broadleaf Forest (2)	0.124
Deciduous Needle leaf Forest (3)	0.235
Deciduous Broadleaf Forest (4)	0.128
Mixed Forests (5)	0.153
Closed Shrublands (6)	0.139
Open Shrublands (7)	0.277
Woody Savannas (8)	0.135
Savannas (9)	0.141
Grasslands (10)	0.229
Permanent Wetland (11)	0.228
Croplands (12)	0.157
Urban and Built-Up (13)	0.134
Cropland/Natural Veg. Mosaic (14)	0.145
Snow and Ice (15)	0.765
Barren or Sparsely Vegetated (16)	0.299

Table 4.4. Glossary of symbols used in this study.

Parameters	Definition
TC	Temperature Coefficient ($\%/°C$)
T_a	Ambient Temperature ($°C$)
T_M	Module Temperature ($°C$)
P_{in}/P_{out}	Input Optical Power Collected by the Panel / Output Electrical Power (W/m^2)
η	Power conversion efficiency (%)
I/Irradiance	Input optical power over the plane of array (W/m^2)
a,b	Fitting parameters in the King's model (no unit, s/m)
WS	Wind Speed (m/s)
c_T	Correction term used for the daily average temperature data
τ	Transmittance of glazing (no unit)
α	Absorbed fraction (no unit)
u_L	Heat loss coefficient (W/m^2K)
γ	Coefficient of sub-band power contribution to heating (No unit)
θ_Z	Zenith Angle (degrees)
θ_F	Angle of incidence at the front face of the panel
Pitch (p)	Row-to-row distance between the bottom edges of consecutive arrays (m)
Height (h)	Height of the panel (m)
E	Elevation (m)
β	Tilt angle (°)
γ_A	Azimuth angle from measure from the North(°)
R_A	Albedo (no unit)
$C/\mathbb{C}$	Cost / Cost per unit meter
M	Number of rows/arrays of modules
Z	Number of modules in an array
D	Yearly degradation rate in energy conversion (%/year)
Y	Lifetime of a farm (in years)
YY	Yearly Yield of a PV farm (kWh/m)
R	Discount rate (%)
F	Fitting parameter in Alam-Sun model, which effectively accounts for module assembly and its related effects (like transmittance, glazing, heat loss coefficient)

Table 4.5. Glossary of symbols used in this study.

Sub/Super-scripts	Definition
a	Ambient
Alb	Albedo
bos	Balance of system
bot	Back side
DHI	Diffuse Horizontal Irradiance
diff	Diffuse
dir	Direct
dl	Differential element along the height of a panel
DNI	Direct Normal Irradiance
F	Front
f	Fixed cost
Farm	PV Farm
GHI	Global Horizontal Irradiance
Gnd	Ground
in	Input
l/L	Land
M, cell	cell/module
om	Operation and maintenance
Panel	PV panel
PV	Photovoltaic
rv	Residual value
STC	Standard testing condition
sys	System
top	top side
Total	Total
Z	Zenith

5. MACHINE LEARNING ALLOWS SYNTHESIS AND FUNCTIONAL INTERPOLATION OF COMPUTATIONAL AND FIELD-DATA FOR WORLDWIDE UTILITY-SCALE PV SYSTEMS

In the previous chapters we comprehensively modeled a tracking bifacial solar PV farm, analyzed the trends in yearly energy yield and LCOE, and found optimum designs for each location around the world. Now, since there is an accelerated pace of installations of variety of optimally-designed utility-scale solar farms across the world, therefore, the field data are streaming in from existing plants. The location-specific field data can be used to validate these highly sophisticated physics-based numerical models and software for a solar PV system over its lifetime. By necessity, the results of numerical models are specific to a finite number of arbitrarily chosen geographical locations and require substantial computational resources for a worldwide energy estimation, making it difficult to extrapolate the results to new locations. In this chapter, we demonstrate a novel machine learning-based tool that reduces the computational time by 4-orders of magnitude with an accuracy of $R^2 \sim 0.99$. The tool utilizes the simulation-derived utility-scale solar PV energy yield to functionally interpolate the location-specific inputs and energy yields. This compact, efficient, and versatile representation will transform how large-scale modeling is used to predict the energy yield of various farm configurations for any location around the world.

5.1 Introduction

Fast-paced growth in the demand and supply of solar PV systems – residential, commercial, and utility-scale – has accelerated the deployment of PV systems around the world. Parallel to this field deployment, there has been a concerted effort to model emerging PV systems to estimate their energy yield and levelized cost of energy (LCOE). The modeling effort is particularly important because there has been a proliferation of farm topologies (e.g., monofacial, vertical and tilted bifacial, E/W and N/S tracking systems, etc.) available for deployment. To make this comparison feasible, several models and software have been

developed to predict the energy yield over the lifetime of the PV farm [39]. SunPower Corp. has developed EnergyLink that constantly monitors various types of PV systems [40]. Sandia National Labs has created a library of codes and software called PVLib that can be used for PV system analysis [41]. National Renewable Energy Laboratory (NREL) provides Bifacial Radiance for energy estimation of bifacial PV systems and RdTools for PV degradation analysis [42], [43]. Driesse et al. [44] have performed a comparative analysis on several module efficiency models for energy prediction and rating. Similarly, the Purdue Group has designed physics-based numerical models for energy yield and LCOE calculation [45], [46].

These sophisticated models can not only accurately predict the energy yield and LCOE, but they can also find the optimum design of standalone PV modules and utility-scale solar PV farms. Due to their computational and algorithmic complexities, however, the existing models require significant computational resources to calculate the energy yield of a specific farm configuration located anywhere in the world, even for a relatively coarse grid of latitudes and longitudes [45]. Moreover, it is often difficult to validate the model prediction because the location of the actual farm may not coincide with the simulation grid. Unfortunately, traditional nearest-neighbor or spline-based interpolation techniques cannot be used because the weather and terrain can vary dramatically over few miles, let alone several degrees of latitude/longitude (coarse grid).

The emerging field of physics-based machine learning allows us to tackle the complexity and computation time issues of the PV simulation model. Physics-based machine learning utilizes the already existing physical/empirical models in conjunction with machine learning tools to perform symbolic regression [47], for efficient compact modeling [48], for forecasting complex dynamical phenomena [49], to improve the accuracy of ML models in data-deprived applications [50], [51], and for reduction in computation time, as we will see in this chapter. A survey of physics-guided and hybrid physics-ML models is presented in Ref. [52]. The following reasons led us to explore a hybrid physics-ML model for estimation of worldwide energy yield of solar PV farms.

1. A recent IEA-PVPS report [53] informs us that there are 15-16 models with various degrees of accuracy. ML will make this duplication of effort unnecessary, saving enormous time in code development.

2. Even with a debugged code, it may take years to generate highly refined results that can be used to develop policies. ML will do it in minutes.

3. The model will show that if one uses 2 locations per latitude, we can create a world-map. The ability to accurately perform worldwide prediction from scarce data depends on latitudinal-diversity of the information, not the number of datapoints themselves. It has implications of creating databases and validation protocols (Not all locations are the same).

4. An earth-based modeling can be functionally extrapolated to other planets, giving an approximate prediction of the energy yield. This transfer learning will become a validation tool for solar simulators used for planetary missions .

In this study, we develop a novel **functional** interpolation tool based on machine learning that can accurately estimate the yearly energy yield (YY) and effective levelized cost of energy (LCOE*) [45] in minimal computation time. As a new and potentially transformative approach to computational modeling, this tool addresses many challenges of traditional PV modeling, namely, the need for supercomputing resources, expertise in scientific computing, long run-time, etc. First, as shown in Fig. 5.1, we use the advanced computational models to calculate the energy yield for a coarse grid of locations (say 60 lats. x 20 longs.) around the world. This high-quality, high-precision data will serve as the training dataset for the ML algorithm. Second, the neural network tool is trained with location-specific weather inputs i.e., global horizontal irradiance (GHI), ambient temperature (T_{amb}), and clearness index (k_t); and the calculated outputs: YY and LCOE*. The artificial neural network then absorbs this data to generate a functional relationship (f) between the inputs and outputs. Finally, we validate the tool/function generated with a test dataset and find it to be remarkably accurate in predicting the output for any location around the world. Additionally, this tool reduces

the computational time by four orders of magnitude! The tool is available on DEEDS – an online data platform for scientific research [149], [151].

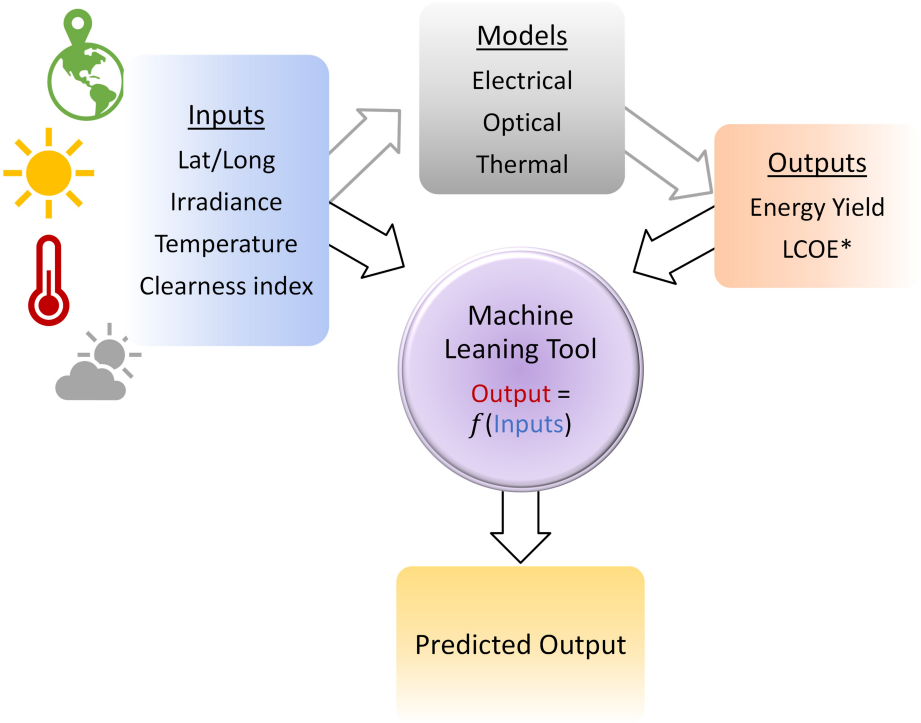

Figure 5.1. A schematic describing a machine learning tool as a functional extension to the sophisticated physics-based numerical model for energy yeild and effective levelized cost of energy estimation.

5.2 Methodology

5.2.1 Data collection/synthesis

Data collection is the first step in the analysis of a problem. Since machine learning is data-intensive, data collection and pre-processing is an important pre-requisite. In this study, we aim to estimate the energy yield of a solar farm at any location around the world. To this end, data can be collected from already deployed utility-scale solar PV farms or it can be generated/synthesized using sophisticated energy estimation numerical models. For this study, we will focus on the latter method of synthesizing data using already available physics-based numerical models [45], [46]. These models have been previously validated for standalone PV modules (row) as seen in Table 1 of Ref. [26] and few rows of vertical bifacial

PV modules. Thus, the validation of our numerical models can be extended to utility-scale large solar farms as well. Following are the input parameters required for these models: (i) Latitude and longitude of the geographical location, (ii) Global Horizontal Irradiance (GHI) at that location, (iii) Ambient temperature (T_{amb}) at that location, (iv) Clearness index (k_t) at that location. Monthly average values of GHI, T_{amb}, and k_t are derived from the satellite-based NASA Surface meteorology and Solar Energy (SSE) data archive [69]. A higher temporal resolution of GHI, T_{amb}, and k_t increases the accuracy of estimation. Next, we select the physical dimensions of the solar farm i.e., spacing between the rows, height of the PV panel, and ground clearance are defined. Then, simulating the PV farm model delivers us the following the outputs: (i) Yearly energy yield (YY) of the solar PV farm, (ii) Effective levelized cost of energy (LCOE*), (iii) Optimum tilt angle of fixed-tilt solar PV farm.

We run these simulations for 1200 location grid of the world with 60 latitudes and 20 longitudes. Fig. 5.2 displays the trend in yearly energy yield (YY) with the input parameters for all these locations. It appears that YY has a linear relation with GHI and k_t, whereas a non-linear dependence on latitude and ambient temperature. However, the combined effect of all the input parameters on YY is complex and a straight-forward interpolation is impossible. Next, we format input and output data according to the machine learning tool used for the functional interpolation. This interpolation method will offer an accurate YY and LCOE* estimation given the input parameters for any location around the world. We investigate and discuss two tools for the machine learning-based estimation in the next sections.

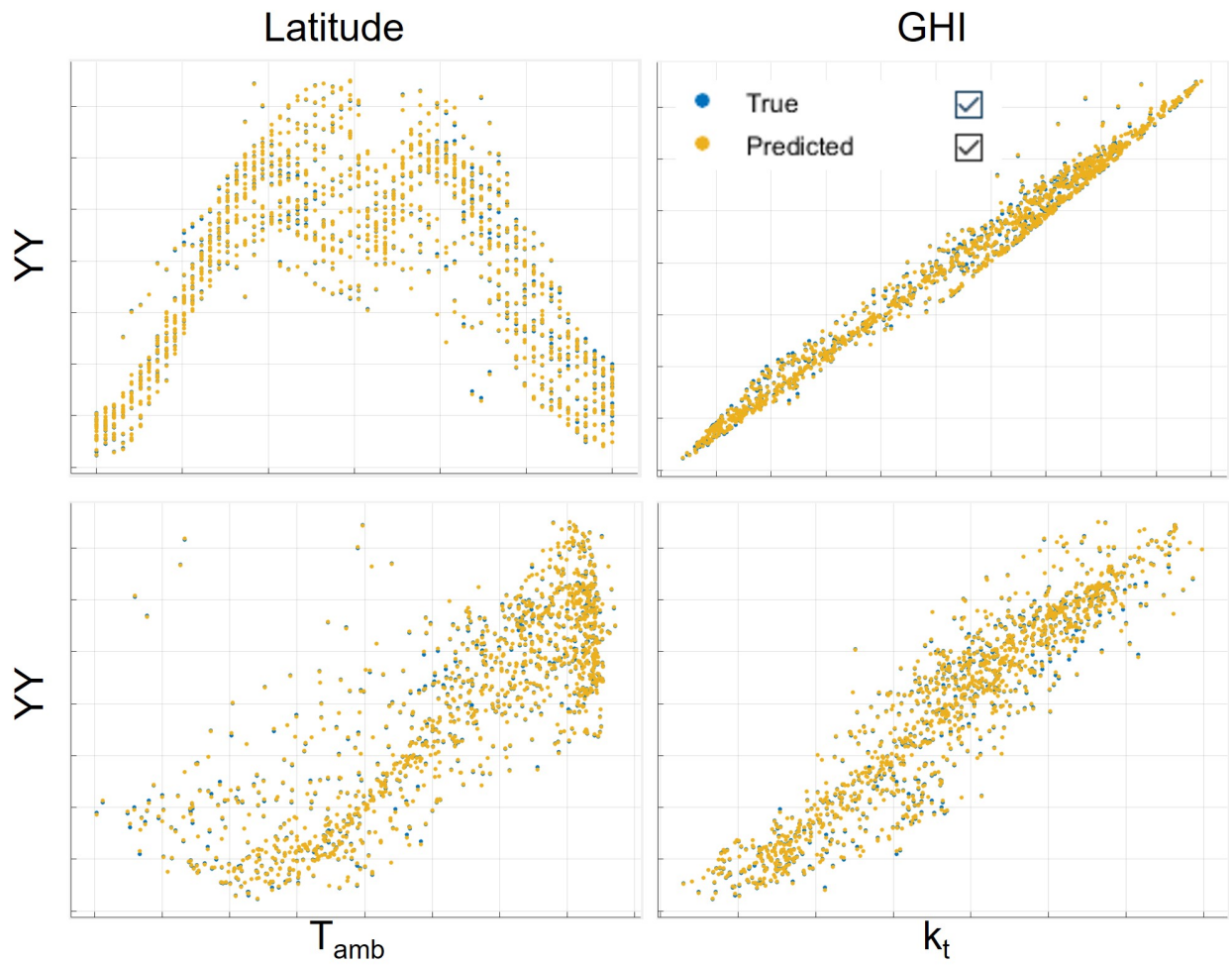

Figure 5.2. Variation of yearly energy yield (YY) with 4 input parameters: Latitude, Global Horizontal Irradiance (GHI), Ambient temperature(T_{amb}), and Clearness index (k_t). True response is simulated using the physics-based numerical model while predicted response is the output of the regression learning model.

5.2.2 Machine learning tools

Method 1: Regression Learner

We start with the Regression Learner application (app) in the MATLAB software package. This app requires the data to be formatted into a columned format. Thus, we format the 1200 location data in the required format. Next, we randomize and split the data into a training set (1000 locations) and a testing set (200 locations). Once the regression learner

app is evoked and the data is loaded, we need to include all the inputs and only one output in a matrix variable column-wise. Finally, we can try various algorithms/models to find the best one in terms of least root mean square error (RMSE) and R-squared (R^2) close to 1. For our dataset, we find the Gaussian Process Regression to be the most effective fitting algorithm with an RMSE of 7.03 and $R^2 = 0.99$ (see Fig. 5.3). Finally, we export this trained model to use as an interpolating function.

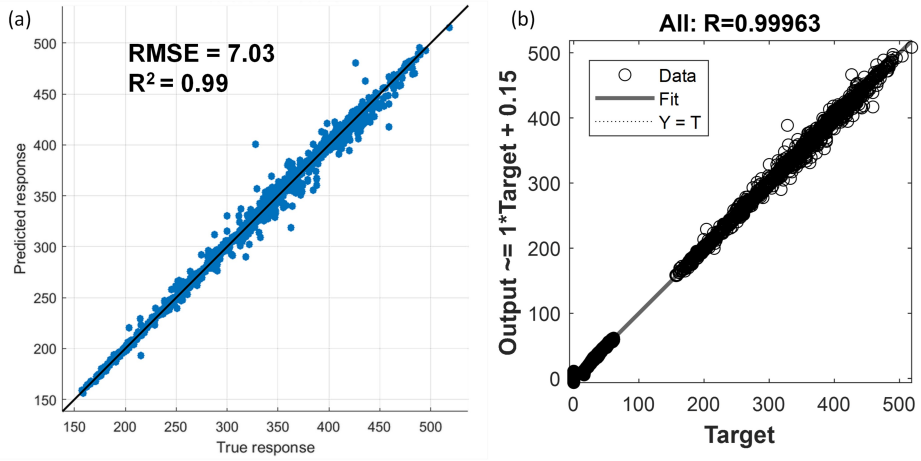

Figure 5.3. (a) The regression learner graph plots the predicted vs. true response for yearly yield with $R^2 = 0.99$ and RMSE = 7.03. The black line signifies an ideal model that predicts the outputs with 100% accuracy i.e., $R^2 = 1$. (b) The Neural Network graph shows the data points plotted with the fitting line. R values of ALL – training (70%), validation (15%), and testing (15%) – data sets together are 0.99 signifying high accuracy of the model.

Table 5.1. Results of the trained neural network.

	No. of samples/datapoints	MSE	R
Training (70%)	840	18.412	0.999639
Validation (15%)	180	17.535	0.999634
Testing (15%)	180	19.382	0.999604

Method 2: Neural Networks

The second, and more powerful tool, that we employed is the Neural Network Fitting tool (nftool) in the MATLAB software package. As the name suggests, the tool engages artificial neural networks to find the relationship between inputs and outputs. For this tool, we can organize the data in both column and row-wise formats. The inputs and outputs are in two separate matrices. In “nftool", we can include multiple output parameters in the same row-wise matrix. Next, we select 70% of the data (1200 locations) for training, 15% for validation, and 15% for testing. We choose 10 hidden layers of neural network for this problem and the Levenberg-Marquardt algorithm for training the neural network. Table I below, shows the results of the training, validation, and testing with an R $\sim$ 0.999. Finally, we export this trained neural network as a working tool that can substitute the physics-based numerical model for estimation of yearly energy yield and effective levelized cost of energy.

5.2.3 Mechanism of the NN-model

The mathematics behind the working of neural networks is well-described in machine learning literature. With regards to our PV dataset, for training the Feed Forward Neural Network, we organize the input data, multiply it with weights and add biases. The processed input data is then passed through a hidden layer of neurons that are essentially non-linear mathematical functions e.g., tanh, sigmoid, ReLu etc. The output of the hidden layer is then passed through an output layer of neurons that comprise of linear functions to yield the predicted output. The predicted output data is then recursively compared to the actual data by the machine learning algorithm (Levenberg-Marquardt) to optimize the afore-mentioned weights and biases to train an accurate model. Fig. 5.4(a) demonstrates a schematic of this training process. Once the model is trained to produce accurate results, it can be deployed in real world for predicting output for unknown scenarios.

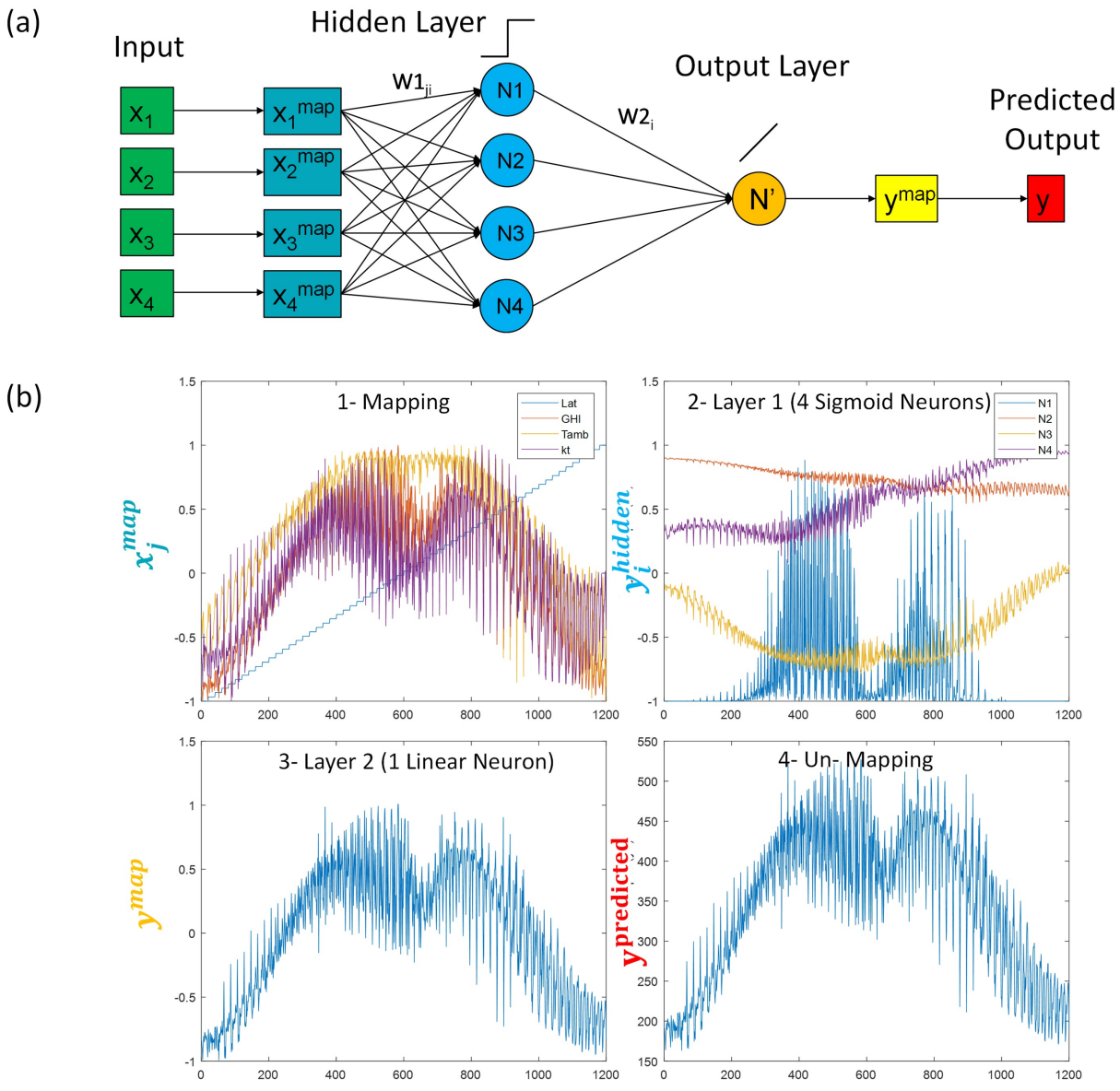

Figure 5.4. (a) A schematic of a neural network with input data, hidden layer of non-linear neurons, output layer of linear neurons, and the predicted output. (b) Plots displaying output after each step.

For the PV dataset that we have used, the following equations describe the complete process shown in Fig. 5.4.

Input mapping (with M input parameters):

$$x_j^{map} = (x_j - x_{0,offset})/x_{0,gain} + x_{0,min} \tag{5.1}$$

Hidden layer (with N non-linear neurons):

$$y_i^{hidden} = \tanh\left(\sum_j^M \left(w_{1j}\ x_j^{map}\right) + b_{1i}\right) \tag{5.2}$$

Output layer (with 1 linear neuron):

$$y^{map} = \sum_i^N \left(\ w_{2i} \times y_i^{hidden}\right) + b_{2i}\ \right) \tag{5.3}$$

Input mapping (with M input parameters):

$$y^{predict} = \left(y^{map} - y_{0,min}\right)/y_{0,gain} + y_{0,offset} \tag{5.4}$$

Fig. 5.4(b) (top left) shows the mapped inputs (x_j^{map}) using the mapping coefficients (x_0's). We observe that the inputs are mapped to values between 0 and 1. Further, one of the inputs (Lat) is taken as the basis and is plotted linearly while other inputs are mapped onto the basis input. These mapped inputs for our dataset (1200 points) look approximately symmetric around the middle point (600th point). This middle point is the Equator – the left of it is the southern hemisphere and the right is the northern hemisphere. Thus, some of the neurons capture this symmetry as seen in the output (y_i^{hidden}) of the 4-neuron hidden layer in Fig. 5.4b (top right). A weighted combination of the output of neurons from the hidden layer is then passed through the linear neuron in the output layer to yield the mapped output (y^{map}) that ranges between [0,1], see Fig. 5.4b (bottom left). Finally, the mapped output is reverse mapped (or unmapped) using the reverse mapping coefficients (y_0's) to give the predicted output parameter ($y^{predict}$) of the neural network, as shown in Fig. 5.4(b) (bottom right). While training the model, the algorithm calculates the error between the predicted output and the actual output and then the training algorithm optimizes the values of weights (w's) and biases (b's) to minimize the error. The trained model can thence be used for predicted test or field data. Next, we will look at the results of the functional interpolation.

5.3 Results and Discussions

To assess the accuracy of the tools/functions developed using regression learning and neural networks, we compared the actual and predicted outputs. Actual outputs are the ones simulated using the physics-based numerical models, whereas the predicted outputs are a result of the trained models from the two above-mentioned machine learning tools.

Fig. 5.2 demonstrates two aspects of this study. First, it shows an independent relationship between the response i.e., yearly energy yield (YY), and the input parameters as described in the previous section. Second, it compares the actual (true) response from the numerical model with the predicted response of the trained regression learning model. The accuracy of the model can be observed from Fig. 5.3(a) where predicted and true responses are plotted for energy yield (YY) estimation. The linear black line implies an ideal model with an accuracy of $R^2 = 1$. Fig. 5.3(a) gives us the confidence that the model trained using the regression learner app can be used for an accurate energy estimation for any location around the world. The training, validation, and testing results of the model created using the neural network tool are shown in Fig. 5.3(b). An R-value of approximately 0.99 for all the stages of model development displays the accuracy of the model. Remember that we used all the outputs at once to train the model. Thus, the neural network is highly potent in generating a function/relationship between the 5 input variables (Lat, Long, GHI, T_{amb}, and k_t) and the 3 output variables ($YY, LCOE^*$, and β_{opt}). Finally, we export and save the finalized model that can be easily deployed as a standalone or embedded tool for functional interpolation, and accurate estimation of yearly energy yield and effective levelized cost of energy of a utility-scale solar PV farm. Fig. 5.5 displays the overall improvement in the 10000-point interpolated world map with four orders of magnitude in computational speedup and with new insights not available in the original data. The tool is available on the Digital Environment for Enabling Data-Driven Science (DEEDS) online platform; Fig. 5.6 shows an interactive world map.

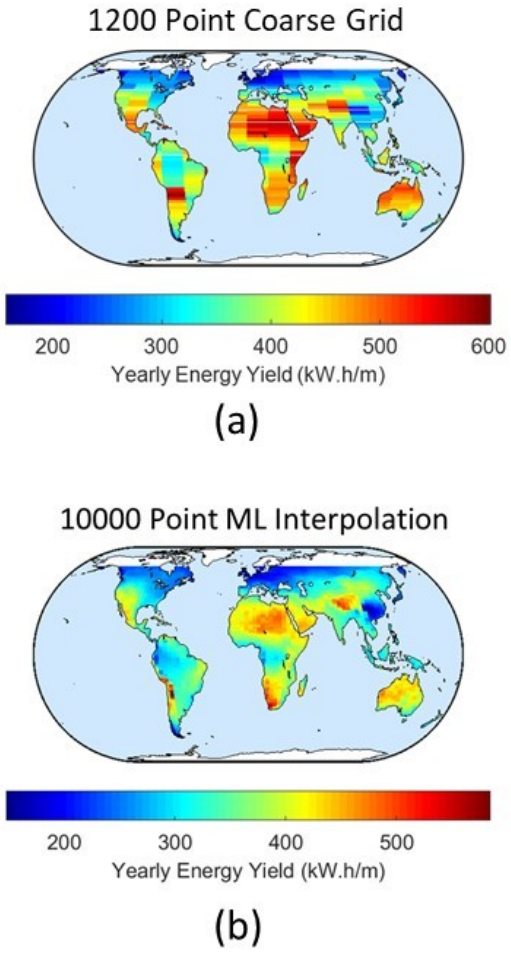

Figure 5.5. Estimated yearly energy yield of a solar PV farm using (a) physics-based numerical models with a coarse grid of 1200 points that requires ∼10 hours of computation time on a workstation with a 20-core node. (b) Neural network-based functional interpolation of 10000 points computed within a second using a single core personal computer.

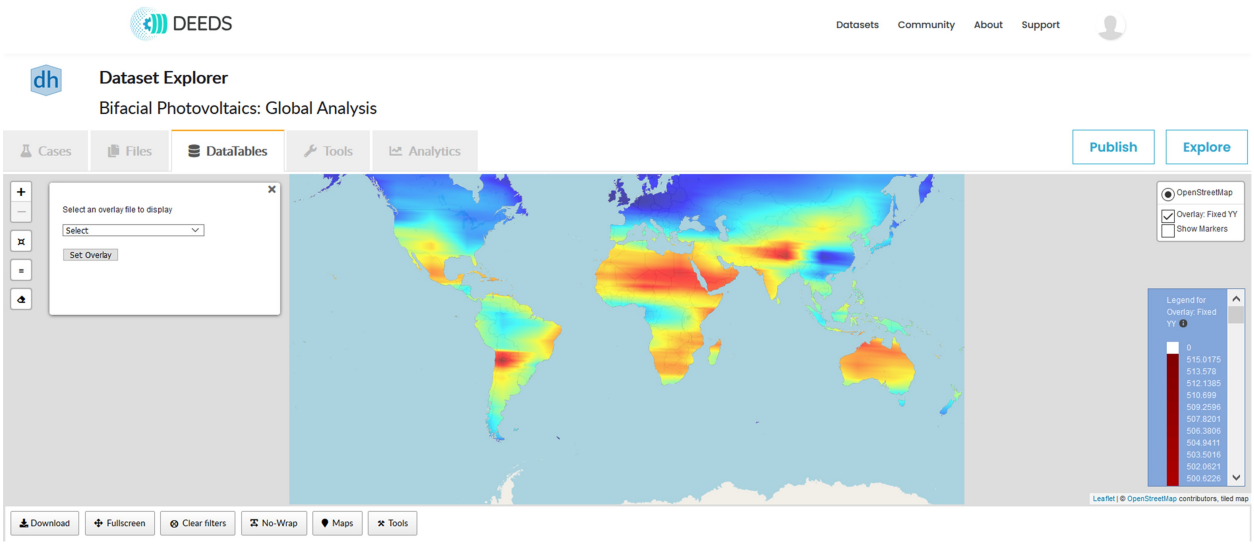

Figure 5.6. A screenshot of the DEEDS online platform displaying an interactive world map. DEEDS is an online platform that preserves end-to-end scientific research with computation and plotting capabilities.

5.3.1 Linear geographical vs. functional interpolation

In this section, we compare the two methods of interpolating (predicting) YY using data for 100 (or 1200) geographical locations, namely, linear geographical interpolation vs. functional interpolation. The first method involves creating a mesh grid of linearly interpolated latitudes and longitudes. This linearly interpolated mesh grid is further used to interpolate YY for 1200 locations to 10000 locations. The interpolated YY is labeled as YY_{geo}^{Linear} in Fig. 5.7. The second method employs machine learning (Neural networks) to predict YY for 10000 locations by creating a functionally interpolated mesh grid of all the input parameters namely, lat/long, GHI, T_{amb}, and k_t (not just latitude and longitude). The predicted YY using this method is labeled as YY_{func}^{NN} in Fig. 5.7. The comparison between predicted YY for 10000 geographical locations using these methods is shown in Fig. 5.7. It is evident from the location-dependent percentage error ($\sim 20 - 60\%$) in YY prediction that the method of geographical linear interpolation performs erroneous calculation. Whereas, NN-based functional interpolation is the more accurate strategy since it utilizes all the input parameters for YY interpolation. Moreover, we further observe that the percentage error is higher for regions with high direct light fraction e.g., Kalahari, Great Basin, and other

deserts around the world. This is because functional interpolation also accounts for GHI, T_{amb}, and k_t for all the locations.

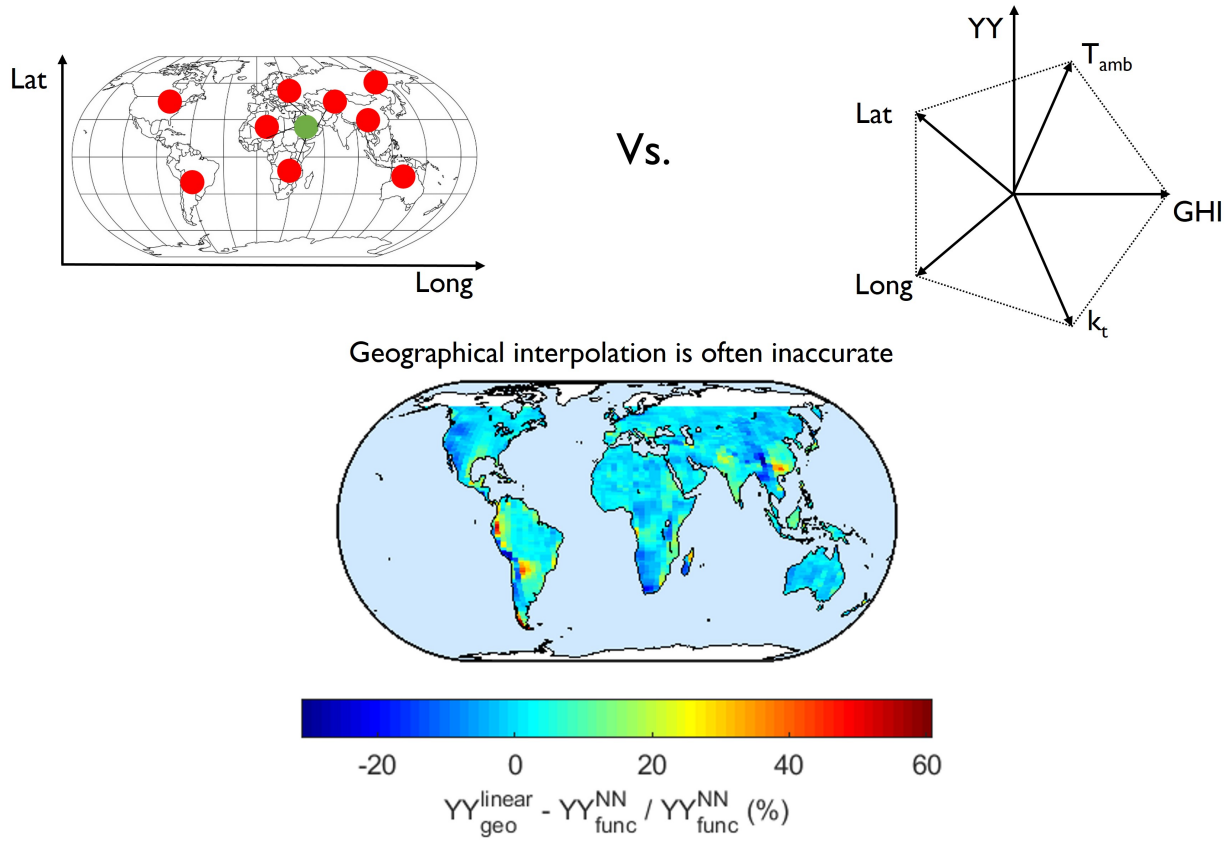

Figure 5.7. A comparison between the previously used linear geographical interpolation and NN-based functional interpolation shows a percentage error ranging from $\sim$ 20% to 60%. Evidently, functional interpolation is vital for accurate prediction.

5.3.2 Cross-validation: Two algorithms. Threshold number of sample points for high model accuracy

Given that functional interpolation is a more accurate scheme, we would like to explore the threshold number of sample/data points required to develop an accurate NN-based YY prediction model. The metric that we use for threshold evaluation is RMSE (Root-mean-squared error), which is estimated using two cross-validation algorithms. The first algorithm takes NS (say 1200) number of sample points, i.e., inputs and output (YY_{actual}), to train the

NN. The trained NN model is then used to predict YY for 10k input data points. Finally, using the 10000 predicted $YY^{NN}_{predict}$ values, we find YY values for the original 1200 sample points and compare the extracted vs. original YY values to find the RMSE (Algo 1). The second algorithm skips the middle step in the previous algorithm, i.e., we do not predict 10000 points. Instead, we use the 100 (or 1200) sample points (inputs and output) to train the NN model and then use only the input values of the same 1200 locations to predict $YY^{NN}_{predict}$ as an output. In Fig. 5.8, the root-mean squared error (Algo 2) is the error between the predicted output using algorithm 2, $YY^{NN}_{predict}$ and the actual 1200 simulated values of YY, YY_{actual}.

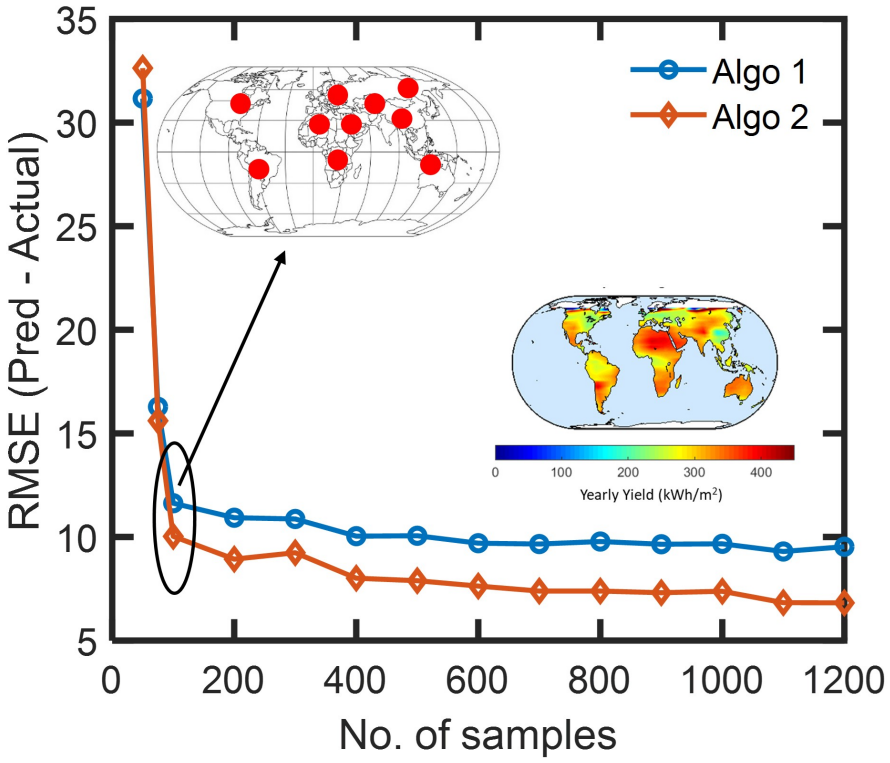

Figure 5.8. The plot displays the root mean squared error varying with the number of input samples used as input to train the neural network. A critical number of 100 samples is sufficient to train an accurate model for prediction. Algorithms 1 and 2 are described in the main text.

Fig. 5.8 shows the results (RMSE) of the two above-mentioned cross-validation algorithms as a function of number of samples (NS). We find that NS=100 is the critical value of samples required to train a fairly accurate NN model for YY prediction.

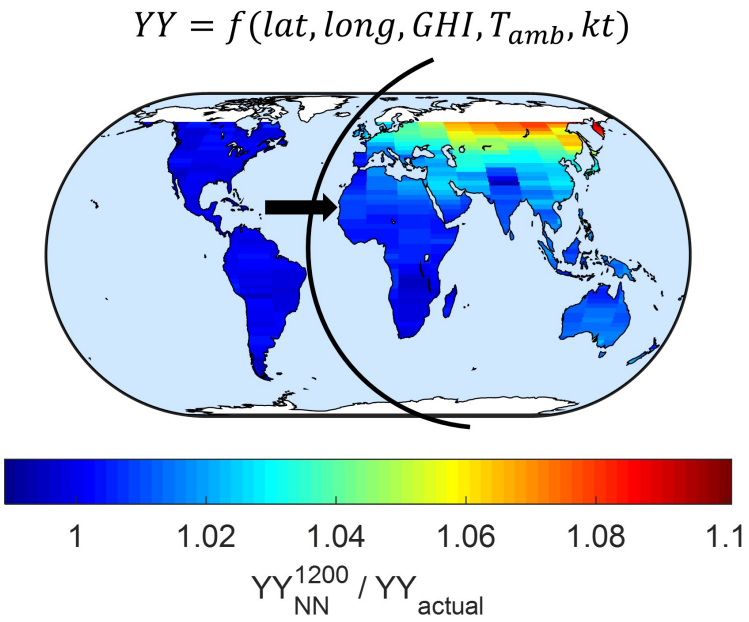

Figure 5.9. The global map demonstrates the ability of the NN-based interpolation method to be used for geographical extrapolation. We used the data-points from North and South America to train the neural network for YY prediction. The trained model is then used to predict YY for the rest of the world. When the predicted and actual values are compared, we observe a highly accurate prediction within 10% of actual YY.

5.3.3 Geographical extrapolation: NA/SA to world

Hitherto, we have seen the power of NN to perform functional interpolation. Subsequently, the NN-based functional interpolation can be applied to geographical extrapolation as well. To observe this, we train the model with $\sim$ 400 data points from North and South America (NA/SA) and then predict YY for all (1200) the locations around the world. A comparison between the predicted YY and actual is displayed on the world map in Fig. 5.9. Since we made use of the NA/SA data points to train the model, thus the prediction for NA/SA is accurate with a ratio $YY_{NN}/YY_{actual} \approx 1$. Interestingly, however, the prediction for rest

of the world also shows reasonable accuracy with a ratio between 1 to 1.1, i.e., the error in prediction is less than 10%. In fact, most of the predictions lie within 5% of actual value.

The geographical extrapolation of the NN model can be reasoned out as follows. The input variables (Lat, GHI, T_{amb}, and k_t) except longitude (long) exhibit a clear trend with the output (YY), and these are already accounted for in the trained model. The NN model creates a functional map/relationship between these input parameters and the output (Fig. 5.10). Since the trained model already knows about the functional form, thus a geographical extrapolation would still be part of the already learnt functional interpolation. Hence, NN model's functional interpolation using NA/SA data can perform a geographical extrapolation for rest of the world.

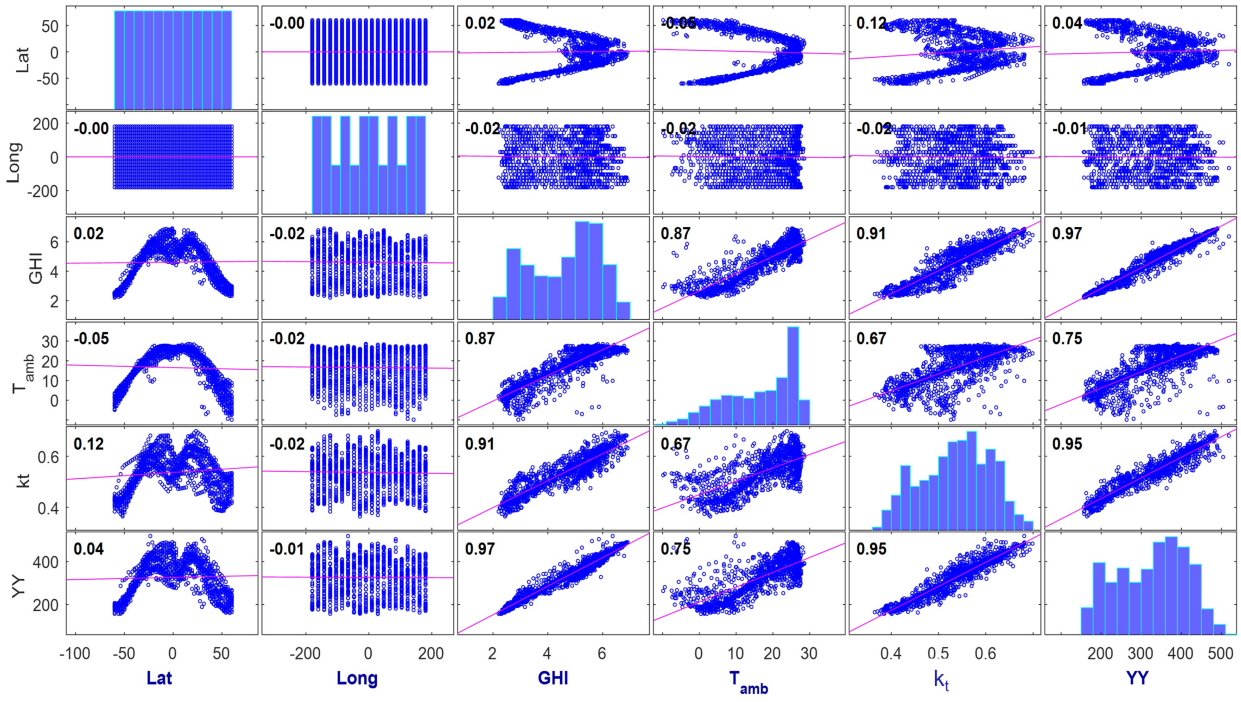

Figure 5.10. The correlation plot shows the individual relationships and the respective R-values of the input (Lat, Long, GHI, T_{amb}, and k_t) and output variables (YY) with each of the other. A functional (non-noisy) correlation between output and input variables improves the accuracy of the trained neural network (NN).

5.3.4 Generalized Yearly Energy Yield Tool

In the previous sections, we have observed the accuracy of the PVML model for YY prediction – functional interpolation and geographical extrapolation – of a specific PV farm design worldwide. The specific farm design meant a single value of physical parameters, viz. elevation, row-spacing, albedo, was used. Now, we will show the exceptional ability of neural networks to predict YY of any farm design around the world. Again, we start with collecting/synthesizing worldwide data for training the NN. As shown in Fig. 5.11, however, this time we include several different values of elevation (0.2, 0.5, 1, and 1.5 m) and albedo (0.2, 0.5, and 0.7) to cover the entire 2D space of practical values used in deployed PV farms. An array of 1000's of data points is simulated and fed to the NN tool for training. The trained model has an R value of 0.999 and MSE = 9.5 as shown in Table II below.

Table 5.2. Results of the trained neural network for a generalized PV system.

	No. of samples/datapoints	MSE	R
Training (70%)	5880	9.548	0.99929
Validation (15%)	1260	9.788	0.99927
Testing (15%)	1260	8.620	0.99936

The trained NN model with 10 neurons in a single hidden layer can accurately predict YY for various farm designs.

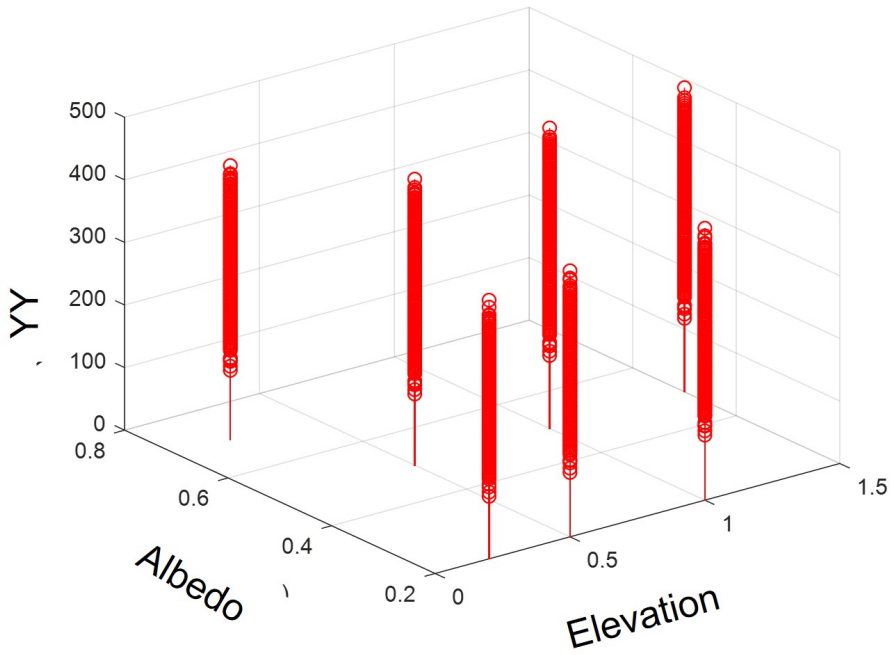

Figure 5.11. Yearly yield is simulated for practical values of albedo and elevation above the ground. This covers the practical 2-D space for prediction of all values of albedo and elevation, in addition to the aforementioned inputs i.e., lat/long, GHI, T_{amb}, and k_t.

This method of employing machine learning for functional interpolation can be further used to find levelized cost of energy (LCOE) and optimum farm designs (optimum tilt angle, optimum row-spacing etc.).

5.4 Conclusion

In this chapter, we demonstrate the methodology and develop a tool to perform a functional interpolation of yearly energy yield and effective levelized cost of energy of any utility-scale solar PV system. The tool requires a coarse grid (1200 locations around the world) of geographical (lat, long), weather (global horizontal irradiance, ambient temperature, and clearness index) data (inputs), and simulated or field-derived energy yield (output). The data is fed into a machine learning tool to train a predictive model. We demonstrate the results of two different tools namely, regression learner tool and neural network tool. The

models trained using the Gaussian Process Regression algorithm in the regression tool and Levenberg-Marquardt algorithm in the NN tool. Both models show high accuracy with $R^2 = 0.99$ and RMSE = 7.03. Once the machine learning model is trained and tested, it can be used to accurately predict the yearly energy yield for any specific location around the world in a matter of seconds.

Employing the trained model, we showed that the percentage error between a simple linear geographical interpolation and NN-based functional interpolation can range from $\sim 20 - 60\%$ for different regions worldwide. Moreover, we found that the critical number of sample points required for a reasonably accurate ($R^2 = 0.99$) prediction is NS=100. Further, we investigated the power of NN-based models to accurately predict YY at an extrapolated geographical location within 10% error margin. Finally, we generalized the NN-model for all types PV farm designs by including various values of physical attributes of a PV farm, for example, elevation, row-spacing, albedo, and bifaciality.

In conclusion, we demonstrated a machine learning based scheme that allows an accurate functional interpolation of simulated and field data for utility-scale solar PV farms. Starting with only **100** actual field data points, the tool can calculate the yearly energy yield of a PV farm deployed at any of the **10000 (or 1 million)** geographical sites globally with very low computational times ($\sim$ seconds). This methodology can be further used to predict several other PV farm-related quantities such as levelized cost of energy, optimum tilt angles, degradation rates, lifetime etc. Depending on the problem statement, however, the machine learning based tools may require higher quantity and good quality of field data for experimental validation. We would encourage the PV community to develop a strategy to acquire, store, and organize the PV farm data in order to perform precise predictions using very few data points.

6. THERMODYNAMIC LIMIT OF SOLAR TO FUEL CONVERSION FOR GENERALIZED PHOTOVOLTAIC-ELECTROCHEMICAL SYSTEM

Daily and seasonal variability of solar irradiation poses a major hurdle to the widespread adoption of photovoltaic systems. An integrated photovoltaic (PV)-electrochemical (EC)-storage system offers a solution, but the thermodynamic efficiency (η_{sys}) of the "ideal" integrated system and the optimum configuration needed to achieve the limit are known only for a few simple cases. Moreover, these limits are often derived through complex numerical simulations. In this chapter, we show that a simple, conceptually-transparent and physically-intuitive analytical formula can precisely describe the η_{sys} of a 'generalized' PV-EC integrated system. An M-cell PV module of N-junction bifacial tandem cells is illuminated under S-suns mounted over ground of albedo R. There are K-EC cells in series, each defined by their reaction potential, exchange current, and Tafel slope. We derive the optimum thermodynamic limit $\eta_{sys}(N, M, K, R, S)$ for all possible combinations of a PV-EC design. For a setup with optimal-(M, K) and large N, under 1-sun illumination and albedo $= 0$, the ultimate limit is $\eta_{sys} \sim 52\%$. A comparison of our results with experimental results published by various groups worldwide suggests opportunities for further progress towards the corresponding thermodynamic limit.

6.1 Introduction

Solar energy is an important source of clean, and renewable energy. There has been extensive investment, research and development in this field with the objective of maximizing efficiency and output power from solar cells (device-level)[153] to solar farms (system-level). Regardless of the aforementioned efforts, there exists a fundamental issue with solar energy: Earth's rotation around the sun leads to spatial (latitude), seasonal, and diurnal variation in sunlight intensity. Storing solar energy in other forms of energy (e.g. chemical, mechanical,

↑**Note:** The material in this chapter has been adapted from Ref. [152].

gravitational) provides a solution to this challenge. For electrochemical (EC) energy storage, a variety of approaches have been proposed, including batteries, organic and/or inorganic reactions, artificial photosynthesis [54], etc. In this chapter, we report the thermodynamic performance limit of PV-to-EC energy conversion through an illustrative example of splitting of water into hydrogen and oxygen.

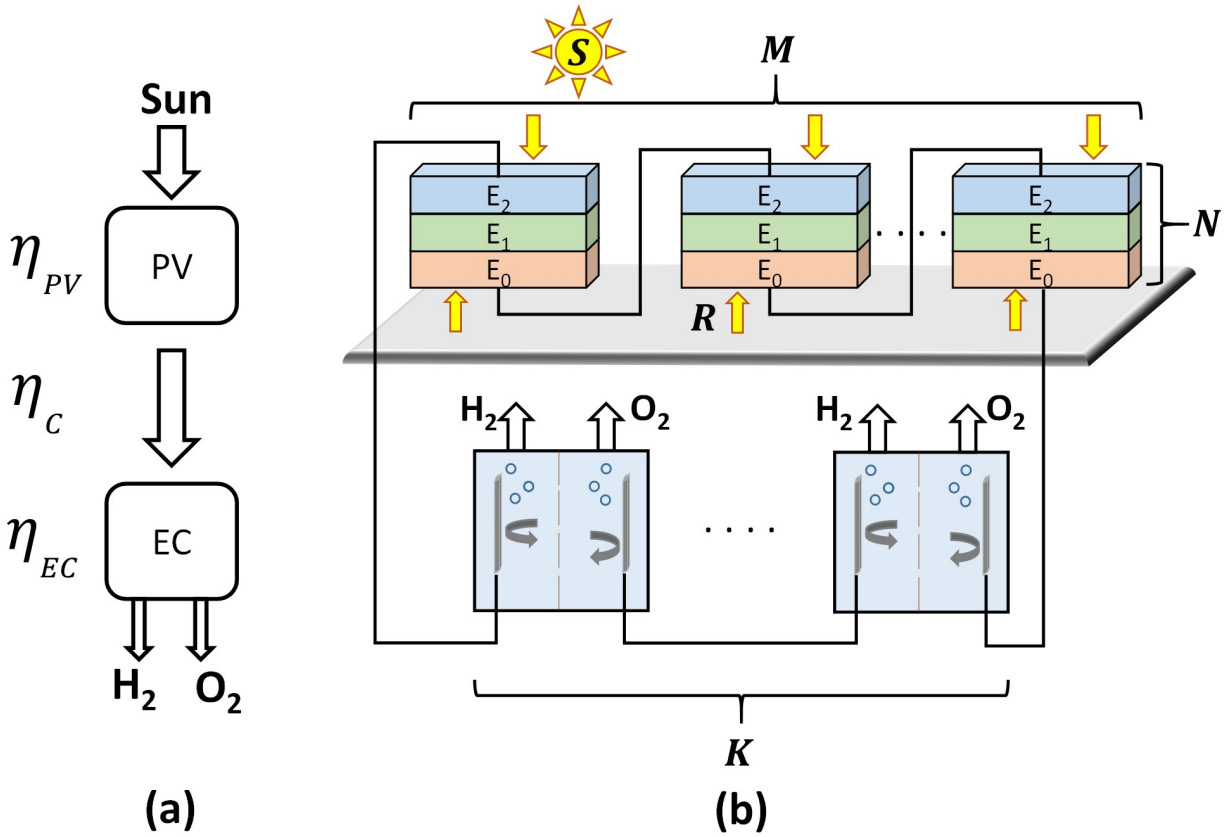

Figure 6.1. (a) Energy flow diagram of a general PV-EC system (b) Schematic of the integrated system photovoltaic cell (module of tandem solar cells) - electrochemical cell.

A review of the literature [54], [56]–[58], [154]–[162] shows that various papers on water-splitting generally consider a subset of the thermodynamically – relevant fundamental PV-EC parameters. Others derive the efficiency limit (η_{sys}) by using detailed numerical simulations including a combination of fundamental and practical parameters [162], [163]. These contributions are critically important but reliance on numerical modeling often makes it difficult to gauge how η_{sys} depends explicitly on the key physical variables. In this regard,

here we develop an analytical model that describes the optimum combination of parameters required to maximize efficiency of the generalized PV-EC integrated system in an intuitively transparent form, compares the results from different configurations explored by various groups, and suggests opportunities for significant improvement by using newly developed bifacial tandem cells.

A generalized configuration for such PV-to-EC conversion (relevant for research efforts worldwide) is shown in Fig. 6.1. This system is characterized by five PV and four EC variables. The PV variables are: the intensity of sunlight (S), the fraction of incident light reflected from the ground (albedo, R), number of series-connected cells in the PV module (M), number of subcells in a multi-junction (Tandem) solar cell (N) and the set of bandgaps of the solar cell ($[E_g]$)). The EC parameters are: the number of series-connected electrochemical cells (K), the thermodynamic potential of the reaction (μ_{th}), effective exchange current density ($J_{0,ec}$) and effective Tafel slope (β).

This set of 9 variables is sufficient to calculate the thermodynamic upper limit of an 'idealized' PV-EC system, with the same level of rigor and relevance as the Shockley-Queisser (SQ) analysis for a stand-alone PV system [55]. Similar to the SQ limit, we realize that practical considerations, such as series and shunt resistances [56]–[58], diode non-ideality factor, self-heating in both PV and EC, spectral difference, and non-ideal Tafel slope, may in practice make it impossible to reach the PV-EC limit derived here. Nonetheless, the PV-EC thermodynamic limit provides physical insights and scope of improvement for modeling experts and experimentalists alike.

Note that PV-EC systems may be configured in different ways [56], [155], [161]. Fig. 6.1 describes an approach called a PV-Electrolyzer design that comprises of two independent subsystems, namely photovoltaic (PV) cell and electrochemical (EC) cell, see Fig. 6.1(a). The photovoltaic part converts solar energy into electrical energy, which is supplied to the electrochemical cell that further converts this electrical energy into chemical energy in the form of fuels. This design, with physically independent subsystems, is more stable and reliable with respect to material degradation as opposed to the PEC designs where the PV parts are in physical contact with the electrolyte in the electrochemical cell [155], [161]. The fuels generated from cathode and anode are then stored in containers or passed onto another

electrochemical system to produce other chemicals (e.g. hydrocarbons). We assume that PV is directly connected to EC, to avoid losses associated with power electronics based couplers. Thus, the overall efficiency (η_{sys}) is a product of PV efficiency (η_{pv}), EC efficiency (η_{ec}) and coupling efficiency (η_c), see Fig. 6.1(a). We will now calculate the individual efficiencies so as to maximize η_{sys}.

6.2 I-V CHARACTERISTICS AND EFFICIENCIES OF PV AND EC SYSTEMS

6.2.1 I-V Characteristics of an EC System

The generalized electrochemical system comprises of 'K' electrochemical cells connected in series. A single cell consists of two electrodes (called anode (A) and cathode (C)), a solution (electrolyte) and a salt-bridge (permeable membrane). The current-voltage (I-V) characteristics of the oxidation and reduction (redox) reactions occurring at the electrodes is described by Butler-Volmer equations [164] based on standard cell potential (μ_{th}), exchange current density (J_0) and Tafel slope (β) [58]. An EC cell can be described by a single-diode characterized by an effective threshold voltage ($\mu_{th} \equiv |\mu_C| + |\mu_A|$), effective exchange current density ($J_{0,ec}$) and effective Tafel slope ($\beta \equiv \beta_C + \beta_A$), as shown in the equivalent circuit analysis below.

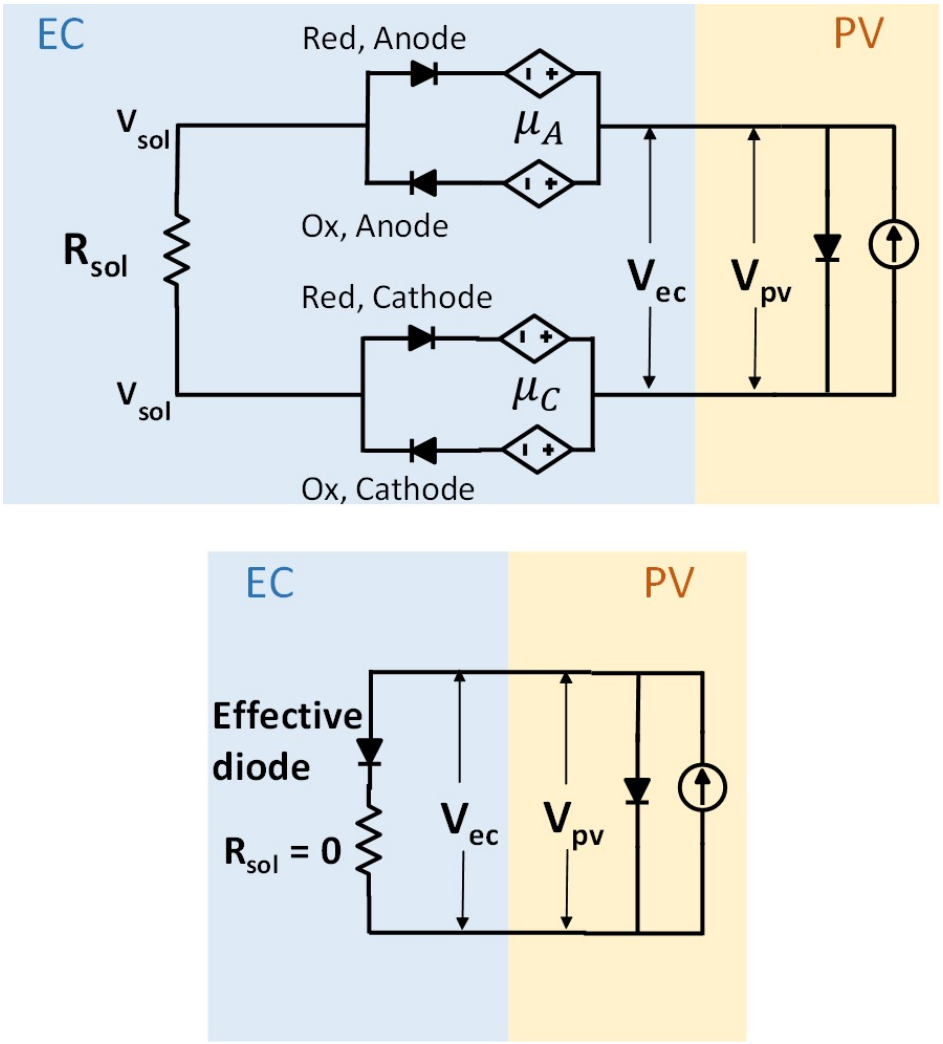

Figure 6.2. (Top) Electrical equivalent circuit for EC-PV subsystems connected in series (Back-to-back-diode model). (Bottom) The redox reaction of the complex electro-chemical system can be presented by a diode equivalent circuit.

Based on the Butler-Volmer formulation, the reactions taking place at the two electrodes (cathode and anode) of an electrochemical cell can be represented by Eq. 6.1 and Eq. 6.2 respectively [165]–[167]. Assuming the electrodes have equal areas, the series current density passing through them is given by J_{ec}. The reduction reaction dominates at cathode while oxidation reaction dominates at anode, leading to evolution of chemicals (fuels) associated

to that particular electrochemical cell. For example, in a water-splitting reaction, hydrogen evolution occurs at cathode and oxygen evolution occurs at anode [168].

$$J_{ec} = J_{ox,A} - J_{red,A} = J_{0,A}\left[\exp\left(\frac{V_{pv} - V_{sol} - \mu_A}{\beta red, A}\right) - \exp\left(\frac{V_{pv} - V_{sol} - \mu_A}{\beta ox, A}\right)\right] \tag{6.1}$$

$$J_{ec} = J_{red,C} - J_{ox,A} = J_{0,C}\left[\exp\left(\frac{V_{sol} - \mu_C}{\beta red, C}\right) - \exp\left(\frac{V_{sol} - \mu_C}{\beta ox, C}\right)\right] \tag{6.2}$$

where $J_{0,A}$ and $J_{0,C}$ are exchange current densities at anode and cathode, respectively, $\eta_A = V_{pv} - V_{sol} - \mu_A$ and $\eta_C = V_{sol} + \mu_C$ are the overpotentials, and β is the Tafel slope of respective reactions at anode and cathode. The J-V relation of a diode is given by the following:

$$J = J_0\left[\exp\left(\frac{qV}{nkT}\right) - 1\right] \tag{6.3}$$

Hence, each exponential term in Eq. 6.1 and Eq. 6.2 can be represented as a "diode" with μ_A and μ_C as respective built-in potentials. Therefore, each electrode can be represented by a pair of back-to-back diodes as depicted in the form of an electrical circuit in Fig. 6.2(Top). This EC circuit is connected in series with a PV cell circuit, represented on the right by a current source and a diode. Note that, while estimating the thermodynamic limit, the shunt and series resistances need not be considered [92].

When a reaction proceeds, one of the two back-to-back diodes at an electrode begins dominating its companion, because the first diode is forward biased, while the companion is reverse biased. In this situation, we can neglect the reverse-biased diode, because it draws negligible current as compared to the forward-biased diode. Now, we are left with two diodes, one for each electrode. The parameters for these electrodes are marked by subscript A (or C), as shown in Eq. 6.4. The voltage across the EC system is given by the sum of voltage drops across the diode, as shown in the following equation:

$$V_{ec} = \mu_{th} + \beta_C \ln\left(\frac{J_{ec}}{J_{0,C}}\right) + \beta_A \ln\left(\frac{J_{ec}}{J_{0,A}}\right) + J_{ec}R_{sol} \tag{6.4}$$

where R_{sol} is the solution resistance. Assuming an idealized case of $R_{sol} = 0$, $\mu_{th} = |\mu_C| + |\mu_A|$, and $\beta \equiv \beta_C + \beta_A$, we can rewrite Eq. 6.4 in the following form:

$$J = J_{0,ec} \exp\left(\frac{V_{cell}}{\beta}\right) = J_{0,ec} \exp\left(\frac{V_{ec}}{K\beta}\right) \tag{6.5}$$

where the voltages across one cell (V_{cell}) and across a system of K cells (V_{ec}) are related by $V_{cell} = V_{ec}/K$. Moreover, the effective exchange current density of the EC is given by the following:

$$J_{0,ec} = J_{0,C}^{\frac{\beta_C}{\beta}} J_{0,A}^{\frac{\beta_A}{\beta}} \exp\left(\frac{-\mu_{th}}{\beta}\right) \tag{6.6}$$

The effective exchange current density can be perceived as the weighted average of the exchange current densities of individual electrodes. Note that Eq. 6.4 is valid for $V_{ec} > \mu_{th}$. In the final circuit, the EC cell is represented as an effective single diode, as shown in Fig. 6.2(Bottom). Now, to calculate the ideal PV-EC efficiency, we assume that: (1) Tafel slopes are independent of the current, (2) the system is maintained at ambient temperature, and (3) the resistance of the solution/electrolyte is negligible (i.e., $R_{sol} \to 0$).With these assumptions, we obtain the J-V relationship for the EC cell given by Eq. 6.5. An illustrative I-V characteristics for $K = 1$ system for electrolysis of water is shown in Fig. 6.3.

6.2.2 I-V Characteristics of a PV System

The general PV module is constructed from M number of series-connected cells. Each cell may have a single junction (SJ) or multi-junction (MJ) with N subcells. The module can be bifacial (with albedo, R) or it can be illuminated by a solar concentrator (S). As shown in [92], the J-V relationship of such a tandem-module can still be described by a superposition of dark and photo-current, i.e.,

$$J_M(V_M, S, R) = -J_{SC}(S, R) + J_{0,MJ} \exp\left(\frac{qV_M}{MNk_BT_D}\right) \tag{6.7}$$

where q is electronic charge, k_B is Boltzmann constant, T_D is the device temperature, J_{sc} is the photocurrent that is a function of S and R, and $J_{0,MJ}(\equiv q\,\Omega_D\,\gamma\,exp(-E_{g,av}/k_BT))$ is

the "reverse saturation current" of a tandem cell. Here, Ω_D is the geometric mean of emission angle of each subcell, $\gamma(E_g, T)$ is a factor that accounts for photon recycling within the subcells [92], and $E_{g,av}$ is the arithmetic mean of the bandgaps of subcells ($E_{g,i}$) that maximizes the power output of the tandem cell. Equation Eq. 6.7 also describes the performance of a bifacial cell with front-side intensity, S, and an albedo, R, defined by the fraction of light reflected off ground and incident on the back surface of the cell. For reference, the bandgap sequence is given by

$$E_{g,i} = \frac{i}{\alpha N} - \frac{(N-i)\left[\alpha(1+R)E_0 - R\right]}{\alpha N} \tag{6.8}$$

where $i = 1, 2, \ldots N-1$ is the subcell index, $\alpha = 0.428\ eV^{-1}$ and E_0 is the lowest bandgap of the tandem cell. It is clear from Eq. 6.8 that the set of bandgaps can be uniquely described by the parameters N, R and E_0. Note that the traditional tandem-cell requirement that the lowest bandgap (E_0) subcell resides at the bottom of the tandem stack is dictated by the relationship $N \leq (1 + R^{-1})$ [92]. Even for relatively high albedo of $R = 0.5 \implies N \leq 3$. For most electrochemical reactions $\mu_{th} \leq 2\ V$ and thus $N \leq 3$ suffices for an optimized system.

Being consistent with the traditional PV thermodynamic-limit calculation, the derivation above presumes shunt/series resistances are absent, and self-heating is negligible. Substituting $N = 1$ in Eq. 6.7 gives us the $J - V$ relationship of a photovoltaic module comprising of series-connected single-junction solar cells. Further, substituting $N = 1$ and $M = 1$ yields the standard $J - V$ characteristics of a single-junction solar cell, as shown in Fig. 6.3.

6.2.3 Optimum PV-EC System

For a given PV – EC system, we can now find an operating point (V_{op}, J_{op}) by solving for $I_{ec} = I_{pv} \implies A_{ec}J_{ec}(V_{op}) = A_{pv}J_M(V_{op})$, as shown in Fig. 6.3. Note that the ratio of cell areas ($AF = A_{pv}/A_{ec}$) is another system parameter that will appear in the discussions later. While analyzing the system, a coupling loss described by the difference in maximum power of PV and the operating power should be taken into consideration as well.

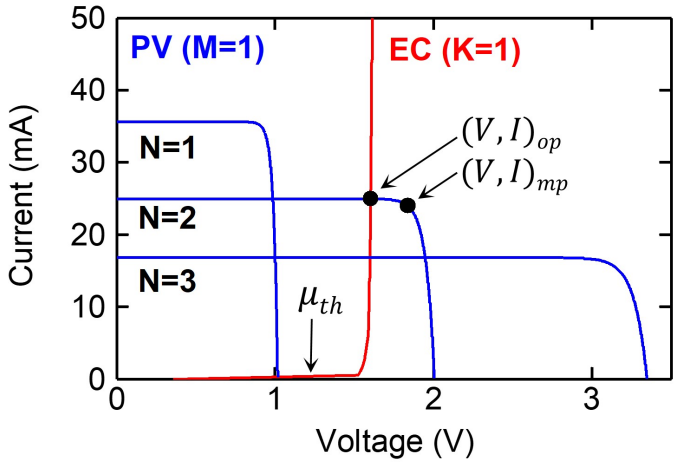

Figure 6.3. I-V characteristics of PV (M=1,N=1,2,3) and EC (K=1). The operating point is different from the maximum power point of PV.

Intuitively, when the EC is operated at the MP of the PV (i.e., $(V,J)_{op} = (V,J)_{mp}$), the coupling is 100%, and the system is optimized. Therefore, for the global design and optimization of the PV-EC system, we will choose $(V,J)_{op} = (V,J)_{mp}$ constraint so that $\eta_c = 1$. Since current remains almost constant (see Fig. 6.3) for $V \leqslant V_{mp}$, therefore, we assume that $J_{mp} \sim J_{sc}$. This allows us to use the analytical form of J_{sc} as given by the following equation [92].

$$J_{op} = J_{sc,N} = J_{sc,top} = S\, J_{sun}(1 - \alpha E_{g,top}) \tag{6.9}$$

where $J_{sun} = 83.75$ mA/cm^2 and $\alpha = 0.428$ eV^{-1} are constants. Further, the MP voltage can be analytically expressed as follows [56]:

$$V_{mp} = \left(\frac{MN}{q}\right)\left[E_{g,av}\left(1 - \left(\frac{T_D}{T_S}\right)\left(\frac{E_{g,top}}{E_{g,av}}\right)\right) - k_B T_D\, ln\left(\frac{\Omega_D}{S\Omega_S}\right)\right] \tag{6.10}$$

$$E_{g,av} = \frac{E_0}{N} + \frac{(N-1)\left[\alpha(1+R)E_0 - R + 1\right]}{2\alpha N} \tag{6.11}$$

$$E_{g,top} = \frac{N-1}{\alpha N} + \frac{\alpha(1+R)E_0 - R}{\alpha N} \tag{6.12}$$

where q is the electronic charge, T_D is the device temperature, T_S is the temperature of the sun, Ω_D is the emission angle of the device and Ω_S is the angle subtended by sun on the device. Eq. 6.8 allows us to calculate the remaining two parameters: $E_{g,av}$ (the arithmetic mean of the bandgaps, Eq. 6.11) and $E_{g,top}$ (the bandgap of the topmost subcell, Eq. 6.12).

Using Eq. 6.5 for the K electrochemical cells in series, the voltage at point of operation is given by Eq. 6.13:

$$V_{op} = V_{mp} = V_{ec} = K\beta \ln\left(\frac{J_{ec}}{J_{0,ec}}\right) \tag{6.13}$$

Next, we substitute V_{mp} from Eq. 6.10 and $J_{sc,N}$ from Eq. 6.9 into Eq. 6.13 to arrive at the key equation of this chapter:

$$K\beta \ln\left[\left(\frac{SJ_{sun}(1-\alpha E_{g,top})}{J_{0,ec}}\right)AF\right] = \left(\frac{MN}{q}\right)\left[E_{g,av}\left(1-\left(\frac{T_D}{T_S}\right)\left(\frac{E_{g,top}}{E_{g,av}}\right)\right) - k_B T_D \, ln\left(\frac{\Omega_D}{S\Omega_S}\right)\right] \tag{6.14}$$

As mentioned earlier, $AF = A_{pv}/A_{ec}$. Eq. 6.14 determines the optimum parameters (M, N, E_0) for a given EC system $(K, \mu_{th}, J_{0,ec}, \beta)$ and particular values of S and R. Note that $E_{g,top}$ and $E_{g,av}$ are functions of E_0, the smallest bandgap of the tandem cell. Therefore, for a given value of (M, N, S, R) for the PV and given EC system, one can solve for E_0 from Eq. 6.14 for an optimal design. As we will show later, for a given EC system, a global maximum system efficiency requires: (i) co-optimization of (N, E_0) at given PV module with (M, S, R), or (ii) co-optimization of (M, E_0) for given tandem (N, S, R).

Since we find the point of operation, i.e., the intersection of I-V characteristics of PV and EC for maximum power output, Eq. 6.14 provides the optimum parameters for system design. These parameters can be substituted in the following definition of normalized output (or overall system efficiency) [92], [169], to achieve the thermodynamic limit:

$$\eta_{sys} \equiv \eta_{pv}\eta_c\eta_{ec} = \frac{V_{mp}I_{mp}}{SP_{sun}(MA_{pv})} \times \frac{V_{op}I_{op}}{V_{mp}I_{mp}} \times \frac{K\mu_{th}I_{op}}{V_{op}I_{op}} = \frac{K\mu_{th}I_{op}I_{op}}{M\,S\,P_{sun}A_{pv}} = \frac{K\mu_{th}J_{op}^{PV}}{M\,S\,P_{sun}} \tag{6.15}$$

Here, P_{sun} is the solar intensity reaching the PV system ($\sim 1\,kW/m^2$ for $AM1.5G$) and $(V,I)_{mp}$ is the maximum power point of the PV module. The power required to initiate the electrochemical process at the thermodynamic equilibrium potential μ_{th} is $\mu_{th}I_{op}$. The factor K accounts for the number of ECs in series. The losses in PV and EC are taken into account with their respective definitions of efficiency [55], [58], [170]. The coupling loss is included using the coupling efficiency, defined as the ratio of operating power over the maximum power that can be generated by the PV cell.

It is important to note that maximizing η_{sys} may not necessarily mean an optimum PV and EC components. However, since the efficiency of the PV subsystem drops precipitously beyond the maximum power point, the PV subsystem must operate close to the efficiency of the stand-alone system. Therefore, optimized EC subsystem efficiency can be easily estimated by the ratio: $\eta_{ec} \sim \eta_{sys}/\eta_{pv}$. We conclude this section by highlighting two important assumptions regarding η_{ec}. First, we use equilibrium potential (lower heating value) of the reaction and not the thermoneutral potential (higher heating value) because equilibrium potential gives an upper bound to theoretical system efficiency. Further, we assume a Faradaic efficiency of 100%, which is seldom achieved in practice.

6.3 Results and Discussions

6.3.1 System Setup and Basic Operation

As described in Sec. 6.2, the PV system can be configured as a module consisting of series-connected single junction or multi-junction (tandem) cells. For an illustrative example, we take a water-splitting cell as the electrochemical system (load). The parameters that define a water-splitting experiment are $\mu_{th} = 1.23\ V$, $J_{0,ec} = 4.06 \times 10^{-36}\,\mathrm{mA/cm^2}$ and $\beta = 70\,\mathrm{mV/decade}$ [58].

For an intuitive understanding of the numerical optimization process, consider a single-MJ cell ($M = 1, N = 1, 2, 3$) in a PV system optimized for maximum efficiency (i.e., PV-optimized), as shown in Fig. 6.3. We find that the double-junction PV ($N = 2, M = 1$) provides the best coupling to the water-splitting EC ($K = 1$) and the highest system efficiency. This is because the point of operation $(V,I)_{op}$ is closest to $(V,I)_{mp}$. Fig. 6.3 shows that current

is negligible at the point of intersection of the I-V of a single junction cell ($N = 1, M = 1$) and the EC. For a triple junction ($N = 3, M = 1$) tandem cell, the overall efficiency is also lower than that of double junction cell due to poorer coupling efficiency (current matching). On the other hand, ($N = 1, M = 2$) delivers the highest system efficiency as compared to ($N = 1, M = 1 \text{ or } 3$), as shown in Appendix Fig. 6.10. This analysis implies that the optimum system efficiency depends on the number of subcells (N) in the tandem PV as well as the number of series-connected cells (M) in the module.

6.3.2 PV-EC System Limit: Comparison with Literature

To illustrate the power of Eq. 6.14 in defining the thermodynamic limits of a variety of systems, Fig. 6.4 compares the experiments presented in the literature [156], [158]–[160] with the thermodynamically limited efficiencies.

The thermodynamic limits are calculated numerically (exact solution), and then analytically using Eq. 6.15 for the specific PV (i.e., $[E_g], S, R, M, N$) and EC setup used in the respective references. (See appendix Fig. 6.8 for cross-validation between analytical and numerical results.) There are several highlights: The analytical results (up-triangle) are in almost perfect agreement with numerical solution (open circles), demonstrating the validity of the results.

The considerable gap between thermodynamic limit and efficiency achieved in the laboratories shows that there is room for considerable improvement and opportunity to quantify and reduce losses in practical systems. One of the reasons for the gap between global maximum and laboratory results is that the experimental groups often use the cells that are readily available, but the bandgaps may not be optimum. We can calculate the global maximum efficiency for the same (M, N, K, S, R) but with an optimum set of bandgaps, shown by green symbols in Fig. 6.4, using Eqs. 6.14 and 6.15. The optimization proceeds as follows. For a given combination of (M, N), the maximum system efficiency varies with R. In fact, this efficiency is attained for an optimum bandgap of the lowest bandgap subcell (E_0), which determines the set of bandgaps of the multi-junction cell. A similar analysis was performed,

numerically, by Shu Hu et al. [168] for tandem photoelectrochemical systems (which is different from the PV-Electrolyzer design considered here).

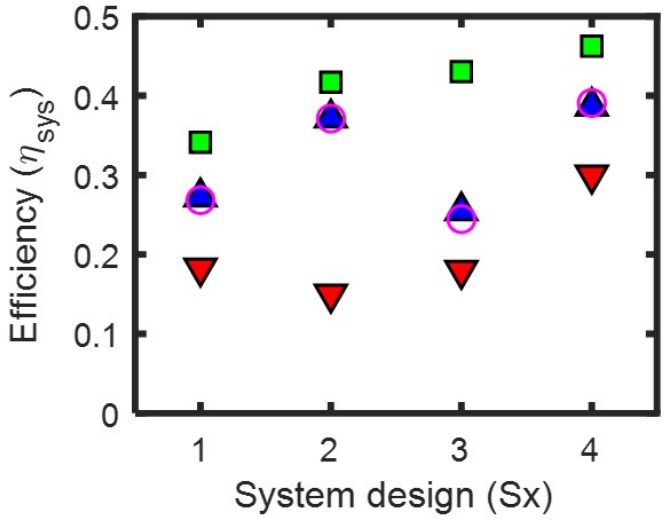

Format: Sx: (S,R,M,N,K,AF)[Ref.]	
S1: (1.35,0,1,2, 1,1) [158]	S3: (500,0,1,2,1, 0.19/30) [156]
S2: (10,0,2,3,3,1/4) [159]	S4: (42,0,1,3,2,0.316/6.25) [160]

Figure 6.4. Comparison of reported solar to hydrogen efficiencies with the thermodynamic limit calculated analytically and numerically. Global maximum gives the best efficiency for that particular system with an optimum set of bandgaps.

6.3.3 PV-EC System Limit: K=1 Case

For best system efficiency, E_0 varies with R. This is evident from Fig. 6.5(a) and Fig. 6.10(b), which have (1,2) and (2,1) as their respective combinations of (M, N). The contour plot in Fig. 6.5(a) distinctly shows the effect of increasing albedo (R) on overall efficiency. From Fig. 6.5(b), we also realize that η_{sys} for a tandem PV increases from 33% ($R = 0$) to $\sim 50\%$ ($R = 1$) (50% increase). Similar improvements are also expected for other combinations of M, N, R.

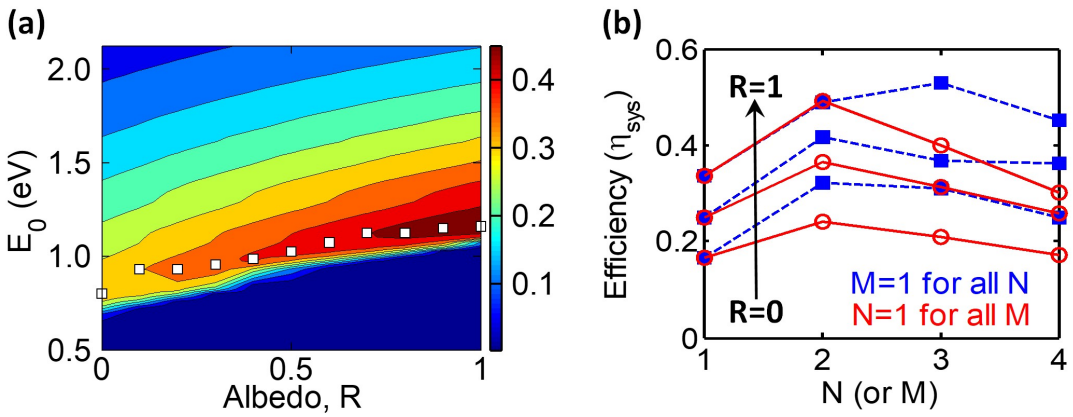

Figure 6.5. (a) System efficiency as a function of E_0 and R for $N = 2, M = 1, K = 1$ – indicating an optimum in E_0. (b) System efficiency increases with higher albedo and varies with N (or M). Of course, each point in this plot has a corresponding optimum E_0.

6.3.4 PV-EC System Limit: General Case

If we revisit Eq. 6.14, we observe that, for N-junction tandem, we cannot independently set both M and K for an optimized design. In fact, (M/K)-ratio would be another optimization parameter for maximizing η_{sys}.

In most practical cases, for example on rooftops or solar farms, single junction solar cells are used. Therefore, let us first study the optimum combination of (M, K) for a module of SJ ($N = 1$) solar cells connected to a K- cell electrochemical system. For any SJ cell with bandgap E_g, and known EC, one can readily calculate (M/K) for optimum design using Eq. 6.14. The corresponding η_{sys} is found from Eq. 6.15. The optimum η_{sys} and the corresponding (M/K) are shown as a function of E_g in Fig. 6.6. For a water-splitting EC system, $\eta_{max} \sim 26.46\%$ for $M/K \sim 1.67 \sim 8/5$, implying that an optimum combination of 8 SJ cells in series with 5 EC cells will yield the best overall-system efficiency. Further, this efficiency is achieved at $E_g = 1.33\ eV$, that in fact is the optimum SJ PV bandgap. This is a significant new result that can be explained as follows.

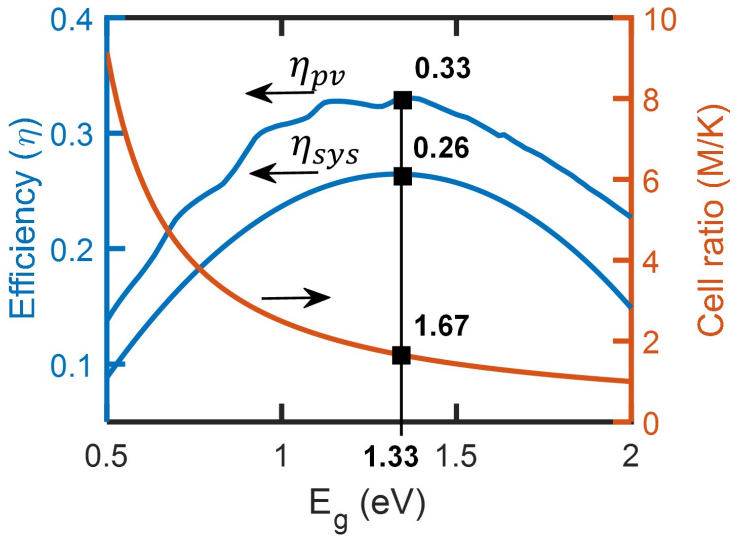

Figure 6.6. Variation of efficiency (η) and cell ratio (M/K) with E_g (bandgap of single junction cell). Notice that maximum η_{sys} occurs at 1.33 eV, which is also the optimum bandgap of best η_{pv} achievable (where $\eta_{ec} \sim 0.8$).

Due to logarithmic change in V_{op} with current (see Eq. 6.13), the EC efficiency η_{ec} does not change significantly as long as the change in current is relatively small (i.e., S is essentially a constant). Now, with η_c=1, we find that the system efficiency (η_{sys}) is maximized when η_{pv} is asymptotically close to its maximum [90], [167]. The difference in η_{pv} and η_{sys} arise due to kinetic losses in EC, which are incorporated in η_{ec}. Therefore, choosing an (M/K)-ratio so as to couple optimum-PV to the EC will indeed give the optimum system design. While we have explained the result in the context of SJ-PV and EC coupling, this analysis also holds true for tandem-PV and EC coupling, see below.

Fig. 6.7 shows optimum η_{pv} and overall optimized η_{sys} for N-junction tandems. The corresponding optimum (M/K)-ratio calculated from Eq. 6.14 is also shown in the same plot. The V_{mp} of the optimum tandem increases with N, which is compensated by decreasing (M/K)-ratio to ensure perfect coupling between the PV module and the EC cells. The system efficiency η_{sys} increases from 26.46% to 34.82% for $N = 1$ to 2, and starts to saturate for $N > 4$. We predict the ultimate limit of $\eta_{sys} \to 52.09\%$ as $N \to \infty$ under 1-sun with no albedo ($S = 1, R = 0$).

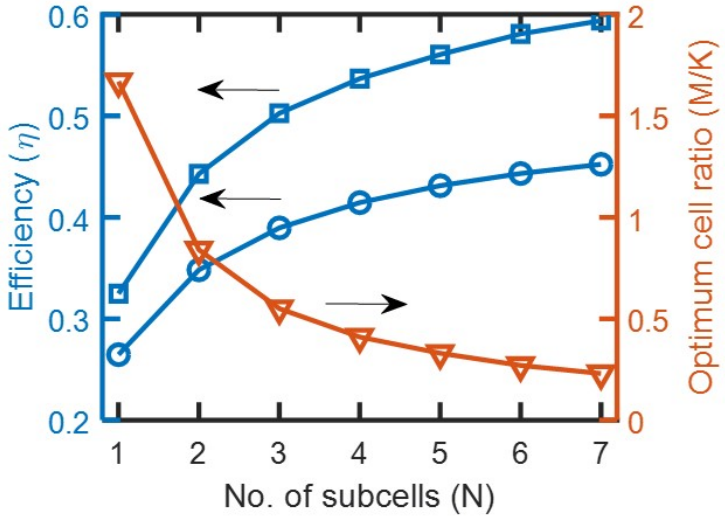

Figure 6.7. Variation of efficiency (η_{pv}, η_{sys}) and optimum cell ratio (M/K) with number of subcells (N) in a multi-junction cell. For every N, the corresponding optimum cell ratio gives the thermodynamic limit of system efficiency.

Although this chapter focuses on the theoretical (thermodynamic) efficiency limit of a PV-EC system, it is important to note that a practical system will seldom reach this efficiency limit because of the variation of intensity and spectral content of solar illumination throughout the day and over the seasons. Indeed, a practical system may optimize for slightly different combination of PV-EC parameters. One may even consider adding additional components, such as maximum power point trackers and DC-DC converters, to recover a fraction of energy lost due to "non-ideal" illumination. The advantage must be balanced against concerns regarding efficiency, reliability and cost of these new components. Therefore, system optimization for stand-alone and grid-integrated system under practical weather and illumination conditions will an important topic of future research.

6.4 Summary and Conclusions

To summarize, we have developed an analytical theory to find the thermodynamic limit of solar to fuel conversion. Given (S, R) and an EC $(K, \mu_{th}, J_{0,ec}, \beta)$, system efficiency is an implicit function of number of EC cells (K), number of subcells (N), number of module cells (M), albedo (R) and bandgap (E_0) i.e., $\eta_{sys} = f(S, R, N, M, K, E_0, AF)$. Therefore,

an optimum combination of (M, N, E_0) provides the thermodynamically limited maximum efficiency that is evident from Fig. 6.5. The analytical formulation mentioned above provides a convenient way to find this limit and the associated parameters viz. $(M/K, N, E_0)$ and provides insights into the system with respect to recent developments in using bifaciality (R) and concentrated light (S).

The difference between the global maximum and experimental values in Fig. 6.4 should encourage refinement and optimization of the PV-EC design. We have considered an idealized system i.e., $R_{sol} = 0$, and it is evident that overall optimized systems, with optimum M, N, E_0 and K can achieve much higher efficiencies compared to the laboratory results reported in the literature [171]. The analytical model developed in this work can be easily used to integrate other kinds of loads [54] to the PV system. This work can also be extended to include hourly variations in solar illumination to find daily storage capabilities and location-based optimal design.

6.5 Appendix

6.5.1 Comparing analytical and simulation results

System operating point (I_{op}, V_{op}) can be exactly determined by numerically finding the point of intersection of the $I - V$ curves of PV and EC. Substituting the values of current in Eq. 6.15 of the main text can be used to calculate the efficiency. On the other hand, the analytical Eq. 6.14 in the main text provides the optimum parameters of the system that can be used to find the current and hence the efficiency using Eq. 6.15.

Fig. 6.8 demonstrates that the analytical results for $M = 2, 3$ (and $N = 1, K = 1$), respectively, compare well with the numerical simulation results. The analytical results hold true for $\mu_{th} < V < V_{mp}$ and hence, E_0 should be large enough so that voltage across the PV can overcome the threshold voltage of EC.

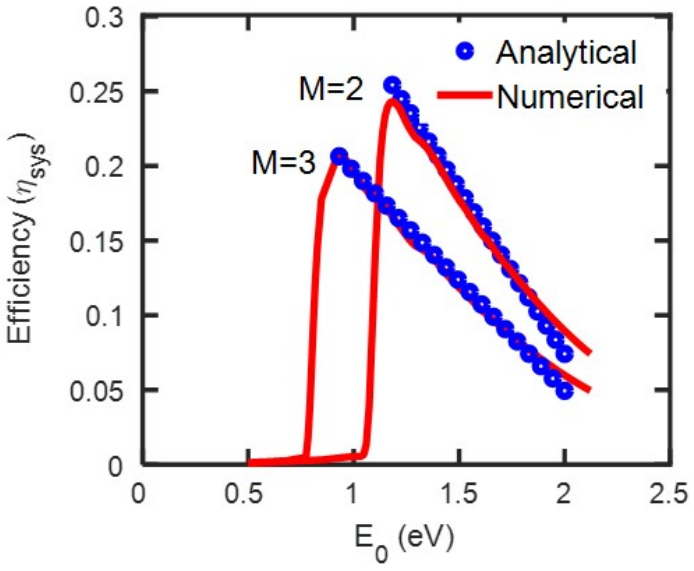

Figure 6.8. Analytical vs. numerical results for $M = 2, 3; N = 1$ and $K = 1$.

As the number of SJ solar cells increase the module voltage is simply an addition of single cell voltages, implying that voltage required from a single cell decreases, which further implies requirement of a lower value of bandgap for each cell. Fig. 6.9 depicts how optimum E_0 decreases with increase in the number of cells in the module.

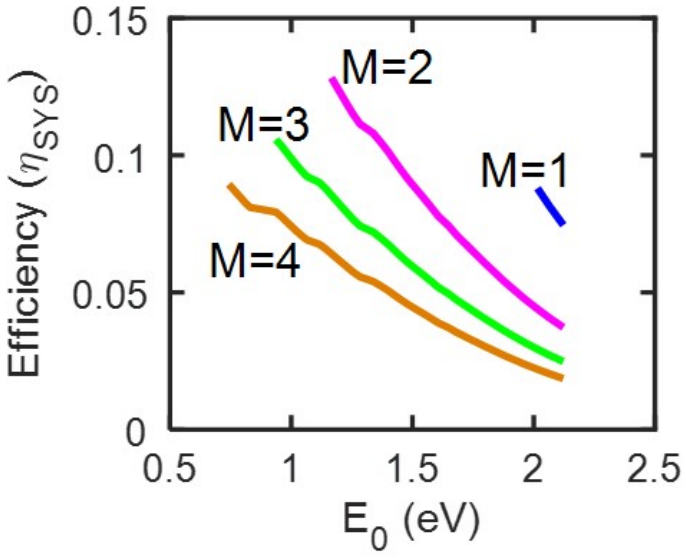

Figure 6.9. For SJ module PV, the energy bandgap required for efficiently powering the EC ($K = 1$), decreases with increasing number of subcells.

As an alternative example for the PV-EC system limit: $K = 1$ case, Fig. 6.10 shows results for a PV system that has modules (1, 2 and 3) of single junction solar cells. Fig. 6.10(a) displays the optimization in M while the contour plot in Fig. 6.10(b) reaffirms the effect of increasing albedo (R) on overall efficiency.

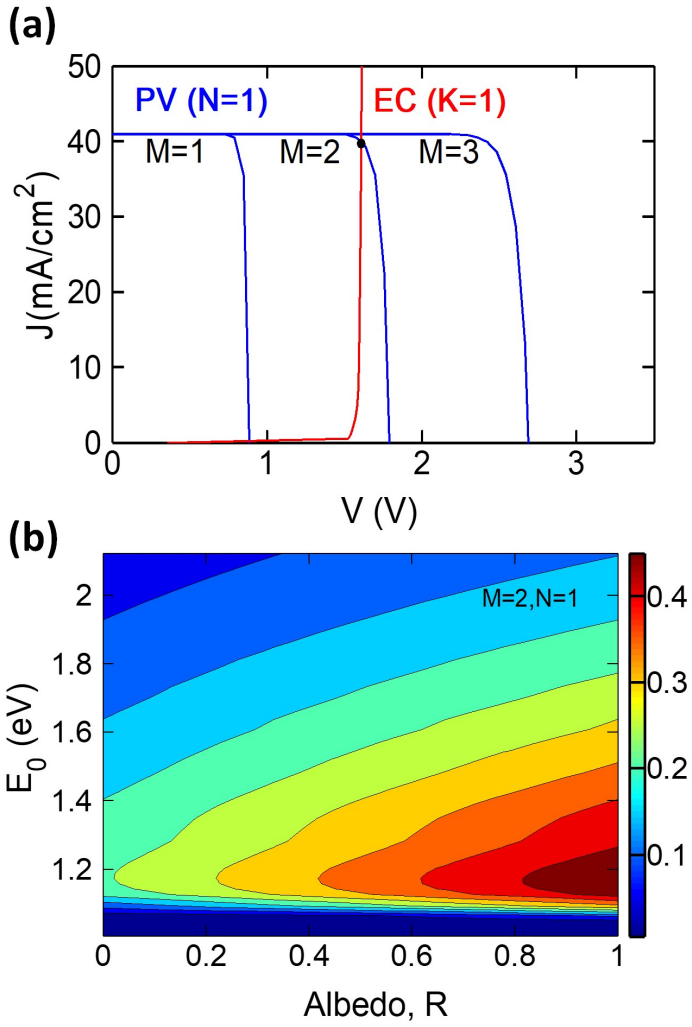

Figure 6.10. (a) I-V characteristics of SJ module PV ($N = 1, M = 1, 2, 3$) and EC ($K = 1$) show that there is an optimum value of M required for best coupling and highest system efficiency. (b) For $M = 2, N = 1, K = 1$ system efficiency is plotted for for various values of E_0 and R.

7. CONCLUSIONS AND FUTURE WORK

To conclude this thesis, in this chapter we sequentially summarize each of the topics discussed in the previous chapters. Next, we describe some future ideas and new challenges that can be extended from our thesis. Finally, we present our closing remarks of the thesis.

7.1 Summary of Chapter 2: LCOE* and fixed-tilt bifacial solar farms

We parametrically explored the economic viability of ground-mounted tilted bifacial solar farms and explained how the farm topology must be optimized for a given location, and module and land cost considerations. We have redefined the levelized cost of energy (LCOE) in terms of 'essential levelized cost of energy' (LCOE*) that is ultimately a function of module to land cost ratio (M_L) and array tilt angle (β). The redefined LCOE* decouples cost analysis from energy yield modeling, thereby dramatically simplifying the optimization of solar farms based on new technologies. Our model provides an optimistic lower bound for LCOE (for ground-mounted cells with a fixed albedo). In practice, various non-idealities (e.g. efficiency degradation with temperature, power mismatch among the strings due to spatially and spectrally varying albedo, etc.) will increase the LCOE. Therefore, our idealized lower-bound LCOE is a necessary (but not sufficient) precondition for the economic viability of the bifacial technology.

Using a previously developed global irradiance model [61], we calculated the spatial distribution of light on the ground and panel faces while considering all variations of shadows for all the locations in the world. The collection of direct, diffuse, and albedo light on the panels were then integrated over time to obtain the yearly yield for the specific solar farm configuration (defined by panel tilt and array period). Once we correlate the configuration of a farm to the cost of its installation and the yearly yield, we can determine LCOE*.

The array tilt β defines the array period through the mutual shading constraint, which in turn sets the number of panels required in a solar farm. Therefore, β is implicitly related to the farm cost (and of course the energy). Note that the mutual shading at 9 am on the shortest day of the year constraints the global optimization using array tilt (β) and period (p) as dependent variables. In the end, cost ratio (M_L) and the array tilt angle (β) are the

handles to control the LCOE*. For a fixed M_L, we numerically and analytically found an optimum tilt angle (β_{opt}) for each location.

Our analysis leads to the following key **conclusions**:

1. For places where land is scarce and expensive ($M_L \to 0$), panels should be laid flat on the ground ($\beta_{opt} = 0°$) to ensure maximum energy collection over a given land area. On the contrary, for practical values of $M_L (\sim 1 - 15)$ when the land is relatively inexpensive, panels have location-specific optimum tilt ($\beta_{opt} \sim 0° - 60°$) to achieve the lowest LCOE*.

2. PV installers can use an analytical expression of the form of Eq. 2.21 to find the location-specific optimum array tilt angle (β_{opt}) as a function of M_L. Moreover, β_{opt} is constantly zero until a threshold value (M_L^*) of cost ratio. The threshold value depends on the location (latitude/longitude) of the solar farm.

3. The difference in the optimum tilt angle ($\Delta\beta_{opt}$) between bifacial and monofacial designs can reach up to $10° - 15°$ for $|latitude| > 30°$ and places with high diffuse light fraction, e.g., Canada, Western Europe, Central China, etc. Moreover, higher tilt angle makes the design soiling-resistant, in turn reducing the cleaning cost.

4. For the same module-to-land cost ratio and similar lifetimes (reliability), ground-mounted bifacial solar farm design is more economically viable over monofacial design for locations where the diffuse fraction is high. The relative reduction in LCOE* (Bifacial $\text{Gain}_{\text{LCOE}^*}$) is $\sim 2 - 6\%$, for bifacial solar farm design over monofacial for locations with higher fractions of diffuse light (low clearness index, k_T) e.g., locations with $|latitude| > 30°$ (Central Europe, Northern parts of North America, and Central China). Alternatively, bifacial modules can be at most $\sim 2 - 6\%$ more expensive compared to monofacial modules for a bifacial solar farm to be cost-competitive compared to a monofacial farm.

Future Direction

Although this is the first report of LCOE-optimized farm design inclusive of land costs, the present work can be generalized in a number of ways. One can use the current approach to easily account for location-specific albedo and tilt-angle. Furthermore, currently the bifacial panels are slightly more expensive (but also known to be more reliable [13], [26]) than monofacial modules. This cost and reliability differences can be easily accounted for in our formulation. Instead of ground-mounted panels, the farm design can deploy elevated panels. The elevation of panels could increase the albedo light collection depending on the farm design, but this gain must be balanced against the increase in the installation (module) cost. It is also possible to sculpt the ground to increase albedo and re-optimize the configuration. Moreover, the effect of temperature on estimation of energy output and maintenance costs can be included to make the analysis more comprehensive.

To conclude, the reduction in LCOE through optimized farm design and continually reducing bifacial module prices makes bifacial PV technology an economically preferable alternative over monofacial solar farm.

7.2 Summary of Chapter 3: Temperature-dependent efficiency models for bifacial solar farms

In this chapter, we have analyzed the effects of temperature-dependent efficiency degradation on the energy yield and LCOE of monofacial and bifacial solar PV farms. Our approach involved combining an irradiance model, an updated light collection model for elevated farms, and temperature-dependent efficiency models to arrive at the final energy output of a solar farm. The light collection and temperature estimation models had to be solved self-consistently in order to arrive at the practical and more accurate efficiency for a particular location. We applied these models for locations around the world to deliver the global maps that quantify the percentage change in energy yield (YY) and LCOE* between temperature-dependent and constant temperature calculations while presenting general global trends.

Our analysis leads to the following key **conclusions**:

1. A comparison between energy yield and LCOE for temperature-dependent efficiency ($\eta(T)$) and temperature-independent efficiency (η_{STC}) conveys a percentage change of $\mathbf{-7}\%$ (Al-BSF), $\mathbf{-5}\%$ (SHJ) for locations close to the equator ($|latitude| < 30°$) and $\mathbf{+12}\%$ (Al-BSF), $\mathbf{+5}\%$ (SHJ) for locations close to the poles ($|latitude| > 30°$).

2. The bifacial gain for SHJ (bifacial) vs. traditionally used Al-BSF (monofacial) with temperature-dependent efficiency conveys a percentage change of $\mathbf{+12}\%$ for hotter locations close to the equator ($|latitude| < 30°$) and can reach up to $\mathbf{25-45}\%$ for colder places close to the poles ($|latitude| > 30°$). Whereas, bifacial gain for Al-BSF shows a percentage change of $\sim \mathbf{0-30}\%$. This presents an incredible opportunity for SHJ bifacial farm deployment.

3. Elevated farms show two counter-balancing trends, where light collection on the panels (I_{POA}) increases leading to an increase in temperature and a decrease in efficiency. Overall, temperature-dependent elevated farms ($E = 1-2\ m$) outperform unelevated farms in terms of yearly energy yield by $\sim 1-20\%$ depending on the latitude.

4. Bifacial PV technologies (SHJ) with lower TC and low sub-bandgap (IR) absorption can outperform their monofacial counterparts. The extent of enhancement in performance depends on the bifacial technology used and the geographical location of the farm.

In conclusion, it is important to accurately calculate the energy yield (YY) and LCOE*. The bifacial solar farm energy yield using temperature-dependent efficiency fulfills this purpose. Although the design of the farms in terms of the optimum tilt angle is not affected significantly, the absolute values of energy yield and LCOE for field-deployed temperature-dependent solar farms differ considerably for several locations around the world. This affects the overall economic evaluation of location-specific solar farms. Since bifacial panels have a lower temperature coefficient compared to monofacial panels, therefore, they are advantageous for relatively steady energy output due to daily and monthly temperature variations, especially for locations with lower total irradiance. Moreover, using PV materials with lower temperature

coefficients, e.g., Silicon Heterojunction (SHJ) and PERC, would lead to stable outputs and enhanced performance of bifacial solar farms throughout the world.

Future Direction

The scope of this study was limited to the initial temperature-dependent efficiency degradation associated with a newly installed solar farm. The long-term analysis of temperature-dependent degradation mechanisms and PV lifetime are not considered in our study. Moreover, the spectral dependence of PV efficiency is beyond the scope of this work and needs further investigation [107], [109]–[111]. Moreover, given the importance of TC, it will be important to focus on methods to lower the temperature coefficient of bifacial solar materials/ technologies and reduce cell temperature variation through improved packaging. These would become a central issue for concentrated solar photovoltaics as well. Further, one could improve the power output at the back surface by using a different kind of solar cell, e.g. DSSC, that performs better under low-light illumination [112]–[114]. Thus, the temperature-dependent energy-gain of a tandem [92], [104], [115] or 'mixed' bifacial solar cell will be an interesting and important generalization of the results presented in this chapter.

7.3 Summary of Chapter 4: Tracking algorithms and their analysis for bifacial solar farms

In this chapter, we have investigated the energy yield and comparative performance of various solar farm design configurations such as single-axis tracking vs. fixed-tilt and bifacial vs. monofacial. Our modeling framework combines the irradiance model, light collection model, temperature-dependent efficiency model, and a single-axis tracking model to estimate the energy yield of a solar farm. The tracking algorithm constraints the panel tilt angle to vary such that the angle of incidence is 0° i.e., the direct light falls normally on the panel. These models are simulated for locations worldwide that finally output global maps that quantify the percentage change in energy yield while comparing various farm designs.

Our analysis in this study leads to the following key **conclusions**:

1. An E/W single-axis tracking bifacial PV farm generates up to $\sim 45\%$ higher yearly energy yield than an N/S facing fixed-tilt bifacial PV farm for locations at $|latitude| < 30°$, see Fig. 4.9. A higher fraction of direct light leads to higher energy gain. An E/W tracking monofacial farm vs. fixed-tilt bifacial farm shows similar global trends with maximum energy gain reaching $\sim 10\%$ near the equator (Fig. 4.13). However, fixed-tilt bifacial farm outperforms tracking monofacial farm by $\sim 5-15\%$ for $|latitude| > 30°$ (Fig. 4.14).

2. As shown in Fig. 4.10, an E/W single-axis tracking bifacial PV farm tracks the hourly movement of the Sun whereas an N/S single-axis tracking bifacial farm mostly tracks the seasonal/monthly movement of the Sun. The former provides up to $\sim 15\%$ more energy for locations close to the equator ($|latitude| < 50°$) and the latter generates up to 5% for locations close to the poles ($|latitude| > 50°$).

3. Monthly/Seasonal variation in energy yield shows that the E/W tracking produces higher energy output in summer months whereas N/S tracking is favorable in winter months due to a southward inclination of the solar path in the Northern hemisphere and vice versa for the Southern hemisphere, as seen in Fig. 4.6.

4. An optimum pitch over height ratio yields minimum LCOE of an E/W tracking farm. The value of optimum p/h increases with the module-to-land cost-ratio (M_L) and varies with the geographical location of the farm. Whereas the yearly energy of the farm increases monotonically with p/h and saturates for very high values of pitch, as shown in Fig. 4.7. For a typical value of $M_L = 12$, the optimum p/h lies between 2 and 3, as seen globally in Fig 4.8.

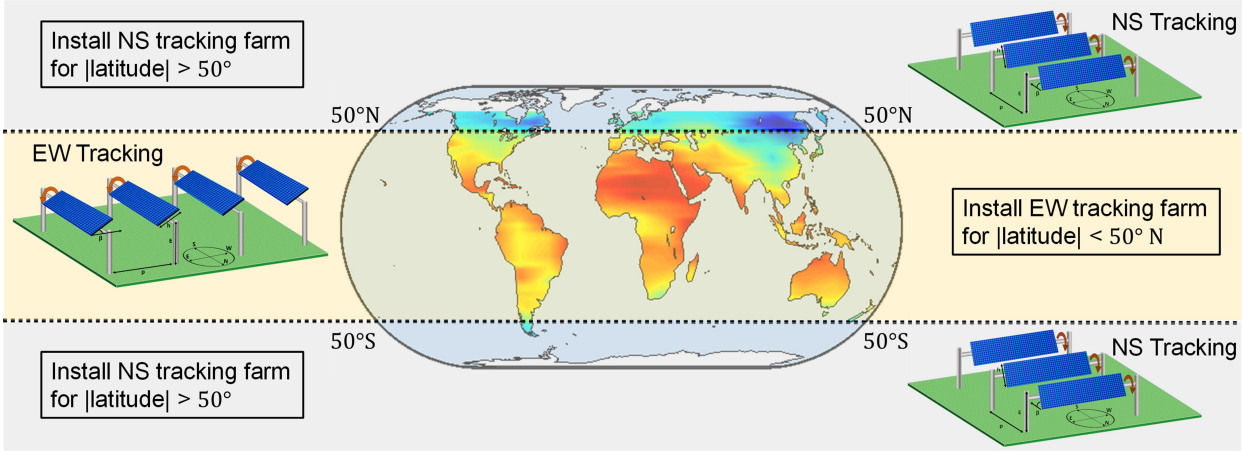

Figure 7.1. In conclusion, EW tracking bifacial farms outperform NS tracking bifacial farms for $|latitude| < 50°$ and vice-versa for $|latitude| > 50°$.

Fig. 7.1 (same as Fig. 4.12) summarizes our key conclusion that an E/W single-axis tracking bifacial PV farm is the best PV farm design for most regions ($|latitude| < 50°$) around the world. The energy gain with respect to a fixed-tilt bifacial or an N/S tracking farm varies according to the incident direct light fraction and the solar path at the geographical location of the solar PV farm. Moreover, for minimizing LCOE of a farm an optimum pitch can be used according to the estimated essential module to land cost ratio (M_L) for the deployment site. Thus, in terms of energy maximization, a bifacial tracking PV would be a worthwhile farm technology in most locations of the world.

In principle, the results can be easily generalized to any bifacial module technology with appropriate modification of front and backside efficiency. Thus, this study can be extended to a quantitative investigation of location-specific advantages of different solar cells. Our conclusions about the latitude-dependent choice of various farms are very general and should apply to various solar cell technologies.

Future Directions

As future applications of our model beyond the scope of this work, one can consider the possibility of using bifacial PV for AgroPV applications, for potential reduction in cost due to reduced height associated with vertical and tracking bifacial modules **Younas2019**,

[141], [142]. Our model can be extended to include various types of crop-specific tracking algorithms to control shading and perform co-optimization of the farm design. The energy yield of E/W bifacial tracking farms for various land types is presented in this study to show that croplands are well-suited for these PV farms. Similarly, N/S tracking solar PV farms can also be built on agricultural lands with optimum spacing and design to self-sustain the energy needs of the agricultural farms while minimally altering the crop yield. N/S tracking farms could be specifically interesting to explore since these would provide lower shadow depth in the mornings and evenings for the sunlight to reach the crops. In fact, in the past few years, several AgroPV farms with monofacial and bifacial tracking have been deployed in Italy and China, as collated in Table 1 of Ref. [172].

The role of bifacial PV in floating solar is unclear. In our models, we do not include the direct effects of relative humidity (RH). For floating solar PV, the relative humidity would be an essential parameter that needs to be taken into account.

Moreover, next generation PVK-HIT tandem solar cells could improve the efficiency further [104], [144], [145]. Furthermore, the reliability and lifetime are important concerns, especially regarding the mechanical failure of the trackers [18], [146]–[148]. The practical viability of solar tracking vs. power-tracking are not fully understood. Storage-integrated solar farming is another important aspect to consider in worldwide optimization of farm design. Finally, spectral dependence of albedo can slightly modify our numerical results, however, that will not change the conclusions. The static global maps displayed in this study can be explored interactively to find data point values for each location using DEEDS – a web-based platform for scientific research [149]–[151].

7.4 Summary of Chapter 5: Physics-based machine learning for performance of solar farms

In this chapter, we demonstrate the methodology and develop a tool to perform a functional interpolation of yearly energy yield and effective levelized cost of energy of any utility-scale solar PV system. The tool requires a coarse grid (1200 locations around the world) of geographical (lat, long), weather (global horizontal irradiance, ambient temperature, and clearness index) data (inputs), and simulated or field-derived energy yield (output). The

data is fed into a machine learning tool to train a predictive model. We demonstrate the results of two different tools, namely, Regression learner tool and Neural Network fitting tool. The models trained using the Gaussian Process Regression algorithm in the regression tool and Levenberg-Marquardt algorithm in the NN tool. Both models show high accuracy with $R^2 = 0.99$ and RMSE = 7.03. Once the machine learning model is trained and tested, it can be used to accurately predict the yearly energy yield for any specific location around the world in a matter of seconds.

Employing the trained model, we showed that the percentage error between a simple linear geographical interpolation and NN-based functional interpolation can range from $\sim 20 - 60\%$ for different regions worldwide. Moreover, we found that the critical number of sample points required for a reasonably accurate ($R^2 = 0.99$) prediction is $NS = 100$. Further, we investigated the power of NN-based models to accurately predict YY at an extrapolated geographical location within 10% error margin. Finally, we generalized the NN-model for all types PV farm designs by including various values of physical attributes of a PV farm, for example, elevation, row-spacing, albedo, and bifaciality.

In conclusion, we demonstrated a machine learning based scheme that allows an accurate functional interpolation of computational and field data for utility-scale solar PV farms. Starting with only **100** actual field data points, the tool can calculate the yearly energy yield of a PV farm deployed at any of the **1 million** geographical sites globally with very low computational times ($\sim$ seconds). This methodology can be further used to predict several other PV farm-related quantities such as levelized cost of energy, optimum tilt angles, degradation rates, lifetime etc. Depending on the problem statement, however, the machine learning based tools may require higher quantity and good quality of field data for experimental validation. This work would encourage the PV community to develop a strategy to acquire, store, and organize the PV farm data in order to perform precise predictions using very few data points.

7.5 Summary of Chapter 6: Ideal efficiencies for PV-EC storage systems

To summarize this chapter, we have developed an analytical theory to find the thermodynamic limit of solar to fuel conversion. Given (S, R) and an EC $(K, \mu_{th}, J_{0,ec}, \beta)$, system efficiency is an implicit function of number of EC cells (K), number of subcells (N), number of module cells (M), albedo (R) and bandgap (E_0) i.e., $\eta_{sys} = f(S, R, N, M, K, E_0, AF)$. Therefore, an optimum combination of (M, N, E_0) provides the thermodynamically limited maximum efficiency that is evident from Fig. 6.5. The analytical formulation mentioned above provides a convenient way to find this limit and the associated parameters viz. $(M/K, N, E_0)$ and provides insights into the system with respect to recent developments in using bifaciality (R) and concentrated light (S).

Future Directions

The difference between the global maximum and experimental values in Fig. 6.4 should encourage refinement and optimization of the PV-EC design. We have considered an idealized system i.e., $R_{sol} = 0$, and it is evident that overall optimized systems, with optimum M, N, E_0 and K can achieve much higher efficiencies compared to the laboratory results reported in the literature [171]. The analytical model developed in this work can be easily used to integrate other kinds of loads [54] to the PV system. This work can also be extended to include hourly variations in solar illumination to find daily storage capabilities and location-based optimal design.

7.6 Future work

Although our goal to create a comprehensive multi-module numerical model for bifacial solar farms was achieved, we further want to push the boundaries of applied PV research. Hitherto, we already began working on using machine learning for PV performance and reliability analysis. Moreover, we also inspected PV storage system efficiencies. In this regard, we have some ideas and projects that can be pursued in future as described below.

7.6.1 Worldwide forward and inverse degradation model

On the basis of the above-mentioned toy model for reliability of PV systems, one can develop a complete sophisticated forward and inverse model for PV degradation mechanisms.

Forward model: The goal is to predict lifetime of a solar PV system starting with a satellite-based or field meteorological dataset (NSRDB, NREL), see Fig. 7.2. From weather data, we can acquire physical parameters, for example, Ultra-violet light intensity, relative humidity, ambient temperature, snowing or soiling rate for various locations around the world. Next, we can develop and utilize multi-module degradation mechanism toolbox to estimate the time-dependent electrical parameters (refer to the double-diode compact model in Fig. **??**) of the PV system. As an aside, the degradation mechanism toolbox can be a package of computationally fast machine learnt sub-modules for each mechanism. Combining these time-varying degradation of electrical parameters allows us to predict the lifetime of the PV system. Performing this prediction workflow for several latitudes/longitudes will provide us a global map of the lifetime PV systems.

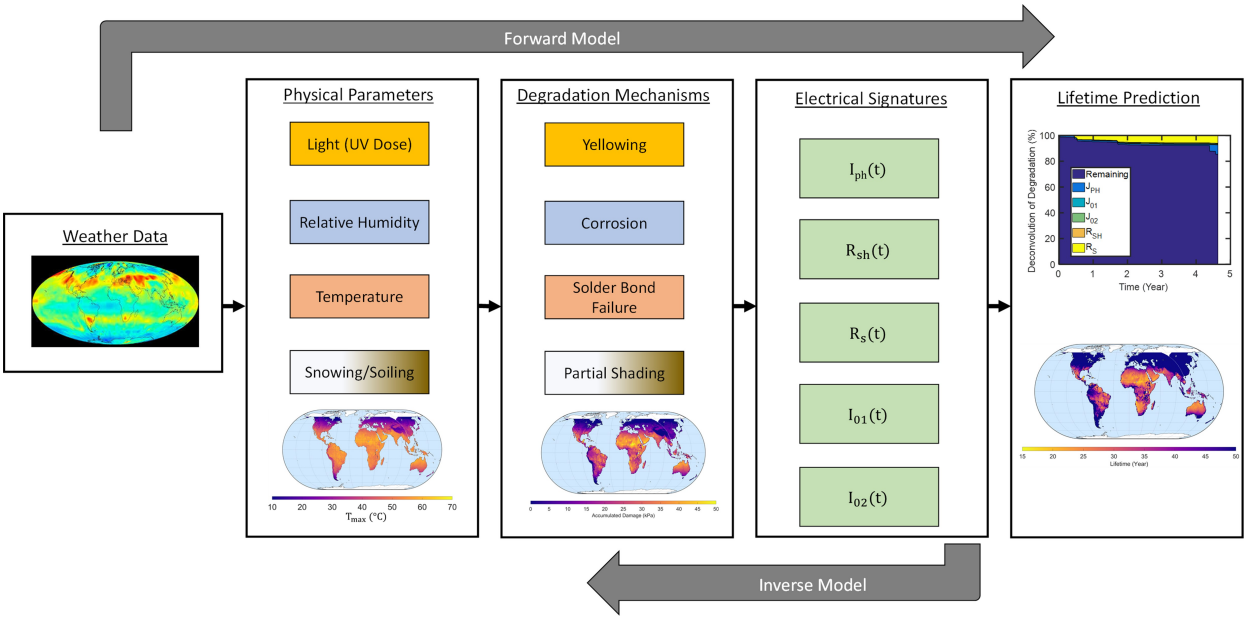

Figure 7.2. Worldwide forward and inverse modeling framework.

Inverse model: Converse to the above process of predicting lifetime, the aim of the inverse model is to deconvolve and identify the degradation mechanisms by analyzing the patterns

in the electrical signatures. This approach would require synthesized or field-measured time-dependent IV curves and electrical parameters of a PV system. Next, we would use convolutional neural networks for recognizing the pattern of degradation of electrical parameters so that they ca be connected to the associated degradation mechanism. Once we identify the dominant mechanisms at a particular location, the manufacturing process can be tweaked to become more resilient towards the local weather conditions and the corresponding degradation pathways. This will eventually enhance the lifetime of the PV system. Again, we can generalize our approach so that the inverse model can be extended to the entire world.

7.7 Final Thoughts

With a steady increase in world population and subsequently the ever-increasing sustainable and renewable energy demand, solar photovoltaics has been one of the key solutions. To reduce the costs of generating electricity using solar PV, utility-scale solar PV farms have been found to be most economically viable.

Therefore, in this thesis, we set out with a goal of modeling, simulating, and analyzing the latest technology of bifacial solar PV farms. We have delineated the challenges and solutions in pursuit of this goal. Moreover, we went above and beyond our goal to further incorporate computationally fast and easy to handle machine learnt toolbox to accurately emulate our numerical models. After working on the performance aspect of PV systems, we demonstrated a toy model to analyze the PV degradation pathways and improve reliability of these systems. Furthermore, we present a future guide for solving the so called machine leaning based “forward-inverse" problem for performance and reliability of solar PV systems worldwide.

Through this work, we aspire to solve existing problems and inspire next generation of researchers to pursue new challenges in the field of photovoltaics, specifically, and science, in general.

References

[1] OCDE & IEA, "Market Report Series: Renewables 2017, analysis and forecats to 2022," *Executive Summary*, p. 10, 2017, ISSN: 0027-8424. DOI: 10.1073?pnas.0603395103. [Online]. Available: https://www.iea.org/Textbase/npsum/renew2017MRSsum.pdf.

[2] S. Chu and A. Majumdar, "Opportunities and challenges for a sustainable energy future," *Nature*, vol. 488, no. 7411, pp. 294–303, 2012, ISSN: 00280836. DOI: 10.1038/nature11475.

[3] S. Chu, Y. Cui, and N. Liu, "The path towards sustainable energy," *Nature Materials*, vol. 16, no. 1, pp. 16–22, 2016, ISSN: 14764660. DOI: 10.1038/nmat4834. [Online]. Available: http://dx.doi.org/10.1038/nmat4834.

[4] E. Kabir, P. Kumar, S. Kumar, A. A. Adelodun, and K. H. Kim, "Solar energy: Potential and future prospects," *Renewable and Sustainable Energy Reviews*, vol. 82, no. October 2017, pp. 894–900, 2018, ISSN: 18790690. DOI: 10.1016/j.rser.2017.09.094.

[5] K. Branker, M. J. Pathak, and J. M. Pearce, "A review of solar photovoltaic levelized cost of electricity," *Renewable and Sustainable Energy Reviews*, vol. 15, no. 9, pp. 4470–4482, 2011, ISSN: 13640321. DOI: 10.1016/j.rser.2011.07.104. [Online]. Available: http://dx.doi.org/10.1016/j.rser.2011.07.104.

[6] F. Ueckerdt, L. Hirth, G. Luderer, and O. Edenhofer, "System LCOE: What are the costs of variable renewables?" *Energy*, vol. 63, pp. 61–75, 2013, ISSN: 03605442. DOI: 10.1016/j.energy.2013.10.072. [Online]. Available: http://dx.doi.org/10.1016/j.energy.2013.10.072.

[7] Lazard, *Lazard- LCOE analysis*. [Online]. Available: https://www.lazard.com/perspective/levelized-cost-of-energy-levelized-cost-of-storage-and-levelized-cost-of-hydrogen/.

[8] Lazard, "Lazard's levelized cost of energy analysis — version 14.0," October, 2020. [Online]. Available: https://www.lazard.com/media/451419/lazards-levelized-cost-of-energy-version-140.pdf.

[9] V. V. Tyagi, N. A. Rahim, N. A. Rahim, and J. A. Selvaraj, "Progress in solar PV technology: Research and achievement," *Renewable and Sustainable Energy Reviews*, vol. 20, pp. 443–461, 2013, ISSN: 13640321. DOI: 10.1016/j.rser.2012.09.028. [Online]. Available: http://dx.doi.org/10.1016/j.rser.2012.09.028.

[10] M. A. Green, Y. Hishikawa, W. Warta, E. D. Dunlop, D. H. Levi, J. Hohl-Ebinger, and A. W. Ho-Baillie, "Solar cell efficiency tables (version 50)," *Progress in Photovoltaics: Research and Applications*, vol. 25, no. 7, pp. 668–676, 2017, ISSN: 1099159X. DOI: 10.1002/pip.2909. arXiv: 1303.4604.

[11] N. L. Chang, A. W. Y. Ho-Baillie, D. Vak, M. Gao, M. A. Green, and R. J. Egan, "Manufacturing cost and market potential analysis of demonstrated roll-to-roll perovskite photovoltaic cell processes," *Solar Energy Materials and Solar Cells*, vol. 174, no. May 2017, pp. 314–324, 2018, ISSN: 09270248. DOI: 10.1016/j.solmat.2017.08.038. [Online]. Available: http://dx.doi.org/10.1016/j.solmat.2017.08.038.

[12] *Sunshot-photovoltaic-manufacturing-initiative @ www.energy.gov*. [Online]. Available: https://www.energy.gov/eere/solar/sunshot-photovoltaic-manufacturing-initiative.

[13] R. Fu, D. Chung, T. Lowder, D. Feldman, K. Ardani, R. Fu, D. Chung, T. Lowder, D. Feldman, and K. Ardani, "U.S. Solar Photovoltaic System Cost Benchmark : Q1 2017 U.S.," *Nrel*, no. September, pp. 1–66, 2017. DOI: 10.2172/1390776. [Online]. Available: www.nrel.gov/publications..

[14] M. A. Green, "The Path to 25% Silicon Solar Cell Efficiency: History of Silicon Cell Evolution," *PROGRESS IN PHOTOVOLTAICS: RESEARCH AND APPLICATIONS*, vol. 17, pp. 183–189, 2009. DOI: 10.1002/pip.892.

[15] D. B. Needleman, J. R. Poindexter, R. C. Kurchin, I. Marius Peters, G. Wilson, and T. Buonassisi, "Economically sustainable scaling of photovoltaics to meet climate targets," *Energy and Environmental Science*, vol. 9, no. 6, pp. 2122–2129, 2016, ISSN: 17545706. DOI: 10.1039/c6ee00484a.

[16] A. Shah, J. Meier, A. Buechel, U. Kroll, J. Steinhauser, F. Meillaud, H. Schade, and D. Dominé, "Towards very low-cost mass production of thin-film silicon photovoltaic

(PV) solar modules on glass," *Thin Solid Films*, vol. 502, no. 1-2, pp. 292–299, 2006, ISSN: 00406090. DOI: 10.1016/j.tsf.2005.07.299.

[17] A. Le Donne, V. Trifiletti, and S. Binetti, "New earth-abundant thin film solar cells based on chalcogenides," *Frontiers in Chemistry*, vol. 7, no. APR, 2019, ISSN: 22962646. DOI: 10.3389/fchem.2019.00297.

[18] D. C. Jordan, S. R. Kurtz, K. VanSant, and J. Newmiller, "Compendium of photovoltaic degradation rates," *Progress in Photovoltaics: Research and Applications*, vol. 24, no. 1, pp. 978–989, 2016, ISSN: 10627995. DOI: 10.1002/pip.2744. eprint: 1303.4604.

[19] P. Hacke, S. Spataru, K. Terwilliger, G. Perrin, S. Glick, S. Kurtz, and J. Wohlgemuth, "Accelerated Testing and Modeling of Potential-Induced Degradation as a Function of Temperature and Relative Humidity," *IEEE Journal of Photovoltaics*, vol. 5, no. 6, pp. 1549–1553, Nov. 2015, ISSN: 2156-3381. DOI: 10.1109/JPHOTOV.2015.2466463.

[20] A. Cuevas, A. Luque, J. Eguren, and J. del Alamo, "50 Per cent more output power from an albedo-collecting flat panel using bifacial solar cells," *Solar Energy*, vol. 29, no. 5, pp. 419–420, 1982, ISSN: 0038092X. DOI: 10.1016/0038-092X(82)90078-0.

[21] "International Technology Roadmap for Photovoltaic— Results 2017 including maturity report 2018," Tech. Rep. September, 2018. [Online]. Available: https://resources.solarbusinesshub.com/images/reports/248.pdf.

[22] R. Guerrero-Lemus, R. Vega, T. Kim, A. Kimm, and L. E. Shephard, "Bifacial solar photovoltaics - A technology review," *Renewable and Sustainable Energy Reviews*, vol. 60, pp. 1533–1549, 2016, ISSN: 18790690. DOI: 10.1016/j.rser.2016.03.041. [Online]. Available: http://dx.doi.org/10.1016/j.rser.2016.03.041.

[23] A. Luque, E. Lorenzo, G. Sala, and S. López-Romero, "Diffusing reflectors for bifacial photovoltaic panels," *Solar Cells*, vol. 13, no. 3, pp. 277–292, 1985, ISSN: 03796787. DOI: 10.1016/0379-6787(85)90021-3.

[24] Y. K. Chieng and M. A. Green, "Computer simulation of enhanced output from bifacial photovoltaic modules," *Progress in Photovoltaics: Research and Applications*,

vol. 1, no. 4, pp. 293–299, Oct. 1993, ISSN: 10627995. DOI: 10.1002/pip.4670010406. [Online]. Available: http://doi.wiley.com/10.1002/pip.4670010406.

[25] U. A. Yusufoglu, T. H. Lee, T. M. Pletzer, A. Halm, L. J. Koduvelikulathu, C. Comparotto, R. Kopecek, and H. Kurz, "Simulation of energy production by bifacial modules with revision of ground reflection," *Energy Procedia*, vol. 55, pp. 389–395, 2014, ISSN: 18766102. DOI: 10.1016/j.egypro.2014.08.111. [Online]. Available: http://dx.doi.org/10.1016/j.egypro.2014.08.111.

[26] X. Sun, M. R. Khan, C. Deline, and M. A. Alam, "Optimization and performance of bifacial solar modules: A global perspective," *Applied Energy*, vol. 212, no. September 2017, pp. 1601–1610, 2018, ISSN: 03062619. DOI: 10.1016/j.apenergy.2017.12.041. arXiv: 1709.10026. [Online]. Available: https://doi.org/10.1016/j.apenergy.2017.12.041.

[27] C. K. Lo, Y. S. Lim, and F. A. Rahman, "New integrated simulation tool for the optimum design of bifacial solar panel with reflectors on a specific site," *Renewable Energy*, vol. 81, pp. 293–307, 2015, ISSN: 18790682. DOI: 10.1016/j.renene.2015.03.047. [Online]. Available: http://dx.doi.org/10.1016/j.renene.2015.03.047.

[28] G. J. M. M. Janssen, B. B. Van Aken, A. J. Carr, and A. A. Mewe, "Outdoor Performance of Bifacial Modules by Measurements and Modelling," *Energy Procedia*, vol. 77, pp. 364–373, Aug. 2015, ISSN: 18766102. DOI: 10.1016/j.egypro.2015.07.051. [Online]. Available: http://dx.doi.org/10.1016/j.egypro.2015.07.051%20http://linkinghub.elsevier.com/retrieve/pii/S187661021500819X.

[29] J. E. Castillo-Aguilella and P. S. Hauser, "Bifacial photovoltaic module best-fit annual energy yield model with azimuthal correction," in *2016 IEEE 43rd Photovoltaic Specialists Conference (PVSC)*, IEEE, Jun. 2016, pp. 3109–3112, ISBN: 978-1-5090-2724-8. DOI: 10.1109/PVSC.2016.7750238. [Online]. Available: http://ieeexplore.ieee.org/document/7750238/.

[30] J. S. Stein, L. Burnham, and M. Lave, "Performance Results for the Prism Solar Installation at the New Mexico Regional Test Center : Field Data from February 15 -

August 15 , 2016," Sandia Report (SAND2017-5872), Tech. Rep. June, 2017. [Online]. Available: http://energy.sandia.gov/download/38750/.

[31] F. Fertig, S. Nold, N. Wöhrle, J. Greulich, I. Hädrich, K. Krauß, M. Mittag, D. Biro, S. Rein, and R. Preu, "Economic feasibility of bifacial silicon solar cells," *Progress in Photovoltaics: Research and Applications*, vol. 24, no. 6, pp. 800–817, Jun. 2016, ISSN: 10627995. DOI: 10.1002/pip.2730. arXiv: 1303.4604. [Online]. Available: http://doi.wiley.com/10.1002/pip.2730.

[32] S. Guo, T. M. Walsh, and M. Peters, "Vertically mounted bifacial photovoltaic modules: A global analysis," *Energy*, vol. 61, pp. 447–454, 2013, ISSN: 03605442. DOI: 10.1016/j.energy.2013.08.040. [Online]. Available: http://dx.doi.org/10.1016/j.energy.2013.08.040.

[33] M. Ito and E. Gerritsen, "Geographical Mapping of The Performance of Vertically Installed Bifacial Modules," in *32nd PVSEC*, 2016, pp. 1603–1609.

[34] VDMA, *International Technology Roadmap for Photovoltaics 2020 - Results 2019 including maturity report*, 2020.

[35] A. Onno, N. Rodkey, A. Asgharzadeh, S. Manzoor, Z. J. Yu, F. Toor, and Z. C. Holman, "Predicted Power Output of Silicon-Based Bifacial Tandem Photovoltaic Systems," *Joule*, vol. 4, no. 3, pp. 580–596, 2020, ISSN: 25424351. DOI: 10.1016/j.joule.2019.12.017. [Online]. Available: https://doi.org/10.1016/j.joule.2019.12.017.

[36] R. Fu, D. Feldman, and R. Margolis, "U.S. Solar Photovoltaic System Cost Benchmark: Q1 2018," *Nrel*, no. Novmnber, pp. 1–47, 2018. [Online]. Available: https://www.nrel.gov/docs/fy19osti/72399.pdf.

[37] *Pv magazine: Tracking solar*. [Online]. Available: https://www.pv-magazine.com/2019/11/19/a-record-year-for-trackers/.

[38] C. D. Rodriguez-Gallegos, O. Gandhi, S. K. Panda, and T. Reindl, "On the PV Tracker Performance: Tracking the Sun Versus Tracking the Best Orientation," *IEEE Journal of Photovoltaics*, vol. 10, no. 5, pp. 1474–1480, 2020, ISSN: 21563403. DOI: 10.1109/JPHOTOV.2020.3006994.

[39] J. S. Stein, C. Reise, J. B. Castro, G. Friesen, G. Maugeri, E. Urrejola, and S. Ranta, *Bifacial PV modules & systems Experience and Results from International Research and Pilot Applications*. IEA-PVPS Task 13, 2021, ISBN: 9783907281031.

[40] Sunpower Corp., *Energylink @ us.sunpower.com*. [Online]. Available: https://us.sunpower.com/commercial-solar/products/energylink.

[41] . Sandia National Laboratories, *PVLIB Toolbox*. [Online]. Available: https://pvpmc.sandia.gov/applications/pv_lib-toolbox/.

[42] NREL, *Bifacial Radiance Documentation*. [Online]. Available: https://bifacial-radiance.readthedocs.io/en/latest/.

[43] NREL, *RdTools, version 2.0.4*, 2020. DOI: 10.5281/zenodo.1210316. [Online]. Available: https://github.com/NREL/rdtools.

[44] A. Driesse, M. Theristis, and J. S. Stein, "A New Photovoltaic Module Efficiency Model for Energy Prediction and Rating," *IEEE Journal of Photovoltaics*, vol. 11, no. 2, pp. 527–534, 2021, ISSN: 21563403. DOI: 10.1109/JPHOTOV.2020.3045677.

[45] M. T. Patel, M. R. Khan, X. Sun, and M. A. Alam, "A worldwide cost-based design and optimization of tilted bifacial solar farms," *Applied Energy*, vol. 247, no. April, pp. 467–479, 2019, ISSN: 03062619. DOI: 10.1016/j.apenergy.2019.03.150.

[46] M. T. Patel, R. A. Vijayan, R. Asadpour, M. Varadharajaperumal, M. R. Khan, and M. A. Alam, "Temperature-dependent energy gain of bifacial PV farms: A global perspective," *Applied Energy*, vol. 276, no. March, p. 115 405, 2020, ISSN: 03062619. DOI: 10.1016/j.apenergy.2020.115405. [Online]. Available: https://doi.org/10.1016/j.apenergy.2020.115405.

[47] S. M. Udrescu and M. Tegmark, "AI Feynman: A physics-inspired method for symbolic regression," *Science Advances*, vol. 6, no. 16, 2020, ISSN: 23752548. DOI: 10.1126/sciadv.aay2631. arXiv: 1905.11481.

[48] M. Li, O. Irsoy, C. Cardie, and H. G. Xing, "Physics-inspired neural networks for efficient device compact modeling," *IEEE Journal on Exploratory Solid-State Computational Devices and Circuits*, vol. 2, no. October 2016, pp. 44–49, 2016, ISSN: 23299231. DOI: 10.1109/JXCDC.2016.2636161.

[49] V. L. Guen, Y. Yin, J. Dona, I. Ayed, E. de Bézenac, N. Thome, and P. Gallinari, "Augmenting Physical Models with Deep Networks for Complex Dynamics Forecasting," no. 2016, pp. 1–22, 2020. arXiv: 2010.04456. [Online]. Available: http://arxiv.org/abs/2010.04456.

[50] X. Jia, J. Willard, A. Karpatne, J. S. Read, J. A. Zwart, M. Steinbach, and V. Kumar, "Physics-Guided Machine Learning for Scientific Discovery: An Application in Simulating Lake Temperature Profiles," vol. 2, no. 3, 2020, ISSN: 2691-1922. DOI: 10.1145/3447814. arXiv: 2001.11086. [Online]. Available: http://arxiv.org/abs/2001.11086.

[51] R. Swischuk, L. Mainini, B. Peherstorfer, and K. Willcox, "Projection-based model reduction: Formulations for physics-based machine learning," *Computers and Fluids*, vol. 179, pp. 704–717, 2019, ISSN: 00457930. DOI: 10.1016/j.compfluid.2018.07.021. [Online]. Available: https://doi.org/10.1016/j.compfluid.2018.07.021.

[52] J. Willard, X. Jia, S. Xu, M. Steinbach, and V. Kumar, "Integrating Physics-Based Modeling with Machine Learning: A Survey," vol. 1, no. 1, pp. 1–34, 2020. arXiv: 2003.04919. [Online]. Available: http://arxiv.org/abs/2003.04919.

[53] J. Stein, C. Reise, J. Castro, G. Friesen, G. Mauger, E. Urrejola, S. Ranta, M. Alam, M. Anoma, S. Pelaez, D. Berrian, E. Bertrand, M. Chiodetti, D. Chudinzow, H. Colin, I. Devoto, R. French, E. Fuentealba, F. Haffner, A. Halm, J. Haysom, K. Hinzer, I. Horvath, H. Huerta, M. Khan, M. Klenk, R. Kopecek, J. Libal, M. Lindh, B. Marion, M. Mikofski, R. Molinero, M. Monarch, A. Neubert, M. Patel, A. Petersson, G. Poulin, S. Ramesh, O. Rhazi, N. Riedel-Lyngskær, D. Riley, A. Russell, A. Schneider, C. Stark, T. Timofte, D. Tune, J. Tymchak, C. Valdivia, F. Valencia, and M. Wang, *Bifacial Photovoltaic Modules and Systems: Experience and Results from International Research*

and Pilot Applications: Report IEA-PVPS T13-14:2021, English. International Energy Agency, 2021, ISBN: 978-3-907281-03-1.

[54] K. K. Sakimoto, A. B. Wong, and P. Yang, "Self-photosensitization of nonphotosynthetic bacteria for solar-to-chemical production," *Science*, vol. 351, no. 6268, pp. 74–77, 2016, ISSN: 0036-8075. DOI: 10.1126/science.aad3317. arXiv: 1011.1669.

[55] W. Shockley and H. J. Queisser, "Detailed balance limit of efficiency of p-n junction solar cells," *Journal of Applied Physics*, vol. 32, no. 3, pp. 510–519, 1961, ISSN: 00218979. DOI: 10.1063/1.1736034. arXiv: 9809069v1 [arXiv:gr-qc]. [Online]. Available: http://aip.scitation.org/doi/pdf/10.1063/1.1736034.

[56] M. R. Singh, E. L. Clark, and A. T. Bell, "Thermodynamic and achievable efficiencies for solar-driven electrochemical reduction of carbon dioxide to transportation fuels," *Proceedings of the National Academy of Sciences*, no. 3, p. 201 519 212, 2015, ISSN: 0027-8424. DOI: 10.1073/pnas.1519212112. [Online]. Available: http://www.pnas.org/lookup/doi/10.1073/pnas.1519212112.

[57] S. Haussener, C. Xiang, J. M. Spurgeon, S. Ardo, N. S. Lewis, and A. Z. Weber, "Modeling, simulation, and design criteria for photoelectrochemical water-splitting systems," *Energy & Environmental Science*, vol. 5, no. 12, pp. 9922–9935, 2012, ISSN: 1754-5692. DOI: 10.1039/c2ee23187e.

[58] M. T. Winkler, C. R. Cox, D. G. Nocera, and T. Buonassisi, "Modeling integrated photovoltaic-electrochemical devices using steady-state equivalent circuits," *Proceedings of the National Academy of Sciences of the United States of America*, vol. 110, no. 12, E1076–E1082, 2013, ISSN: 0027-8424. DOI: 10.1073/pnas.1301532110.

[59] EIA, "Levelized Cost and Levelized Avoided Cost of New Generation Resources in the Annual Energy Outlook 2018," no. March, pp. 1–20, 2018.

[60] J. Appelbaum, "Bifacial photovoltaic panels field," *Renewable Energy*, vol. 85, pp. 338–343, 2016, ISSN: 18790682. DOI: 10.1016/j.renene.2015.06.050.

[61] M. R. Khan, A. Hanna, X. Sun, and M. A. Alam, "Vertical bifacial solar farms: Physics, design, and global optimization," *Applied Energy*, vol. 206, pp. 240–248, 2017, ISSN: 03062619. DOI: 10.1016/j.apenergy.2017.08.042. arXiv: 1704.08630.

[62] M. R. Khan, E. Sakr, X. Sun, P. Bermel, and M. A. Alam, "Ground sculpting to enhance energy yield of vertical bifacial solar farms," *Applied Energy*, vol. 241, no. August 2018, pp. 592–598, 2019, ISSN: 03062619. DOI: 10.1016/j.apenergy.2019.01.168.

[63] L. Podlowski, S. Wendlandt, and P. I. P.-i. Berlin, "Yield Study on Identical Bifacial Rooftop Systems installed in the USA and in Germany," in *4th Workshop on Bifacial PV - Konstanz (Germany)*, 2017.

[64] C. D. Rodríguez-Gallegos, M. Bieri, O. Gandhi, J. P. Singh, T. Reindl, and S. Panda, "Monofacial vs bifacial Si-based PV modules: Which one is more cost-effective?" *Solar Energy*, vol. 176, no. October, pp. 412–438, 2018, ISSN: 0038092X. DOI: 10.1016/j.solener.2018.10.012. [Online]. Available: https://linkinghub.elsevier.com/retrieve/pii/S0038092X18309915.

[65] A. Luque and H. Steven, *Handbook of Photovoltaic Science and Engineering*, 2nd. Wiley, 2011, p. 1164, ISBN: 978-0-470-72169-8.

[66] I. Reda and A. Andreas, "Solar position algorithm for solar radiation applications," *Solar Energy*, vol. 76, no. 5, pp. 577–589, 2004, ISSN: 0038092X. DOI: 10.1016/j.solener.2003.12.003.

[67] B. Haurwitz, *Insolation in Relation To Type*, 1946. DOI: 10.1175/1520-0469(1946)003<0123:IIRTCT>2.0.CO;2.

[68] B. Haurwitz, *Insolation in Relation To Cloud Amount*, 1954. DOI: 10.1175/1520-0493(1954)082<0317:IIRTCA>2.0.CO;2.

[69] NASA, *POWER. Surface meteorology and solar energy: a renewable energy resource web site (release 6.0); 2017.* [Online]. Available: https://eosweb.larc.nasa.gov/cgi-bin/sse/sse.cgi?.

[70] B. W. Duffie JA, *Solar engineering of thermal processes.* 4th ed. Wiley.

[71] P. G. Loutzenhiser, H. Manz, C. Felsmann, P. A. Strachan, T. Frank, and G. M. Maxwell, "Empirical validation of models to compute solar irradiance on inclined surfaces for building energy simulation," *Solar Energy*, vol. 81, no. 2, pp. 254–267, 2007, ISSN: 0038092X. DOI: 10.1016/j.solener.2006.03.009.

[72] E. L. Maxwell, "A quasi-physical model for converting hourly global to direct normal insolation," no. SERI/TR-215-3087, pp. 35–46, 1987. [Online]. Available: http://rredc.nrel.gov/solar/pubs/PDFs/TR-215-3087.pdf.

[73] D. G. Erbs, S. A. Klein, and J. A. Duffie, "Estimation of the diffuse radiation fraction for hourly, daily and monthly-average global radiation," *Solar Energy*, vol. 28, no. 4, pp. 293–302, 1982, ISSN: 0038092X. DOI: 10.1016/0038-092X(82)90302-4.

[74] J. A. Galtieri, "Differential Power Processing for Increased Solar Array Energy Harvest," 2015.

[75] *McIntosh Keith R, Baker-Finch Simeon C. Tracey; November 2013. Available: https://www2.pvlighthouse.com.au/Simulation/Hosted/Tracey/Tracey.aspx.*

[76] K. R. M. et al., "An Optical Comparison of Silicon And EVA Encapsulants for Conventional Silicon PV Modules: A Ray-Tracing Study," *Ieee*, pp. 544–549, 2009. [Online]. Available: http://ieeexplore.ieee.org/stamp/stamp.jsp?arnumber=5411624.

[77] K. R. Mclntosh, J. N. Cotsell, A. W. Norris, N. E. Powell, and B. M. Ketola, "An optical comparison of silicone and EVA encapsulants under various spectra," *Conference Record of the IEEE Photovoltaic Specialists Conference*, pp. 269–274, 2010, ISSN: 01608371. DOI: 10.1109/PVSC.2010.5615830. eprint: /doi.org/10.1109/PVSC.2010.5615830.

[78] M. Schweiger and J. Bonilla, "Performance characteristics of bifacial PV modules and power labeling Performance of commercial bifacial PV modules Introduction," 2017.

[79] C. Deline, A. Dobos, S. Janzou, J. Meydbray, and M. Donovan, "A simplified model of uniform shading in large photovoltaic arrays," *Solar Energy*, vol. 96, pp. 274–282, Oct. 2013, ISSN: 0038092X. DOI: 10.1016/j.solener.2013.07.008.

[80] N. Martin and J. M. Ruiz, "Annual angular reflection losses in PV modules," *Progress in Photovoltaics: Research and Applications*, vol. 13, no. 1, pp. 75–84, 2005, ISSN: 10627995. DOI: 10.1002/pip.585.

[81] D. Passias and B. Kallback, "Shading effects in rows of solar cell panels," *Solar Cells*, vol. 11, no. 3, pp. 281–291, 1984, ISSN: 03796787. DOI: 10.1016/0379-6787(84)90017-6.

[82] J. Appelbaum, "View Factors to Grounds of Photovoltaic Collectors," *Journal of Solar Energy Engineering*, vol. 138, no. 6, p. 64 501, Sep. 2016, ISSN: 0199-6231. DOI: 10.1115/1.4034316.

[83] M. Modest, *Radiative Heat Transfer*, 3rd ed. New York: Academic Press, 2011, vol. 211 Suppl, p. 1, ISBN: 9780444594556. DOI: 10.1016/S0014-2565(11)70001-7.

[84] S. Kurtz, J. Granata, and M. Quintana, "Photovoltaic-reliability R&D toward a solar-powered world," no. August 2009, 74120Z, 2009. DOI: 10.1117/12.825649. [Online]. Available: http://proceedings.spiedigitallibrary.org/proceeding.aspx?doi=10.1117/12.825649.

[85] C. Ran Fu, D. Chung, T. Lowder, D. Feldman, K. Ardani, and R. Margolis, "U . S . Solar Photovoltaic System Cost Benchmark : Q1 2018," *National Renewable Energy Laboratory*, no. November, pp. 1–64, 2018. DOI: 10.7799/1325002. [Online]. Available: https://www.nrel.gov/docs/fy16osti/66532.pdf.

[86] M. I. Gerritsen and Eric, "GEOGRAPHICAL MAPPING OF THE PERFORMANCE OF VERTICALLY INSTALLED BIFACIAL MODULES Masakazu," in *32nd European Photovoltaic Solar Energy Conference and Exhibition GEOGRAPHICAL*, 2016, pp. 1603–1609.

[87] J. Cano, J. J. John, S. Tatapudi, and G. Tamizhmani, "Effect of tilt angle on soiling of photovoltaic modules," *2014 IEEE 40th Photovoltaic Specialist Conference, PVSC 2014*, pp. 3174–3176, 2014, ISSN: 978-1-4799-4398-2. DOI: 10.1109/PVSC.2014.6925610.

[88] J. Libal, D. Berrian, and R. Kopecek, "Overview: energy yield simulations and calculation of LCOE for bifacial PV systems," *bifi PV workshop*, 2017.

[89] *Watt per unit area*. [Online]. Available: http://www.suncyclopedia.com/en/area-required-for-solar-pv-power-plants/.

[90] M. A. Green, Y. Hishikawa, E. D. Dunlop, D. H. Levi, J. Hohl-Ebinger, and A. W. Ho-Baillie, "Solar cell efficiency tables (version 51)," *Progress in Photovoltaics: Research and Applications*, vol. 26, no. 1, pp. 3–12, 2018, ISSN: 1099159X. DOI: 10.1002/pip.2978. arXiv: 1303.4604.

[91] J. S. Stein, D. Riley, C. Deline, and F. Toor, "Bifacial Solar Photovoltaic Systems : A promising advance in solar performance with interesting challenges," 2017.

[92] M. A. Alam and M. R. Khan, "Thermodynamic efficiency limits of classical and bifacial multi-junction tandem solar cells: An analytical approach," *Applied Physics Letters*, vol. 109, no. 17, 2016, ISSN: 00036951. DOI: 10.1063/1.4966137. [Online]. Available: http://dx.doi.org/10.1063/1.4966137.

[93] R. Dubey, P. Batra, S. Chattopadhyay, A. Kottantharayil, B. M. Arora, K. L. Narasimhan, and J. Vasi, "Measurement of temperature coefficient of photovoltaic modules in field and comparison with laboratory measurements," *2015 IEEE 42nd Photovoltaic Specialist Conference, PVSC 2015*, pp. 1–5, 2015. DOI: 10.1109/PVSC.2015.7355852.

[94] D. L. King, J. A. Kratochvil, and W. E. Boyson, "Temperature Coefficient," *Encyclopedia of Computational Neuroscience*, pp. 2951–2951, 2015. DOI: 10.1007/978-1-4614-6675-8-100603.

[95] J. Zhao, A. Wang, S. J. Robinson, and M. A. Green, "Reduced temperature coefficients for recent high-performance silicon solar cells," *Progress in Photovoltaics: Research and Applications*, vol. 2, no. 3, pp. 221–225, 1994, ISSN: 1099159X. DOI: 10.1002/pip.4670020305.

[96] M. A. Green, *Solar cells: Operating principles, technology, and system applications*. Englewood Cliffs, NJ, Prentice-Hall, Inc., 1982, p. 288.

[97] A. Huebner, A. G. Aberle, and R. Hezel, "Temperature behavior of monofacial and bifacial silicon solar cells," *Conference Record of the IEEE Photovoltaic Specialists Conference*, pp. 223–226, 1997, ISSN: 01608371. DOI: 10.1109/pvsc.1997.654069.

[98] J. C. C. Fan, "THEORETICAL TEMPERATURE DEPENDENCE OF SOLAR CELL PARAMETERS," *Energy*, vol. 17, pp. 309–315, 1986.

[99] J. Lopez-Garcia, D. Pavanello, and T. Sample, "Analysis of temperature coefficients of bifacial crystalline silicon pv modules," *IEEE Journal of Photovoltaics*, vol. 8, no. 4, pp. 960–968, 2018, ISSN: 21563381. DOI: 10.1109/JPHOTOV.2018.2834625.

[100] W. Gu, T. Ma, M. Li, L. Shen, and Y. Zhang, "A coupled optical-electrical-thermal model of the bifacial photovoltaic module," *Applied Energy*, vol. 258, no. November 2019, p. 114 075, 2020, ISSN: 03062619. DOI: 10.1016/j.apenergy.2019.114075. [Online]. Available: https://doi.org/10.1016/j.apenergy.2019.114075.

[101] E. H. Adeh, S. P. Good, M. Calaf, and C. W. Higgins, "Solar PV Power Potential is Greatest Over Croplands," *Scientific Reports*, vol. 9, no. 1, pp. 1–6, 2019, ISSN: 20452322. DOI: 10.1038/s41598-019-47803-3.

[102] M. W. Lamers, E. Özkalay, R. S. Gali, G. J. Janssen, A. W. Weeber, I. G. Romijn, and B. B. Van Aken, "Temperature effects of bifacial modules: Hotter or cooler?" *Solar Energy Materials and Solar Cells*, vol. 185, no. March, pp. 192–197, 2018, ISSN: 09270248. DOI: 10.1016/j.solmat.2018.05.033.

[103] P. Tillmann, K. Jäger, and C. Becker, "Minimising the Levelised Cost of Electricity for Bifacial Solar Panel Arrays using Bayesian Optimisation," pp. 254–264, 2019, ISSN: 23984902. DOI: 10.1039/c9se00750d. eprint: 1909.01660.

[104] M. A. Alam and M. Ryyan Khan, "Shockley–Queisser triangle predicts the thermodynamic efficiency limits of arbitrarily complex multijunction bifacial solar cells," *Proceedings of the National Academy of Sciences of the United States of America*, vol. 116, no. 48, pp. 23 966–23 971, 2019, ISSN: 10916490. DOI: 10.1073/pnas.1910745116.

[105] S. Kurtz, K. Whitfield, G. TamizhMani, M. Koehl, D. J. Miller, Joyce, J. Wohlgemuth, N. Bosco, M. Kempe, and T. Zgonena, "Evaluation of high-temperature exposure of photovoltaic modules," *PROGRESS IN PHOTOVOLTAICS: RESEARCH AND APPLICATIONS*, no. 19, pp. 954–965, 2011. DOI: 10.1002/pip.1103.

[106] E. Skoplaki and J. A. Palyvos, "Operating temperature of photovoltaic modules: A survey of pertinent correlations," *Renewable Energy*, vol. 34, no. 1, pp. 23–29, 2009, ISSN: 09601481. DOI: 10.1016/j.renene.2008.04.009.

[107] I. M. Peters and T. Buonassisi, "Energy Yield Limits for Single-Junction Solar Cells," *Joule*, 2018, ISSN: 25424351. DOI: 10.1016/j.joule.2018.03.009.

[108] G. A. Barron-Gafford, R. L. Minor, N. A. Allen, A. D. Cronin, A. E. Brooks, and M. A. Pavao-Zuckerman, "The photovoltaic heat island effect: Larger solar power plants increase local temperatures," *Scientific Reports*, vol. 6, no. May, pp. 1–7, 2016, ISSN: 20452322. DOI: 10.1038/srep35070.

[109] S. Pal and R. Saive, "Experimental study of the spectral and angular solar irradiance," *Optics InfoBase Conference Papers*, vol. Part F136-, 2019. DOI: 10.1364/PVLED.2019.PW2C.4.

[110] T. C. Russell, R. Saive, A. Augusto, S. G. Bowden, and H. A. Atwater, "The Influence of Spectral Albedo on Bifacial Solar Cells: A Theoretical and Experimental Study," *IEEE Journal of Photovoltaics*, vol. 7, no. 6, pp. 1611–1618, 2017, ISSN: 21563381. DOI: 10.1109/JPHOTOV.2017.2756068.

[111] T. C. Russell, R. Saive, and H. A. Atwater, "Thermodynamic Efficiency Limit of Bifacial Solar Cells for Various Spectral Albedos," pp. 1531–1536, 2018. DOI: 10.1109/pvsc.2017.8366261.

[112] C. P. Lee, C. A. Lin, T. C. Wei, M. L. Tsai, Y. Meng, C. T. Li, K. C. Ho, C. I. Wu, S. P. Lau, and J. H. He, "Economical low-light photovoltaics by using the Pt-free dye-sensitized solar cell with graphene dot/PEDOT: PSS counter electrodes," *Nano Energy*, vol. 18, pp. 109–117, 2015, ISSN: 22112855. DOI: 10.1016/j.nanoen.2015.10.008.

[113] K. Kakiage, Y. Aoyama, T. Yano, K. Oya, T. Kyomen, and M. Hanaya, "Fabrication of a high-performance dye-sensitized solar cell with 12.8% conversion efficiency using organic silyl-anchor dyes," *Chemical Communications*, vol. 51, no. 29, pp. 6315–6317, 2015, ISSN: 1364548X. DOI: 10.1039/c5cc00464k.

[114] R. A. Marsh, C. R. McNeill, A. Abrusci, A. R. Campbell, and R. H. Friend, "A unified description of current-voltage characteristics in organic and hybrid photovoltaics under low light intensity," *Nano Letters*, vol. 8, no. 5, pp. 1393–1398, 2008, ISSN: 15306984. DOI: 10.1021/nl080200p.

[115] M. Dürr, A. Bamedi, A. Yasuda, and G. Nelles, "Tandem dye-sensitized solar cell for improved power conversion efficiencies," *Applied Physics Letters*, vol. 84, no. 17, pp. 3397–3399, 2004, ISSN: 00036951. DOI: 10.1063/1.1723685.

[116] M. T. Patel, M. S. Ahmed, H. Imran, N. Z. Butt, M. R. Khan, and M. A. Alam, "Global analysis of next-generation utility-scale PV: Tracking bifacial solar farms," *Applied Energy*, vol. 290, no. January, p. 116 478, 2021, ISSN: 03062619. DOI: 10.1016/j.apenergy.2021.116478.

[117] United Nations, *World population prospects 2019*, 141. 2019, ISBN: 9789211483161. [Online]. Available: https://population.un.org/wpp/.

[118] S. A. Pelaez, C. Deline, P. Greenberg, J. S. Stein, and R. K. Kostuk, "Model and Validation of Single-Axis Tracking with Bifacial PV," *IEEE Journal of Photovoltaics*, vol. 9, no. 3, pp. 715–721, 2019, ISSN: 21563403. DOI: 10.1109/JPHOTOV.2019.2892872.

[119] G. Janssen, A. Burgers, A. Binani, A. Carr, B. v. Aken, I. Romijn, M. Klenk, H. Nussbaumer, and T. Baumann, "How to Maximize the KWH/KWP Ratio: Simulations of Single-axis Tracking in Bifacial Systems," in *International Conference EU PVSEC for Photovoltaics Research, 24-28 September 2018, Brussels, Belgium, 1-5*, 2018.

[120] M. A. Egido and E. Lorenzo, "Bifacial photovoltaic panels with sun tracking," *International Journal of Solar Energy*, vol. 4, no. 2, pp. 97–107, 1986, ISSN: 01425919. DOI: 10.1080/01425918608909842.

[121] J. Pérez Oria and G. Sala, "A good combination: Tracking of the sun in polar axis and bifacial photovoltaic modules," *Solar and Wind Technology*, vol. 5, no. 6, pp. 629–636, 1988, ISSN: 0741983X. DOI: 10.1016/0741-983X(88)90060-4.

[122] I. Shoukry, J. Libal, R. Kopecek, E. Wefringhaus, and J. Werner, "Modelling of Bifacial Gain for Stand-alone and in-field Installed Bifacial PV Modules," *Energy Procedia*, vol. 92, pp. 600–608, Aug. 2016, ISSN: 18766102. DOI: 10.1016/j.egypro.2016.07.025. [Online]. Available: http://dx.doi.org/10.1016/j.egypro.2016.07.025%20http://linkinghub.elsevier.com/retrieve/pii/S1876610216304520.

[123] Z. Zengwei, Z. Zhen, J. Yongfeng, L. Haolin, and Z. Shengcheng, "Performance analysis on bifacial pv panels with inclined and horizontal east-west sun trackers," *IEEE Journal of Photovoltaics*, vol. 9, no. 3, pp. 636–642, 2019, ISSN: 21563403. DOI: 10.1109/JPHOTOV.2019.2899472.

[124] F. Bizarri, "Innovative bifacial PV plant at La Silla observatory in Chile.," in *4th Bifi PV Workshop, Konstanz, Germany.*.

[125] T. P. Chang, "Performance study on the east-west oriented single-axis tracked panel," *Energy*, vol. 34, no. 10, pp. 1530–1538, 2009, ISSN: 03605442. DOI: 10.1016/j.energy.2009.06.044. [Online]. Available: http://dx.doi.org/10.1016/j.energy.2009.06.044.

[126] D. L. King, W. E. Boyson, and J. A. Kratochvil, "Photovoltaic array performance model," *Sandia Report No. 2004-3535*, vol. 8, no. November, pp. 1–19, 2004. DOI: 10.2172/919131.

[127] F. B. A Di Stefano, G Leotta, "La Silla PV plant as a utility-scale side-by-side test for innovative modules technologies," in *33rd European Photovoltaic Solar Energy Conference and Exhibition*, 2017.

[128] J. S. Stein, D. Riley, M. Lave, C. Hansen, C. Deline, and F. Toor, "Outdoor Field Performance from Bifacial Photovoltaic Modules and Systems," pp. 3184–3189, 2018. DOI: 10.1109/pvsc.2017.8366042.

[129] T. Huld and M. Suri, "Performance of Single-Axis Tracking Photovoltaic Systems in Europe," *Photovoltaic International*, pp. 1–5, 2009.

[130] M. S. Thomas Huld and E. D. Dunlop, "Comparison of Potential Solar Electricity Output from Fixed-Inclined and Two-Axis Tracking Photovoltaic Modules in Europe," *Prog. Photovolt: Res. Appl. 2008; 16:47–59*, 2007.

[131] L. N. Lorenzo and E., "Tracking and Ground Cover Ratio," *Prog. Photovolt: Res. Appl. 2008; 16:703–714*, 2008.

[132] P. Henrique, A. Veríssimo, R. A. Campos, M. V. Guarnieri, A. Veríssimo, L. Rafael, and R. Rüther, "Area and LCOE considerations in utility-scale , single-axis tracking PV power plant topology optimization," vol. 211, no. October, pp. 433–445, 2020. DOI: 10.1016/j.solener.2020.09.070.

[133] C. D. Rodríguez-Gallegos, H. Liu, O. Gandhi, J. P. Singh, V. Krishnamurthy, A. Kumar, J. S. Stein, S. Wang, L. Li, T. Reindl, and I. M. Peters, "Global Techno-Economic Performance of Bifacial and Tracking Photovoltaic Systems," *Joule*, vol. 4, no. 7, pp. 1514–1541, 2020, ISSN: 25424351. DOI: 10.1016/j.joule.2020.05.005.

[134] R. Perez, R. Seals, P. Ineichen, R. Stewart, and D. Menicucci, "A new simplified version of the perez diffuse irradiance model for tilted surfaces," *Solar Energy*, vol. 39, no. 3, pp. 221–231, 1987, ISSN: 0038092X. DOI: 10.1016/S0038-092X(87)80031-2.

[135] D. Berrian and J. Libal, "A comparison of ray tracing and view factor simulations of locally resolved rear irradiance with the experimental values," *Progress in Photovoltaics: Research and Applications*, vol. 28, no. 6, pp. 609–620, 2020, ISSN: 1099159X. DOI: 10.1002/pip.3261.

[136] M. T. Patel, R. Asadpour, M. Woodhouse, C. Deline, and M. A. Alam, "LCOE: Re-thinking LCOE for Photovoltaic Systems," *Conference Record of the IEEE Photovoltaic Specialists Conference*, pp. 1711–1713, 2019, ISSN: 01608371. DOI: 10.1109/PVSC40753.2019.8980486.

[137] NASA. (2014). "NASA MODIS Albedo: datasetId=MCD43C3_M_BSA," [Online]. Available: https://neo.sci.gsfc.nasa.gov/view.php?.

[138] M. T. Patel, M. Ryyan Khan, A. Alnuaimi, O. Albadwawwi, J. J. John, and M. A. Alam, "Implications of Seasonal and Spatial Albedo Variation on the Energy Output of Bifacial Solar Farms: A Global Perspective," *Conference Record of the IEEE Photovoltaic Specialists Conference*, pp. 2264–2267, 2019, ISSN: 01608371. DOI: 10.1109/PVSC40753.2019.8981163.

[139] B. Marion, "Albedo Data Sets for Bifacial PV Systems," no. September 2018, p. 73 375, 2019. [Online]. Available: https://datahub.duramat.org/project/about/albedo-study..

[140] P. D. Broxton, X. Zeng, D. Sulla-Menashe, and P. A. Troch, "A global land cover climatology using MODIS data," *Journal of Applied Meteorology and Climatology*, vol. 53, no. 6, pp. 1593–1605, 2014, ISSN: 15588432. DOI: 10.1175/JAMC-D-13-0270.1.

[141] C. K. Miskin, Y. Li, A. Perna, R. G. Ellis, E. K. Grubbs, P. Bermel, and R. Agrawal, "Sustainable co-production of food and solar power to relax land-use constraints," *Nature Sustainability*, vol. 2, no. 10, pp. 972–980, 2019, ISSN: 23989629. DOI: 10.1038/s41893-019-0388-x.

[142] E. Gençer, C. Miskin, X. Sun, M. R. Khan, P. Bermel, M. A. Alam, and R. Agrawal, "Directing solar photons to sustainably meet food, energy, and water needs," *Scientific Reports*, vol. 7, no. 1, pp. 1–7, 2017, ISSN: 20452322. DOI: 10.1038/s41598-017-03437-x.

[143] M. H. Riaz, H. Imran, R. Younas, M. A. Alam, and N. Z. Butt, "Module Technology for Agrivoltaics: Vertical Bifacial Versus Tilted Monofacial Farms," *IEEE Journal of Photovoltaics*, vol. 11, no. 2, pp. 469–477, 2021, ISSN: 21563403. DOI: 10.1109/JPHOTOV.2020.3048225.

[144] R. Asadpour, R. V. K. Chavali, M. R. Khan, and M. a. Alam, "Bifacial Si heterojunction-perovskite organic-inorganic tandem to produce highly efficient ($\eta_T^* \sim 33\%$) solar cell," vol. 243902, pp. 0–4, 2015, ISSN: 00036951. DOI: 10.1063/1.4922375.

[145] Oxford PV, *Bifacial Tandem Oxford PV*. [Online]. Available: https://www.pv-magazine.com/2020/12/21/oxford-pv-retakes-tandem-cell-efficiency-record/.

[146] X. Sun, R. V. K. Chavali, and M. A. Alam, "Real-time monitoring and diagnosis of photovoltaic system degradation only using maximum power point-the Suns-Vmp method," *Progress in Photovoltaics: Research and Applications*, vol. 27, no. 1, pp. 55–66, Jan. 2019, ISSN: 10627995. DOI: 10.1002/pip.3043.

[147] R. Asadpour, X. Sun, and M. A. Alam, "Electrical Signatures of Corrosion and Solder Bond Failure in c-Si Solar Cells and Modules," *IEEE Journal of Photovoltaics*, vol. 9, no. 3, pp. 759–767, 2019, ISSN: 21563403. DOI: 10.1109/JPHOTOV.2019.2896898. arXiv: 1808.05685.

[148] D. C. Jordan, C. Deline, S. R. Kurtz, G. M. Kimball, and M. Anderson, "Robust PV Degradation Methodology and Application," pp. 2–4, DOI: 10.1109/JPHOTOV.2017.2779779.

[149] R. Asadpour, M. Patel, A. Catlin, and M. Alam, "DEEDS: A Next-Generation Scientific Data Sharing and Analyzing Platform for PV Applications," in *47TH IEEE PHOTOVOLTAIC SPECIALISTS CONFERENCE*, 2020. [Online]. Available: https://par.nsf.gov/biblio/10164269.

[150] A. C. Catlin, C. Hewanadungodage, S. Pujol, L. Laughery, C. Sim, A. Puranam, and A. Bejarano, "A Cyberplatform for Sharing Scientific Research Data at DataCenterHub," *Computing in Science and Engineering*, vol. 20, no. 3, pp. 49–70, 2018, ISSN: 15219615. DOI: 10.1109/MCSE.2017.3301213.

[151] A. C. Catlin, C. Hewanadungodage, and A. Bejarano, "Lifecycle Support for Scientific Investigations: Integrating Data, Computing, and Workflows," *Computing in Science and Engineering*, vol. 21, no. 4, pp. 49–61, 2019, ISSN: 1558366X. DOI: 10.1109/MCSE.2019.2901433.

[152] M. Patel, M. Khan, and M. Alam, "Thermodynamic limit of solar to fuel conversion for generalized photovoltaic-electrochemical systems," *IEEE Journal of Photovoltaics*, vol. 8, no. 4, 2018, ISSN: 21563381. DOI: 10.1109/JPHOTOV.2018.2831446.

[153] A. Polman, M. Knight, E. C. Garnett, B. Ehrler, and W. C. Sinke, "Photovoltaic materials: Present efficiencies and future challenges," *Science*, vol. 352, no. 6283,

aad4424–aad4424, 2016, ISSN: 0036-8075. DOI: 10.1126/science.aad4424. [Online]. Available: http://www.sciencemag.org/cgi/doi/10.1126/science.aad4424.

[154] M. G. Walter, E. L. Warren, J. McKone, S. W. Boettcher, Q. Mi, E. A. Santori, and N. S. Lewis, "Solar Water Splitting Cells," *Chem. Rev.*, vol. 110, pp. 6446–6473, 2010. DOI: Doi10.1021/Cr200102n.

[155] M. Gratzel, "Photoelectrochemical cells.," *Nature (London, United Kingdom)*, vol. 414, no. 6861, pp. 338–344, 2001, ISSN: 0028-0836. DOI: 10.1038/35104607. arXiv: 5.

[156] G. Peharz, F. Dimroth, and U. Wittstadt, "Solar hydrogen production by water splitting with a conversion efficiency of 18%," *International Journal of Hydrogen Energy*, vol. 32, no. 15 SPEC. ISS. Pp. 3248–3252, 2007, ISSN: 03603199. DOI: 10.1016/j.ijhydene.2007.04.036.

[157] G. Kim, M. Oh, and Y. Park, "Solar-rechargeable battery based on photoelectrochemical water oxidation : Solar water battery," *Scientific reports*, no. August, pp. 1–9, 2016, ISSN: 2045-2322. DOI: 10.1038/srep33400. [Online]. Available: http://dx.doi.org/10.1038/srep33400.

[158] S. Licht, "Multiple band gap semiconductor/electrolyte solar energy conversion," *Journal of Physical Chemistry B*, vol. 105, no. 27, pp. 6281–6294, 2001, ISSN: 10895647. DOI: 10.1021/jp010552j. [Online]. Available: http://pubs.acs.org/doi/pdf/10.1021/jp010552j.

[159] K. Fujii, S. Nakamura, M. Sugiyama, K. Watanabe, B. Bagheri, and Y. Nakano, "Characteristics of hydrogen generation from water splitting by polymer electrolyte electrochemical cell directly connected with concentrated photovoltaic cell," *International Journal of Hydrogen Energy*, vol. 38, no. 34, pp. 14 424–14 432, 2013, ISSN: 03603199. DOI: 10.1016/j.ijhydene.2013.07.010. [Online]. Available: http://dx.doi.org/10.1016/j.ijhydene.2013.07.010.

[160] J. Jia, L. C. Seitz, J. D. Benck, Y. Huo, Y. Chen, J. W. D. Ng, T. Bilir, J. S. Harris, and T. F. Jaramillo, "Solar water splitting by photovoltaic-electrolysis with a solar-to-

hydrogen efficiency over 30%," *Energy Procedia*, vol. 77, no. 23, p. 13 237, 2016, ISSN: 2041-1723. DOI: 10.1038/ncomms13237.

[161] J. W. Ager, M. R. Shaner, K. A. Walczak, I. D. Sharp, and S. Ardo, "Experimental demonstrations of spontaneous, solar-driven photoelectrochemical water splitting," *Energy Environ. Sci.*, vol. 8, no. 10, pp. 2811–2824, 2015, ISSN: 1754-5692. DOI: 10.1039/C5EE00457H. [Online]. Available: http://xlink.rsc.org/?DOI=C5EE00457H.

[162] B. Seger, O. Hansen, and P. C. K. Vesborg, "A Flexible Web-Based Approach to Modeling Tandem Photocatalytic Devices," *Solar RRL*, vol. 1, no. 1, e201600013, 2017, ISSN: 2367198X. DOI: 10.1002/solr.201600013.

[163] M. Dumortier, S. Tembhurne, and S. Haussener, "Holistic design guidelines for solar hydrogen production by photo-electrochemical routes," *Energy Environ. Sci.*, vol. 8, no. 12, pp. 3614–3628, 2015, ISSN: 1754-5692. DOI: 10.1039/C5EE01821H. [Online]. Available: http://xlink.rsc.org/?DOI=C5EE01821H.

[164] V. R. Stamenkovic, B. Fowler, B. S. Mun, G. Wang, P. N. Ross, C. a. Lucas, N. M. Marković, C. Song, Y. Tang, J. Lu, J. Zhang, H. Wang, J. Shen, S. Mcdermid, J. Li, P. Kozak, P. Pietrasz, B. Orr, T. Simes, A. Staff, S. Daniel, and C. Lim, "III . Reaction Kinetics Lecture 1 3 : Butler-Volmer equation," *Science (New York, N.Y.)*, vol. 315, no. June, pp. 493–7, 2007, ISSN: 1095-9203. DOI: 10.1016/j.electacta.2006.09.008. [Online]. Available: http://www.ncbi.nlm.nih.gov/pubmed/17218494.

[165] J. A. V. Butler, "Studies in heterogeneous equilibria. Part II. Kinetic interpretation of the Nernst theory of electromotive force," *Trans. Faraday Society*, no. 19, pp. 729–733, 1924. [Online]. Available: http://pubs.rsc.org/-/content/articlepdf/1924/tf/tf9241900729.

[166] M. Erdey-Gruz, T.; Volmer, "Zur theorie der wasserstoffüberspannung.," *Z. Phys. Chem. 1930*, no. 150 (A), pp. 203–213, 1930. [Online]. Available: https://www.degruyter.com/downloadpdf/j/zpch.1930.150.issue-1/zpch-1930-15020/zpch-1930-15020.pdf.

[167] J. Newman, *Electrochemical Systems*, 2nd ed. Prentice-Hall, Inc.: Englewood Cliffs, NJ, 1991.

[168] S. Hu, C. Xiang, S. Haussener, A. D. Berger, and N. S. Lewis, "An analysis of the optimal band gaps of light absorbers in integrated tandem photoelectrochemical water-splitting systems," *Energy & Environmental Science*, vol. 6, no. 10, p. 2984, 2013, ISSN: 1754-5692. DOI: 10.1039/c3ee40453f. [Online]. Available: http://xlink.rsc.org/?DOI=c3ee40453f.

[169] G. Jia, A. Gawlik, J. Plentz, and G. Andrä, "Bifacial multicrystalline silicon thin film solar cells," *Solar Energy Materials and Solar Cells*, vol. 167, no. December 2016, pp. 102–108, 2017, ISSN: 09270248. DOI: 10.1016/j.solmat.2017.04.004. [Online]. Available: http://dx.doi.org/10.1016/j.solmat.2017.04.004.

[170] L. C. Hirst and N. J. Ekins-Daukes, "Fundamental losses in solar cells," *Progress in Photovoltaics: Research and Applications*, vol. 19, no. 3, pp. 286–293, May 2011, ISSN: 10627995. DOI: 10.1002/pip.1024. arXiv: 1303.4604. [Online]. Available: http://doi.wiley.com/10.1002/pip.1024.

[171] M. R. Singh, E. L. Clark, and A. T. Bell, "Effects of electrolyte, catalyst, and membrane composition and operating conditions on the performance of solar-driven electrochemical reduction of carbon dioxide," *Phys. Chem. Chem. Phys.*, vol. 17, no. 29, pp. 18 924–18 936, 2015, ISSN: 1463-9076. DOI: 10.1039/C5CP03283K. [Online]. Available: http://xlink.rsc.org/?DOI=C5CP03283K.

[172] A. Weselek, A. Ehmann, S. Zikeli, I. Lewandwski, S. Schindele, and P. Högy, "Agrophotovoltaic systems: applications, challenges, and opportunities. A review," *Agronomy for Sustainable Development*, vol. 39, no. 4, 2019, ISSN: 17730155. DOI: 10.1007/s13593-019-0581-3.

VITA

Tahir graduated from Indian Institute of Technology Bombay (IIT Bombay), India, with a Bachelors and Masters in Electrical Engineering (Micro-electronics), in 2016. He is a Honda Young Engineers and Scientists (YES) Awardee and a Kishore Vaigyanik Protsahan Yojana (KVPY) scholar. As a Honda YES Plus awardee, he was selected for a research internship at the Someya Flexible Electronics Lab at The University of Tokyo, Japan. Since Fall 2016, he has been working towards the Ph.D. degree with Alam CEED Group, School of Electrical and Computer Engineering, Purdue University, West Lafayette, IN, USA. He is currently working on energy optimization, storage solutions, and reliability issues for solar energy farms. Apart from solar photovoltaics, his research interests also include semiconductor device physics, physics-based machine learning, organic electronics and nano-bio-technology. During graduate school, he was thrice the best student paper and poster award finalist at the 46^{th} and 48^{th} IEEE Photovoltaic Specialists Conference (PVSC). He mentored a team of high school students that received the overall first prize at 46^{th} IEEE PVSC.